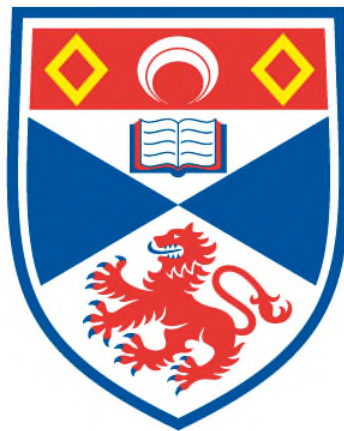


**A STUDY OF U AQUARII AND THE NUCLEOSYNTHESIS
OF NEUTRONS AND S-PROCESS ELEMENTS IN
EVOLVED STARS OF LOW MASS**

Robert A. Malaney

**A Thesis Submitted for the Degree of PhD
at the
University of St Andrews**



1986

**Full metadata for this item is available in
St Andrews Research Repository
at:**

<http://research-repository.st-andrews.ac.uk/>

Please use this identifier to cite or link to this item:

<http://hdl.handle.net/10023/4604>

This item is protected by original copyright

**This item is licensed under a
Creative Commons Licence**

A Study of U Aquarii and the Nucleosynthesis of Neutrons and
S-Process Elements in Evolved Stars of Low Mass

by

R. A. Malaney

A dissertation submitted for the degree of Doctor of Philosophy
at the University of St. Andrews

St. Andrews

September 1985



To
Mum and Dad

CERTIFICATE

I certify that Robert Anderson Malaney has spent nine terms in research work at the University Observatory, St. Andrews, that he has fulfilled the conditions of Ordinance General No. 12 and Senate Regulations under Resolution of the University Court, 1967, No. 1, and that he is qualified to submit the accompanying dissertation in application for the degree of Ph.D.



P.W. Hill

DECLARATION

Except where reference is made to others, the research described in this thesis and the composition of the thesis are my own work. No part of this work has been submitted for another degree at this or any other University. Under Ordinance General No. 12, I was admitted to the Faculty of Science of the University of St. Andrews as a research student on 1st. October 1982, to carry out an investigation on the origin of the hydrogen deficiency observed in some evolved stars. I was accepted as a candidate for the degree of Ph.D. on 1st. October 1983, under Resolution of the University Court, 1967, No. 1.

A handwritten signature in cursive script, which appears to read "Robert A. Malaney", is written on a dark, textured rectangular background.

Robert A. Malaney

In submitting this thesis to the University of St. Andrews I understand that I am giving permission for it to be made available for use in accordance with the regulations of the University Library for the time being in force, subject to any copyright vested in the work not being affected thereby. I also understand that the title and abstract will be published, and that a copy of the work may be made and supplied to any bona fide library or research worker.

ABSTRACT

The origin of the extreme hydrogen deficiency observed in the R Coronae Borealis (RCrB) stars remains poorly understood. A likely mechanism for producing this deficiency is one whereby the original hydrogen envelope of the star is engulfed and destroyed in its interior. One of the few RCrB stars so far analysed, U Aquarii, in fact shows emphatic evidence of such an event having indeed occurred. This evidence takes the form of the large s-process enhancements observed in U Aquarii. Such enhancements are caused by the production of significant neutron fluxes which are directly produced by envelope engulfment giving rise to the $^{12}\text{C}(p,\gamma)^{13}\text{N}(\beta^+\gamma)^{13}\text{C}(\alpha,n)^{16}\text{O}$ sequence of nuclear reactions. In order to obtain vital information regarding the nature of the envelope mixing event from observed s-process enhancements, detailed nucleosynthesis calculations investigating neutron production and s-process synthesis are carried out using a series of nuclear reaction networks and covering a wide range of parameter space. These calculations are mainly based on low-mass AGB and post-AGB stellar models since it is widely believed that the RCrB's are in some way related to this group of stars. It is shown how the ingestion rate of envelope material, the initial abundances and the type of mixing model used have a large influence on the neutron and s-process production.

New spectral observations of U Aquarii are presented, and it is shown how these new observations allow a new interpretation of the mixing event which occurred in this star and how further improved abundance data of the star will lead to an unambiguous determination of the nature of the mixing event. The RCrB stars are also thought to be related to the extreme helium stars. Discovery of variability in two of these latter stars is presented.

ACKNOWLEDGEMENTS

I am indebted to my supervisor, Dr. P.W.Hill, for his support, guidance and help during the period of my studies at St.Andrews. I am very grateful to Professor D.W.N. Stibbs for making available to me the facilities at the University Observatory and also for his overall support. I would like to extend thanks to Drs. C.S.Jeffery and T.R.Carson for their help and also to the rest of the staff and research students at the University Observatory for their support. I would like to thank Dr. D.Schönberner for supplying stellar models and for his hospitality at the Institut für Theoretische Physik, Kiel, W.Germany during my visit there. I thank the Directors of both the Anglo-Australian Observatory and the South African Astronomical Observatory for the use of facilities. Many thanks to Drs. D.Kilkenny and H.J.Walker for supplying additional spectra, to Dr. R.A.Bell for kindly making available his spectral synthesis package, and to Dr. A.E.Lynas-Gray for his support in producing model atmospheres and for his hospitality during my visits to University College London. I am very grateful to the following scientists for their valuable correspondence and information regarding this study; Drs. K.Despain, J.M.Scalo, A.Renzini, R.H.Deupree, J.W.Truran, I.S.Duff, A.Maeder and to Professors W.A.Fowler and S.E.Woosley. The use of computing facilities made available by the University of St.Andrews Computing Laboratory and the Royal Observatory Edinburgh STARLINK node are gratefully acknowledged. I would finally like to acknowledge the Science and Engineering Research Council for their generous allocation of travel funds and financial support through a post-graduate studentship.

CONTENTS

CHAPTER 1. INTRODUCTION

- 1.1) Stellar Neutron Synthesis
- 1.2) Discovery of Extremely Hydrogen Deficient Stars
- 1.3) Evolution of EHe and RCrB Stars
- 1.4) Mixing Mechanisms
- 1.5) Abundance Analyses
- 1.6) Variability
- 1.7) Plan of Thesis

CHAPTER 2. BASIC NUCLEOSYNTHESIS THEORY

- 2.1) Nuclear Reactions in Stellar Interiors
 - a) Generalities
 - b) Non-Resonant Reactions
 - c) Resonant Reactions
 - d) Neutrons
 - e) Beta Decay
- 2.2) Heavy Element Synthesis by the S-Process
- 2.3) Numerical Analysis of a Reaction Network
 - a) Numerical Solution
 - b) Errors
 - c) Computations
- 2.4) The Reaction Networks

CHAPTER 3. NEUTRON PRODUCTION AT A HELIUM SHELL FLASH

- 3.1) The Helium Shell Flash
 - a) Details of the Flash
 - b) Neutron Sources
- 3.2) Calculations
- 3.3) Results
 - a) Parameters Affecting Neutron Production
 - b) Effect of Intershell Splitting
 - c) Delayed Mixing by Semiconvection
- 3.4) Neglect of Energy Generation and Conclusions

CHAPTER 4. HEAVY ELEMENT SYNTHESIS

- 4.1) Preliminary Calculations
- 4.2) Fe to Mo Enhancement Neglecting Intershell Splitting
- 4.3) Fe to Mo Enhancement Including Intershell Splitting
 - a) Total Element Enhancement
 - b) Individual Isotopic Enhancement
- 4.4) Repeated Shell Flashes
- 4.5) Conclusions

CHAPTER 5. COARSE DIFFERENTIAL ABUNDANCE ANALYSIS OF U AQUARI

- 5.1) Discovery of Sr and Y Enhancements in U Aquarii
- 5.2) Observations and Method of Analysis
- 5.3) Results
- 5.4) Conclusions

CHAPTER 6. THE ORIGIN OF U AQUARI

- 6.1) Hydrogen Deficiency
- 6.2) AGB and Post-AGB Comparison
- 6.3) Nature of the Neutron Exposure
- 6.4) The Helium Core Flash
- 6.5) FG Sagittae
- 6.6) Conclusions

CHAPTER 7. PHOTOMETRIC STUDY OF EXTREME HELIUM STARS

- 7.1) Purpose for Photometric Study of EHe Stars
- 7.2) Variability of BD-9^o4395
 - a) Observations
 - b) Nature of the Variability
- 7.3) Variability of BD+1^o4381
- 7.4) Conclusions

CHAPTER 8. CONCLUSIONS AND FUTURE WORK

8.1) Neutron Production in Low-Mass AGB and Post-AGB Stars

8.2) Heavy Element Production

8.3) Origin of the RCrB and EHe Stars

8.4) Future Analyses of RCrB Type Spectra

8.5) Future Calculations

APPENDIX

REFERENCES

TABLES

Table 1.1	Known EHe stars
Table 1.2	Known RCrB stars
Table 2.1	Light particle network
Table 2.2	Heavy element network (no branching)
Table 3.1	Properties of 13th and 24th flashes
Table 3.2	Initial abundances
Table 3.3	Changes of light particle abundances
Table 3.4	Summary of peak neutron fluxes
Table 3.5	$^{13}\text{C}/^{14}\text{N}$ and neutron fluxes following splitting for $T_b=2.4 \times 10^8 \text{ }^\circ\text{K}$
Table 3.6	$^{13}\text{C}/^{14}\text{N}$ and neutron fluxes following splitting for $T_b=2.75 \times 10^8 \text{ }^\circ\text{K}$
Table 3.7	$^{13}\text{C}/^{14}\text{N}$ and neutron fluxes following splitting for $T_b=2.75 \times 10^8 \text{ }^\circ\text{K}$ and for low initial carbon
Table 3.8	Different $^{13}\text{C}/^{14}\text{N}$ and neutron fluxes following splitting for $T_b=2.4 \times 10^8 \text{ }^\circ\text{K}$
Table 3.9	Initial ^{13}C rich region
Table 3.10	Neutron densities arising from Iben and Renzini mixing
Table 4.1	Initial abundances for initial heavy element calculations
Table 4.2	Heavy element preliminary enhancements
Table 4.3	Enhancements from $2.5 \times 10^{-5} M_\odot$ mixing (no splitting)
Table 4.4	Enhancements for different average flux conditions
Table 4.5	Enhancements after intershell splitting
Table 4.6	Enhancements of the individual isotopes of table 4.5
Table 4.7	Final enhancements for figures 4.9 to 4.20
Table 4.8	Isotopic enhancements for figures 4.9 to 4.20
Table 4.9	Direct repeated mixing enhancements
Table 4.10	Direct repeated mixing enhancements for isotopes

Table 5.1	UBV Photometry of U Aquarii and HD182040
Table 5.2	Equivalent widths
Table 5.3	$[N_{\text{Fe}}/N_{\text{op}}]$ For FeI lines
Table 5.4	Logarithmic abundances
Table 5.5	[E1/Fe] Ratios of U Aquarii relative to HD182040
Table 5.6	Observed abundances compared to exponential exposure curve
Table 6.1a	Comparison of models of table 4.5 for $d=10$
Table 6.1b	Comparison of models of table 4.5 for $d=30$
Table 6.2	Comparison of models for repeated shell flash calculations
Table 6.3	Observed FG Sagittae enhancements
Table 7.1	BD-9 ^o 4395 photometry
Table 7.2	Adopted frequency solution for BD-9 ^o 4395
Table 7.3	BD+1 ^o 4381 photometry
Table 8.1	Comparison of single with repeated mixing

FIGURES

- Figure 1.1 Light curve of RCrB
- Figure 1.2 Evolutionary track of RCrB-EHe stars in $\text{Log } g\text{-Log } T_{\text{eff}}$ plane
- Figure 1.3 $1.45M_{\odot}$ evolutionary track
- Figure 2.1 Tunnelling effect of particle with $E < E_c$
- Figure 2.2 $\sigma(E)$ behaviour
- Figure 2.3 Nuclear branching diagram
- Figure 2.4 Fe to Mo reaction network
- Figure 3.1 Basic structure of low-mass AGB star
- Figure 3.2 Luminosity behaviour for 7th 8th and 9th flashes
- Figure 3.3 Luminosity of helium, hydrogen and total for 9th flash
- Figure 3.4 Structure at maximum convection extent
- Figure 3.5 Schönberner evolutionary track
- Figure 3.6 Run of temperature and density
- Figure 3.7 Diffusion of ingested envelope material
- Figure 3.8 Mixing of $2.5 \times 10^{-6} M_{\odot}$ of envelope material into an intershell with $T_b = 2.4 \times 10^8 \text{ }^{\circ}\text{K}$
- Figure 3.9 Same as figure 3.8 only showing effect of high initial ^{18}O
- Figure 3.10 Mixing of $2.5 \times 10^{-6} M_{\odot}$ of envelope material into an intershell with $T_b = 2.75 \times 10^8 \text{ }^{\circ}\text{K}$
- Figure 3.11 Same as figure 3.10 only neglecting absorptions on heavy nuclei
- Figure 3.12 Neutron densities
- Figure 3.13 Neutron densities for v_c varied
- Figure 3.14 Final zone abundances for $10 \times 2.5 \times 10^{-7} M_{\odot}$ mixing
- Figure 3.15 Final zone abundances for $10 \times 2.5 \times 10^{-6} M_{\odot}$ mixing
- Figure 3.16 $^{13}\text{C}/^{14}\text{N}$ ratio as a function of mixing
- Figure 4.1 Path of linear flow-no branching
- Figure 4.2 Heavy element enhancements Br to Zr as function of time (from model B table 4.5)
- Figure 4.3a Heavy element enhancements Cu to Se as function of time

- Figure 4.3b Heavy element enhancements Br to Zr as function of time
(from 2nd model table 4.4)
- Figure 4.4 Late slow flux on total element enhancements
- Figure 4.5 Light particle reactions
- Figure 4.6 Importance of unthermalised nuclei
- Figure 4.7 Late synthesis by slow flux on individual isotopes
- Figure 4.8 r as a function of shell flash
- Figure 4.9a Repeated mixing for $r=0.7$, thermalised
4.9b
- Figure 4.10a Repeated mixing for $r=0.7$, unthermalised
4.10b
- Figure 4.11a Repeated mixing for $r=0.8$, unthermalised
4.11b
- Figure 4.12a Repeated mixing for $r=0.85$, thermalised
4.12b
- Figure 4.13a Repeated mixing for $r=0.85$, unthermalised
4.13b
- Figure 4.14a Repeated mixing for $r=0.9$, thermalised
4.14b
- Figure 4.15a Repeated mixing for $r=0.9$, unthermalised
4.15b
- Figure 4.16a Repeated mixing for $r=0.9$, thermalised (0.1 solar seed)
4.16b
- Figure 4.17a Repeated mixing for $r=0.9$, unthermalised (0.1 solar seed)
4.17b
- Figure 4.18a Repeated mixing for $r=0.85$, unthermalised (0.1 solar seed)
4.18b
- Figure 4.19a Repeated mixing for $r=0.9$, unthermalised (Ne=0.01, Fe normal)
4.19b
- Figure 4.20a Repeated mixing for $r=0.85$, unthermalised (high ^{12}C)
4.20b
- Figure 4.21a Repeated direct mixing for $r=0.85$, thermalised
4.21b
- Figure 4.22a Repeated direct mixing for $r=0.85$, unthermalised
4.22b
- Figure 4.23 Repeated mixing distribution
- Figure 4.24 Single mixing distribution

- Figure 5.1 U Aquarii
- Figure 5.2 HD182040
- Figure 5.3 Abundances from exponential distribution of neutron exposures
- Figure 6.1 Loop mechanism for RCrB stars
- Figure 6.2 Model B ratios as a function of d
- Figure 6.3 Model C ratios as a function of d
- Figure 6.4 Model E ratios as a function of d
- Figure 6.5 Model G ratios as a function of d
- Figure 6.6 Repeated mixing for $r=0.85$, as a function of d (solar seed)
- Figure 6.7 Repeated mixing for $r=0.85$, as a function of d (0.1 solar seed)
- Figure 6.8 Comparison of single and repeated mixing distributions
- Figure 6.9 Core flash heavy element build up
- Figure 7.1 BD-9^o4395 photometry
- Figure 7.2 BD+1^o4381 photometry
- Figure 7.3 BD+1^o4381 phased with period of 21.3 days
- Figure 8.1 Synthesized SrII 4077 for C/He=0.01
- Figure 8.2 Synthesized YII 3950 for C/He=0.01
- Figure 8.3 Synthesized SrII 4077 for C/He=0.03
- Figure 8.4 Synthesized SrII 4077 for C/He=0.001
- Figure 8.5 Synthesized spectra for $H=10^{-4}$
- Figure 8.6 Synthesized spectra for $H=10^{-5}$

CHAPTER 1. INTRODUCTION

1.1) Stellar Neutron Synthesis

Burbidge et al. (1957, hereafter designated B²FH) showed that neutron capture processes have played the primary role in stars of the heavy elements beyond the iron group. Because of repulsive Coulomb forces, charged particle reactions have been rather ineffective at the temperatures (10^8 to 10^9 °K) at which the main line heavy element synthesis has apparently occurred. It was suggested by Suess and Urey (1956) and Coryell (1956), and shown in detail by B²FH that two quite different and independent neutron capture processes are necessary to synthesize the abundant heavy elements. In one of these processes called the s-process, the neutron captures occur at a slow (s) rate compared to the intervening beta decays. Thus the synthesis path lies along the bottom of the valley of mass stability and in general by-passes both the proton rich, lightest isotopes and the neutron rich, heaviest isotopes of the elements involved. On the other hand, in the second neutron process, called the r-process, the neutron capture processes occur at a rapid (r) rate compared to the intervening beta decays. The captures lead rapidly from stable seed nuclei, predominantly ⁵⁶Fe, to the very neutron rich side of the mass valley and are stopped only by photo-ejection of the weakly bound neutrons by the ambient gamma-ray flux associated with the high temperatures necessary for the production of neutrons. Equilibrium between (n, γ) and (γ, n) reactions is established and the progress along the synthesis path occurs only through electron-antineutrino ejection or beta decay which permits further neutron capture. It follows that since these processes

occur at quite different rates, then two separate and distinct stages of stellar evolution are required. B²FH assigned the s-process to the red giant stage of stellar evolution and the r-process to events taking place in exploding envelopes or cores of supernovae. The s-process is believed to operate at neutron densities of typically 10^7 neutrons/cm³ (Blake and Schramm 1975), while the r-process occurs at 10^{23} neutrons/cm³ (Clayton 1968).

More recent work of neutron synthesis in stars has been based upon the identification of a new site for s-process synthesis. This site is the convective helium shells accompanying helium shell flashes in low and intermediate-mass Asymptotic Giant Branch (AGB) stars (Schwarzschild and Härm 1965,1967). Two possible neutron sources first identified by Cameron (1955, 1960), the $^{13}\text{C}(\alpha, n)^{16}\text{O}$ and the $^{22}\text{Ne}(\alpha, n)^{25}\text{Mg}$ source can be produced in substantial quantities in the convective intershells of such stars. Neutron production via the ^{13}C source is thought to more likely occur in low-mass ($M < 2M_{\odot}$) AGB stars and has been investigated by Sanders (1967), Cowan and Rose (1977), Despain (1977) and Iben and Renzini (1982b). The ^{22}Ne source is believed to be more dominant in the intermediate stars ($2M_{\odot} < M < 8M_{\odot}$), and the operation of this source in such stars has been studied extensively by Iben (1975a, b) and Truran and Iben (1977).

The neutron densities found from calculations of AGB neutron synthesis (10^{11} to 10^{14} neutrons/cm³) are roughly midway between those densities believed to be responsible for the classical s-process and the r-process. This led to the term i-process (intermediate-process) by Cowan and Rose (1977) for the neutron synthesis occurring on the AGB. An attractive feature of the AGB production of neutrons is that

repeating helium shell flashes can lead quite naturally to an exponential distribution of neutron exposures to iron seeds (Ulrich 1973). Seeger, Fowler and Clayton (1965) pointed out that the solar-system heavy element abundances were well modelled by such an exponential exposure. The work of Truran and Iben (1977) indicates that the ^{22}Ne source is the more attractive of the two neutron sources for production of the solar system abundances, mainly due to the filtering action of the progeny of the ^{22}Ne source (see later). Also, the intermediate-mass stars, in which the ^{22}Ne source operates, are thought to contribute substantially to the enrichment of the interstellar medium (Iben and Truran 1978).

However, many low-mass evolved red giants show enhancements of heavy elements at their surfaces (Scalo 1980), and these enhancements usually form a non-solar distribution. The ^{13}C source is believed to be operational in these stars. Surprisingly, little detailed work coupling the production of neutrons and heavy element build up in low-mass AGB stars has been carried out. This leaves an important gap when it comes to interpreting the observed enhancements in low-mass evolved stars. Cowan and Rose (1977) used a light particle network to investigate neutron production from the ^{13}C source. However, their stellar model was appropriate to a stellar mass of $M > 3M_{\odot}$, and they neglected the important effect of heavy element neutron absorption on their calculated neutron densities. No attempt to follow the heavy element synthesis was made. Despain (1977) constructed a light particle network to investigate the neutron production in a $1M_{\odot}$ AGB star. However, in these calculations a full convective link up of the envelope with the intershell was assumed, which resulted in a large amount of hydrogen being mixed in. The highest base temperature used was $2.5 \times 10^8 \text{ }^{\circ}\text{K}$ and

the calculations were stopped after 10^6 s. The heavy element enhancements were calculated analytically and as such did not allow the inclusion of the important effect of nuclear branching (see later). It would be important to extend these calculations to a much wider range of conditions applicable to AGB evolution. In particular, it would be important to investigate the neutron production resulting from smaller hydrogen mixing events which occur when a full convective link up does not occur. Also, the calculations should investigate the effect of higher base temperatures, and the heavy element network should include nuclear branching if a comparison with observed enhancements is to be of any value.

In order to investigate in detail the parameters which effect neutron production in a low-mass AGB star a light particle network larger than any previously used was constructed. This network was coupled directly to a large heavy element network which included nuclear branching for the element region of interest. The stellar model used was appropriate to a $1.45M_{\odot}$ AGB star undergoing mass loss via stellar wind. The network was numerically solved under a wide range of conditions relevant to possible situations which could arise on the AGB and on the post-AGB. These calculations provide a theoretical basis for comparison with observed heavy element enhancements. In particular, a comparison of the observed enhancements of a star which belongs to a group of peculiar stars is made, in the hope that this may shed some light on the unknown origin of these stars. The group of stars in question is the class of stars known as the extremely hydrogen deficient stars. The following sections describe the initial discovery of these stars and the subsequent theoretical and observational work done on them.

1.2) Discovery of Extremely Hydrogen Deficient Stars

The first extremely hydrogen deficient star was discovered by Popper in 1942 (HD124448). On analysis of this star he found that there were no lines of hydrogen in the visible spectrum and that the lines originally attributed to hydrogen were due to neutral helium. This discovery led to a search by Thackeray and Wesselink (1952) for stars with similar properties. As a consequence of this search, they discovered the hydrogen deficient star HD168476. This was followed by the discovery of hydrogen deficiency in HD160641 by Bidelman (1952). Gould et al. (1957) discovered the first subdwarf (BD+75°325) to be deficient in hydrogen, and a year later Greenstein and Wallerstein (1958) found a member of the multiple σ Ori E system was hydrogen deficient although not to the same extent as the earlier discoveries. This star is often regarded as the prototype star of the group of stars known as the intermediate helium-rich stars. Another group of stars discovered to be hydrogen deficient are the helium-rich close binaries (Hack 1967).

Hunger (1975) proposed a classification scheme for the hydrogen deficient stars. The extreme helium stars (hereafter termed EHe stars) are defined as those stars in which the number ratio of hydrogen to helium is given by $n_{\text{H}}/n_{\text{He}} < 0.1$ (these stars are also termed in the literature, "extreme helium-rich", "extremely hydrogen poor", or "extremely hydrogen deficient" stars). The EHe stars usually have spectral type B or O and typically the $n_{\text{H}}/n_{\text{He}}$ ratio is as low as 10^{-4} . The intermediate helium stars have $n_{\text{H}}/n_{\text{He}} > 0.1$ and are spectral type

B. The helium rich subdwarfs have similar hydrogen abundances to the intermediates and are usually of spectral type O. The EHe stars are mostly found at high galactic latitudes, whereas the intermediate helium stars are found in the galactic plane. In general the EHe stars have high galactic latitudes although Hunger (1975) shows that these stars follow the galactic rotation and so the stars may not be necessarily be population II objects as suggested by their high radial velocities. They have present masses in the range $0.6M_{\odot}$ to $1M_{\odot}$ with their initial masses thought to be in the range of $0.9M_{\odot}$ to $2.1M_{\odot}$ (Heber 1983). The difference in these masses being accounted for by stellar wind. The EHe stars and the intermediate stars are not thought to be linked by evolution and it is thought that they form completely independent groups of stars. The hydrogen deficiency of the intermediate helium-rich stars has been suggested by Osmer and Peterson (1974) to be due to diffusion and gravitational settling. The hydrogen deficiency of the helium-rich close binaries is believed to be related to mass transfer mechanisms (Hack 1967). The subdwarfs are not believed to be genetically linked with the EHe stars, however, at the present it is not yet clear whether the subdwarfs are related to the intermediates.

At the present time roughly 20 EHe stars are known. A major contribution to this list comes from the spectral survey of the southern sky by MacConnell, Frye and Bidelman (1972), with the most recent additions to the list reported by Drilling (1973 and 1978) for SS3778 and LSII+33⁰5 respectively, and Drilling (1979) for BD+1⁰4381 and LSIV-14⁰109. The known EHe stars are listed in table 1.1 arranged in order of increasing right ascension, with their visual magnitudes also listed. Johnson colours for the stars, galactic coordinates, proper motions and other details are given by Hunger (1975).

Warner (1967) included some of the hot EHe stars in his list of cool hydrogen deficient carbon (HdC) stars. These HdC stars can be further divided into variable and non-variable HdC stars. The variable stars are more commonly known as the R Coronae Borealis (RCrB) stars. These stars are believed to be old disc population stars (although the dangers of assigning such a small sample of stars to one particular population should be stressed) with masses similar to those of the EHe stars. They are found in the spectral classes F-K and they too are depleted in hydrogen by factors of typically 10^4 . Carbon is enhanced in their atmospheres by factors of about 20 compared to the carbon enhancements of between 5 and 10 found in the EHe stars. A peculiar property of the RCrB stars is the large irregular variations undergone by them (Warner 1967; Feast 1975). Figure 1.1 shows such variations for the first RCrB star discovered. This star is RCrB itself and was discovered by Piggot in 1795. It is normally a sixth magnitude star and it remains so for months and sometimes years at a time. At irregular intervals however it will suddenly fade without any warning to about twelfth magnitude. After passing through these deep minima the star will commence to climb back to its original brightness, this ascent being marked in almost every case by quite pronounced fluctuations. What may be termed the classical view of RCrB stars is that this phenomenon is in some way associated with a dust shell, ejected somehow by the star, surrounding a stellar core. This view is supported by infra-red observations which show infra-red excesses surrounding several RCrB stars (Feast 1975; Kilkenny and Whittet 1984) which can be associated with cool dust shells. However, this view has not gone uncontested. Humphrey and Ney (1974) suggest the infra-red excess originates from a cool companion star and matter from the companion

flows onto the RCrB star causing the large light variations. But studies of the RCrB star RY Sgr (Feast 1978), which also happens to be a pulsating variable with a period of 38.6 days (Alexander et al. 1972), show the infra-red excess of this star also has this period. This would tend to support the idea of a dust cloud intrinsically linked to the star. The known RCrB stars are listed in table 1.2.

The origin of the extreme hydrogen deficiency of both the RCrB and the EHe stars and an understanding of their evolutionary status is at the present time still unclear. These problems form the thrust of this thesis project. It has been suggested that the RCrB and the EHe stars are evolutionary linked. This is discussed in the next section.

Table 1.1

Known EHe stars

Star	R.A.	Dec	Mag
BD +37 442	1 55 36	+38 19.5	10.0
BD +37 1977	9 21 17	+36 55.0	10.1
BD +10 2179	10 36 17.2	+10 19 27	10.0
CPD -58 2721	10 45 58.1	-58 53 01	10.3
AE 1	13 20 49.7	-41 28 56	13 - 17
HD 124448	14 11 46.6	-46 03 22	10.0
CoD -48 10153	15 35 24.3	-48 26 14	11.4
HD 144941	16 06 23	-27 08.9	8
BD -9 4395	16 25 51.6	-9 12 54	10.6
V652 Her	16 45 45.9	+13 20 57	10.6
HDE 320156	17 34 37.5	-35 21 21	9.8
V2076 Oph	17 38 55.0	-17 55 00	9.9
LS IV -1 2	17 48 51.0	-1 42 34	11.0
BD -1 3438	18 01 20.5	-1 00 33	10.4
HD 168476	18 18 59.8	-56 39 15	9.4
LS IV -14 109	18 56 49.1	-14 30 30	11.2
LS II +33 5	19 43 23.7	+33 51 05	10.4
BD +1 4381	20 48 49.5	+2 07 29	9.7

Table 1.2

Known RCrB stars

Star	R.A.	Dec.	Mag
XX Cam	4 04 46.1	+53 13 44	8.2- 10.3
W Men	5 27 05	-71 13.6	13.8->18.3
SU Tau	5 46 09	+19 03.1	9.1- 16.0
UW Cen	12 40 26	-54 15.3	9.6->13
Y Mus	13 02 34	-65 14.7	10.5- 12.1
S Aps	15 04 20	-71 52.0	9.6- 15.2
R CrB	15 46 30.7	+28 18 32	5.8- 14.8
RT Nor	16 20 04	-59 13.9	11.3- 16.3
RZ Nor	16 28 39	-53 10	11.1- 12.7
LR Sco	17 24 17	-43 48.4	10.9- 12.3
WX CrA	18 05 27	-37 20.1	11.0->16.5
VZ Sgr	18 11 57	-29 43.4	11.8->14.0
RS Tel	18 15 07	-46 34.0	9.3->13.0
GU Sgr	18 21 12	-24 16.8	11.3- 15.0
V348 Sgr	18 37 18.2	-22 57 18	10.6- 17
MV Sgr	18 41 32.9	-21 00 21	12.7- 15.6
V CrA	18 44 07	-38 12 51	8.3->16.5
SV Sge	19 05 58	+17 32.9	11.8- 16.2
RY Sgr	19 13 16.8	-33 36 41	6 - 11
U Aqr	22 00 36	-16 52.2	10.5->14.4
UV Cas	23 00 08	+59 20.5	11.8- 16.5

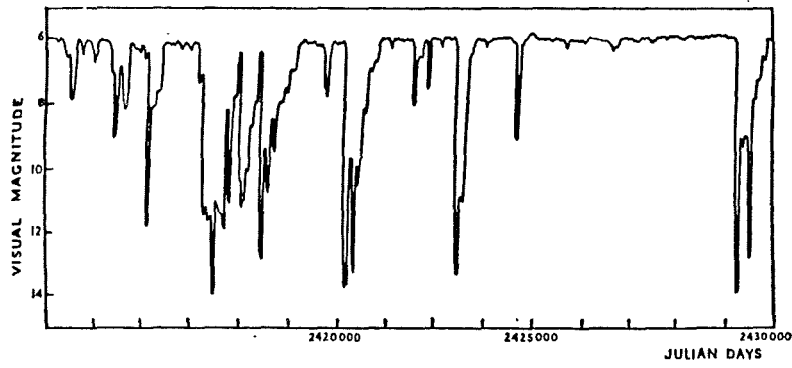


Figure 1.1 Light curve of RCrB (taken from Glasby 1968)

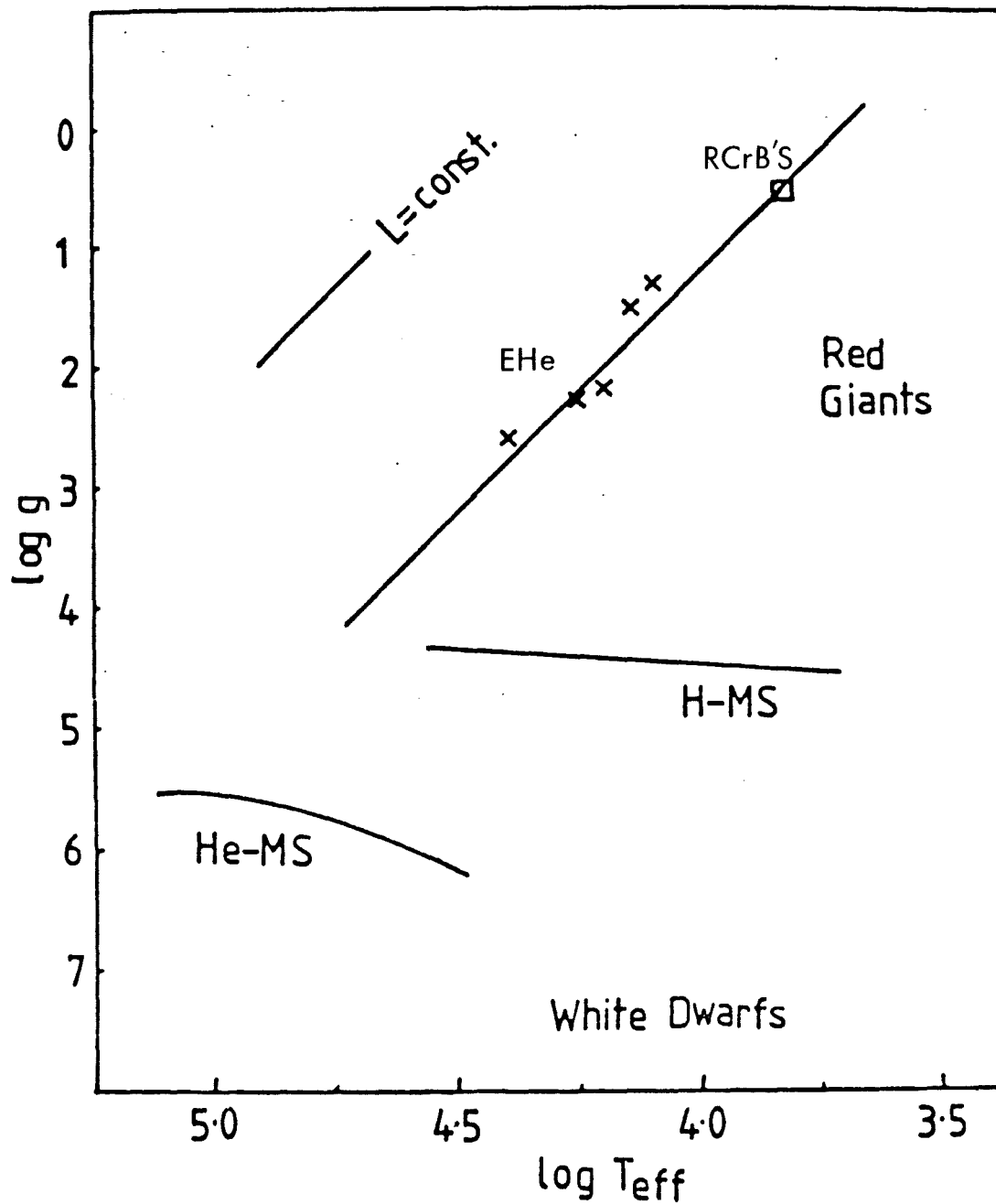


Figure 1.2 Evolutionary track of RCrB-EHe stars in Log g -Log T_{eff} plane

1.3) Evolution of EHe Stars and RCrB Stars

Schönberner (1975,1977) has suggested the RCrB stars may be the progenitors of the EHe stars. Evidence for this, apart from the obvious similarity with respect to hydrogen deficiency can be found from a study of where these stars are placed on the $\log g$ - $\log T_{\text{eff}}$ diagram. The parameters, gravity and effective temperature are used because they are directly obtained from a fine analysis of the atmosphere without taking recourse to the mostly ill-defined distances and luminosities of both the RCrB and EHe stars. The g, T_{eff} plane is morphologically a Hertzsprung-Russell diagram. A line of constant luminosity for a given mass is transformed by $L \propto R^2 T_{\text{eff}}^4$ and $g \propto 1/R^2$ to $g \propto T_{\text{eff}}^4$. From figure 1.2 it can be seen that the RCrB and the EHe stars lie on a line of roughly constant luminosity. This may be an indication of an evolutionary link between the two groups (Schönberner 1977). Also shown in the diagram is the position of the white dwarfs, the hydrogen main sequence and the hypothetical helium main sequence. The EHe star BD+13^o3224 is not shown here as this star is relatively hydrogen rich compared with other EHe stars and is thought to be in a different evolutionary phase (Jeffery 1984).

Schönberner (1977) has followed numerically the evolution of stars with a condensed C/O core and helium envelope, from the red giant phase. He suggests that the RCrB stars are remnant asymptotic giant branch (AGB) stars which lose their hydrogen envelopes by some means during their rise up the AGB. The RCrB stars then contract towards higher temperatures becoming EHe stars and then helium rich (DB) white dwarfs. He further suggests that the birth rate of DB white dwarfs is

not very different to the predicted death rate of EHe stars, so that a large number of all low-mass stars pass through the RCrB-EHe phase. Bues (1970), however, claims that a metal deficiency of 10 to 100 observed in the DB white dwarfs rule out any connection with the EHe stars which have a much higher metal abundance. The rapid evolutionary timescales of a few thousand years at the RCrB-EHe phase of evolution would account for the few number of stars observed. Further evidence for a link between the RCrB and the EHe stars is indicated from variability studies of these stars (see section 1.6).

Even if this evolutionary scheme for the RCrB and the EHe stars is correct the problem of explaining the extreme hydrogen deficiency of these objects remains. This has remained the most outstanding problem concerning these stars since Popper's original discovery. It would seem very unlikely for the objects all to have been originally formed from hydrogen free material. The more plausible explanation is that the stars have evolved to their current evolutionary state, either by converting their hydrogen envelopes to helium by complete mixing, or by ejection of the envelope, or by a combination of both. Schönberner (1979) has evolved low-mass AGB models from the early stages of the AGB where helium shell flashes (Schwarzschild and Härm 1965, 1967) commence, through to the phase where the models approach the white dwarf regime. A track from these models is shown (full line) in figure 1.3 (the dashed track is due to a possible mixing mechanism discussed in section 1.4). The model commenced with an initial total mass of $1.45M_{\odot}$ and an initial helium core mass of $M_c = 0.475M_{\odot}$. This represents a post helium core flash model. The model undergoes up to 34 helium shell flashes as the star rises up the AGB. Large scale mass loss occurs via a stellar wind given by Reimers' (1975) mass loss rate. The value of

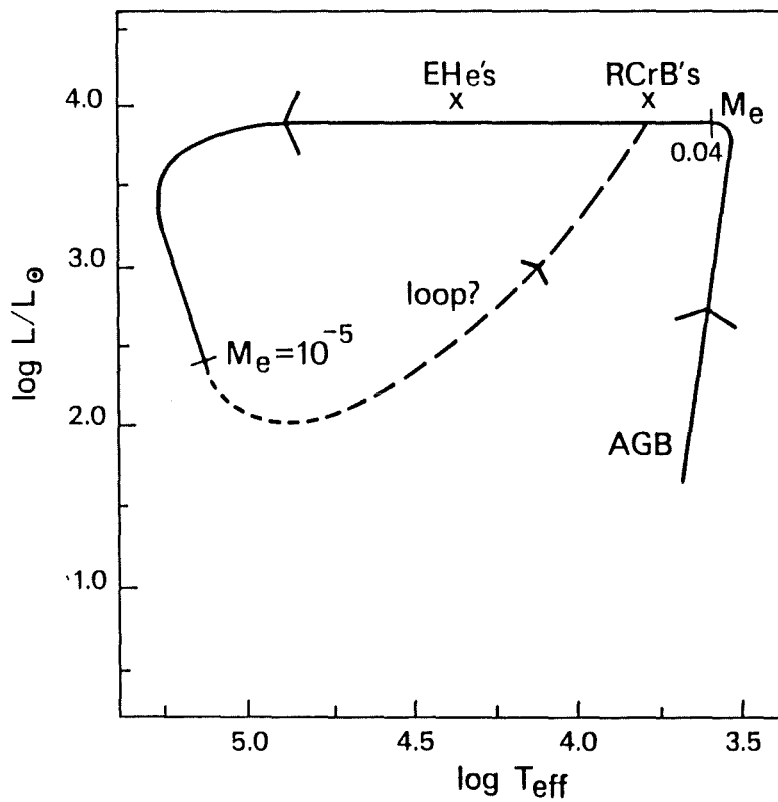


Figure 1.3 $1.45 M_{\odot}$ evolutionary track

the hydrogen envelope mass, M_e (in solar masses), at different phases of the stars evolution, having taken account of the stellar wind, is indicated. Also shown is the observed position of the RCrB and the EHe stars. It was found that the hydrogen envelope can never be completely removed by this means. This is consistent with a problem first discussed by Paczynski (1971) in attempting to explain the hydrogen deficiency of RCrB stars simply by continual mass loss or ejection. The problem being if that such mass loss occurred from the envelope then a compact helium-rich stellar core remains. It is difficult to envisage circumstances which would allow such a remnant core to expand to the high luminosities and large radii found for the RCrB stars.

It would therefore seem likely that at least some mixing of hydrogen envelope material into the interior regions of these stars has occurred. This conclusion is further enhanced by the discovery by Bond et al. (1979) of large s-process enhancements in the RCrB star U Aquarii. Such enhancements can readily be explained by hydrogen mixing into a stellar interior. This is discussed at length in chapter 2. The possible mixing mechanisms which can occur in red giants are discussed in the following section.

1.4) Mixing Mechanisms

There is good evidence for some sort of mixing process taking place in red giants in general. This evidence takes the form of the anomalous abundances of carbon and various other chemical elements seen in the atmospheres of these stars. These anomalous abundances suggest that somehow, material which has undergone nuclear burning processes, have been transported to the surface. There have been several models put forward which attempt to explain the mixing processes going on within these stars. Most of these models depend on thermal instabilities in evolved stars. These instabilities are the helium core flash (discovered by Schwarzschild and Selberg 1962; Schwarzschild and Härm 1962), and the helium shell flash (discovered by Schwarzschild and Härm 1965, 1967). A full review of the abundance anomalies and mixing mechanisms in red giants is given by Scalo (1980).

The helium core flash occurs when helium is ignited in a degenerate core at the tip of the first red giant branch just prior to the horizontal branch phase of evolution. This has been shown to occur in stars with masses less than $2.2M_{\odot}$ when the core mass reaches $0.45M_{\odot}$ (Iben 1967). The burning is thermally unstable and the helium core flash ensues. Most of the energy goes into expanding the core and removing the degeneracy. It is not clear at the present time whether substantial mixing between the stellar envelope and the stellar interior takes place as a consequence of the flash. The most recent calculations by Deupree (1984b) indicate that substantial mixing may indeed take place.

After the core flash subsides the star becomes a stable helium core burning object on the horizontal branch. After a period of about 10^5 years helium is burning in a thin shell surrounding an inert C/O core. Further out in the star hydrogen re-ignites, also in a thin shell, the star is now said to be in a double shell source structure and starts to commence its rise up the AGB. The luminosity of the star arises mainly from the hydrogen shell at this phase of quiescent burning. Depending on the conditions of the helium burning shell (mostly the thickness of the shell) a thermal instability can occur within it. A thermal runaway ensues within the helium shell which causes a rapid rise in the helium shell luminosity (this is termed a "helium shell flash", or a "thermal pulse"). One of main consequences of this luminosity rise is the appearance of an intershell convective zone rising upwards from the helium shell. If this convective zone can reach up to and penetrate the hydrogen shell then the possibility of mixing between the envelope and the interior can occur. The interior structure of the star at this stage for a $1.45M_{\odot}$ model is shown in figure 3.1 and is discussed in detail in chapter 3.

In low-mass stars it is not yet clear whether such mixing takes place. Most of the previously published calculations e.g. Rose and Smith (1972), Sweigart (1974) and Schönberner (1979) showed that for low-mass stars the convective region closely approaches but does not penetrate the hydrogen shell. The lack of penetration being mainly due to an entropy barrier (Iben 1976) at the hydrogen shell. However, it is plausible in view of the approximate nature of such model calculations, that penetration could arise as a result of physical processes that have not been included in the calculations.

In intermediate-mass stars the explanation of nuclear synthesized material appearing in the star's atmosphere is more readily explained. Following a thermal pulse (pulse powerdown phase) in such stars, when the hydrogen shell is extinguished, the base of the convective envelope of the star can penetrate down into the carbon-helium rich region left behind by the now extinct convective intershell zone (Iben 1975a, 1976, 1977). Hydrogen is then mixed into this carbon rich region and freshly synthesized material (i.e. carbon and other nuclei produced in the intershell) can be "dredged up" to the surface. However, in low-mass AGB stars ($M < 2M_{\odot}$) the convective envelope does not penetrate deep enough for any dredge up to occur. The smallest mass for which the dredge up phenomenon has been found in any calculations is that of Wood's (1982) model which had a core mass $M_c = 0.67M_{\odot}$ and a total mass of $M = 2M_{\odot}$. Further, it is suggested that as the total mass of the star decreases, the minimum core mass for convective dredge up increases (Wood 1981). Yet recent observations of carbon stars in the Magellanic Clouds (eg. Richer 1981) suggests that some form of dredge up occurs in any AGB star irrespective of its mass (Iben 1982). This discrepancy led Iben and Renzini (1982a, 1982b) to show that mixing could arise when the effects of the increased opacity of carbon (generated by the flash) in the cooler regions of the intershell is considered. This increased opacity forms a semi-convective region at the outer edge of the carbon rich region which pushes the carbon rich region further outwards. This new extension of the carbon rich region now enables the base of the convective envelope to make contact with this carbon region, thus enabling a dredge up phenomenon. Iben (1983) further shows that this dredge up in low-mass stars only works for low metallicity and low total stellar masses.

Renzini (1979,1981) has also proposed a mechanism for mixing at a post-AGB phase. This arises from a final helium shell flash which causes total mixing of a small residual hydrogen envelope. The energy generated by the hydrogen burning in the intershell region of the star causes an expansion back to the RCrB regime as shown in figure 1.3 (dashed track). This "loop" mechanism offers an explanation for both the hydrogen deficiency and the large radii (roughly $100R_{\odot}$) observed for the RCrB stars. Such total mixing can occur when the envelope mass $M_e < 10^{-4}M_{\odot}$ (Fujimoto 1977; Schönberner 1979; Iben et al. 1983) since for such a low value of M_e the entropy barrier discussed by Iben (1976) no longer exists. However, such an expansion and subsequent evolution following the loop will be very rapid and this leads to difficulties in accounting for the observed number of RCrB stars. So it is clear that the problems surrounding the RCrB and the EHe stars are far from being fully resolved.

It is clear from the large number of low-mass red giants observed which possess carbon and heavy element enhancements that significant mixing events must be occurring in red giants. Further, it has been described how large uncertainties still exist in the present theoretical calculations and indeed how some calculations allow some degree of mixing to take place, either at the helium core flash or the helium shell flash phase on the AGB and post-AGB. In view of the possible connection between EHe and RCrB stars with AGB stars and with a possible explanation of the hydrogen deficiency arising from mixing (either in whole or in part) of the envelope into the interior of these stars, the major part of this thesis investigates the resulting nucleosynthesis that occurs due to mixing on the AGB. The resulting element

enhancements that arise from such mixing can then be compared with observations of these stars.

1.5) Abundance Analyses

Several of the EHe and the RCrB stars have had their atmospheres analysed in order to determine their abundances. These abundance analyses used either a coarse analysis or a fine analysis technique. Aller (1954) used the technique of Unsöld to do a coarse analysis of HD160641. He found helium, carbon, nitrogen and neon all overabundant with respect to oxygen. Klemola (1961) analysed BD+10^o2179 and found the carbon and nitrogen abundances normal. HD124448 and HD168476 were analysed in detail by Hill (1965). Hill found both stars overabundant in helium, carbon, nitrogen and possibly neon. Oxygen in HD168476 was verified to be underabundant by Hill (1970). The technique of fine analysis was first applied to BD+10^o2179 by Hunger and Klinglesmith (1969). Schönberner and Wolf (1974) performed a fine analysis upon HD124448. They also did a differential analysis upon HD168476 relative to HD124448 using Hill's (1964) equivalent widths. Walker and Schönberner (1981) re-analysed HD168476 using the fine analysis technique. BD-9^o4395 was also analysed by Kaufmann and Schönberner (1977) using the same technique. Recently, BD+10^o2179 has been re-analysed by Heber (1983) using both ultraviolet as well as visible spectra. He also re-analysed HD168476, HD124448 and BD-9^o4395 but this time including effects of line blanketing as well as using up to date oscillator strengths. The general conclusion from all the abundance analyses so far attempted on the EHe stars is that hydrogen is deficient by factors typically of the order of 10^4 , but that the deficiency can

vary by up to 1.2 dex from star to star. All the stars are carbon overabundant by a factors of roughly 5 to 10 and oxygen underabundant by similar factors (relative to solar values). The elements of the iron group are so far extensively analysed only in the case of HD168476 and BD+10^o2179 and differ by a substantial amount (Heber 1983): the heavy elements are by more than ten times more abundant in HD168476 than in BD+10^o2179.

With regard to the RCrB stars the first analysis was that of Searle (1961) for RCrB itself. This was followed by Danziger (1965) for RY Sgr, and Orlov and Rodriguez (1974) for XX Cam. Schönberner (1975) re-analysed all three stars using the previously published data. These abundance analyses were based largely upon relatively strong lines in the crowded blue to visible ($\lambda < 5000\text{\AA}$) interval. In this region, continuum placement and line blending impair the measurement of equivalent widths and the strong lines are critically dependent on the microturbulent velocities and only moderately sensitive to the abundances. Cottrell and Lambert (1982) re-analysed RCrB and XX Cam using data from the yellow and red spectral regions using the fine analysis technique. They found both stars to be overabundant in carbon, nitrogen and oxygen by factors of roughly 20, 15 and 5 respectively. They found the heavy element abundances to be consistent with solar values. Hunger et al. (1982), however, find lithium overabundant in RCrB and deficient in XX Cam, while finding barium overabundant in both stars. Finally, Bond et al. (1979) found from low dispersion data that the RCrB star U Aquarii was roughly 100 times overabundant in the s-process elements Sr and Y (relative to the solar value). These large enhancements of heavy elements are the most conclusive evidence that hydrogen mixing into the stellar interior has

in fact occurred in at least one of the RCrB stars (see chapter 2).

It is found that the EHe stars are C, N and O poor relative to the RCrB stars. If the EHe stars are evolved RCrB stars perhaps a better similarity in composition should be observed. However, it is clear that at the present time there is too little abundance data available for any positive conclusions to be made. The possibility exists that the chemical composition of both classes span a broad range and that similarities will emerge only when a larger sample of these objects have been analysed.

1.6) Variability

Hill (1969) reported that the magnitude of the EHe stars HD168476 and HD160641 were variable whilst that of HD124448 was constant. Landolt (1973) made photoelectric UBV observations of several EHe stars, reporting that BD+37^o442 and HD168476 were not variable (although he notes only a few observations of HD168476 were made). He also reported that BD+10^o2179, HD124448, HD160641 and BD+13^o3224 were variable. Landolt (1975) gave a period of 0.1 day for BD+13^o3224 with an amplitude of 0.1 mag, and he also detected variations in the colours of this star. He further suspected that HD160641 may have a period of about 0.6 day. Walker (1979) reported HD168476 to be variable in its V magnitude on a time scale of days. Some of these earlier observations show conflicting results. At the present time variability is confirmed in HD160641 (Walker and Kilkenny 1980), HD168476 (Walker and Hill 1985) whilst BD+10^o2179 is confirmed to be a non-variable (Hill, Lynas-Gray and Kilkenny 1984; Grauer, Drilling and Schönberner 1984). The variable

EHe stars show complicated light and radial velocity variations which make period determinations difficult and which are likely to mask any period changes arising from evolutionary changes in the star. Landolt's (1975) 0.1 day period for BD+13^o3224 remains the only EHe star observed to have a well defined period. Hill et al. (1981) showed that the variations were due to radial pulsations of the star. Kilkenny and Lynas-Gray (1982, 1984) subsequently found the pulsation period to be decreasing at a rate of 4.6×10^{-10} days/cycle. But as stated earlier this star is thought to be in a different phase of evolution from the other EHe stars (Jeffery 1984). Walker and Kilkenny (1980) suggest that variability will be a common feature amongst EHe stars.

With regard to the RCrB stars, some of them are thought to have an underlying small amplitude (roughly 0.5m) variation in addition to their large irregular variations. At the present time there is insufficient evidence to decide in the case of most RCrB stars. UW Cen is reported to vary with a period of 42 days (Bateson 1972). RCrB shows small amplitude variations with a period of about 44 days at least at some epochs (Fennie et al. 1972). XX Cam seems to possess small amplitude, very rapid oscillations (Totochava 1973). It is believed that the small scale variations observed in the RCrB stars are due to pulsations. Indeed, Alexander et al. (1972) have shown that the 38.6 day period of RY Sgr is due to pulsations of the star. The cooler RCrB star S Aps had a period of 120 days (Waters 1966), but recently Kilkenny (1984) has found that the period of this star has changed to 40 days. Kilkenny suggests that a change from the fundamental pulsation mode to the first overtone can explain this change. Kilkenny and Flanagan (1983) also find evidence for a period change in UW Cen. It has been reported (Herbig 1967) that Miskin observed rapid oscillations in RCrB near its

minimum light following one of its rapid declines in brightness. Very high frequency pulsations in RCrB were not detected by Horowitz (1971) in 1969. There are suggestions that the pulsations of RY Sgr may die out from time to time (Mayall 1972) and also those of RCrB (Ferne 1972). It is also suggested that the pulsation amplitude may be largest during the recovery from minimum for UW Cen (Bateson 1972).

It was suspected by Gough (Trimble 1972) that hot helium rich stars would be in an instability strip. The calculations were made mainly for RCrB stars and thus at cooler temperatures than required for the EHe stars. It appeared that there would be an instability strip at around $T_{\text{eff}} = 7850^{\circ}\text{K}$ for $Z=0.03$. A lower metal abundance would bring the start of this instability region up to higher temperatures. Wood (1976) found an overtone instability region occurring between 5500°K and 13000°K (depending on L/M). There was also a tendency for instability to occur around 16000°K . The importance of investigating the pulsation periods in RCrB and EHe stars is two-fold. Firstly, it is possible to derive a distance-independent mass estimate for stars which pulsate. Secondly, changes in the pulsation periods of these stars can be compared with the values anticipated from the evolutionary tracks of Schönberner (1977). Kilkenny (1982) and Marraco and Milesi (1982) have indeed demonstrated that the pulsation period in RY Sgr is decreasing at a rate comparable with that expected for Schönberner's (1977) evolving $1M_{\odot}$ hydrogen deficient supergiant. Again it is clear that a substantial amount of additional data will be of importance in determining the evolutionary properties of the RCrB and the EHe stars.

1.7) Plan Of Thesis

In chapter 2 the basic theory of nuclear reactions in stellar interiors is presented. The nuclear networks used in the calculations are shown and the computer code developed to investigate the nucleosynthesis is discussed. The method of solution for the reaction equations is shown and the input nuclear properties of the nuclei such as reaction rates are discussed. In chapter 3 the details of the stellar models used in the calculations as well as the details of a typical helium shell flash are presented. Also the neutron production and the light particle reactions resulting from envelope mixing into the stellar interior while the star is on the AGB and post-AGB is investigated. This neutron production is crucial to the subsequent investigation of heavy element build up. In chapter 4 preliminary calculations are made of the heavy element build up for a linear flow network. This gives an indication of the enhancements of the elements from Fe to Pb expected for mixing on the AGB. This is followed by a detailed analysis of the heavy element region Fe to Mo. These calculations include the effects of nuclear branching, unthermalised nuclei and a time variation of the neutron flux. The enhancements of Sr, Y and Zr found from these calculations are particularly important since they can be used to gain information on the evolutionary state of the RCrB star U Aquarii. A coarse differential abundance analysis of U Aquarii is given in chapter 5. The abundances of Sr, Y and Zr are obtained by this method using high dispersion spectra taken with the Anglo-Australian Telescope. In chapter 6 a comparison of the observations and the calculations presented here is made. Such a comparison can lead to vital information with regard to the origin and

evolutionary status of U Aquarii. In chapter 7 recent photometric observations of the two EHe stars BD-9^o4395 and BD+1^o4381 are presented. These observations were undertaken to investigate the proposed evolutionary link between the RCrB and the EHe stars. A discovery of variability was made in both stars. The conclusions of the above investigations and a discussion of outstanding problems and possible future research is given in chapter 8. The values of the various nuclear properties used in the nucleosynthesis calculations are presented in the appendix.

CHAPTER 2. BASIC NUCLEOSYNTHESIS THEORY

2.1) Nuclear Reactions in Stellar Interiors

a) Generalities

A brief introduction on nuclear processes in stellar interiors is presented here. A more complete description can be found in Fowler et al. (1967, 1975) and Chiu (1968). The Maxwellian averaged product, $\langle \sigma v \rangle$, of the reaction cross section, σ , and the relative velocity, v , for two interacting nuclei is

$$\langle \sigma v \rangle = \frac{(8/\pi)^{1/2}}{M^{1/2}(kT)^{3/2}} \int_0^{\infty} \sigma(E) E \exp(-E/kT) dE \quad (2.1)$$

where M is the reduced mass, k the Boltzmann constant, T the temperature and E the relative energy of the particles. It is convenient to write the number densities as

$$N_i = \rho N_A X_i / A_i \quad (2.2)$$

where ρ is the mass density (g/cm^3), N_A is Avogadro's number, X_i is the mass fraction of nuclei i , and A_i is the atomic mass of i in AMU (Atomic Mass Units). The mean lifetime, $t_2(1)$ of nucleus 1 for interaction with nucleus 2 is given by

$$\lambda_2(1) = 1/t_2(1) = N_2 \langle \sigma v \rangle = \rho N_A X_2 \langle \sigma v \rangle A_2^{-1} \text{ sec}^{-1}$$

where $\lambda_2(1)$ is the decay rate of 1 for interaction with 2.

Consider the reaction whereby particles 1 and 2 form particles 3 and 4 with an energy release of Q (i.e. an exothermic reaction; for an endothermic reaction Q will be negative), viz. $1+2 \rightarrow 3+4+Q$. Since it may be easier to measure a required cross section in the reverse direction, use is frequently made of the reciprocity theorem, which follows from the assumption of time-reversal invariance for the nuclear and electromagnetic interactions (e.g. Blatt and Weisskopf 1952, Fowler et al. 1967)

$$\frac{\sigma(34)}{\sigma(12)} = \frac{(1 + \delta_{34}) g_1 g_2 A_1 A_2 E_{12}}{(1 + \delta_{12}) g_3 g_4 A_3 A_4 E_{34}}$$

where δ is the Kronecker delta, $g_i = (2J_i + 1)$ is the statistical weight of nucleus i with spin J_i , A_i is the reduced mass of particle i in AMU (similarly A_2 , A_3 and A_4), and E_{12} and E_{34} are the kinetic energies in the centre of mass system on the two sides of the nuclear equation. The introduction of the $(1 + \delta)$ term reflects the fact that cross sections between identical particles are twice those between different particles, other factors being equal. Since $Q = E_{34} - E_{12}$ it is easily found from equation 2.1 that

$$\frac{\langle 34 \rangle}{\langle 12 \rangle} = \frac{(1 + \delta_{34}) g_1 g_2 \left[\frac{A_1 A_2}{A_3 A_4} \right]^{3/2}}{(1 + \delta_{12}) g_3 g_4} \exp(-Q/kT) \quad (2.3)$$

where $\langle 12 \rangle = \langle \sigma v \rangle_{12}$

This equation applies to nuclei which are in their ground states only. In nuclear processes at high temperatures, such as those found in stellar interiors, the excited states of nuclei frequently play an

important part in the reaction. In most cases of interest the excited states of the nuclei will be in equilibrium with the ground state. A test can be made by comparing the lifetime $t(i \rightarrow i^*)$ for photoexcitation from the ground to the excited state, with the time scale, t_a , of the astrophysical circumstance under consideration. Equilibrium will be obtained for $t(i \rightarrow i^*) < t_a$. The lifetime $t(i \rightarrow i^*)$ can be computed from the spontaneous decay lifetime of the excited state $t_{sp}(i^* \rightarrow i)$ which can be calculated (Fowler et al. 1967) by using

$$\frac{t(i \rightarrow i^*)}{t_{sp}(i^* \rightarrow i)} = \frac{g_i}{g_{i^*}} [\exp(E_{i^*}/kT) - 1] \quad (2.4)$$

where E_{i^*} is the excitation energy of the excited state and T is the ambient temperature. The effects of induced emission on $i^* \rightarrow i$ were incorporated by the inclusion of the -1 in equation 2.4. For the case of reactions involving all the excited states of the nuclei in equilibrium with the ground states, equation 2.3 is modified by replacing the g_i by the nuclear partition functions

$$G_i = \sum_{i^*} g_{i^*} \exp(-E_{i^*}/kT)$$

where the sum over i^* includes the ground state and runs through all excited states for $t(i \rightarrow i^*) < t_a$. The rare situation where a long lived excited state is not in thermal equilibrium is important. The importance of these isomeric nuclei is discussed later. A frequent use of the reciprocity theorem is in the measurement of photodisintegration of nuclei at temperatures $T_6 > 500$ (in this notation T_6 signifies units of 10^6 °K). However, since the reactions to be considered in this thesis will be at temperatures $T_6 < 300$ the photodisintegration of nuclei will not be further considered here.

The effect of electron screening was first discussed by Salpeter (1954). This screening is due to the electrons in the ionised gas of a stellar interior, reducing the effective electrostatic repulsion of two nuclei. An ion in a plasma is surrounded by a charge cloud of radius which is of the order of the Debye length, L_d , where

$$L_d = \left[kT / (4\pi n e^2) \right]^{1/2}$$

and where n is the electron density. The electrostatic potential between two nuclei is

$$V(r) = \frac{Z_1 Z_2 e^2}{r} + u(r) \quad (2.5)$$

where r is the distance between the nuclei, $u(r)$ is the screening correction to the coulomb potential $Z_1 Z_2 e^2 / r$ and $u(r)$ varies with the characteristic length r_{char} . The classical turning radius r_c for two bodies interacting through the coulomb interaction is

$$r_c = \frac{Z_1 Z_2 e^2}{E}$$

where E is the relative particle energy. For the conditions of low density, $r_c < r_{char}$. Therefore since $u(r)$ only changes significantly over r_{char} , then $u(r_c) = u(0) = \text{constant} = U_0$. Using equation 2.5 as the new potential it is found that the reaction rate is given by

$$r_{12} = \text{uncorrected } r_{12} \cdot \exp(-U_0/kT)$$

The effect of electron screening is therefore the same as introducing a correction factor $\exp(-U_0/kT)$.

The best method for evaluating the integral in equation 2.1 depends on the type of energy dependence exhibited by $\sigma(E)$. Several commonly occurring cases will now be considered.

b) Non-Resonant Reactions

In the first approximation the effect of electron screening is ignored. Consider two particles with charges Z_1 and Z_2 , and separated by a distance r (the situation of reactions involving neutrons is discussed later). The electrostatic potential energy is given by

$$V(r) = \frac{Z_1 Z_2 e^2}{r}$$

The probability of a nuclear reaction can be written as the product of the probability P_L (Coulomb penetration factor) that the two particles approach one another at a distance $r=R$ (where L is the relative angular momentum of the nuclei and R is the minimum radius of interaction; $R=1.4A^{1/3}$ fm), and the probability P_{nuc} that the particles in contact react in a nuclear fashion. The first stage is illustrated in figure 2.1. It is clear that for the nuclear reaction to proceed the particles must penetrate the coulomb barrier, the height of which is given by

$$E_c = \frac{Z_1 Z_2 e^2}{R}$$

This is true because in almost every case in astrophysics $E \ll E_c$. The

quantum mechanical effect of tunnelling gives the probability that the particles with relative energy E approach, by a tunnel effect, the interaction radius R . The Coulomb barrier penetration factors were first discussed by Gamow (1928), and Gurney and Condon (1928,1929). The penetration factor P_L is given by

$$P_L = [F_L^2(R) + G_L^2(R)]^{-1} \quad (2.6)$$

where $F_L(R)$ and $G_L(R)$ are the regular and irregular solutions of the Schrödinger wave equation for a charged particle in a Coulomb field evaluated at the interaction radius R . The Coulomb wave functions $F_L(R)$ and $G_L(R)$ are discussed and tabulated by Froberg (1955) and Hull and Breit (1959). Approximate values of the penetration factors are derived using the WKB (Wentzel 1926; Kramers 1926; Brillouin 1926) solution to the Schrödinger equation (cf. Bethe 1937, Van Horn and Salpeter 1967). The WKB solution for P_L is

$$P_L = \left(\frac{E_c}{E}\right)^{1/2} \exp \left[\frac{-2\pi Z_1 Z_2 e^2}{\hbar v} + 4 \left(\frac{E_c}{\hbar^2 / 2MR^2} \right)^{1/2} - 2L(L+1) \left(\frac{\hbar^2 / 2MR^2}{E_c} \right)^{1/2} \right] \quad (2.7)$$

where each symbol is as before and \hbar is the rationalised Planck constant. For low energy reactions ($E \ll E_c$) $L=0$ and it can be seen that

$$P_{L=0} \propto \exp \left[\frac{-2\pi Z_1 Z_2 e^2}{\hbar v} \right] E^{-1/2}$$

If the factor P_{nuc} is more or less independent of the energy of the incident particle then

$$\sigma(E) = P_L P_{\text{nuc}} v^{-1} = S(E) E^{-1} \exp [-(E_G/E)^{1/2}] \quad (2.8)$$

where E_G is the Gamow energy and is given by

$$E_G = (2\pi\alpha Z_1 Z_2)^2 (Mc^2/2)$$

where α is the fine structure constant and c is the velocity of light.

The factor $S(E)$ (in units of MeV-barns) is termed the 'astrophysical factor'. It measures the probability of the purely nuclear reaction, and is usually measured experimentally by means of the inverse formula

$$S(E) = \sigma(E) E \exp [(E_G/E)^{1/2}]$$

Far from a nuclear resonance $S(E)$ is a slowly varying function and it may be conveniently expressed in terms of the power series expansion

$$S(E) = S(0) \left[1 + \frac{S'(0)}{S(0)} E + \frac{1}{2} \frac{S''(0)}{S(0)} E^2 + \dots \right] \quad (2.9)$$

where a prime denotes differentiation with respect to the kinetic energy E in the centre of mass system.

The reaction rate r_{12} for a non-resonant charged particle reaction between nuclei 1 and 2 will be

$$r_{12} = \frac{N_1 N_2 \langle \sigma v \rangle_{12}}{(1 + \delta_{12})}$$

where N_1 and N_2 are the number densities given by equation 2.2. It follows from equations 2.8 and 2.1 that

$$r_{12} = \frac{N_1 N_2}{1 + \delta_{12}} \left(\frac{8}{\pi M} \right)^{1/2} \frac{1}{(kT)^{3/2}} \int S(E) \exp \left[- \left(\frac{E_G}{E} \right)^{1/2} - \frac{E}{kT} \right] dE \quad (2.10)$$

Using equation 2.9 Bahcall (1966) and Fowler et al. (1975) evaluated the integral to show

$$r_{12} = \frac{N_1 N_2}{1 + \delta_{12}} \left(\frac{2}{M} \right)^{1/2} \frac{\Delta E_0}{(kT)^{3/2}} S_{\text{eff}} \exp \left[- \frac{3E_0}{kT} - \left(\frac{T}{T_{\text{co}}} \right)^2 \right] \quad (2.11)$$

In this equation, E_0 is the most effective interaction

energy, corresponding to the peak in the integrand of equation 2.10, ΔE_0 is the full width of this effective energy peak at $1/e$ maximum value, S_{eff} is the effective value of the cross section factor $S(E)$, and T_{co} is the cut-off temperature which occurs when the nuclear cross section no longer varies according to the Coulomb penetration factor (this condition may occur when the effective energy E_0 is larger than E_G or when the continuum or a resonance has set in - see later). E_0 is given by (Fowler and Hoyle 1964)

$$E_0 = [\pi\alpha Z_1 Z_2 kT (Mc^2/2)^{1/2}]^{2/3} \quad (2.12)$$

and ΔE_0 is given by

$$\Delta E_0 = 4(E_0 kT/3)^{1/2} \quad (2.13)$$

The effective value S_{eff} of the cross section factor $S(E)$ is given by

$$S_{\text{eff}} = S(0) \left[1 + \frac{5kT}{36E_0} + \frac{S'(0)}{S(0)} \left(E_0 + \frac{35}{36} kT \right) + \frac{1}{2} \frac{S''(0)}{S(0)} \left(E_0^2 + \frac{89}{36} E_0 kT \right) \right] \quad (2.14)$$

Equation 2.14 will give S_{eff} in units of MeV-barn. Equations 2.2, 2.12, 2.13 and 2.14 can be combined to give the useful result

$$N_A \langle \sigma v \rangle = C_1 T_9^{-2/3} \exp[-C_2 T_9^{-1/3} - (T_9/T_{\text{co}})^2] \{ 1 + C_3 T_9^{1/3} + C_4 T_9^{2/3} + C_5 T_9 + C_6 T_9^{4/3} + C_7 T_9^{5/3} \} \text{ cm}^3 (\text{mole})^{-1} \text{ sec}^{-1}$$

where

$$\begin{aligned} C_1 &= 7.8324 \times 10^9 (Z_1^2 Z_2^2 A)^{1/6} S(0)/A^{1/2}, \\ C_2 &= 4.2475 (Z_1^2 Z_2^2 A)^{1/3}, \\ C_3 &= 9.810 \times 10^{-2} (Z_1^2 Z_2^2 A)^{-1/3}, \\ C_4 &= 0.1220 \{ S'(0)/S(0) \} (Z_1^2 Z_2^2 A)^{1/3}, \end{aligned}$$

$$C_5 = 8.377 \times 10^{-2} S'(0)/S(0),$$
$$C_6 = 7.442 \times 10^{-3} \{S''(0)/S(0)\} (Z_1^2 Z_2^2 A)^{2/3},$$
$$C_7 = 1.229 \times 10^{-2} \{S''(0)/S(0)\} (Z_1^2 Z_2^2 A)^{1/3},$$

and where the symbols have their usual meanings, and the quantities $S(0)$, $S'(0)$ and $S''(0)$ have respective units of MeV-barns, barns and barns/MeV. The quantity $N_A \langle \sigma v \rangle$ is conveniently tabulated by Fowler et al. (1967,1975) and Harris et al. (1984).

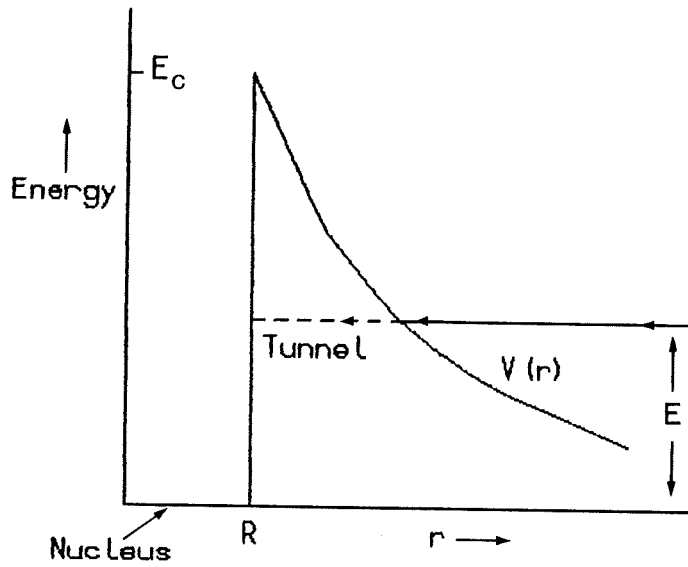


Figure 2.1 Tunnelling effect of particle with $E < E_c$

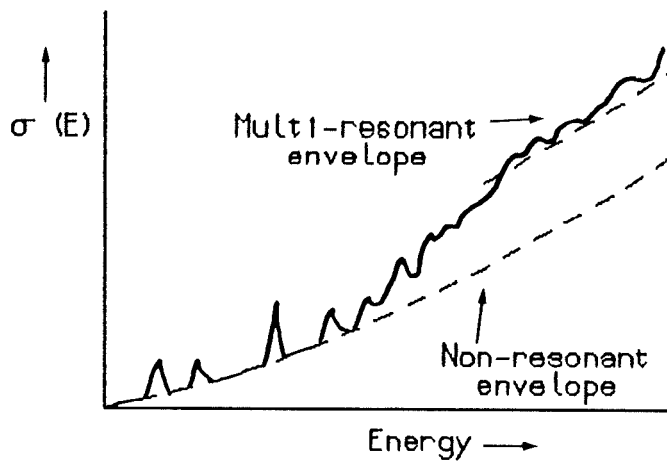


Figure 2.2 $\sigma(E)$ behaviour

c) Resonant Reactions

For a single resonance of energy E_R , the cross section $\sigma(E)$ of the nuclear reaction $1+2 \rightarrow 3+4+Q$ is given by (Breit and Wigner 1936)

$$\sigma(E) = \frac{\pi \lambda^2 w \Gamma_{12} \Gamma_{34}}{(E-E_R)^2 + \left(\frac{\Gamma^2}{4}\right)} \quad (2.15)$$

where E is the centre of momentum energy of 1 and 2 and $\lambda = \hbar/(Mv)$ (where M is the reduced mass) is the reduced de Broglie wavelength. The statistical factor w is given by

$$w = (2J+1)/\{(2J_1+1)(2J_2+1)\}$$

where J is the angular momentum of the resonant state and where J_1 and J_2 are respectively the angular momentum of particles 1 and 2. The total width Γ of the resonant state is given by $\Gamma = \hbar/t_e$, where t_e is the effective lifetime of the state. The partial width Γ_{12} is the width for re-emission of 1 and 2, and Γ_{34} is the width for emission of 3 and 4. The partial widths can be evaluated using the expression

$$\Gamma = 3\hbar v \theta_L^2 P_L / R \quad (2.16)$$

where R is the interaction radius P_L is the Coulomb penetration factor given by equation 2.6 and θ_L^2 is the reduced width for particles with angular momentum L . It follows from equations 2.15, 2.10 and 2.1 that for a resonant reaction in a non-relativistic, non-degenerate gas the reaction rate r_{12} is given by

$$r_{12} = \frac{N_1 N_2}{1 + \delta_{12}} \int_0^{\infty} \frac{0.657}{AE} \frac{w \Gamma_{12} \Gamma_{34}}{(E-E_R)^2 + \left(\frac{\Gamma^2}{4}\right)} \left(\frac{2E}{M}\right)^{1/2} \left[\frac{2E}{\sqrt{\pi} kT} \cdot \exp\left(-\frac{E}{kT}\right) \frac{1}{(kTE)^{1/2}} \right] dE \quad (2.17)$$

When the effective energy E_0 given by equation 2.12 is much smaller than the resonant energy E_R , then the Breit Wigner resonant cross section may be evaluated in its wings to give the cross section factor

$$S(E) = \frac{0.657 w \Gamma_{12}(E) \Gamma_{34}}{A (E-E_R)^2 + (\Gamma^2/4)} \exp(0.98948 Z_1 Z_2 A^{1/2} E^{-1/2}) \quad (2.18)$$

$S(E)$ is in MeV barns and E in MeV. Equation 2.18 may be evaluated using measurements of a resonance at high energies, and then used with the non-resonant formalism of equations 2.11 and 2.14 to obtain reaction rates at low energies. When the range of effective stellar energies includes the resonance energy then equation 2.17 must be used. This is provided that the width of the resonance, Γ , is much less than the effective spread in energy of the interacting particles (i.e. less than ΔE_0). Equation 2.17 can be integrated to give

$$N_A \langle \sigma v \rangle = C_8 T_9^{-3/2} \exp(-C_9/T_9) \quad \text{cm}^3 \text{sec}^{-1} (\text{mole})^{-1} \quad (2.19)$$

where

$$C_8 = 1.53986 \times 10^{11} A^{-3/2} w \Gamma_{12} \Gamma_{34} / \Gamma, \text{ and}$$

$$C_9 = 11.605 E_R.$$

The effect of a single resonance is included in the tabulations of $N_A \langle \sigma v \rangle$ referenced for the non-resonant reaction rates. When several resonances occur within ΔE_0 , the net reaction rate is determined by the

superposition

$$N_A \langle \sigma v \rangle = \sum_n C_{8n} T_9^{-3/2} \exp(-C_{9n}/T_9) \quad (2.20)$$

where C_{8n} and C_{9n} are the appropriate constants given by equation 2.19 for the n th resonance. When the density of resonances lying within ΔE_0 becomes sufficiently large the summation of equation 2.20 can be replaced by the integration dE/D , where D is the average level distance within the Gamow peak. This occurs mainly in elements heavier than about Neon. In this situation where the resonances are so closely spaced such as to form a continuum of resonances, the reaction rate takes the same form as the non-resonant case. This is to be expected since at that time the average behaviour of the nucleus is relatively independent of the energy. The average properties of the nuclei required for this statistical analysis of the reaction rates are usually calculated by using a Wood-Saxon optical potential (Michaud et al. 1970) for the nuclei. Such an analysis was carried out by Holmes et al. (1976) and Woosley et al. (1978) for a large number of heavy nuclei. The $\sigma(E)$ behaviour for the different cases discussed here is illustrated in figure 2.2.

d) Neutrons

The reaction rates for neutron absorption reactions follow the same analysis as given in the previous sections only this time there is no need for the Coulomb penetration factor since the neutron carries zero electric charge. For non-resonant reactions the energy dependence of neutron-interaction cross sections has been discussed by Fowler and Vogl

(1964). At low energies the s wave ($L=0$) interactions dominate and the cross section is proportional to the square of the de-Broglie wavelength λ and the partial width for neutron emission Γ_n . Since λ is proportional to v^{-1} while Γ_n is proportional to v , v being the relative velocity of the neutron and interacting nucleus, it follows that for non-resonant neutron reactions $\sigma \propto v^{-1}$ or $\sigma v = \text{constant}$. The Maxwellian averaged cross section is defined as

$$\langle \sigma \rangle = \langle \sigma v \rangle / v_T$$

where v_T is the most probable velocity of the Maxwell-Boltzmann distribution and is given by

$$v_T = (2kT/M)^{1/2}$$

Measurement of neutron cross sections are usually taken at the most probable energy ($=kT$), then $\langle \sigma \rangle = \sigma_T$ taken at v_T . Values of the cross section σ_T are measured at 30keV or $T_8=3.48$, that is $v_T=2.4 \times 10^8$ cm/s. Values at other temperatures are then extrapolated using the relationship $\langle \sigma \rangle \propto v_T^{-1} \propto T^{-1/2}$. In some cases the thermal neutron cross section σ_{Th} is given. These cross sections are measured at $T=293$ °K, that is at $kT=0.025$ eV. For resonant and continuum neutron reaction rates the analysis follows that given for the charge particle reactions but with the spread of the effective energy ΔE_0 being replaced by kT .

e) Beta Decay

Individual stellar transition rates for electron emission, positron emission, continuum electron capture and K electron capture may be calculated from an expression of the form

$$\lambda = \frac{\ln 2}{\langle ft \rangle} f(Z, W_0)$$

where $f(Z, W_0)$ is the Fermi function characterising the transition, Z is the charge of the parent nucleus and W_0 is the maximum energy release of the beta decay. $\langle ft \rangle = f(Z, W_0) t_{1/2}$ (where $t_{1/2}$ is the beta decay half life) is a factor which is found to be roughly constant for any given degree of forbiddenness of the beta transition. For the different beta processes a different expression is used in order to calculate the Fermi function. In the case of the electron or positron emission this is

$$f = \frac{1}{m^5 c^9} \int_{mc^2}^{W_0} p E (E - W_0)^2 F(\pm Z, E) dE$$

where p is the electron (positron) momentum, m is the electron rest mass, c is the velocity of light and where the $+$ and $-$ signs correspond to the cases of electron and positron emission respectively. The function $F(\pm Z, E)$ corrects for Coulomb effects on the electron (positron) wavefunction and is given by (e.g. Blatt and Weisskopf 1952). The integrated Fermi function for K-capture can be found from the relativistic formula (Blatt and Weisskopf 1952)

$$f_k = 2\pi (2\rho)^{2s-2} \frac{1+s}{\Gamma(2s+1)} \gamma^{2s+1} (W_0+s)^2$$

where

$$\rho = Rmc/\hbar, \quad s = (1 - \{(z-1)\alpha\}^2)^{1/2}$$

$$\gamma = \alpha z, \quad \Gamma_4 \text{ is the Gamma function}$$

and where α is the fine structure constant and R is the nuclear radius. Newman (1973) has shown how to correct the experimental terrestrial rates for K-capture for the effects of ionisation of K electrons. For continuum electron capture the appropriate function f_{ec} was approximated by Bachall (1962) and is given there.

The above expressions can be used to calculate the individual transition rates of stellar beta decays. Laboratory $\langle ft \rangle$ are usually used when possible, otherwise 'average' $\langle ft \rangle$ values appropriate to a given degree of forbiddenness are adopted. Data required for the excited states of the parent nucleus can be found from Nuclear Data Sheets (Volume 26). The total decay rates are determined by summing over all individual excited state contributions weighted by the appropriate statistical factor, i.e.

$$\lambda_{\text{total}} = \sum_i P_i \sum_j \lambda_{i,j}$$

where

$$P_i = \frac{2(I_i + 1) \exp(-E_i/kT)}{U},$$

P_i is the fractional population of the i 'th level (which has spin I_i and

energy E_i) of the parent nucleus, and U is the partition function.

Tables of stellar beta decays for a large number of nuclei which were calculated using the methods outlined here are given in the tables of Newman (1973) and Cosner (1982).

2.2) Heavy Element Synthesis by the S-Process

Merrill's (1952) discovery of Technetium in the atmospheres of red-giant stars is generally accepted as evidence that neutron capture processes are significant with regard to heavy element synthesis in the interiors of stars. This is because the longest lived isotope of Technetium (^{99}Tc) has a terrestrial half life of 2×10^5 years. Since this is short compared to the stellar lifetime it follows that Tc must be produced in the star. Also since the energies of the nuclei in a stellar interior are too low for charge particles to have any effect on Tc production (due to the Coulomb barrier) it follows that neutron absorption reactions must be at work.

The slow neutron capture process, or s-process, for the production of heavy elements was originally discussed by B²FH and was considered in further detail by Clayton et al. (CFHZ), who presented a mathematical formulation of the problem giving both an exact and an approximate solution, both of which assume the initial seed nuclei were all ^{56}Fe . This mathematical formulism is based on the assumption that the nuclear reactions, which produce the s-process neutrons, proceed on a time scale approaching the nuclear burning time scale of the star. This means that

the time between successive neutron captures on a given nucleus is of the order of hundreds to thousands of years, and that the s-process is characterised by a low neutron density (roughly 10^7 neutrons/cm³, Blake and Schramm 1975). If it is assumed the beta decays of unstable nuclei occur much more rapidly than the neutron captures then the nuclear network can be represented by a linear chain in which there is only one nucleus for each value of atomic number A. The number abundance of any nuclide, N'_A (the notation N'_A is used here so as to avoid confusion with Avogadro's number), is then determined by the set of equations

$$\frac{dN_{56}}{dt} = - \langle \sigma_{56} v \rangle N_{56} N_n \quad (2.21)$$

$$\frac{dN'_A}{dt} = - \langle \sigma_A v \rangle N'_A N_n + \langle \sigma_{A-1} v \rangle N_{A-1} N_n$$

$$A = 57, 58, \dots$$

where N_n is the neutron number abundance and assuming the lightest nucleus in the capture chain is ^{56}Fe . The reaction rate $\langle \sigma v \rangle$ can be factorised into $\langle \sigma \rangle$ and $v_T = (2kT/M)^{1/2}$. By defining a neutron exposure, τ , by

$$\tau = \int_0^t N_n v_T dt,$$

the equations 2.21 may be written in the form given by CFHZ

$$\frac{1}{\sigma_i} \frac{d\psi_i}{d\tau} = - \psi_i \quad (2.22)$$

$$\frac{1}{\sigma_k} \frac{d\psi_k}{d\tau} = - \psi_k + \psi_{k-1} \quad , k = 2, 3, \dots$$

where

$$\sigma_k = \langle \sigma \rangle_A \quad \text{and} \quad \psi_k = \frac{\langle \sigma \rangle_A N'_A}{N_{56}^0} \quad \text{for } k = A-55, \dots$$

and N_{56}^0 is the initial ^{56}Fe abundance. An exact solution to the system of equations 2.22 was known from the work of Bateman (1910). This gives the abundance of any nuclide N_A^i as a function of the neutron exposure τ , in the form

$$\sigma_A N_A^i = N_{56}^0 \sum_{i=56}^A C_{A,i} \exp(-\sigma_i \tau) \quad (2.23)$$

where

$$C_{A,i} = \frac{\sigma_{56} \sigma_{57} \dots \sigma_A}{(\sigma_{A-1} - \sigma_i)(\sigma_{A-2} - \sigma_i) \dots (\sigma_{56} - \sigma_i)}$$

However, there are two severe difficulties with this exact solution. The functional form is incorrect for any two cross sections which are equal, and secondly, even for cross sections which have similar values (which is frequently the case) then the $C_{A,i}$'s are difficult and time consuming to evaluate numerically. These difficulties led CFHZ to approximate equations 2.23 for $\sigma_A N_A^i$ by,

$$\sigma_A N_A^i = \frac{N_{56}^0 \lambda_A (\lambda_A \tau)^{m_A - 1} \exp(-\lambda_A \tau)}{\Gamma_G(m_A)}$$

where Γ_G is the gamma function and

$$\lambda_A = \frac{\sum_{i=56}^A 1/\sigma_i}{\sum_{i=56}^A 1/\sigma_i^2}, \quad m_A = \frac{\left(\sum_{i=56}^A 1/\sigma_i \right)^2}{\left(\sum_{i=56}^A 1/\sigma_i^2 \right)}$$

This approximation is 'best' in the sense that it matches the exact solution in its zeroth, first and second moments in τ . CFHZ and Seeger, Fowler and Clayton (1965) used this formalism to demonstrate that the solar system of abundances, presumed to be formed by the s-process, could not be characterised by a single value of τ , but rather as a mixture of nuclei exposed to different values of τ . The

distribution of neutron exposures found to give a best fit to the observed solar system abundances was found to be an exponential weighting function of the form

$$R(\tau) = G \exp(-\tau/\tau_0)$$

where $R(\tau)$ is the fraction of the material having received a neutron exposure τ , and G and τ_0 are constants.

Although satisfactory for qualitative descriptions, this formulism is not satisfactory for detailed quantitative calculations of individual nuclei, especially for high neutron densities. The problem is that the phenomenon of nuclear branching cannot be included in any linear network. Nuclear branching is illustrated in the full lines of figure 2.3 (the dashed lines and primed nuclei are related to isomerism, see later). Nucleus 1 absorbs a neutron and forms nucleus 2. Now nucleus 2 is unstable and can beta decay forming nucleus 4 in a short time. If however nucleus 2 absorbs a further neutron in a time scale similar to its beta decay, then some fraction of nucleus 2 will form nucleus 3. There is then a branch in the flow chart. The amount of flow passing through nuclei 3 and 4 will then depend on the neutron density, and the neutron absorption cross section and the beta decay rate of nucleus 2. Further neutron absorption on nucleus 4 will then mean that two different nuclei in the network now possess the same atomic mass A .

Another effect which the CFHZ formulism cannot accommodate is that due to the non-thermalisation of the excited levels of some nuclei under the conditions found in stellar interiors. Cosner, Iben and Truran (1980) show how the change in the beta decay rates of nuclei affected by non-thermalisation, can alter the resulting nucleosynthesis. The possible significance of this effect is shown in figure 2.3 for an

extreme case where the non-thermalised nuclei $2'$ has a very much longer beta decay time than its thermalised counterpart nuclei 2 . If all the nuclei 2 were in the isomeric state $2'$, then it would all form nuclei 3 with none forming nuclei 4 , and therefore greatly influencing the branching ratio at this part of the network. The effects of nuclear branching and the non-thermalisation of nuclei are effects that will have to be accounted for in any detailed nucleosynthesis calculations. Ward, Newman and Clayton (1976), and Ward and Newman (1978) have further developed the mathematical formalism of the s -process to account for the branching of nuclear species. However, even this more accurate formalism may not give the required accuracy in abundance determinations since it assumes that the branching ratios remain constant throughout the synthesis period (i.e. the neutron density is assumed constant with time). In fact in stellar interiors the neutron density will be a function of time, the density reaching a peak before falling off with increasing time as the neutron producing nuclei are destroyed. The work of Cosner, Iben and Truran (1980) has shown the importance of properly accounting for the variation of the neutron flux in making abundance calculations.

Another method of solving for the abundance of the nuclei is to numerically, simultaneously solve the individual differential equations which describe the rate of production/destruction of each nucleus. This method of calculation can accommodate the effects of nuclear branching and non-thermalisation. With the advent of more powerful computers this technique has become the most popular for nuclear network abundance determinations. It is by this means that the nucleosynthesis calculations presented in this thesis will be carried out. A large computer code was developed by the author in order to simulate a

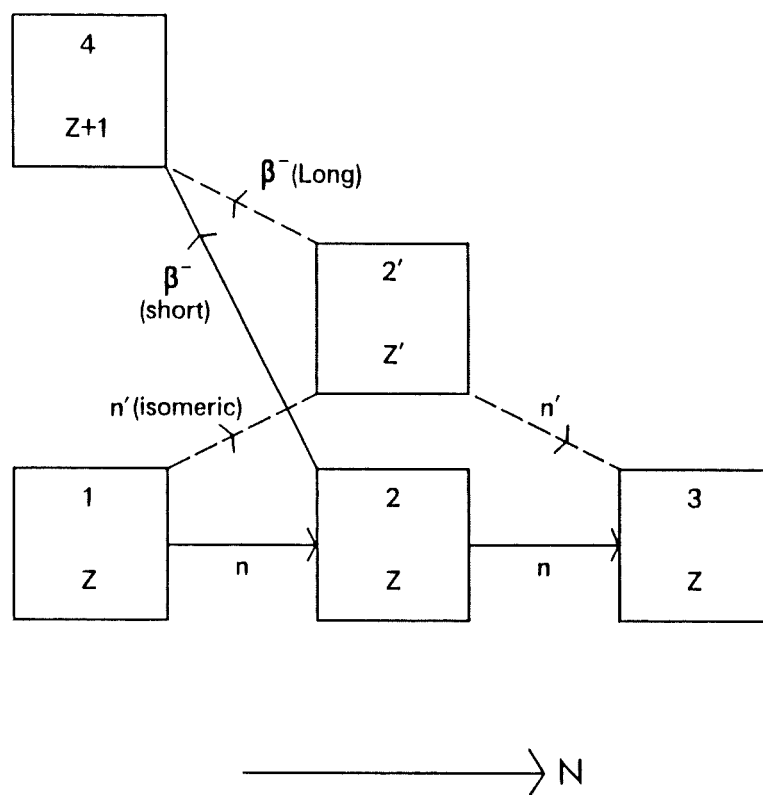


Figure 2.3 Nuclear branching diagram

nuclear reaction network by the use of differential equations. The method of abundance determination used in the code is given in section 2.3.

2.3) Numerical Analysis of a Reaction Network

a) Numerical Solution

The equation governing the transformation by thermonuclear reactions in the number density of the i th species N_i is of the form

$$\frac{d(N_i)}{dt} = - \sum_j N_i N_j \langle \sigma v \rangle_{ij} + \sum_{kl} N_k N_l \langle \sigma v \rangle_{kl} \quad (2.24)$$

where $\langle \sigma v \rangle_{ij}$ is the thermally averaged product of the cross section and the relative velocity for an interaction involving particles of species i and j in the entrance channel. For identical particles $N_i N_j$ is replaced by $N_i^2/2$ (similarly for $k=l$) and the summations are over all reactions which either create or destroy the i th species. For numerical work it is convenient to introduce the parameter

$$Y_i = N_i / \rho N_A$$

where ρ is the mass density and N_A is Avogadro's number. In terms of the mass fraction we have

$$X_i = Y_i A_i$$

where A_i is the atomic mass of the i th species. Using this the differential equation linking all the reactions which create or destroy

the i th nucleus is given by

$$\frac{d(Y_i)}{dt} = - \sum_j f_{ij} + \sum_{kl} f_{kl} \quad (2.25)$$

where the vector flow, f_{ij} , containing nuclei i and j in the entrance channel is given by

$$f_{ij} = Y_i Y_j [ij], \text{ where } [ij] = \rho N_A \langle \sigma v \rangle_{ij}$$

A method of linearisation of equation 2.25 was proposed by Arnett and Truran (1969). Assuming the time step was sufficiently small they showed that the vector flows may be linearised to the form

$$f_{ij}^{n+1} \approx (Y_i^n Y_j^n + \Delta_i Y_j^n + \Delta_j Y_i^n) [ij]$$

where the beginning and end of the time interval is given by n and $n+1$ and $\Delta_i = Y_i^{n+1} - Y_i^n$. Replacing the time derivative of Y_i by

$$\frac{d(Y_i)}{dt} = \frac{\Delta_i}{\Delta t}$$

gives the coupled set of linear equations

$$\begin{aligned} Y_i^{n+1} (1/\Delta t + Y_j^n [ij]) + Y_j^{n+1} (Y_i^n [ij]) - Y_k^{n+1} (Y_l^n [kl]) \\ - Y_l^{n+1} (Y_k^n [kl]) = Y_i^n (1/\Delta t + Y_j^n [ij]) - Y_k^n Y_l^n [kl] \end{aligned} \quad (2.26)$$

Added to equations 2.26 will be any relevant beta decays and any changes due to identical particle reactions. For example, the linearisation technique applied to the triple α reaction gives

$$(Y_\alpha^{n+1})^3 = 3Y_\alpha^{n+1} (Y_\alpha^n)^2 - (2Y_\alpha^n)^3$$

The system of simultaneous equations 2.26 forms an $N \times N$ sparse matrix, where N is the number of species in the network. The solution to equations 2.26 is then found by a version of Gauss elimination involving

sparse matrices outlined in detail by Duff (1980).

b) Errors

The system of difference equations 2.26 is an estimate of the 'true' system of differential equations 2.24. There are two sources of error involved in this transformation from the true to the estimated system. One of these, the truncation error, is due to ignoring the bracketed terms in the expansion

$$\frac{Y_i^{n+1} - Y_i^n}{\Delta t} = \frac{dY_i^n}{dt} + \left[-\frac{1}{2} \Delta t \frac{d^2 Y_i^n}{dt^2} + \dots \right]$$

when the differential was transformed to a difference. If it is assumed for simplicity

$$\frac{dY_i}{dt} = (Y_i)^2 [ij] \quad (2.27)$$

and $[ij]$ is constant during the time step, an estimate of this error is given by (using equation 2.27)

$$\begin{aligned} \frac{1}{2} \Delta t \frac{d}{dt} \left\{ \frac{dY_i^n}{dt} \right\} &= \frac{1}{2} \Delta t \frac{d}{dt} \left\{ (Y_i^n)^2 [ij] \right\} \\ &= \Delta t Y_i^n \frac{dY_i^n}{dt} [ij] \end{aligned}$$

The second source of error arises from the linearisation technique due to the neglect of the quadratic terms in $\delta_i = \Delta_i / Y_i$. If the maximum fractional change in abundance is given by C (C is some constant) then

the maximum error will be of order C^2 . (Maeder, 1983 has shown how to include such quadratic terms into the reaction equations) The value of the time step was chosen such that

$$\Delta t < C \frac{Y_i^n}{(dY_i/dt)^n} \quad (2.28)$$

for all species with mass fraction greater than 10^{-10} and for $C=0.1$. Since both sources of error are proportional to Δt , then they can clearly be reduced arbitrarily by a reduction in the time step. It is also important to make sure that the system of equations 2.26 are stable against amplification of small errors. Such stability would prevent other solutions, particularly one that grows exponentially with time. In the notation of Richtmyer and Morton (1957) we have

$$\frac{Y_i^{n+1} - Y_i^n}{\Delta t} = \pm \sum_{kl} \{ \theta Y_k^{n+1} + (1-\theta) Y_k^n \} \cdot \{ \theta Y_l^{n+1} + (1-\theta) Y_l^n \} [kl] \\ \pm \sum_{kl} \lambda_{kl} \{ \theta Y_k^{n+1} + (1-\theta) Y_k^n \}$$

where λ_{kl} is the beta decay rate. If $\theta=0$ then the system would be explicit in that each of the equations gives one of the unknowns Y^{n+1} in terms of the known Y^n . This system would be unstable to small errors introduced into the system. If $\theta > 0$, as in these calculations then the system is said to be implicit. In an implicit system the equations must be solved simultaneously in order to obtain the unknowns. Analysis of the situation for $\theta=1$ shows that the system of equations 2.26 will be stable for any time step Δt . For the time step as given in equation 2.28 any mathematical errors will be much smaller than errors arising from the input physics.

c) Computations

The computer program package, NUCLEAR, was written and developed by the author in order to carry out the calculations described in the previous sections. No other reaction network package which includes all the relevant light particle and heavy element nuclear reactions required for a study of this kind is presently available. The program consisted mainly of the four subroutines INIT, RATES, ELEMS and SOLVE. Subroutine INIT contains all the initial conditions, such as the initial abundances and initial temperature, required for the start of the calculations. Subroutine RATES contains the equations and data required for calculating the nuclear reaction rates for a given initial temperature and mass density. Subroutine ELEMS calculates the individual elements, a_{ij} of the matrix A which is used in the matrix equation

$$A x = b.$$

The elements of A are essentially the bracketed terms of the left hand side of equation 2.26, while the matrix b is formed from the right hand side of this equation. The solution matrix x contains the abundances of the individual isotopes to be calculated. This solution is calculated by the subroutine SOLVE. The routines used within SOLVE were written and developed by Duff (1980) and were made available to the author via the NAG Subroutine Library.

In subroutine SOLVE the set of simultaneous equations which form the matrix equation are solved. Firstly, given the real sparse matrix A, the LU-decomposition of a permutation of A,

$$PAQ = LU$$

is found, where P and Q are the permutation matrices, L is the unit lower triangular and U is the upper triangular. In obtaining this decomposition it is important to use a correct pivoting strategy for the simultaneous equations to ensure that round off errors (due to the finite precision arithmetic of a computer) do not propagate and produce completely erroneous answers (the pivotal equation is the equation which is used to eliminate one unknown from the other equations). A sparse variant of Gauss elimination is used which utilises a form of total pivoting. In total pivoting the equation which contains the largest coefficient is used as the pivot equation (this information is contained in matrix P), and the unknown corresponding to this coefficient is taken as the first pivot (this information is contained in matrix Q). Details of possible pivoting strategy can be found in Conte and Boor (1965). The pivot strategy used here is designed to compromise between maintaining sparsity and controlling the loss of accuracy due to round off errors. An input parameter into the decomposition is the pivot control PIV . When searching for a pivot, any element is excluded which is less than PIV times the largest of those elements in the row available as pivots. Thus decreasing PIV biases the algorithm to maintaining sparsity at the expense of stability. A value of $PIV = 0.1$ was found to work well in maintaining the sparsity and also in controlling the effect of round off error.

When the new matrix equation is calculated for the next time step, the same pivotal sequence can be used for the new matrix since the sparsity pattern of this new matrix is the same as the previous matrix. This technique of re-using the same pivoting sequence leads to an increase in speed by factors of 4 to 7. However, since the pivoting sequence is not changed, the new composition is potentially unstable.

This is controlled by the input parameter ETA. ETA is set to the relative pivot threshold below which an error diagnostic is provoked. A value of $\text{ETA} = 10^{-4}$ was found to be suitable for these calculations. A new pivoting sequence was calculated for every 25th matrix. If the ETA error diagnostic was provoked before this, a new pivoting sequence was computed then.

The solution x of the equation

$$A x = b$$

is solved by block forward or backward substitution within each diagonal block. The error on the solution can be calculated from the residual

$$r = b - A x$$

and the calling the composition routine again to find a correction, δ_C , for x by solving

$$A \delta_C = r$$

The solution can then be calculated to the accuracy required. It was mostly found, however, that the residuals were less than 1%, and this was deemed an accurate enough solution. A fuller presentation of the methods used for solving the matrix equation and a discussion of the extensive data checks carried out by the solving routines (used within subroutine SOLVE) can be found in Duff (1980).

By using this method of solving the reaction networks accurate solutions can be calculated. The largest source of error in the computations was that due to the use of the finite time step Δt , instead of an infinitesimal time step (see equation 2.28). The effect of round off error was negligible in comparison. The largest error on any individual abundance was 1%, with the errors on the rest of the

abundance determinations usually much less. Such errors in the computations will be much smaller than errors due to the uncertainties in the input physics such as the reaction rates. In double precision mode, it took roughly 40 minutes of c.p.u. time on a Vax 11/780 computer to work out the final abundances of the intershell region following one helium shell flash (see chapter 4).

2.4) The Reaction Networks

The light particle reaction network used in the calculations to follow is given in table 2.1. It contains 30 nuclear species (including neutrons and protons) and consists of all those reactions which are important with regard to ^{13}C production resulting from proton burning, and the subsequent neutron production.

Table 2.2 lists the light heavy ($27 < A < 56$) and the heavy ($A > 56$) element isotopes which undergo neutron absorption reactions. This network was directly coupled to the light particle network of table 2.1 in order to undertake calculations which investigate the neutron production as a result of hydrogen mixing on the AGB and post-AGB (chapter 3). The isotopes of table 2.2 were chosen on the basis that they lie on a synthesis path corresponding to a neutron density of 10^{13} neutrons/cm³. Of course the synthesis path will vary as the neutron density varies. However, for the purposes of investigating the neutron production on the AGB, the important factor is that a distribution of heavy elements (particularly ^{56}Fe and its progeny) are included in order to properly account for neutron absorption effects. For calculations regarding neutron production then, the exact path

(i.e. the choice of isotopes for table 2.2) will not be crucial. The nuclei of table 2.2 enclosed in parenthesis are not included in these calculations but are included in the calculations now to be discussed.

Calculations were carried out which also utilise the coupling of the reaction networks of tables 2.1 and 2.2 in order to conduct a preliminary investigation of the heavy element build up (chapter 4). However, such calculations are limited in their use, particularly since they are restricted to the use of a constant value of the neutron flux, and also since nuclear branching cannot be included. In order to investigate in more detail the heavy element build up in the element region Fe to Mo, the reaction network shown in figure 2.4 was constructed. Nuclei in at which at least 10% of the flow passed through (for the highest neutron flux considered in the calculations) were included in the network. The non-thermalisation of those isotopes which were considered to be significant (i.e. a significant fraction of the isotope was in the isomeric state) for the conditions under which the calculations are carried out are shown in black.

The reaction rates for the charged light particle reactions and light particle neutron absorptions were taken from the tables of Fowler, Caughlan and Zimmerman (1967, 1975) and Harris, Fowler, Caughlan and Zimmerman (1984). For reactions involving neutron absorptions on heavier nuclei, measured values were used where possible. These experimental values were taken from Allen, Gibbons and Macklin (1971); Steiglitz (1971); Weigmann et al. (1976); Spencer and Macklin (1976); Musgrove et al. (1976, 1977); Pandey et al. (1977); Beer et al (1979); Allen and Macklin (1980); Halperian et al. (1980); Walter et al. (1982); Aleneida and Käppelen (1983). For those reactions which had

unmeasured rates the theoretical estimates of Holmes et al. (1976) and Woosley et al. (1978) based on the statistical theory of nuclear reactions were used. For the few remaining nuclei which had no estimate given, values based on the extrapolation of the Allen, Gibbons and Macklin (1971) data were used. The beta decay, electron capture and gamma decay rates were taken from the tables of Cosner (1982) (assuming an electron density of 10^{27} cm^{-3}) or else taken as terrestrial ground state decays. The isomeric branching ratios were taken from the experimental values of Holden and Walker (1972).

The appendix lists the nuclear properties of the isotopes in the important Fe to Mo range. The heavy element build up in this mass range is investigated in detail in chapter 4.

Table 2.1

Light particle network

3He(3He,2p)4He	22Ne(A,n)25Mg
3He(A,G)7Be	22Ne(n,G)-23Na
4He(2A,G)12C	23Na(n,G)24Mg
7Li(p,A)4He	24Mg(n,G)25Mg
7Be(e-,v)7Li	25Mg(n,A)22Ne
7Be(n,p)7Li	25Mg(n,G)26Mg
7Be(p,G)8B	26Mg(n,G)-27Al
8B(G,p)7Be	
8B(B+v)8Be(2A)	
12C(p,G)13N	
12C(n,G)13C	
12C(A,G)16O	
13N(n,p)13C	
13N(p,G)14O	
13N(B+v)13C	
13C(p,G)14N	
13C(n,G)14C	
13C(A,n)16O	
14C(p,G)15N	
14C(A,G)18O	
14N(p,G)15O	
14N(n,G)15N	
14N(n,p)14C	
14N(A,G)18F	
14O(B+v)14N	
15O(B+v)15N	
15O(n,p)15N	
15O(n,A)12C	
15N(p,A)12C	
15N(p,G)16O	
15N(A,G)19F	
16O(n,G)17O	
16O(p,G)17F	
16O(A,G)20Ne	
17O(p,A)14N	
17O(n,A)14C	
17O(A,n)20Ne	
17O(p,G)18F	
17F(B+v)17O	
18O(p,A)15N	
18O(p,G)19F	
18O(A,G)22Ne	
18O(A,n)21Ne	
18F(n,A)15N	
18F(n,p)18O	
18F(p,A)15O	
18F(B+v)18O	
19F(p,A)16O	
19F(p,G)20Ne	
20Ne(n,A)17O	
20Ne(n,G)21Ne	
21Ne(n,G)22Ne	
21Ne(n,A)18O	

A=alpha particle

G=gamma ray

v=neutrino

e=electron

B+=positron

Table 2.2

Heavy element network (no branching)

Element	Atomic Mass Number
Al	27
Si	28 29 30 31 32
P	(31) (32) 33
S	34 35 36
Cl	37
Ar	38 39 40
K	41 42 43
Ca	(42) (43) 44 45 46 47 48
Sc	49
Ti	(49) 50
V	51
Cr	52 53 54
Mn	55
Fe	56 57 58 59 60
Co	61
Ni	62 63 64 65 66
Cu	67
Zn	68
Ga	69
Ge	70 71 72 73 74 75 76 77 78
As	79
Se	80
Br	81 82 83 84
Kr	85 86
Rb	87
Sr	88 89 90 91 92
Y	93 94 95
Zr	96 97
Nb	98
Mo	99 100
Tc	101
Ru	102 103 104 105
Rh	106 107
Pd	108 109 110
Ag	111 112 113
Cd	114 115 116 117 118
Sn	119 120 121 122
Sb	123 124 125 126 127
Te	128
I	129 130 131 132 133
Xe	134 135 136
Cs	137
Ba	139 140

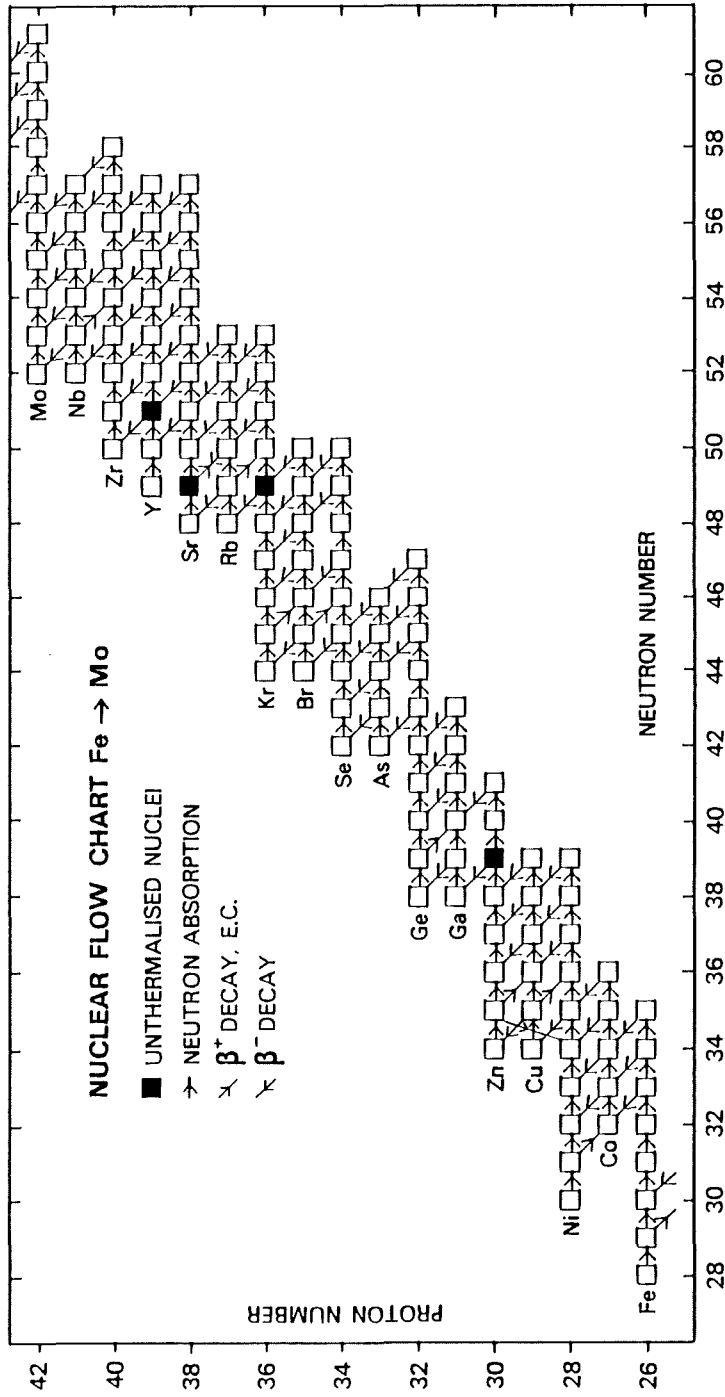


Figure 2.4 Fe to Mo reaction network

CHAPTER 3. NEUTRON PRODUCTION AT A HELIUM SHELL FLASH

3.1) The Helium Shell Flash

a) Details of the Flash

When a star leaves the quiescent phase of its evolution where its luminosity is supplied by helium burning in its core, it ascends the red giant branch for the second time. This second giant branch is more commonly known as the asymptotic giant branch (AGB). Whilst on the AGB the luminosity of the star arises from two different shell sources. One of these is a helium burning shell which surrounds the inert C/O core from the previous phase of core helium burning. The second of these shells is a hydrogen burning shell separated from the helium burning shell by a helium-carbon-rich zone. This zone is termed the intershell region. The basic structure of a $1.45M_{\odot}$ AGB star is shown schematically in figure 3.1 (this figure corresponds to the 8th flash of the Schönberner 1979 $1.45M_{\odot}$ model when the intershell convection was near maximum extent). In the quiescent phase most of the luminosity of the star arises from the hydrogen burning shell. However, the occurrence of a thermal instability within a helium burning shell source was encountered in an investigation of the evolution of a population II star of $1M_{\odot}$ (Schwarzschild and Härm 1965). The same phenomenon was found soon thereafter in two other independent investigations, the first (Weigart 1966) referring to a population I star of $5M_{\odot}$, and the second (Rose 1966, 1967) referring to helium stars of $1M_{\odot}$ or less. The thermal instability in the population II $1M_{\odot}$ star was further investigated by Schwarzschild and Härm (1967).

ENVELOPE ($M \approx 0.8 M_{\odot}$)			
ΔR (R_{\odot})	ΔM (M_{\odot})	_____	T (10^8 °K)
0.014	0.06	<u>HYDROGEN SHELL</u>	2.4 2.7
0.028	0.032	INTERSHELL	
0.004	0.05	_____	23
		<u>HELIUM SHELL</u>	14
0.013	0.456	C/O CORE	

Figure 3.1 Basic structure of low-mass AGB star

All of these investigations showed that the thermal instability leads to thermally driven relaxation oscillations (also termed in the literature as thermal pulses or helium shell flashes). What is meant by a thermal pulse or helium shell flash is this. The helium burning shell of figure 3.1 is degenerate. It can also be thermally unstable in the sense that a positive temperature perturbation does not lead to an expansion and cooling of the shell back to an equilibrium temperature, as would be expected for non-degenerate matter. Since there is no substantial cooling, the temperature of the helium shell keeps rising and a thermal runaway ensues. This causes a rapid luminosity rise of the helium burning shell. When the helium burning reaches values far above its average value, it changes the thermal structure of the layers in the vicinity of the helium burning shell in such a way as to quench the instability.

The behaviour of the luminosity of the helium shell is shown in figure 3.2. These calculations are from Schwarzschild and Härm (1967) and show the luminosity as a function of time for the 7th, 8th and 9th flashes. The time is the time elapsed since the onset of the first flash. As can be seen the helium luminosity can rise by nearly 5 orders of magnitude greater than its quiescent value. The behaviour of the helium shell, hydrogen shell and the total surface luminosity during the activated phases of the ninth cycle from the same calculations are shown in figure 3.3. When the helium luminosity rises, the hydrogen burning shell is pushed spatially outwards to cooler temperatures and is extinguished. The helium burning reaches a maximum then relaxes rapidly. In some circumstances the relaxation from the initial main

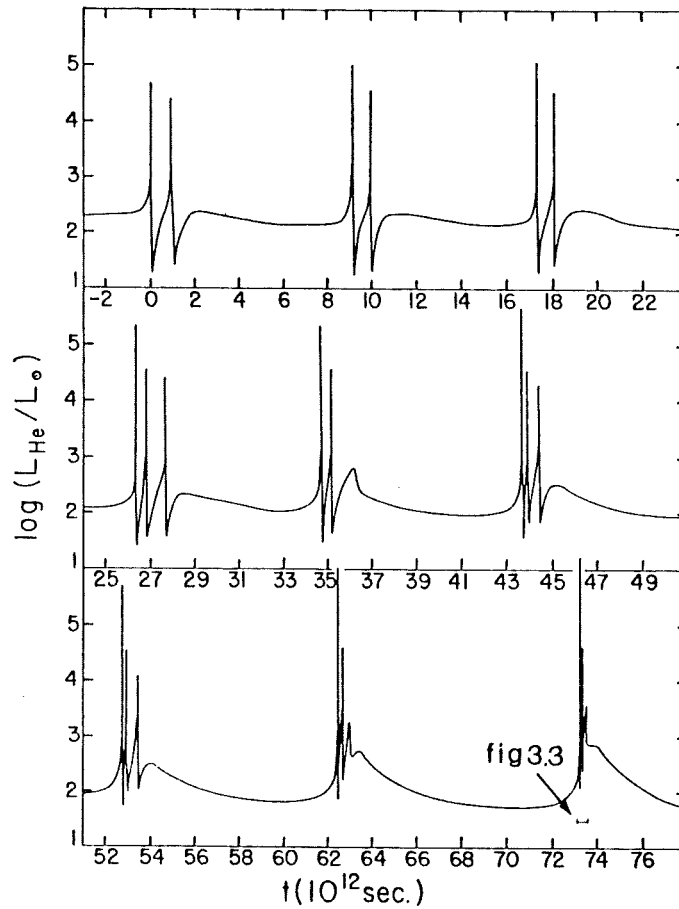


Figure 3.2 Luminosity behaviour for 7th 8th and 9th flashes
(taken from Schwarzschild and Härm 1967)

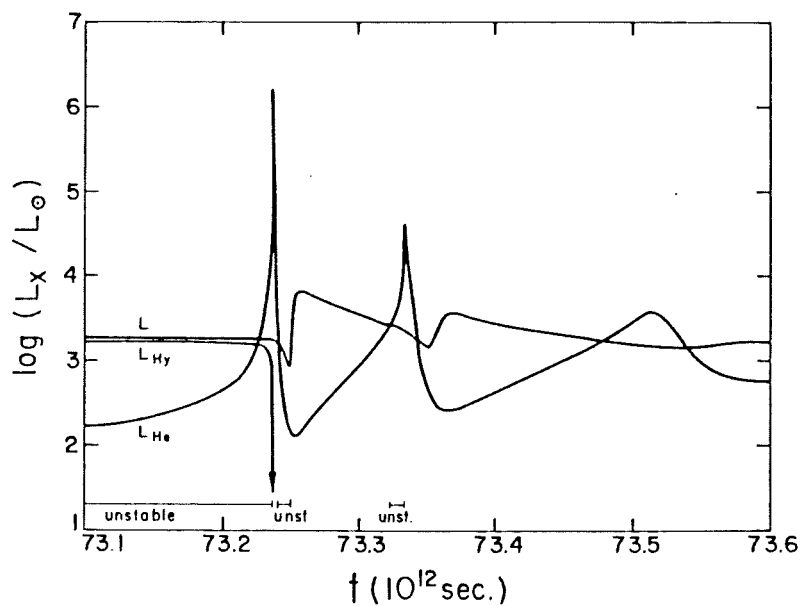


Figure 3.3 Luminosity of helium, hydrogen and total for 9th flash
(taken from Schwarzschild and Härm 1967)

flash leads the helium shell into a new thermally abnormal state in which it is again thermally unstable. This time the instability drives the already rapidly declining helium burning rate down to abnormally low values. Soon after the second unstable phase of the cycle ends, a new relaxation oscillation ensues, which causes a second though less violent helium shell flash. After a while the flash subsides and the hydrogen burning shell will again become active and the star returns to its pre-flash configuration. Although a slight rise in the surface luminosity occurs, it will be difficult to observe such a rise since it only occurs over $1/3000$ of the flash cycle. Many authors have shown what triggers the flash (Giannone and Weigart 1967; Kippenhanh 1967; Hoshi 1968; Unno 1970; Dennis 1971; Henyey and Ulrich 1972; Stothers and Chin 1972; Rose 1972). There are essentially three necessary conditions. The first of these is that the percentage pressure change be less than the percentage density change. The second is that there be nuclear burning in the region in question, and the third is that the increase in the nuclear energy output outweigh the increase in the flux leaving the region (this is best fulfilled by shells of high heat capacity). All these conditions have to be met in the helium shell in order to start the flash.

An important consequence of these shell flashes is the onset of an intershell convective zone extending from the helium burning shell upwards. The maximum extent of this convective shell always occurs after the peak in the helium shell luminosity (Sackmann 1977). This situation is illustrated in figure 3.4. The consequence of this convective intershell zone will be forthcoming in the following discussion.

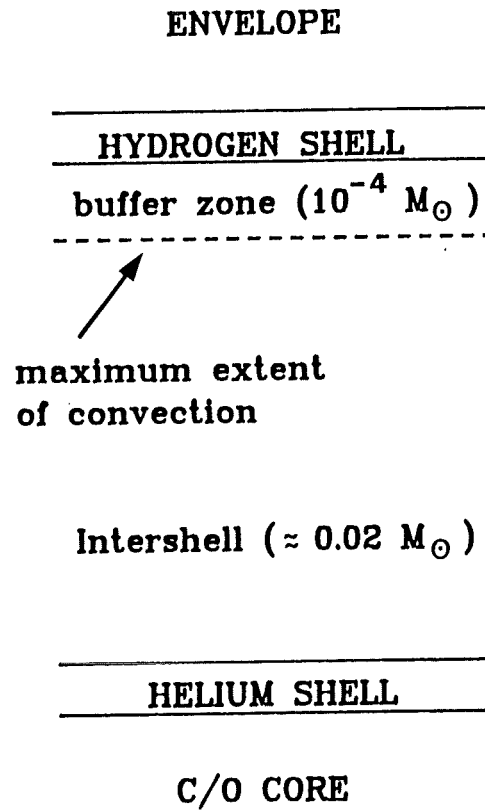


Figure 3.4 Structure at maximum convection extent

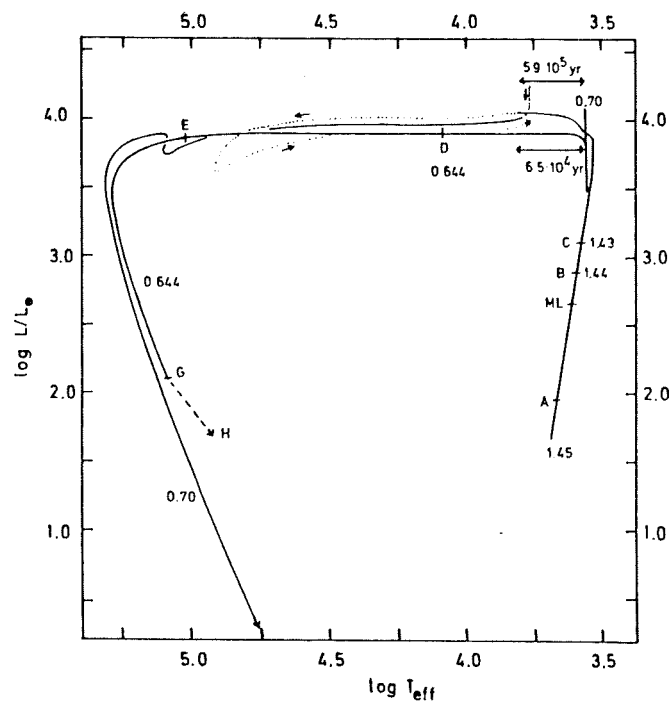


Figure 3.5 Schönberner evolutionary track (taken from Schönberner 1979)

b) Neutron Sources

Two main reactions are generally believed to be the main source of neutrons in stellar interiors. These two sources were first identified by Cameron as the $^{13}\text{C}(\alpha, n)^{16}\text{O}$ source (Cameron 1955) and the $^{22}\text{Ne}(\alpha, n)^{25}\text{Mg}$ source (Cameron 1960). The ^{22}Ne source has been studied extensively. Peters (1960) identified the core of a massive star near the end of the core helium burning phase as a promising site for the operation of this source. Couch, Schmiedekamp and Arnett (1974) and Lamb et al. (1977) have shown that the ^{22}Ne source is ineffective in stars less massive than $15M_{\odot}$. In stars more massive than this, however, the ^{22}Ne source is able to produce the light ($A < 70$) s-process elements in copious amounts.

Truran and Iben (1977) identified a mechanism of continually replenishing the ^{22}Ne in the intershell zones of intermediate-mass ($M=2-8M_{\odot}$) AGB stars. This replenishment of ^{22}Ne is based on the convective properties of the intershell region following a helium shell flash. During the interpulse phase, the outward progression of the hydrogen burning shell leaves in its wake a substantial concentration of ^{14}N (comprising of most of the initial CNO concentration). Following the next thermal pulse, the convection zone extending almost outwards almost to the helium-hydrogen interface mixes this ^{14}N -rich material downwards into the hot helium-rich region. The ^{14}N is then readily transformed into ^{22}Ne via $^{14}\text{N}(\alpha, \gamma)^{18}\text{F}(\beta^+ \nu)^{18}\text{O}(\alpha, \gamma)^{22}\text{Ne}$. The ^{22}Ne can then burn due to a further α capture i.e. $^{22}\text{Ne}(\alpha, n)^{25}\text{Mg}$, thus forming a potent source of neutrons. This procedure can then be repeated every thermal pulse cycle. Truran and Iben (1977) and Cosner et al. (1980)

have shown how this source can reproduce a large range of the solar system s-process abundances.

In low-mass stars ($M < 2M_{\odot}$) the ^{22}Ne source is ineffective. However, if during a thermal pulse in a low-mass AGB star, the convective intershell zone penetrated the hydrogen shell and into the hydrogen envelope, then the possibility of mixing protons into the hot intershell zone occurs. Sanders (1967) demonstrated that only a very small admixture of protons into the helium, carbon-rich convective intershell would lead to a large flux of neutrons via the $^{12}\text{C}(p,\gamma)^{13}\text{N}(\beta^+\nu)^{13}\text{C}(\alpha,n)^{16}\text{O}$ reactions. There have been many investigations of this scheme (Cameron and Fowler 1971; Ulrich and Scalo 1972; Scalo and Ulrich 1973; Ulrich 1973; Sackmann, Smith and Despain 1974; Cowan and Rose 1977; Despain 1977). However, there has always been a serious difficulty with this scheme. Most of the previously published calculations (eg. Rose and Smith 1972; Sweigart 1974; Gingold 1974; Schönberner 1979) show that for low-mass AGB stars, the convective zone closely approaches but does not penetrate the hydrogen shell. Indeed the only calculations to show such a penetration were those of Schwarzschild and Härm (1967). But in their calculations these authors neglected the effects of radiation pressure. Iben (1976) has shown that the inability of calculations which include radiation pressure, to produce penetration is a result of an entropy barrier at the helium-hydrogen interface. However, it is plausible in view of the approximate nature of such model calculations, that penetration could arise as a result of physical processes that have not been included in the calculations. Indeed, recent work by Iben and Renzini (1982 a,b) has shown that mixing may arise when the effects of the increased opacity of carbon (generated by a previous flash) in the cooler regions

at the top of the intershell region is considered. This mixing mechanism is however, more involved than a simple penetration as outlined above and is discussed in more detail later. Furthermore, many of the observed low-mass red giants indicate that significant mixing events have occurred during their evolution, resulting in large enhancements of carbon and heavy elements at their surfaces. Since the ^{22}Ne source can not operate in such low-mass stars, these objects are then prime sites for the operation of the ^{13}C source. A full discussion of these observations and of the various mixing mechanisms possible in red giants is given by Scalo (1980).

The ^{22}Ne source rather than the ^{13}C source is most commonly believed to be the main neutron source for the production of the solar system s-process elements. This is because in the case of the ^{13}C source, the introduction of either too many or too few protons into the intershell region produces an elemental distribution of the elements quite distinct from the solar system distribution (Truran 1973; Ulrich 1973). If the solar system s-process distribution is due to the ^{13}C source then the ratio of protons (hence neutrons) to the ^{56}Fe seed nuclei must be restricted to a very narrow range of possibilities. The ^{22}Ne source, however, does not suffer from such a restriction. This is due to the large neutron absorption cross section of the progeny of ^{22}Ne (^{16}O has a small absorption cross section). If a large amount of ^{22}Ne is consumed at a shell flash, this means a large amount of neutrons will be absorbed by the progeny of ^{22}Ne , and vice-versa for a small amount of ^{22}Ne consumed. This filtering action of the ^{22}Ne progeny is such that the ratio of neutrons captured by ^{56}Fe and its progeny to the number of fresh ^{56}Fe seed is constant to within a factor of 2, and is roughly independent of the amount of ^{22}Ne consumed (Iben 1975b). This nearly

constant value is the value required to produce the solar system s-process distribution (Ulrich 1973). The reason that the ^{22}Ne source can produce the s-process elements with $A > 70$ in thermally pulsing intermediate-mass AGB stars and fails to do so in the cores of more massive stars, is due to the fact that some of the matter in the convective shell of the pulsing star has been exposed to many bursts of neutrons whereas the matter in the core of a massive star experiences just one burst.

The purpose of this thesis is not to attempt a simulation of the solar system s-process distribution. As stated earlier many low-mass red giants show evidence of the ^{13}C neutron source having been in operation. The distribution of the heavy elements observed in these stars is very non-solar system like. This work investigates the neutron production and heavy element synthesis of such low-mass stars, particularly of those stars on the AGB. The synthesis of the heavy element enhancements of a low-mass AGB star is investigated in detail in chapter 4. In this chapter the neutron production arising from hydrogen mixing on the low-mass AGB is investigated. The influence of the initial intershell abundances, the intershell temperature, the adopted convective velocity and the ingestion rate on the level of neutron production is investigated.

3.2) Calculations

The temperature-density intershell grids used in the following nucleosynthesis calculations are from the stellar models of Schönberner (1979). These grids were kindly supplied to the author by Dr. D. Schönberner. The models are from the evolutionary sequences of an AGB star with an initial core mass of $0.475M_{\odot}$ and an initial mass of $1.45M_{\odot}$. The model undergoes significant mass loss via stellar winds as the star evolves. The mass loss rate is given by Reimers (1975) as

$$\dot{M} = -3.2 \times 10^{-13} (L/L_{\odot})^{1.66} (M/M_{\odot})^{-1} [M_{\odot}/\text{year}]$$

The core mass increases steadily due to fuel consumption, as the star evolves along the Hayashi-track. The growth of the core at this stage is given by

$$\dot{M}_c = 1.5 \times 10^{-11} L/L_{\odot} [M_{\odot}/\text{year}]$$

The evolutionary track of the $1.45M_{\odot}$ model from Schönberner's calculations is shown in figure 3.5. The total mass at various phases of the evolution is indicated (in M_{\odot}). After termination of central helium burning (at point A), helium burns in a thick shell and the luminosity rises. The onset of mass loss is indicated by ML. At B the luminosity of the hydrogen shell surpasses that of the helium shell. The first thermal pulse develops at C. The evolution then proceeds rapidly as the star moves from the Hayashi-track almost horizontally. At the tip of the AGB the model has a luminosity and mass loss rate of $L/L_{\odot}=3.93$ and $\dot{M}=10^{-6}M_{\odot}/\text{year}$ respectively. At point D, $\dot{M}/M=\dot{M}_c/M_c$ and thus the stellar mass remains constant at $0.644M_{\odot}$. A total number of 23 helium shell flashes had occurred up to this point. The time to cross the H.R. diagram at this phase is of equal duration to the interflash period. Consequently, while the model cools to a white dwarf

configuration a 24th helium flash occurs at G. The convective intershell zone arising from this flash was found to penetrate the hydrogen-rich layers (such mixing can now occur at this stage due to the diminishing strength of the hydrogen burning and hence a decrease in the entropy jump at the helium-hydrogen interface). The calculations were then stopped at this point due to the numerical difficulties associated with the rapid influx of the hydrogen into the hot helium-rich layers. In his calculations Schönberner constructed a second series of models. These started from the point in the $1.45M_{\odot}$ sequence when the total mass was reduced to $0.7M_{\odot}$. The mass loss mechanism was cut off at this point and the model was allowed to evolve at a constant $0.7M_{\odot}$. Due to the slower evolution of this model a further 11 thermal pulses were found to occur while the model evolved from the Hayashi-track.

The temperature-density grids employed in the following nucleosynthesis calculations correspond to the run of temperature and density through the intershell region for the maximum convective phases of the 13th and 24th helium flashes of the $1.45M_{\odot}$ continuous mass loss Schönberner model. The onset of these flashes in the H.R. diagram are indicated in figure 3.5. The nucleosynthesis arising from the 13th flash will correspond to a mixing event on the AGB while that arising from the 24th flash will correspond to a post-AGB event. The run of temperature and density throughout the intershell region for these two flashes are shown in figure 3.6, and some of the parameters for the different flashes are given in table 3.1 (as in all other tables the exponent is enclosed in parentheses). T_b is the base temperature of the grid used, M_{int} is the mass contained within the intershell region and M_{buff} is the mass between the maximum extent of the convective zone and the hydrogen shell. For the 24th flash M_{buff} is zero since the low

entropy jump at the helium-hydrogen interface allows mixing. The small value of M_{buff} for the 13th flash, due to the high value of the entropy barrier prevents any mixing at this phase in Schönberner's calculations. However, as stated earlier there is strong evidence that mixing does in fact occur on the low-mass AGB. It will therefore be assumed in what is to follow that for the 13th flash a small amount of hydrogen material is mixed into the intershell region. That is, it will be assumed that the convective intershell zone does in fact reach the hydrogen shell. This change in the extent of the convection, does not significantly change the run of temperature and density of the 13th flash illustrated in figure 3.6, especially at the important hotter regions near the helium shell.

The most important parameter with regard to the level of neutron production will be the ingestion rate of envelope matter into the intershell region. The rate of ingestion will be controlled by the advancement of the convective boundary into the hydrogen-rich envelope. The advancement of the convective boundary will be much slower than the subsequent downward transfer by the convective motions of the intershell region. No attempt will be made here to calculate the ingestion rates which could occur in low-mass AGB stars. Instead, a range of ingestion rates, from the theoretical calculations of previous workers, will be used in the neutron production calculations. An upper limit on the ingestion rate can be estimated from the calculations of Despain (1977). In these calculations a full convective link up between the convective intershell region and the convective envelope was assumed. This in effect meant that a convective region extended from the helium burning shell all the way to the stellar surface. Despain found from his calculations a maximum of 1.5×10^{47} protons/s being mixed in and

burned in the hot regions of the star. This mixing rate is, as expected, much higher than the earlier calculations of Schwarzschild and Härm (1967). With the neglect of radiation pressure these authors found an ingestion rate of roughly 2×10^{43} protons/s. This mixing rate was due to the convective intershell penetrating into the hydrogen-rich region for 10^7 s, during which time a total of $2.5 \times 10^{-7} M_{\odot}$ was mixed into the intershell. In the calculations to be presented here ingestion rates in the range 10^{43} to 10^{47} will be investigated. The method of simulating these ingestion rates are achieved by injecting different amounts of envelope material into the intershell and allowing it to diffuse through the entire intershell. This is described in more detail shortly.

The phenomenon of intershell splitting should be discussed at this point. For an ingestion rate of 5×10^{43} protons/s, Sweigart (1974) discovered no significant structural changes in the intershell region of a $0.7 M_{\odot}$ population II star. However, for an ingestion rate of 10^{44} protons/s Sweigart discovered a splitting of the intershell region into two different convective regions separated by a thin radiative shell caused by the large amount of hydrogen burning in this shell. This phenomenon had earlier been suggested by Scalo and Ulrich (1973). Of the ingestion rates to be investigated here it can be seen that only those rates at the low end of the range will not be effected by intershell splitting. For the higher rates, which simulate a complete convective link up of intershell and envelope, Despain (1977) argues that it is not yet clear whether such a splitting will in fact occur for such high ingestion rates. He points out that the nuclear energy generation and the mean molecular weight gradient from descending hydrogen (effects not generally included in evolutionary calculations) will effect the character of the convection, perhaps altering the mixing

lengths and velocities. Such changes may then enable a continued connection of the convective regions to continue.

It is, however, more likely that intershell splitting will in fact occur. This splitting would effectively cut off the supply of ^{13}C -rich material to the hot regions of the intershell. If the duration of the hydrogen burning radiative shell does not last a substantial period of time, then following its disappearance, the ^{13}C -rich material will be swept down into the hot regions at the onset of the intershell once again becoming fully convective. Neutron production will then commence. Cowan and Rose (1977) conducted an investigation of the effects of such a "delay" arising from intershell splitting and concluded that the resulting nucleosynthesis would not be significantly altered from assuming the envelope matter was swept down to the hot regions without any intershell splitting being encountered.

In the high ingestion rate calculations presented here the nucleosynthesis and neutron production is at first investigated with no intershell splitting effects included. A second series of calculations are then presented which attempt to include the intershell splitting effect in order to investigate the importance of this effect on the neutron densities expected from high ingestion rates. It will be assumed in these calculations that mixing of hydrogen envelope material has occurred into the hot carbon-rich intershell region. The initial abundances of the envelope and the intershell region are given in table 3.2. It will also be assumed that at the time of this mixing the region between the hydrogen shell and the helium shell is fully convective. Following this initial injection of hydrogen-rich matter, the growth of the neutron flux and the subsequent nucleosynthesis of the nuclear

isotopes in the intershell region is followed as the initial envelope matter diffuses throughout this region. The diffusion of matter in turbulent motion was first discussed by Taylor (1921). The method of simulating convective diffusion in the intershell convective region of the following calculations is described below. This is essentially the same procedure as that given by Cowan and Rose (1977).

When considering the diffusion of particles in a gas it is well known that the time for the particles to diffuse a distance X , say is given by

$$t_d = X^2/D$$

where D is the diffusion coefficient given by the product of the mean velocity of the particle, v , and the mean free path, L . In the convective region of an intershell zone, v is associated with v_c the convective velocity and L with the mixing length, λ_m . It will be assumed that $\lambda_m = H_p$ where H_p is the pressure scale height given by

$$H_p^{-1} = \frac{1}{P} \left| \frac{dP}{dr} \right|$$

In the AGB models used here, the intershell region has $H_p = 2.2 \times 10^8$ cm and has a thickness ΔR extending over approximately 8 of these pressure scale heights. The diffusion equation can now be used to estimate the time scale for matter initially mixed in at the top of the zone to diffuse to the bottom. This is given by

$$t_d \approx \frac{\Delta R^2}{\lambda_m v_c}$$

If we take $v_c = 1 \text{ km/s}$ (Levy and Rose 1974) then for $\Delta R = 2 \times 10^9 \text{ cm}$ we find $t_d = 7.5 \times 10^4 \text{ s}$. The intershell region is then split up into 50 equal mass zones. This means that on average, the average time, t_z , taken for matter to be convected through one of these mass zones is approximately 1500s. This time will be slightly longer for the top zones (near the hydrogen shell) and slightly shorter for the lower zones of the intershell since the mass density is increasing as the helium shell is approached.

As the initial envelope matter mixes down through the intershell region and reaches a certain zone for the first time, the nuclear network is 'turned on' (only in that one zone) for a time equal to the time taken for the matter to diffuse through a zone ($t_z = 1500 \text{ s}$). After this time has elapsed the new abundances are thus calculated for this zone and the diffusion is then allowed to take place to the next lower lying zone. The initial starting abundances for this lower level zone will be given by

$$MF = \frac{IMF}{\text{zone number}} + \left[1 - \frac{1}{\text{zone number}} \right] FMF$$

where MF is the new mass fraction of an isotope before the reaction network is turned on, IMF is the initial intershell abundance of the isotope and FMF is the final mass fraction of the isotope in the immediate upper zone just after the network had been turned off in that zone. The reactions are then switched on in this new lower zone, again for 1500s. Of course nucleosynthesis will still be occurring in the upper zones, but these reactions are not included as we are essentially investigating the reactions of the isotopes in the intershell as the

first of the envelope material diffuses past them. The procedure is repeated until the original envelope matter is completely diffused throughout the intershell region, i.e. until the zone at the helium burning shell is reached.

This process, then describes the diffusion of the original envelope matter from the time when it is first injected into zone 1 of the intershell. For example, when using the above equation for the calculation of the starting abundances of say, zone 30 (i.e. after a time $29 \times 1500s$) the original injected material can be thought of as homogeneously diffused through the above 29 zones. Of course in each of these upper zones some of the original material may be in the form of other nuclei mainly due to the proton burning reactions. Below zone 30 neither the original nor the transformed envelope material has had enough time to diffuse to these deeper lying intershell zones and thus the abundances in them remain as the original intershell abundances until the diffusion front reaches them. Figure 3.7 shows schematically the mixing mechanism. The nuclear reactions undergone at the diffusion front as it advances down through the intershell are the only reactions that are followed. The neutron production occurring behind the diffusion front will be essentially at the same level as that found for the diffusion front as it passed through that particular mass zone. That is, the change in the chemical composition of the matter behind the front will not significantly change the neutron level from the earlier calculation (this is confirmed in a later calculation). Previous methods of treating turbulent mixing in a neutron producing reaction network have either used the simple approximation of infinitely fast mixing of all nuclei other than the neutrons (e.g. Truran and Iben 1977) or the more accurate treatment of coupling the diffusion equation

to the reaction network (Despain 1977). The schematic treatment of the diffusion equation described here represents an improvement on the instantaneous mixing approximation although clearly not as accurate as the proper treatment of solving a diffusion equation simultaneously with the reaction equations. However, for the points concerning the neutron production levels presented here this schematic representation of diffusion is sufficient and also economical with regard to computer time (for the same conditions used in Despain's calculations, which were halted after 10^6 s, the method of simulating the diffusion used in these calculations gave similar neutron densities at the bottom of the intershell).

When the reaction network is "turned on" in a particular zone, the temperature and density of the midpoint of the zone are used in order to calculate the stellar reaction rate. This reaction rate is then taken as the rate for the entire mass zone. The stellar reaction rates and the method of solving the reaction network have been discussed in chapter 2. In all the following calculations the excess energy generated by the hydrogen mixing is neglected. This is a common practice in such calculations due to the difficulties in properly accounting for energy generation in a convective region. These results should then be looked upon only as an approximation to the real situation.

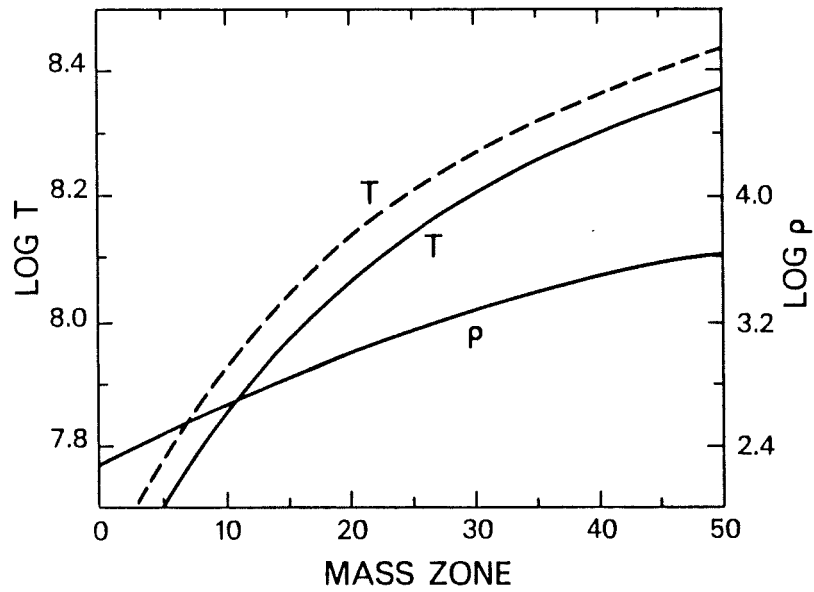


Figure 3.6 Run of temperature and density

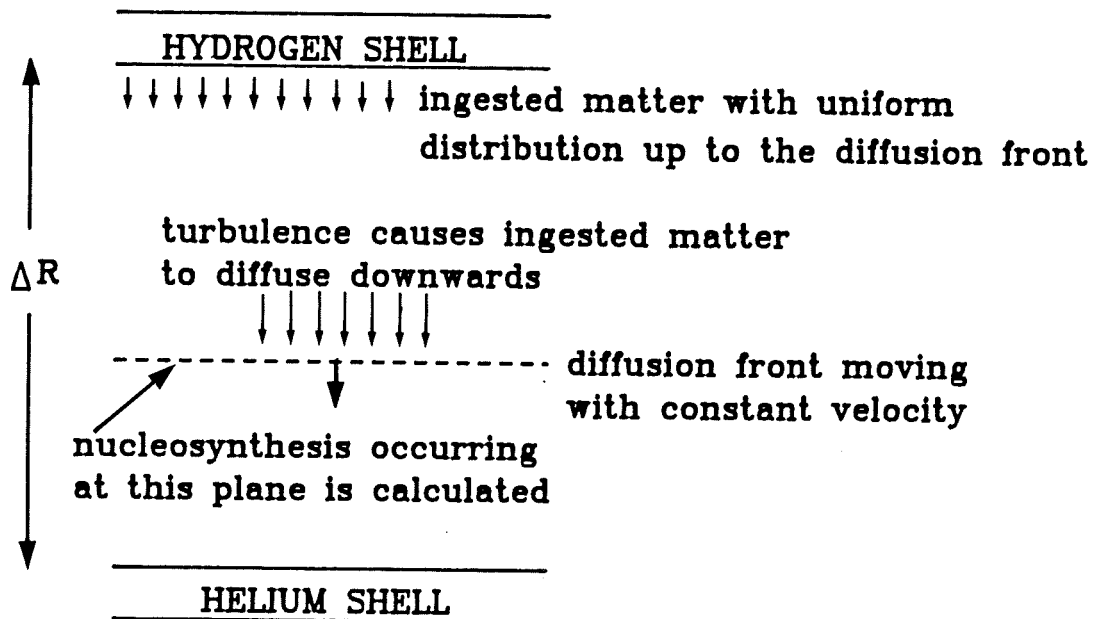


Figure 3.7 Diffusion of ingested envelope material

Table 3.1

Properties of 13th and 24th flashes

Flash	T_b (10^8 °K)	M_{int} (M_\odot)	M_{buff} (M_\odot)
13	2.4	0.028	1 (-4)
24	2.75	0.0158	0.0

Table 3.2

Initial abundances

Isotope	Envelope mass fraction	Intershell mass fraction
1H	0.77	0.0
3He	1.0(-4)	0.0
4He	0.21518	0.483
12C	3.5(-3)	0.4861
14N	1.5(-3)	0.0
16O	8.0(-3)	0.02
18O	2.0(-5)	0.0 *
19F	1.0(-6)	0.0
22Ne	8.0(-4)	0.01 *
56Fe	9.0(-4)	9.0(-4)

All other abundances initially zero.

*Uncertain, see text.

Table 3.3

Changes of light particle abundances

T_b (10^8 K)	t (s)	Final Zone Abundance (t)/Final Zone Abundance(t=1500s)						
		n	^{13}C	^{14}C	^{14}N	^{15}N	^{17}O	^{18}O
2.4	150	3.2	4.5	0.7	0.5	0.04	0.2	0.03
2.4	5000	0.02	0.02	1.4	1.1	3.2	1.1	4.2
2.75	150	4.8×10^4	5.6×10^4	0.5	1.0	0.03	0.9	0.03
2.75	5000	0.3	0.2	1.2	0.5	1.0	0.9	7.6

3.3) Results

a) Parameters Affecting Neutron Production

The neutron production arising from an ingestion rate equivalent to that expected from a full convective link up with the intershell and envelope will be investigated. Such an ingestion rate is simulated by injecting $2.5 \times 10^{-6} M_{\odot}$ envelope material into the first mass zone of the intershell region. The convective motion of the intershell is then allowed to diffuse this matter in the manner outlined in section 3.2. This simulation gives rise to an effective ingestion rate for the hydrogen mixing at the top of the intershell of 1.3×10^{47} protons/s, and an effective mixing rate for the ^{13}C passing down to the bottom of the intershell of $10^{-3} M_{\odot}$ /year. Such ingestion rates are found for a full link up of the intershell with the envelope (Despain 1977). The effect of intershell splitting (anticipated for such a high mixing rate) on the neutron production levels is ignored in the following exploratory calculations. The effect of this phenomenon on the neutron production is presented in a following section.

Figs. 3.8-3.11 show the results of hydrogen mixing into the intershell region under differing initial conditions. The plots show the final mass fractions for the light isotopes in each mass zone immediately after the first of the original material had diffused down to that zone and nuclear burning had proceeded for 1500s. The hydrogen shell is just above zone 1 and the helium shell is at zone 50. The abscissa is analogous to a time scale since matter is being followed as it is mixed downward to higher temperatures at a constant velocity

$\Delta R/t_d$. It can be seen how the different nuclear isotopes are affected by the injection of proton-rich material and how the reactions of these isotopes with this material control and influence the production of neutrons at different levels of the intershell region. The neutron mass fraction for each of the different initial conditions is shown in figure 3.12. The neutron density for each zone can simply be calculated from,

$$N_n = \rho N_A X_n$$

where ρ =mass density, N_A =Avogadro's number and X_n =neutron mass fraction. The neutron flux is then given by,

$$F_n = N_n v_T$$

where v_T is the neutron velocity.

Figure 3.8 shows the results of mixing $2.5 \times 10^{-6} M_\odot$ of envelope matter into an intershell region with a $T_b = 2.4 \times 10^8$ °K. As the initial hydrogen starts being mixed down into the hotter regions it begins to be destroyed and the CNO isotopes ^{13}C , ^{14}N , and ^{17}O are produced via the reactions $^{12}\text{C}(p,\gamma)^{13}\text{N}(\beta^+\gamma)^{13}\text{C}$, $^{13}\text{C}(p,\gamma)^{14}\text{N}$ and $^{16}\text{O}(p,\gamma)^{17}\text{F}(\beta^+\gamma)^{17}\text{O}$ respectively. The initial drop in the ^{14}N abundance is due to the dilution of the isotope as it mixes downward and its subsequent build up is helped by the slow reaction rate for the reaction $^{14}\text{N}(p,\gamma)^{15}\text{O}$. Such a build up of these isotopes is typical of CNO burning. The abundances of these isotopes reach their peak round about mass zone 17 (i.e $T_8=1.0$; T_8 is in units of 10^8 °K). This is because at these temperatures the hydrogen begins to burn very rapidly and its abundance quickly becomes very small causing the reaction rates for the CNO producing reactions to become negligible. The radioactive nuclei ^{13}N , ^{14}O , ^{15}O , ^{17}F and ^{18}F beta decay by emission of a positron in a matter of seconds and are not shown on the plot. At the helium shell their abundances are negligible in comparison with the stable isotopes into which they decay.

However, the radioactive isotope ^{14}C which has a half life of 5730 years against beta decay into ^{14}N is plotted. Its mass fraction becomes larger than 10^{-10} at approximately zone 25 ($T_8=1.4$) and its production is due to the increasing neutron flux, shown in figure 3.12 (line a), causing neutron absorption by ^{14}N , via the $^{14}\text{N}(n,p)^{14}\text{C}$ reaction, to become important. As the matter mixes downward to higher temperatures the $^{13}\text{C}(\alpha,n)^{16}\text{O}$ reaction becomes more important and the ^{13}C rapidly produces a high flux of neutrons. This neutron flux has a peak at roughly zone 47 ($T_8=2.3$). The slight drop in the higher zones is due to the ^{13}C now dropping due to the increasing reaction rate of the ^{13}C with α particles. The ^{18}O originally present in the envelope material was quickly destroyed via $^{18}\text{O}(p,\alpha)^{15}\text{N}$. It is produced again in the hotter regions via the reactions $^{14}\text{N}(\alpha,\gamma)^{18}\text{F}(\beta^+\gamma)^{18}\text{O}$ and $^{17}\text{O}(p,\gamma)^{18}\text{F}(\beta^+\gamma)^{18}\text{O}$. The ^{15}N abundance also begins to rise significantly in the higher neutron flux regions via $^{14}\text{N}(n,\gamma)^{15}\text{N}$ to a final mass fraction of approximately 10^{-7} . Of the remaining light isotopes not shown, the ^4He in the envelope material rapidly burns with an α particle forming ^7Be . The ^7Be is destroyed in the hot zones of the intershell region by the $^7\text{Be}(n,p)^7\text{Li}$ reaction. The final abundance of ^7Li was approximately 10^{-11} . This production of ^7Li is not to be confused with the mechanism attributed to the production of the 'super-lithium stars' i.e. the Be transport mechanism described by Sackmann et al. (1974). The ^{19}F abundance remained essentially constant throughout the region.

During earlier quiescent CNO burning ^{18}O is built up in the intershell region via $^{14}\text{N}(\alpha,\gamma)^{18}\text{F}(\beta^+\gamma)^{18}\text{O}$. This ^{18}O is then destroyed by further α capture by $^{18}\text{O}(\alpha,\gamma)^{22}\text{Ne}$. This is the cause of the initial ^{22}Ne abundance in the model of figure 3.8. However the value of the ^{18}O

abundance in the intershell region at the onset of the flash may not be zero as assumed in figure 3.8 . To see what effect a higher initial ^{18}O abundance has on the results, figure 3.9 shows the nucleosynthesis arising when the intershell ^{18}O abundance was 0.01 and the ^{22}Ne abundance was assumed solar. As can be seen this high ^{18}O abundance causes significant differences to the results. The maximum ^{13}C mass fraction is now significantly lower. This is due to the $^{18}\text{O}(p,\alpha)^{15}\text{N}$ reaction which now competes with $^{12}\text{C}(p,\gamma)^{13}\text{N}$ for the available protons. For the conditions at the top of the intershell region the ^{18}O captures roughly 50 more protons than ^{12}C . The dramatic rise of ^{15}N is a direct result of these proton captures on ^{18}O . As a result of the now lower ^{13}C abundance the neutron density will be lowered. This is shown in figure 3.12 (line b) . The peak neutron flux is now down by a factor of about five. The lower abundances of the other isotopes are a consequence of this reduced neutron density. The consequences of mixing the hydrogen material into a convective region with a higher base temperature of $T_b = 2.75 \times 10^8 \text{ }^\circ\text{K}$ was investigated. The behaviour of the isotopes for this hotter environment is shown in figure 3.10. The initial abundances were again set to those of table 3.2. The important point to note from these results is the dramatic drop in the ^{13}C abundance in the very hot ($T_8 > 2.5$) zones near the helium shell due to the high $^{13}\text{C}(\alpha, n)^{16}\text{O}$ reaction rate. Due to this drop in ^{13}C the neutron density shown in figure 3.12 (line c) peaked at zone 44 with a value of $X_n = 6 \times 10^{-14}$. It can be seen that the neutron density at the base of such a hot convective region is relatively small and that the most significant s-processing will occur off the base at a temperature of $T_8 = 2.5$.

It is worthwhile here to point out the crucial importance in reaction networks such as these of the effects of absorption of neutrons by the light heavy (e.g. ^{22}Ne) elements and of the heavy elements (e.g. ^{56}Fe). If the initial intershell abundance of ^{22}Ne and ^{56}Fe are put to 0.001 of their value given in table 3.2 and the base temperature is again $T_b = 2.75 \times 10^8$ °K the resulting abundances are shown in figure 3.11. As the neutron abundance increases ^{14}N is destroyed much more rapidly than previously via $^{14}\text{N}(n,p)^{14}\text{C}$, since this reaction no longer has any significant competition from the ^{56}Fe or ^{22}Ne reactions. As the ^{14}N is destroyed, producing more ^{14}C , it can no longer act as an important neutron poison. ^{13}N briefly becomes the main neutron poison via $^{13}\text{N}(n,p)^{13}\text{C}$ until it too becomes quickly depleted. When this happens the $^{12}\text{C}(n,\gamma)^{13}\text{C}$ reaction becomes the most important neutron absorber, and since ^{12}C remains with a high constant value throughout the region it remains as an important neutron poison. It is these absorptions by ^{13}N and ^{12}C which can now proceed due to the lower ^{22}Ne and ^{56}Fe abundances that produce new ^{13}C and thus maintain a high ^{13}C value as shown in figure 3.11. Figure 3.12 (line d) shows how the neutron density has a value greater by over an order of a magnitude than the previous calculation due to the lower ^{22}Ne and ^{56}Fe .

To investigate the importance of the initial intershell carbon and helium abundances the above calculations were repeated with the initial abundances of table 3.2 except ^{12}C was set to 0.2 and ^4He set to 0.78. The main effect of this change was a doubling of the neutron density for a period, simply as a consequence of the doubling of the α burning rate on ^{13}C .

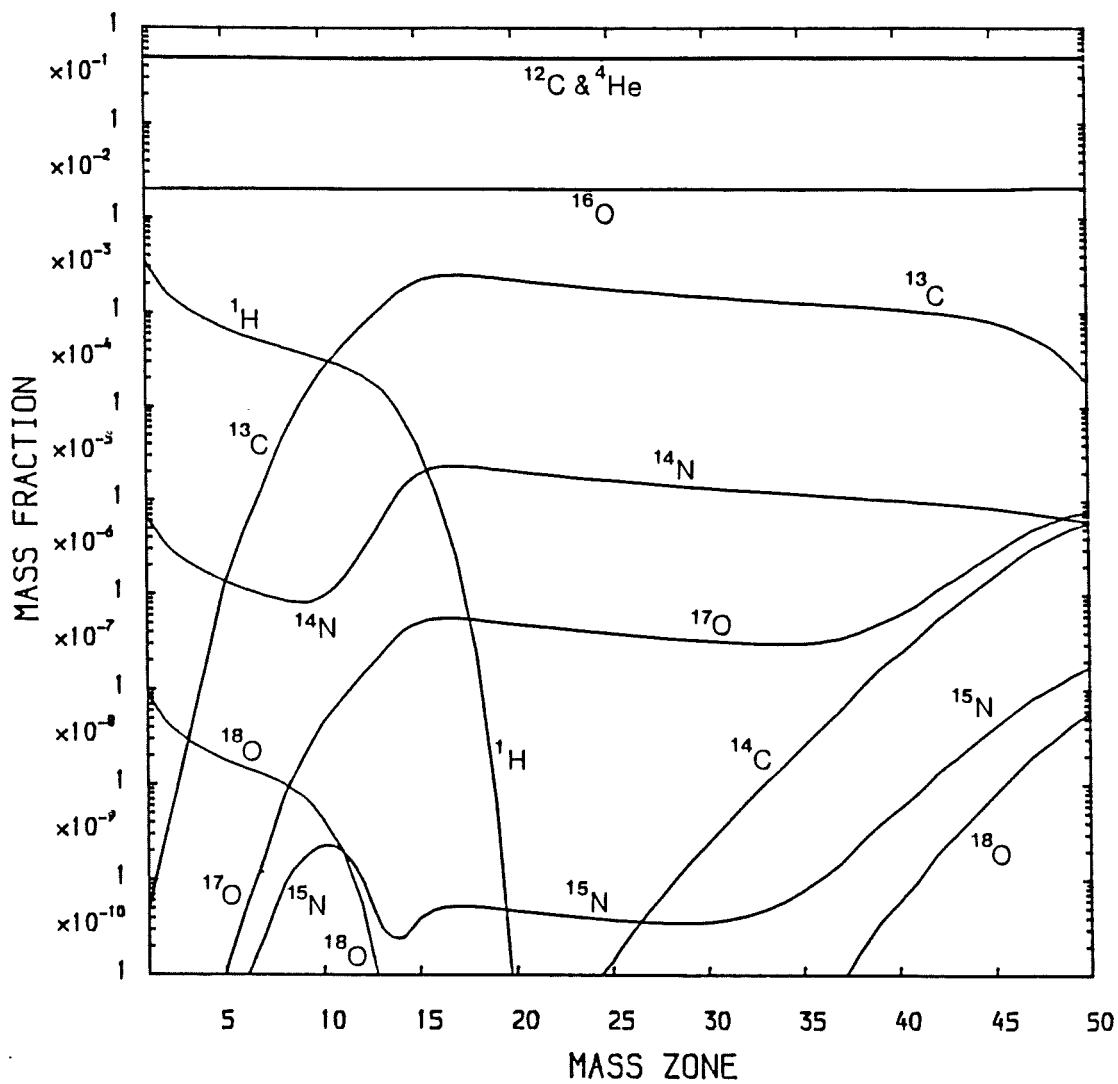


Figure 3.8 Mixing of $2.5 \times 10^{-6} M_{\odot}$ of envelope material into an intershell with $T_b = 2.4 \times 10^8 \text{ }^{\circ}\text{K}$

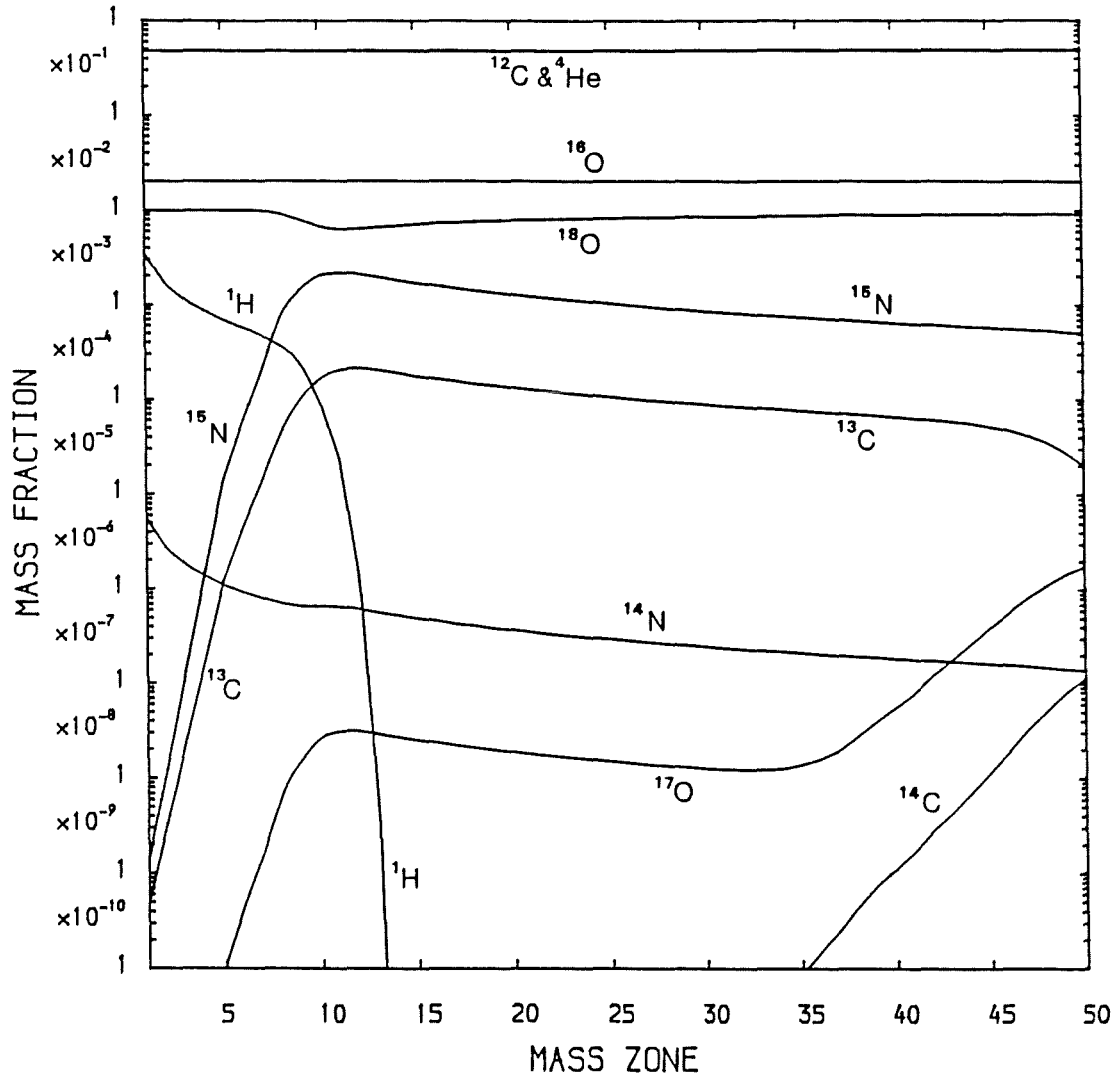


Figure 3.9 Same as figure 3.8 only showing effect of high initial ^{18}O

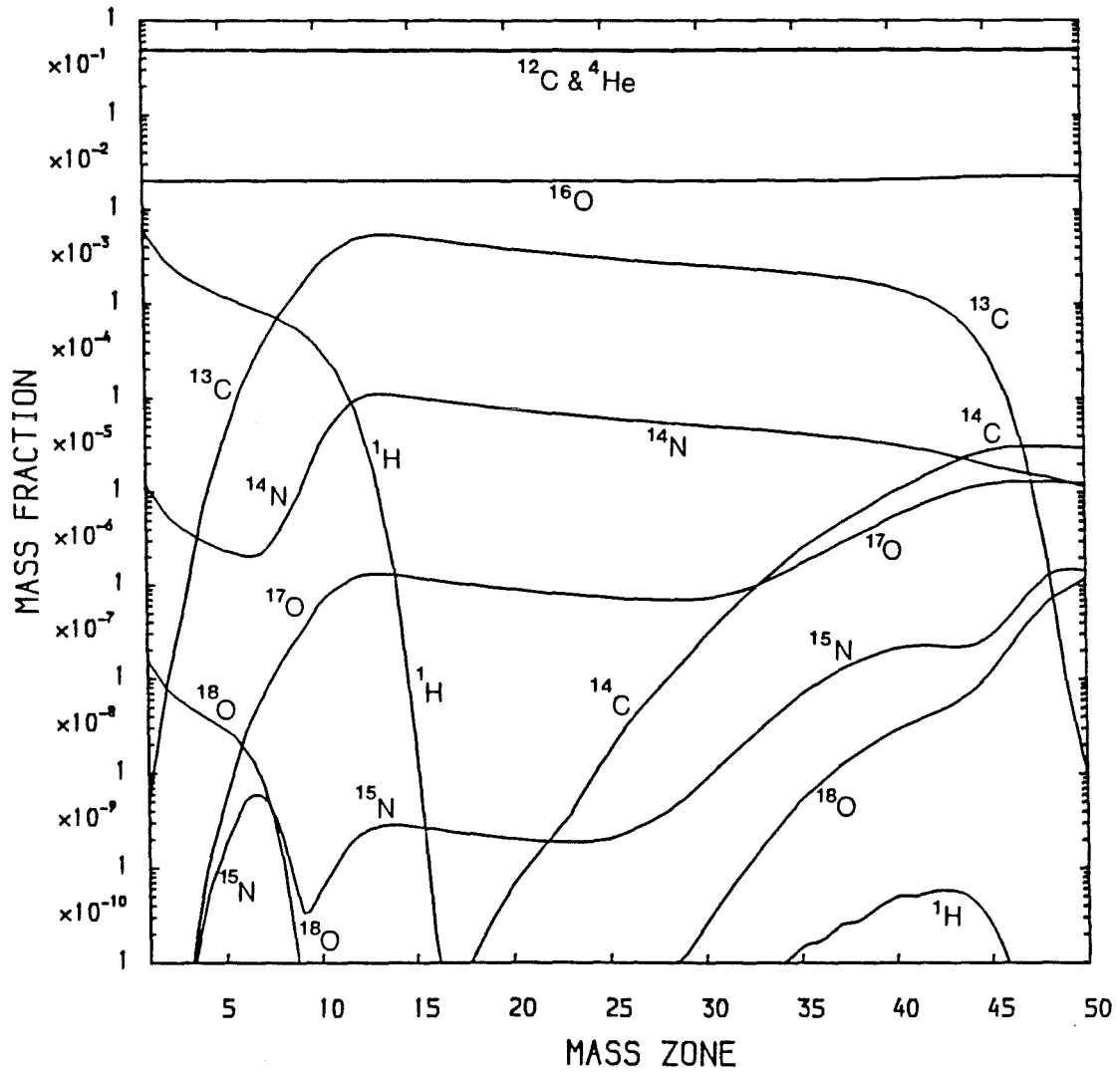


Figure 3.10 Mixing of $2.5 \times 10^{-6} M_{\odot}$ of envelope material into an
intershell with $T_b = 2.75 \times 10^8 \text{ }^{\circ}\text{K}$

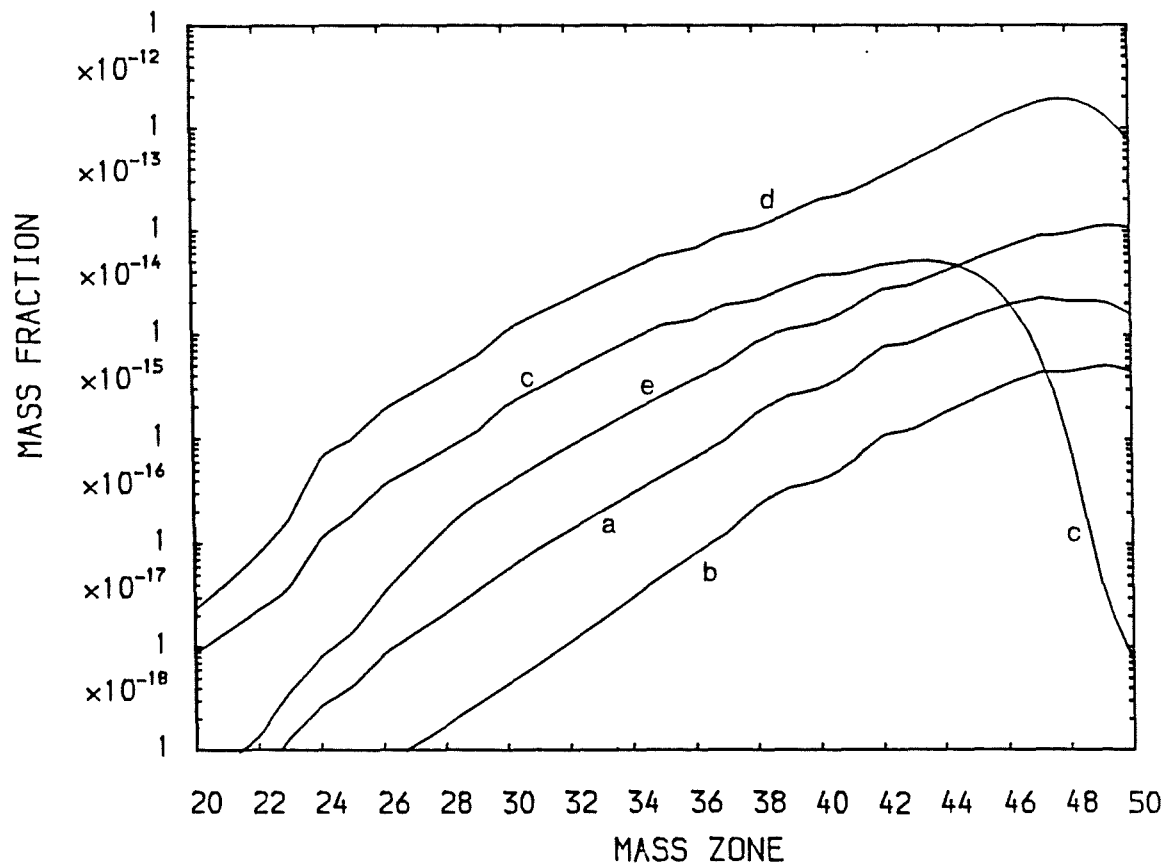


Figure 3.12 Neutron densities

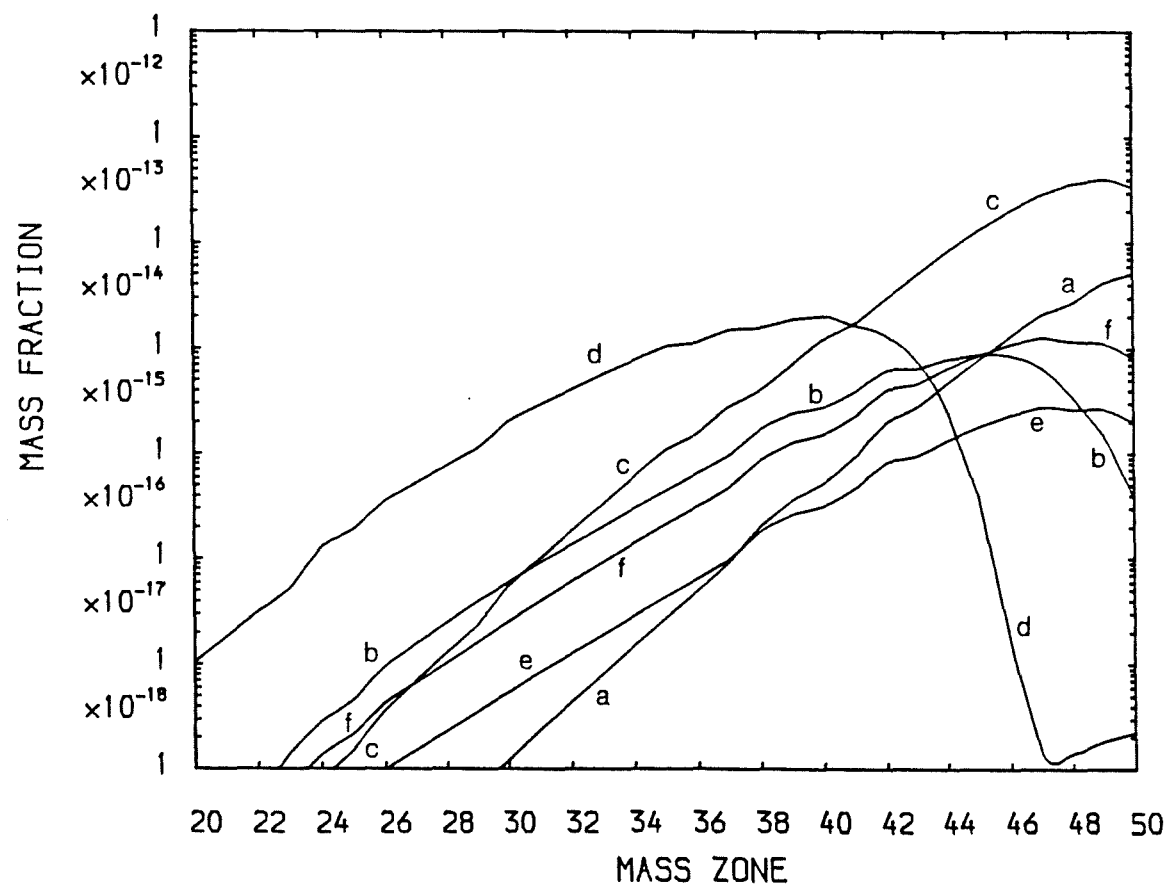


Figure 3.13 Neutron densities for v_c varied

Figures 3.8-3.12 show the behaviour of the nuclear isotopes at different levels of the intershell region as the original envelope material passes downwards through each level. When the envelope material reaches the helium shell (at zone 50) after 7.5×10^4 seconds the calculations are stopped. However, the intershell convection will continue for approximately 100 years for such a low-mass star (Christy-Sackmann and Paczynski 1975). During this time the nuclear isotopes in figures 3.8-3.11 will be affected by continuing α particle reactions especially at the hotter zones near the helium shell. This α burning will slowly increase ^{16}O and ^{18}O with a corresponding decrease in ^{13}C , ^{14}C and ^{14}N (see chapter 4). The neutron flux distributions in the intershell region will remain essentially the same as shown in figure 3.12 during this time but with the magnitude of the fluxes slowly decreasing with time as the ^{13}C is destroyed (assuming hydrogen ingestion is halted at some point). As can be seen, when the heavy elements are fully accounted for, the neutron mass density varies between 5×10^{-15} and 6×10^{-14} depending on the initial conditions. This transforms into neutron densities of 10^{13} and 10^{14} neutrons/cm³. This peak neutron density is about 3 orders of magnitude lower than the peak density calculated by Cowan and Rose (1977) for an AGB star of roughly twice the core mass of the models used in these calculations. This difference in neutron density is partly due to the neglect of the heavy elements by these authors. These calculated densities fall in between the densities required for the classical s and r processes. Because of this, neutron synthesis of heavy elements by these densities was termed the i-process (intermediate-process) by Cowan and Rose (1977).

In all of these calculations up to now no significant heavy element synthesis occurred. This result can be simply explained. An estimate of the total number of neutrons possible per ^{56}Fe seed is given by

$$T_n \approx N(^{13}\text{C})/N(^{56}\text{Fe})$$

which for the model of figure 3.10 gives $n_c=8$ (n_c is the number of neutron captures per ^{56}Fe). Of course not all of these neutrons are absorbed by ^{56}Fe . The fraction captured by the ^{56}Fe seed is given by

$$f \approx \frac{\sigma(^{56}\text{Fe}) N(^{56}\text{Fe})}{\sigma(^{56}\text{Fe}) N(^{56}\text{Fe}) + \sigma(^{22}\text{Ne}) N(^{22}\text{Ne}) + \sigma(^{14}\text{N}) N(^{14}\text{N})} \approx 0.2$$

where $N(X)$ is the number density of isotope X . Clearly for any significant heavy element build up to take place the neutron densities will have to be maintained by a continual inflow of hydrogen-rich envelope material or by a higher initial degree of envelope mixing. Such a situation is discussed in the next chapter. Due to this small amount of heavy element synthesis, inserting a solar distribution for the initial heavy element abundances of those elements heavier than ^{56}Fe had a negligible effect on the results.

The calculations were further investigated to determine what effect variations in the adopted convective velocity, v_c , of 1km/s had on the nucleosynthesis. The calculations of the previous section were re-calculated with the average diffusion time, t_z , through a mass zone (1500s for $v_c=1\text{km/s}$) being set at values within the range 150s to

5000s. The initial abundances were again set to those of table 3.2. Figure 3.13 shows the resulting neutron densities in the intershell for t_z taking the extreme values of 150s and 5000s for $T_b = 2.4 \times 10^8$ °K (lines a and b respectively), and for $T_b = 2.75 \times 10^8$ °K model (lines c and d respectively). From a comparison with line c of figure 3.12 and line c of figure 3.13 it can be seen that for $t_z = 150$ s the $T_b = 2.75 \times 10^8$ °K model has a peak neutron density about an order of magnitude higher than that for $t_z = 1500$ s. A similar result is found for the 2.4×10^8 °K T_b although the increase in peak neutron density for $t_z = 150$ s relative to $t_z = 1500$ s is only about a factor of 2. For the longer diffusion times of $t_z = 5000$ s the peak neutron densities are lower than those obtained for $t_z = 1500$ s, the drop being about a factor 3 for both the 2.4×10^8 °K T_b and the 2.75×10^8 °K T_b . For the values of t_z between 150s and 5000s this trend of shorter diffusion times giving rise to higher peak neutron densities continued.

The most significant changes in the light particle abundances for the different diffusion times are shown in table 3.3. This shows the ratio of the final zone abundance for a given t_z to the final zone abundance calculated for $t_z = 1500$ s. As can be seen the adopted convective velocity can play an important role in the behaviour of light particle production. These differences can be attributed to the convective velocity determining how long the nuclei spend in the hotter regions of the intershell region. This is particularly relevant to the ^{13}C abundance. For the faster diffusion times the ^{13}C retains a higher abundance in the hotter zones due to the shorter time spent at these temperatures, whereas for the slower diffusion times more of the ^{13}C is destroyed at lower temperatures before the hotter zones are reached. This ^{13}C behaviour explains the difference in the neutron densities of

figure 3.13. The higher peak neutron densities for the faster diffusion times being due to more of ^{13}C reaching the hotter zones where the $^{13}\text{C}(\alpha, n)^{16}\text{O}$ reaction rate will be greater.

A preliminary investigation of the effect of variations in the ingestion rate was carried out. The initial injection of envelope matter in the first zone of the intershell was changed from $2.5 \times 10^{-6} M_{\odot}$ to $2.5 \times 10^{-7} M_{\odot}$. This in effect meant that the ingestion rate dropped to 1.3×10^{46} protons/s. Also, a check was made that the neutron production occurring later on behind the diffusion front was not significantly altered by changes in chemical composition caused by the passing front. In order to investigate this, mixing of $2.5 \times 10^{-6} M_{\odot}$ hydrogen matter was approximated by instantaneously injecting $2.5 \times 10^{-7} M_{\odot}$ of hydrogen into the intershell. This was allowed to react and become fully mixed throughout the intershell in 7.5×10^4 s before instantaneously injecting another $2.5 \times 10^{-7} M_{\odot}$ of material. The initial intershell abundances prior to the second mixing episode were taken as the final zone abundances of the previous mixing. The uncertainty from this approximation will not significantly influence the calculated neutron density. This process was repeated ten times until a total of $2.5 \times 10^{-6} M_{\odot}$ material had been burned and fully mixed into the intershell in a total of 7.5×10^5 s. The final zone abundances of the light isotopes after each mixing has been completed (i.e. after 7.5×10^4 s) are shown in figure 3.14. For most of the light particles the final abundances after the tenth mixing are within a factor of 3 of the final abundances found for the mixing of $2.5 \times 10^{-6} M_{\odot}$ material. However, the ^{13}C and the neutron abundance (dashed line) are found to remain constant with the number of mixings and to be an order of magnitude down on the abundances corresponding to the higher mixing. The neutron density throughout the intershell corresponding to

the tenth mixing is shown as line e in figure 3.13 . It is clear that the lower ingestion rate reduces the neutron density relative to the higher ingestion rate by a factor of ten, which is what would be expected. It can also be seen that the level of the neutron density is not greatly affected by the number of mixings. This shows that the change in the chemical composition of the intershell zone following each mixing, does not have a significant effect on the neutron density.

The above calculation was repeated for ten $2.5 \times 10^{-6} M_{\odot}$ mixings of material. The light isotopic abundances after each mixing, as shown in figure 3.15, behaved in a similar fashion to those of figure 3.14 and the neutron density throughout the intershell for the tenth mixing is labelled line f in figure 3.13 . As can be seen these results follow similar trends to the lower scale mixing model with the peak neutron density reduced in the continuous approximation by a factor ten relative to the mixing of $2.5 \times 10^{-5} M_{\odot}$ material initially injected into the intershell (figure 3.12 line e). These reductions in neutron densities for continual mixing are simply due to the amount of hydrogen reacting at the one time being reduced by a factor ten. If the $2.5 \times 10^{-5} M_{\odot}$ mixing of material was simulated by one hundred $2.5 \times 10^{-7} M_{\odot}$ mixings the resulting peak neutron densities would be approximately 2×10^{12} neutrons/cm³ i.e. a reduction by a factor of 100 relative to the higher mixing.

An ingestion rate of 10^{43} protons/s was simulated next in a similar manner as before by injecting $2.5 \times 10^{-10} M_{\odot}$ of envelope material into the intershell zone. Again as expected the neutron density dropped by several orders of magnitude. Such a low ingestion rate is not expected to give rise to intershell splitting. Ingestion rates of 10^{44} and 10^{45} protons/s were also investigated for different initial conditions of

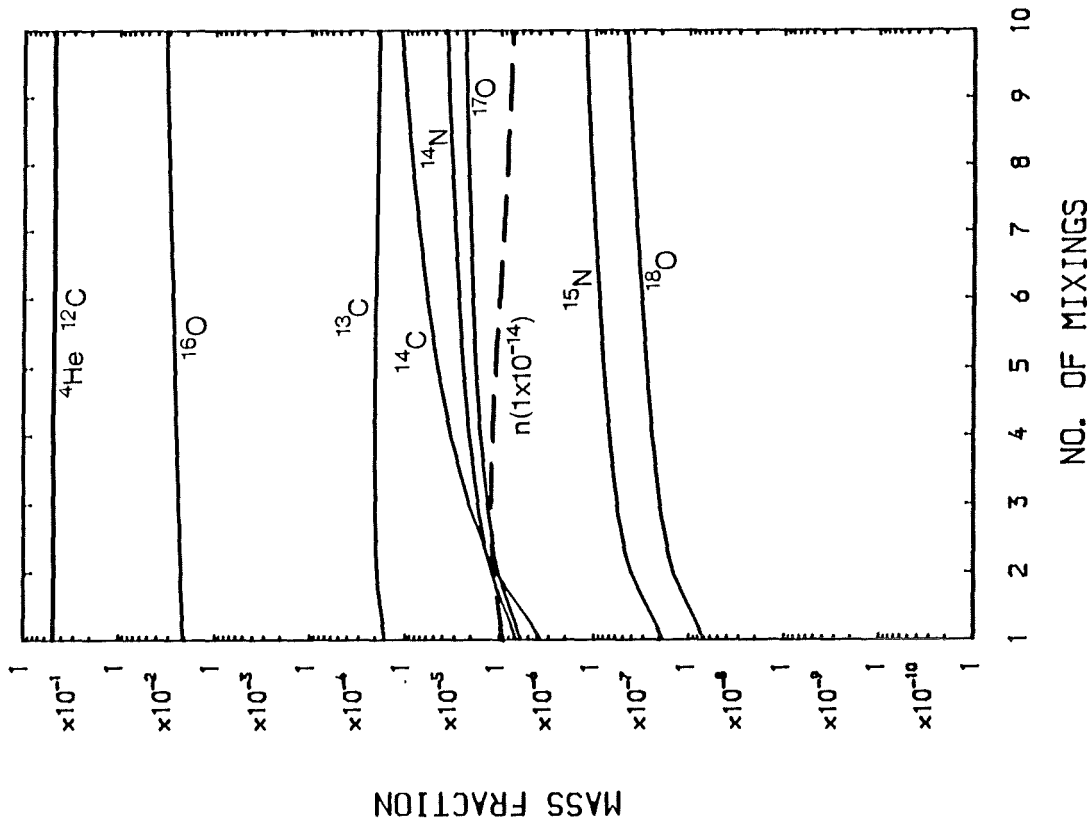


Figure 3.14 Final zone abundances for $10 \times 2.5 \times 10^{-7} M_{\odot}$ mixing

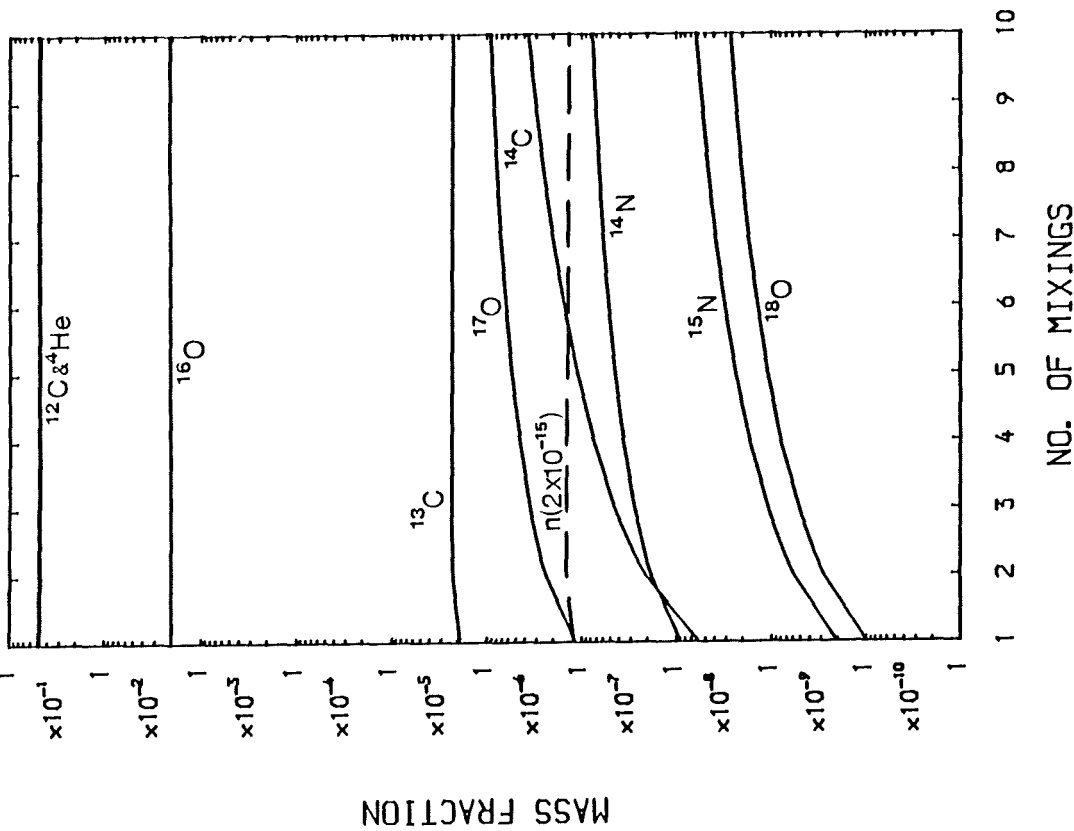


Figure 3.15 Final zone abundances for $10 \times 2.5 \times 10^{-6} M_{\odot}$ mixing

the intershell. Table 3.4 summarises how the peak neutron densities of a low-mass AGB star vary according to the ingestion rate, initial T_b , initial composition and the adopted v_c . The ingestion rate of the hydrogen at the top of the intershell is given in proton/s, while the ingestion rate of the ^{13}C rich material into the hot regions at the bottom of the intershell is given in M_\odot/year . A t_z of 5000s corresponds to $v_c=0.33\text{km/s}$, $t_z=1500\text{s}$ to 1km/s and $t_z=150\text{s}$ to 10km/s . The most important conclusion from table 3.4 is that the main parameter controlling the level of neutron production is the ingestion rate. A drop in the ingestion rate by 4 orders of magnitude leads to a drop in the neutron density by roughly 3 magnitudes. The values of v_c , T_b and the initial abundances are found to play secondary, although still important, roles.

Table 3.4

Summary of peak neutron fluxes

Initial Abundances	T_b (10^8 °K)	t_z (s)	Ingestion Rate		Peak Neutron Density neutrons/cm ³	Peak Neutron Flux neutrons/cm ² /s
			p/s	M_\odot /year		
Table 3.2	2.4	1500	1 (47)	1 (-3)	5.0 (13)	9.7 (21)
¹⁸ O=0.01 ²² Ne=solar	2.4	1500	1 (47)	1 (-3)	1.3 (13)	2.5 (21)
¹² C=0.2 ⁴ He=0.779	2.4	1500	1 (47)	1 (-3)	2.6 (13)	5.0 (21)
Table 3.2	2.75	1500	1 (47)	1 (-3)	9.5 (13)	1.9 (22)
²² Ne= 10^{-5} ⁵⁶ Fe= 9×10^{-7}	2.75	1500	1 (47)	1 (-3)	4.8 (15)	9.6 (23)
Table 3.2	2.4	150	1 (47)	1 (-3)	1.2 (14)	2.3 (22)
Table 3.2	2.4	5000	1 (47)	1 (-3)	1.5 (13)	2.9 (21)
Table 3.2	2.75	150	1 (47)	1 (-3)	9.8 (14)	2.0 (23)
Table 3.2	2.75	5000	1 (47)	1 (-3)	3.2 (13)	6.4 (21)
Table 3.2(step)	2.4	1500	1 (46)	1 (-4)	6.0 (12)	1.1 (21)
Table 3.2	2.4	1500	1 (48)	1 (-2)	2.5 (14)	4.9 (22)
Table 3.2(step)	2.4	1500	1 (47)	1 (-3)	2.1 (13)	4.1 (21)
Table 3.2	2.4	1500	1 (45)	1 (-5)	6.6 (11)	1.3 (20)
⁵⁶ Fe= 9×10^{-7}	2.4	1500	1 (45)	1 (-5)	4.3 (11)	8.4 (19)
Table 3.2	2.4	1500	1 (44)	1 (-6)	6.6 (10)	1.3 (19)
⁵⁶ Fe= 9×10^{-7}	2.4	1500	1 (43)	1 (-7)	8.7 (09)	1.7 (18)
Table 3.2	2.75	1500	1 (43)	1 (-7)	8.0 (09)	1.6 (18)

b) Effect of Intershell Splitting

As stated earlier, for ingestion rates greater than 10^{44} protons/s a splitting of the intershell into two separate convective regions is expected (Sweigart 1974) due to the high proton burning rate giving rise to a thin radiative shell. In the $0.7M_{\odot}$ model investigated by Sweigart, his calculations showed that the splitting occurred such that $0.032M_{\odot}$ and $0.009M_{\odot}$ were contained in the lower and upper regions respectively, of the split intershell. Since such a splitting of the intershell would effectively cut off the supply of the neutron producing ^{13}C nuclei, then it is clear that neutron production within the intershell will be halted until such time that the radiative zone disappears.

For example, consider a total of $2.5 \times 10^{-5} M_{\odot}$ of envelope material to be mixed into the intershell at a rate of 5×10^{46} protons/s ($10^{-3} M_{\odot}$ /year). This ingestion rate is assumed to set up an intershell splitting. At this ingestion rate the splitting will last roughly 7.5×10^5 s, since after this time the ingestion of $2.5 \times 10^{-5} M_{\odot}$ of material will be complete and the luminosity of the radiative shell rapidly drops below $10^3 L_{\odot}$ (at this luminosity Sweigart did not find any intershell splitting). After 7.5×10^5 s the intershell will be no longer split and the ^{13}C -rich processed (as a result of proton burning on ^{12}C) material may then be swept down to the hot region of the intershell on the resumption of the convective shell again becoming fully convective. This is a clear possibility since in low-mass AGB stars the convective intershell region lasts for approximately 3×10^9 s with its maximum extension lasting for approximately 3×10^8 s. The base

temperature, T_b , of the intershell will not significantly change in the period of $\sim 10^6$ s during which time the intershell splitting exists.

In order to follow the neutron production in the intershell after the intershell splitting the following procedure was adopted. The splitting was assumed to take place at a temperature of 10^8 °K causing the intershell to be split in two with approximately a 1/3 of the intershell mass above the radiative zone and 2/3 of the mass below the radiative zone (such splitting at this temperature is consistent with the models of Sweigart). Differing amounts of envelope matter are assumed to be mixed into the top section of the split intershell. Calculations were then carried out (using the same reaction network as before) which simulated the nucleosynthesis occurring in the top section of the split intershell for an ingestion rate of $10^{-3} M_\odot$ /year. For a total mixing of $2.5 \times 10^{-6} M_\odot$ envelope material the calculation ran for 7.5×10^4 s, and similarly for mixings of $2.5 \times 10^{-5} M_\odot$ and $2.5 \times 10^{-4} M_\odot$ material the calculations ran for 7.5×10^5 s and 7.5×10^6 s respectively. On the completion of each calculation the intershell was assumed to be fully convective again and the processed matter at the top of the intershell is then diffused down to the hot regions as before.

Table 3.5 shows a series of such calculations for the case where the intershell has $T_b = 2.4 \times 10^8$ °K and the initial envelope and intershell abundances are taken from table 3.2. Table 3.5 shows the final mass fractions of ^{12}C , ^{13}C and ^{14}N in the top section of the split intershell just prior to the disappearance of the radiative zone for mixings of $2.5 \times 10^{-6} M_\odot$, $2.5 \times 10^{-5} M_\odot$ and $2.5 \times 10^{-4} M_\odot$ of envelope material. Also listed is the important $^{13}\text{C}/^{14}\text{N}$ number ratio, again for the time just prior to the onset of full convection in the intershell. This ratio will be seen

to be an important parameter with regard to subsequent neutron production. The peak neutron density and flux occurring in the intershell as a consequence of full convection being re-established is also shown for each mixing case.

As can be seen from table 3.5 the ^{13}C abundance rises for higher values of mixing. This is due to the larger amount of protons available for the $^{12}\text{C}(p,\gamma)^{13}\text{N}(\beta^+\gamma)^{13}\text{C}$ reactions. However, it can be seen that the rise of ^{13}C with the degree of mixing becomes somewhat inhibited at high mixing values. This is due to the $^{13}\text{C}(p,\gamma)^{14}\text{N}$ reaction becoming more important as the ^{13}C abundance rises. This also explains the rise in the ^{14}N abundance for higher mixing values. As a consequence of these reactions the $^{13}\text{C}/^{14}\text{N}$ ratio decreases from 104 for $2.5 \times 10^{-6} M_{\odot}$ mixing to 0.69 for $2.5 \times 10^{-4} M_{\odot}$ mixing. As can be seen from the listed neutron densities, this ratio has an important effect on neutron production. That is, the neutron production does not just simply depend on the ^{13}C abundance, but also on the ^{14}N abundance. This is because, as pointed out earlier, ^{14}N is an important neutron poison. The drop in the peak neutron flux for $2.5 \times 10^{-4} M_{\odot}$ mixing relative to that for $2.5 \times 10^{-5} M_{\odot}$ mixing is a consequence of the lower $^{13}\text{C}/^{14}\text{N}$ ratio for the higher mixing case. That is, even though the high mixing case produces more ^{13}C the ^{14}N abundance is at such a high level that the resulting neutron flux is reduced.

Table 3.6 lists the same series of calculations of table 3.5 only this time the intershell has $T_b = 2.75 \times 10^8 \text{ }^{\circ}\text{K}$. The behaviour of the neutron production for different values of the mixing is found to follow the same pattern as in the previous calculations. Table 3.7 show the calculations repeated with initial intershell mass fractions

$^{12}\text{C}=0.2$, $^4\text{He}=0.768$ and the other isotopes as given in table 3.2. The intershell again had $T_b=2.75 \times 10^8$ °K. As can be seen the important $^{13}\text{C}/^{14}\text{N}$ ratio remains at the same value as those of table 3.6, however, the actual abundances of ^{13}C and ^{14}N are lowered. This is simply due to the lower amount ^{12}C available for the $^{12}\text{C}(p,\gamma)^{13}\text{N}$ and subsequent reactions. As a consequence the peak neutron fluxes produced are lowered.

In view of the importance of the ^{13}C and the ^{14}N abundances, the calculations of table 3.5 were repeated but with the final products of the nucleosynthesis in the top section of the split intershell varied arbitrarily prior to the intershell becoming fully convective again. This is carried out in order to investigate the importance of the approximations made in the simulation of the nucleosynthesis at the top of the intershell. The slight changes to the nucleosynthesis products resulted in a slightly higher $^{13}\text{C}/^{14}\text{N}$ ratio and an increase in the proton abundance by a factor of roughly 2. The results of these calculations are given in table 3.8. As can be seen a similar pattern for the neutron density as a function of mixing is found. The higher initial proton abundance leads to a slight drop in the neutron density due to the $^{13}\text{C}(p,\gamma)^{14}\text{N}$ reaction destroying more of the ^{13}C nuclei in the cooler zones of the intershell. The results of table 3.8 can be regarded as upper limits on the errors of the neutron densities given in tables 3.5 to 3.7. As already discussed it is seen from tables 3.5 to 3.8 that the neutron density which arises following intershell splitting is largely dependent on the value of the amount of envelope matter mixed in to the top of the intershell. The neutron density does not increase with an increasing amount of envelope mixing as perhaps first expected.

Table 3.5

 $^{13}\text{C}/^{14}\text{N}$ and neutron fluxes following splitting for $T_b = 2.4 \times 10^8 \text{ }^\circ\text{K}$

Mixing (M_\odot)	2.5×10^{-6}	2.5×10^{-5}	2.5×10^{-4}
^{12}C (mass fraction)	0.4834	0.4460	0.2862
^{13}C (mass fraction)	2.8 (-3)	2.6 (-2)	9.1 (-2)
^{14}N (mass fraction)	2.9 (-5)	2.8 (-3)	0.135
$^{13}\text{C}/^{14}\text{N}$ (ratio by number)	104	10	0.69
Peak Neutron Density (neutrons/cm ³)	1.4 (14)	5.8 (14)	3.0 (14)
Peak Neutron Flux (neutrons/cm ² /s)	2.7 (22)	1.1 (23)	5.9 (22)

Table 3.6

 $^{13}\text{C}/^{14}\text{N}$ and neutron fluxes following splitting for $T_b = 2.75 \times 10^8 \text{ }^\circ\text{K}$

Mixing (M_\odot)	2.5×10^{-6}	2.5×10^{-5}	2.5×10^{-4}
^{12}C (mass fraction)	0.4795	0.43	0.132
^{13}C (mass fraction)	6.8 (-3)	5.2 (-2)	5.4 (-2)
^{14}N (mass fraction)	1.8 (-4)	1.45 (-2)	0.355
$^{13}\text{C}/^{14}\text{N}$ (ratio by number)	41	3.8	0.16
Peak Neutron Density (neutrons/cm ³)	2.9 (14)	7.0 (14)	6.5 (13)
Peak Neutron Flux (neutrons/cm ² /s)	5.7 (22)	1.4 (23)	1.3 (22)

Table 3.7

$^{13}\text{C}/^{14}\text{N}$ and neutron fluxes following splitting for $T_b = 2.75 \times 10^8 \text{ }^\circ\text{K}$
and for low initial carbon

Mixing (M_\odot)	2.5×10^{-6}	2.5×10^{-5}	2.5×10^{-4}
^{12}C (mass fraction)	0.197	0.175	5.43 (-2)
^{13}C (mass fraction)	2.8 (-3)	2.15 (-2)	2.2 (-2)
^{14}N (mass fraction)	7.3 (-5)	6.0 (-3)	0.146
$^{13}\text{C}/^{14}\text{N}$ (ratio by number)	42	3.8	0.1
Peak Neutron ₃ Density (neutrons/cm ³)	1.5 (14)	4.3 (14)	6.1 (13)
Peak Neutron ₂ Flux (neutrons/cm ² /s)	2.9 (22)	8.5 (22)	1.3 (22)

Table 3.8

Different $^{13}\text{C}/^{14}\text{N}$ and neutron fluxes following splitting for $T_b = 2.4 \times 10^8 \text{ }^\circ\text{K}$

Mixing (M_\odot)	2.5×10^{-6}	2.5×10^{-5}	2.5×10^{-4}	2.5×10^{-5} ($T_b = 2.75 \times 10^8 \text{ }^\circ\text{K}$)
^{12}C (mass fraction)	0.4834	0.44602	0.2931	0.4317
^{13}C (mass fraction)	2.9 (-3)	2.6 (-2)	0.12	5.2 (-2)
^{14}N (mass fraction)	2.3 (-5)	1.9 (-3)	9.4 (-2)	7.8 (-3)
$^{13}\text{C}/^{14}\text{N}$ (ratio by number)	135	15	1.4	7.2
Peak Neutron ₃ Density (neutrons/cm ³)	6 (13)	2.6 (14)	1.0 (14)	3.5 (14)
Peak Neutron ₂ Flux (neutrons/cm ² /s)	3.1 (21)	5.2 (22)	1.9 (22)	7.1 (22)

This is due to the behaviour of the ^{13}C and ^{14}N production as a function of the amount of envelope mixing. This behaviour is seen in figure 3.16 for the case of the calculations corresponding to table 3.6. Since matter is being continuously ingested at a rate of $10^{-3}M_{\odot}/\text{year}$ the total amount of matter mixed in increases uniformly with time. The time from the beginning of the ingestion period is indicated at the bottom of figure 3.16. The high value of the ^{14}N abundance for higher mixings reduces the subsequent neutron flux due to it acting as a neutron poison.

Therefore from a comparison of the results of table 3.4 (no intershell splitting assumed) with those of tables 3.5 to 3.8, it can be seen that in some circumstances the phenomenon of intershell splitting can significantly affect the neutron density achieved in the intershell. For example, for an ingestion rate of $10^{-3}M_{\odot}/\text{year}$ into an intershell with $T_b = 2.4 \times 10^8 \text{ }^{\circ}\text{K}$ and with splitting neglected (i.e. line 1 of table 3.4) a neutron density of $5 \times 10^{13} \text{ neutrons/cm}^3$ is found. From table 3.5 it can be seen that intershell splitting can increase this density (by up to an order of magnitude) for all the values of mixing investigated. For ingestion at the same rate into an intershell with $T_b = 2.75 \times 10^8 \text{ }^{\circ}\text{K}$ (i.e. line 4 table 3.4), table 3.6 shows that the neutron density can either be increased or decreased from the $9.5 \times 10^{13} \text{ neutrons/cm}^3$ found for no intershell splitting, depending on the degree of initial mixing. It is therefore clear that the phenomenon of intershell splitting can have important consequences for neutron production in low-mass AGB stars. The importance of the effect, however, varies depending on the mixing conditions assumed.

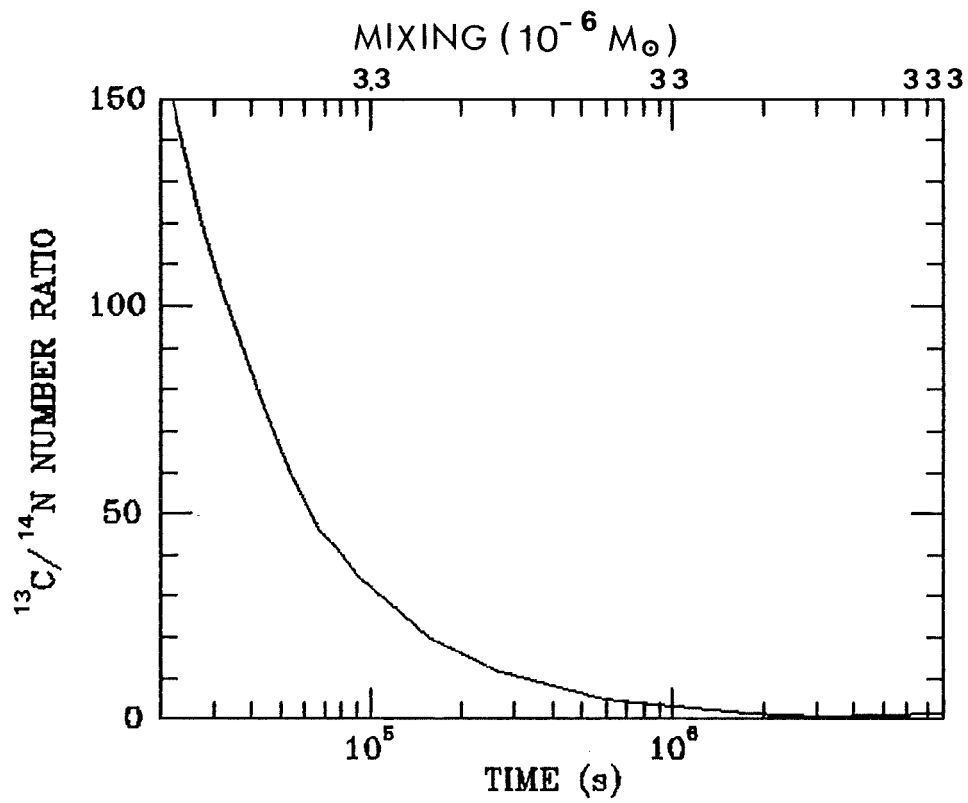


Figure 3.16 $^{13}\text{C}/^{14}\text{N}$ ratio as a function of mixing

c) Delayed Mixing by Semiconvection

Iben and Renzini (1982a,b,) have proposed a method whereby ^{13}C -rich material is engulfed in the hot intershell regions of low-mass AGB stars. These calculations are the only ones at the present time which theoretically predict such an event on the low-mass AGB (as discussed in chapter 1, such an event is also predicted at a post-AGB phase). The method of Iben and Renzini is based on the increased opacity at the outer regions of the intershell convective zone. This increased opacity is due to the carbon generated by the helium shell flash. Following pulse peak this carbon-rich layer of material cools until the opacity at the edge of the layer becomes large enough to force convective motions to arise. As a consequence of the fact that the opacity is a strong function of the carbon abundance, a semiconvection zone is established which carries carbon-rich material further outwards in mass than would have otherwise been the case. When the base of the hydrogen-rich convective envelope moves inwards in mass a dredge up can now occur due to the extension of the carbon-rich region. In previous calculations (which did not take account of the increased carbon opacity) contact between the edge of the carbon-rich region and the base of the convective envelope was not found. The reason dredge up can occur in these new calculations is because the large opacities at the edge of the carbon-rich region causes energy to be abstracted from the outward flow and to be converted locally into thermal motions. This produces an overpressure that drives the region out to sufficiently low temperatures and densities that envelope convection takes over.

Iben and Renzini found for their $0.7M_{\odot}$ model that following the 13th thermal pulse the base of the convective envelope advances inwards into the carbon-rich region through a mass of $2 \times 10^{-4} M_{\odot}$. In this $2 \times 10^{-4} M_{\odot}$ region there then exists a rich $^{12}\text{C}-^1\text{H}$ region. At this phase of the flash period this region of the star is too cool for proton burning reactions to proceed. Apart from some modest diffusion (Iben 1982) this $^{12}\text{C}-^1\text{H}$ region persists for about 10^4 years at which time the region heats up sufficiently for proton burning reactions to proceed, thus forming a ^{13}C -rich region. When the next thermal pulse begins, the convective shell that forms engulfs this region and subsequently the ^{13}C -rich region is swept down to the hotter temperatures where the neutron producing reactions occur. However, a significant difference in T_b at the time of ingestion occurs for this type of mixing compared to the previous mixing calculations. When the ^{13}C -rich region is ingested for the first time T_b has not yet reached its maximum value. In fact in the model of Iben and Renzini the ^{13}C region is ingested when T_b is only 1.5×10^8 °K. This value of T_b will not rise significantly over the timescale of the ^{13}C destruction in the intershell. At this value of T_b the neutron density will be much reduced.

In order to estimate the neutron production arising from this mixing mechanism the initial abundances of the ^{13}C -rich region were taken as shown in table 3.9 (model a). The values of the ^{13}C and ^{14}N abundances are consistent with the values estimated by Iben and Renzini (1982b) for the ^{13}C -rich matter prior to ingestion. The initial abundances were then varied in order to determine their effect on the neutron density. The different initial abundances are listed in table

3.9 under models a, b, c and d (the initial intershell abundances corresponding to each model are also given by table 3.9 except that the initial ^{13}C and ^{14}N abundances are set to zero in the intershell). The peak neutron densities are given in table 3.10 for the different models and for different ingestion rates (Iben and Renzini estimate the ingestion rate at $10^{-3}M_{\odot}/\text{year}$). These peak densities correspond to the peak densities found at the diffusion front as it passes down through the intershell. However, due to the longer lifetime (roughly 10^6s) of the ^{13}C nuclei at these low temperatures a build up of ^{13}C occurs which leads to densities and fluxes of about an order of magnitude greater than those listed in table 3.10. It can be seen that for an ingestion rate of $10^{-3}M_{\odot}/\text{year}$ or less, the resulting neutron fluxes can be several orders of magnitude lower than anticipated for an equivalent hydrogen ingestion rate at peak flash. The drop in the neutron production being due to the lower initial ^{13}C enrichment of the material ingested and of the lower temperature at which the $^{13}\text{C}(\alpha, n)^{16}\text{O}$ reaction proceeds. Iben and Renzini (1982b) estimated the resulting neutron density arising as a consequence of their mixing mechanism. They assumed, however, that the ^{13}C -rich matter was instantaneously ingested into the intershell and estimated the resulting neutron density to be roughly 2×10^{12} neutrons/cm³ (calculations simulating an instantaneous ingestion are also presented in table 3.10 for comparison). Renzini (private comm.) has subsequently pointed out that this value is in error due to the assumption of an instantaneous ingestion, and that the neutron production is likely to be largely influenced by the ingestion rate. As a consequence of the ingestion rate having been ignored, the neutron density quoted by Iben and Renzini is overestimated by roughly at least an order of magnitude.

Table 3.9
Initial ^{13}C -rich region

	Initial Mass Fractions			
	a	b	c	d
^4He	0.4825	0.7788	0.7788	0.7788
^{12}C	0.4861	0.2	0.2	0.2
^{13}C	1.8 (-2)	1.8 (-2)	1.8 (-2)	1.8 (-2)
^{14}N	5.6 (-3)	5.6 (-3)	5.6 (-3)	5.6 (-3)
^{16}O	0.02	0.02	0.02	0.02
^{22}Ne	0.01	0.01	1 (-3)	1 (-3)
^{56}Fe	1.3 (-3)	1.3 (-3)	1.3 (-4)	1.3 (-3)
Heavies	solar	solar	solar/10	solar

Table 3.10

Neutron densities arising from Iben and Renzini mixing

Initial Mass Fractions	Ingestion Rate (M_{\odot}/year)	Peak Neutron Density (neutrons/cm 3)	Peak Neutron Flux (neutrons/cm 2 /s)
a	1 (-3)	1.2 (9)	1.9 (17)
a	1 (-4)	1.2 (8)	1.9 (16)
a	Instantaneous	1.2 (11)	1.9 (19)
b	1 (-3)	2.2 (9)	3.5 (17)
c	1 (-3)	1.2 (10)	1.9 (18)
c	Instantaneous	1.0 (12)	1.6 (20)
d	1 (-3)	2.9 (9)	4.6 (17)

3.4) Neglect of Energy Generation and Conclusions

As stated earlier the excess energy generated by the nuclear reactions arising from the hydrogen mixing has been ignored in the calculations. In a real situation of course this excess energy would affect the run of temperature and density in the intershell. The degree of change in the temperature density grid would depend mainly on the rate of the hydrogen burning in the intershell. It is difficult to estimate quantitatively the change in the structure of the intershell without resorting to very difficult and time consuming calculations. However, it is generally believed that the excess energy generated by the mixing will lead to an expansion of the upper half of the split intershell. In his calculations of an ingestion rate of 10^{44} protons/s, Sweigart (1974) found that this caused a doubling of the expansion rate of the upper region of the split intershell. Such an expansion will lead to a cooling of the outer regions of the intershell. The matter in this expanded region above the radiative zone will be swept down to the hot regions of the intershell once all the hydrogen is burned out and the lower convective zone advances outwards, engulfing the ^{13}C -rich region. To properly calculate the nucleosynthesis, expansion rates and the ingestion rates in the intershells of AGB stars, would require the coupling of the reaction networks, used here, to an evolving AGB model. These calculations would be very difficult and contain a large amount of uncertainty. This is mainly due to the problems encountered when attempting to follow the energy generation, from a nuclear network, in a convective region. The calculations presented here can be regarded as a first approximation to the neutron production levels following a mixing event on the AGB and

post-AGB.

It has been shown that neutron densities covering a wide range (10^9 to 10^{14} neutrons/cm³) can be achieved in low-mass AGB stars as a result of small scale envelope mixing into the star's intershell region. It was shown how the ingestion rate is the main parameter controlling the level of neutron production. The initial abundances, the temperature of the intershell region and the convective velocity were also shown to be important parameters. It was also shown that the peak neutron fluxes, obtained under different initial conditions and different assumptions, can vary over several orders of magnitude, depending on the initial conditions and on the particular mixing model adopted. The effect of intershell splitting was also investigated with the conclusion that the neutron densities can be significantly affected by this phenomenon. Delayed mixing on the low-mass AGB was investigated. This type of mixing leads to very much lower neutron fluxes, mainly as a result of this type of mixing leading to ¹³C destruction at an earlier phase of the flash and consequently at cooler temperatures. In some circumstances such a change in the neutron flux can have significant effects on the enhancement of individual isotopes. Therefore, in such circumstances where the relative abundances of light or heavy isotopes is important, care must be taken to insure that the nucleosynthesis is investigated for an appropriate range in the neutron flux.

CHAPTER 4. HEAVY ELEMENT SYNTHESIS

4.1) Preliminary Calculations

As a preliminary investigation the reaction network of table 2.2 was used in order to investigate the build up of heavy elements expected from a neutron flux typical of those found on the AGB. Of course these preliminary calculations only serve as a very rough approximation to the heavy element distribution resulting from mixing on the AGB. This is mainly due to the network of table 2.2 not including the effects of nuclear branching (see later). However, even though this effect is neglected, some important points for consideration in more detailed calculations can be highlighted. A neutron density of 5×10^{14} neutrons/cm³ was used in these calculations. This corresponds to the flux from an initial mass fraction of ¹³C equal to 7.5×10^{-3} , burning at a temperature $T = 2.4 \times 10^8$ °K. The path through the chart of the nuclides corresponding to this flux is indicated in figure 4.1. The path is chosen in such a way that when a nuclide is reached for which beta decay and further neutron absorption compete with each other, then the path follows the route corresponding to the most significant of the two processes, and the other possible route is neglected (i.e. no nuclear branching is included). This then means that each nucleus of the network is uniquely defined by its atomic mass A. That is, each value of A corresponds to one isotope and one isotope only. The nuclei which were found to lie on figure 4.1 are those heavy nuclei listed in table 2.2 (including the nuclei in parenthesis). The initial abundances at the start of the calculations are given in table 4.1. The initial abundances of all the other heavy elements were provisionally taken as zero. This is termed

case A in table 4.1. A solar system distribution of heavy elements was then taken as the initial heavy element abundances for case B. To investigate the importance of the ^{22}Ne and the ^{56}Fe initial abundances, these abundances were varied as indicated in table 4.1. For case C the ^{22}Ne initial abundance is reduced by a factor 10, and for case D the ^{56}Fe initial abundance is decreased by a factor 10.

The relative abundance by number for each isotope between atomic mass 56 and 90 (investigation of this limited mass range is sufficient for the basic points to be raised in this section) is shown for each case in table 4.2. The calculations were stopped after about 3×10^4 s for each case, since by this time the neutron flux had dropped to insignificant levels and no further neutron synthesis was taking place (any subsequent beta decay was not followed). The drop in the neutron flux is due to the original material which was supplying the neutron source now having been completely destroyed.

In the tables and diagrams to follow, unless otherwise stated, the enhancement and overabundance factors are calculated using the solar system values of Cameron (1981) (Cameron lists these values by number relative to $\text{Si}=10^6$), and the mass fractions and number fractions are relative to the total mass and total number of atoms respectively.

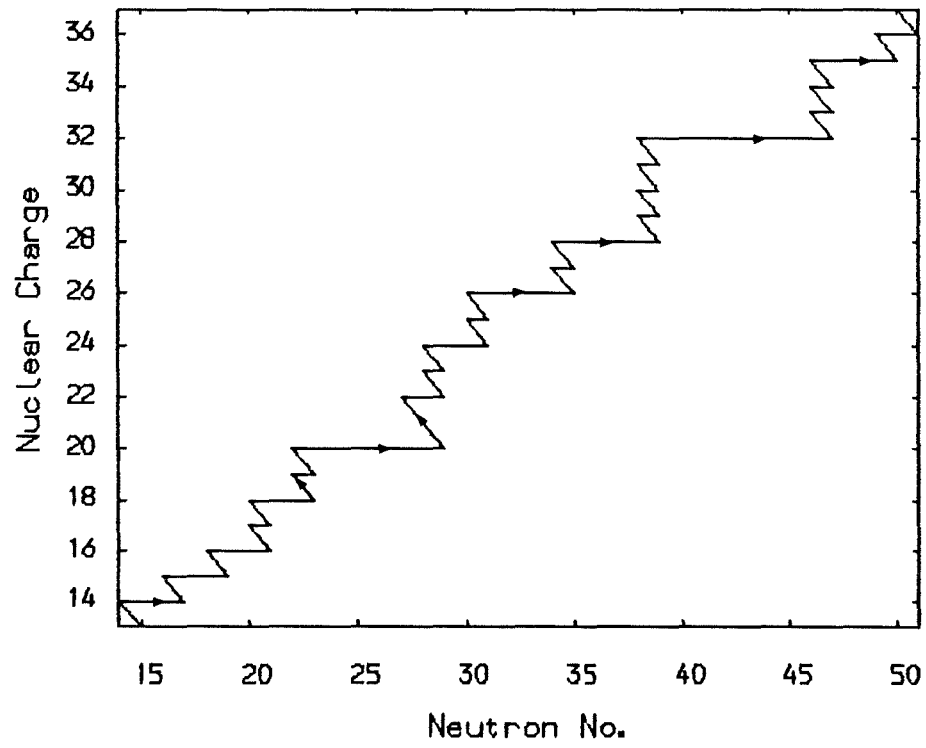


Figure 4.1 Path of linear flow-no branching

Table 4.1

Initial mass fractions for preliminary heavy element enhancements

	Case A	Case B	Case C	Case D
${}^4\text{He}$	0.48	0.48	0.48	0.48
${}^{12}\text{C}$	0.48	0.48	0.48	0.48
${}^{13}\text{C}$	7.5 (-3)	7.5 (-3)	7.5 (-3)	7.5 (-3)
${}^{16}\text{O}$	0.02	0.02	0.02	0.02
${}^{14}\text{N}$	4.0 (-4)	4.0 (-4)	4.0 (-4)	4.0 (-4)
${}^{22}\text{Ne}$	0.01	0.01	1.0 (-3)	0.01
${}^{56}\text{Fe}$	9.0 (-4)	9.0 (-4)	9.0 (-4)	9.0 (-5)
Heavies	0.0	solar	solar	solar

Table 4.2

Heavy element preliminary enhancements

Atomic Mass	Case A	Case B	Case C	Case D
56	1.3 (-9)	2.0 (-8)	7.8 (-9)	1.0 (-8)
57	1.1 (-9)	1.1 (-8)	3.8 (-9)	5.3 (-9)
58	3.6 (-8)	1.1 (-7)	1.5 (-8)	1.9 (-8)
59	7.2 (-8)	1.8 (-7)	1.8 (-8)	1.8 (-8)
60	2.5 (-6)	3.6 (-6)	1.1 (-6)	3.1 (-7)
61	3.8 (-7)	5.4 (-7)	1.7 (-7)	4.6 (-8)
62	1.0 (-6)	1.4 (-6)	5.0 (-7)	1.3 (-7)
63	5.6 (-7)	7.3 (-7)	2.7 (-7)	6.7 (-8)
64	2.9 (-6)	3.3 (-6)	1.8 (-6)	3.8 (-7)
65	9.1 (-7)	9.9 (-7)	6.1 (-7)	1.2 (-7)
66	1.2 (-6)	1.2 (-6)	8.9 (-7)	1.7 (-7)
67	8.4 (-7)	8.2 (-7)	6.9 (-7)	1.3 (-7)
68	9.6 (-7)	8.9 (-7)	9.0 (-7)	1.5 (-7)
69	1.7 (-7)	1.5 (-7)	1.6 (-7)	2.8 (-8)
70	2.6 (-7)	2.3 (-7)	2.6 (-7)	4.4 (-8)
71	4.1 (-8)	3.7 (-8)	4.1 (-8)	6.9 (-9)
72	3.2 (-7)	2.8 (-7)	3.4 (-7)	5.5 (-8)
73	7.7 (-8)	6.7 (-8)	8.2 (-8)	1.3 (-8)
74	5.5 (-7)	4.6 (-7)	6.5 (-7)	1.0 (-7)
75	1.1 (-7)	9.3 (-8)	1.3 (-7)	2.1 (-8)
76	3.4 (-7)	2.7 (-7)	4.4 (-7)	6.6 (-8)
77	1.9 (-7)	1.5 (-7)	2.6 (-7)	3.9 (-8)
78	5.1 (-7)	3.8 (-7)	7.8 (-7)	1.1 (-7)
79	3.8 (-8)	2.8 (-8)	5.9 (-8)	8.3 (-9)
80	6.0 (-7)	4.1 (-7)	1.1 (-6)	1.5 (-7)
81	2.5 (-8)	1.7 (-8)	5.0 (-8)	6.5 (-9)
82	1.6 (-8)	1.1 (-8)	3.1 (-8)	4.0 (-9)
83	5.7 (-8)	3.8 (-8)	1.1 (-7)	1.5 (-8)
84	5.6 (-8)	3.7 (-8)	1.1 (-7)	1.4 (-8)
85	5.5 (-8)	3.6 (-8)	1.1 (-7)	1.4 (-8)
86	6.4 (-7)	3.8 (-8)	2.0 (-6)	2.2 (-7)
87	1.7 (-7)	9.8 (-8)	6.7 (-7)	6.9 (-8)
88	2.4 (-7)	1.2 (-7)	1.4 (-6)	1.3 (-7)
89	2.4 (-8)	1.2 (-8)	1.6 (-7)	1.4 (-8)
90	4.1 (-8)	1.9 (-8)	3.5 (-7)	2.9 (-8)

For case A in table 4.2 a peak in the heavy element build up can be seen at roughly atomic mass 66. This is due to the initial conditions giving rise to roughly 10 neutron absorptions per initial ^{56}Fe nuclei. The reason that the peak in the abundance is not clearly defined is simply due to the individual isotopes having differing neutron absorption cross sections. For case B it can be seen that the introduction of a solar distribution for the initial light heavy and heavy element distribution (i.e atomic mass $A > 27$) does not alter the peak in the final heavy element distribution, although some significant differences for individual isotopes do occur. For case C the reduction in the initial ^{22}Ne abundance allows more of the neutrons to be absorbed by ^{56}Fe rather than on ^{22}Ne . As a consequence of this the peak in the final element distribution is shifted towards higher atomic mass. Roughly 20 neutron absorptions per initial ^{56}Fe nuclei occurs for this case. For case D although roughly 15 neutron absorptions per initial ^{56}Fe nuclei has occurred, the resulting total enhancements of the heavy elements are reduced by a factor of roughly 10. This is simply as a result of the initial ^{56}Fe being reduced by a factor 10. In the detailed calculations to follow the points raised in these preliminary calculations will be taken into consideration.

4.2) Fe to Mo Enhancement Neglecting Intershell Splitting

The calculations presented in the previous section are not accurate enough if reliable information is sought from comparison of observations with theoretical calculations. Such a comparison can lead to valuable information on the level of the neutron flux which led to observed heavy element enhancements. This would give an estimate of the temperature at which the synthesis took place, which in turn would give an indication at what phase in the stars evolution the synthesis occurred. For such a comparison, detailed calculations are required which take into account various effects which were not included in the calculations of section 4.1. A region of the heavy element distribution was chosen to be investigated in detail. The heavy element region between Fe and Mo was chosen for a detailed analysis since this region contains elements which are known to be greatly enhanced in many low-mass red giants, particularly those elements of the Sr-Y magic nuclei peak. A detailed investigation of this region is also crucial for a comparison of the observed heavy element enhancements of the RCrB star U Aquarii (to be discussed later). This comparison with U Aquarii was the main motivation for choosing the Fe to Mo region. In order to investigate the production of the elements between Fe and Mo the nuclear reaction network of table 2.2 was expanded to take into account the effect of nuclear branching and isomeric branching. These effects are shown in figure 2.3 and discussed in Chapter 2. The non-thermalisation of ^{69}Zn , ^{85}Kr , ^{87}Sr and ^{90}Y were considered to be significant for the conditions under which the calculations presented here were carried out.

The full network from Fe to Mo is shown in figure 2.4. This network is added to those of table 2.1 and table 2.2. The neglect of branching effects prior to ^{54}Fe and after ^{103}Mo does not significantly effect the calculated enhancements in the Fe to Mo region. The initial intershell and envelope abundances were taken as those of table 3.2. To simulate the production of the heavy elements in the intershell the average neutron flux experienced by the seed ^{56}Fe nuclei due to the ingestion of $2.5 \times 10^{-5} M_{\odot}$ envelope material into the intershell was considered. Of course ideally, mass averages over the entire intershell should be considered, however, the extra accuracy gained for the large amount of additional work and increased computer time required does not warrant such detailed calculations. The average neutron flux method roughly models the neutron synthesis occurring in the intershell and is sufficient for the present purposes. The average neutron flux is derived from the calculations of chapter 3 by

$$\text{average flux} = (F_n^i \times t_z) / T$$

where F_n^i and is the neutron flux in zone i of the intershell, t_z is the time taken to pass through zone i and T is the total time taken to pass through the entire intershell. As in chapter 3 the energy generated by the nuclear reactions is ignored in these calculations. Finally, in order to roughly simulate the cooling of the intershell base after the peak flash temperature (an important effect was found if such an allowance was not made, see later) the conditions under which the nucleosynthesis took place was changed to a temperature of 1.35×10^8 °K and to a density of 8.6×10^4 g/cm³, 10^9 s after the start of the calculation. Such a change in the intershell conditions after 10^9 s was typical of the AGB models used.

Table 4.3 presents the heavy element build up of the elements within the Fe to Mo range. These represent the enhancements due to a total $2.5 \times 10^{-5} M_{\odot}$ envelope material mixed into the intershell at an ingestion rate of $10^{-3} M_{\odot}/\text{year}$. Calculations are carried out for intershell base temperatures of $T_b = 2.4 \times 10^8 \text{ }^{\circ}\text{K}$ and $T_b = 2.75 \times 10^8 \text{ }^{\circ}\text{K}$. Also indicated in table 4.3 is the average neutron flux used for each ingestion rate. Radioactive isotopes are allowed to decay for 3×10^6 years. The element enhancements listed are the sum of the individual isotopes for each element which is then divided by the solar system abundance for that element (taken from Cameron 1981).

The ingestion of material into the intershell with $T_b = 2.4 \times 10^8 \text{ }^{\circ}\text{K}$ corresponds to an ingestion event on the AGB. As discussed earlier, such large mixings on the AGB are not predicted by current theoretical calculations. The enhancements arising from such a mixing event are listed here, however, for two reasons. Firstly, it is possible that physical processes not included in present calculations may have an effect on the degree of mixing allowed on the AGB. Secondly, comparison of these enhancements with the enhancements arising from currently more plausible mixing events may allow future observations to determine whether the actual mixing event that occurred in a heavy element enhanced star was in fact an event predicted by current theory. That is a comparison of observed enhancements with the calculated enhancements could allow a check to be made on current theoretical ideas regarding mixing events on the AGB and post-AGB.

Table 4.3
 Enhancements for $2.5 \times 10^{-5} M_{\odot}$ mixing (no splitting)

Neutron Flux (neutrons/cm ² /s)	3.5 (19)	3.5 (19)	5.3 (20)
T_b	2.4	2.4	2.75
Thermalised	Yes	No	No
Fe	5.9 (-3)	6.4 (-3)	7.0 (-3)
Co	1.9	2.7	0.13
Ni	6.1	6.5	1.0
Cu	118	124	22
Zn	108	126	36
Ga	679	524	162
Ge	808	882	323
As	490	878	330
Se	1348	1369	912
Br	865	1125	677
Kr	3395	1988	5094
Rb	2972	4422	13903
Sr	1451	932	6319
Y	460	435	3724
Zr	320	628	1811
Nb	215	269	5592
Mo	62	104	5452

An ingestion into an intershell with $T_b = 2.75 \times 10^8$ °K corresponds to an ingestion event on the post-AGB. Such a mixing event is predicted on the post-AGB (Fujimoto 1977, Schönberner 1979, Iben et al. 1983). The ingestion rate of envelope material at this phase could be expected to be roughly $10^{-3} M_{\odot}/\text{year}$, equivalent to that anticipated from a full link up of envelope with intershell (Despain 1977). The enhancements listed in table 4.3 for this particular mixing event represents the most plausible ingestion event in this series of calculations.

It can be seen from the first two columns of table 4.3 that the effect of some of the nuclei being in an unthermalised state can have significant effects on the resulting relative enhancements of the heavy elements. For example at ^{85}Kr the unthermalised nuclei has a decay rate of several hours compared to the thermalised decay of several years. This change in the beta decay rate is the main cause of the Kr/Rb ratio changing from 1.14 for ^{85}Kr assumed thermalised, to 0.45 for the unthermalised case. For the high T_b case it can be seen that the heavy element distribution has shifted to higher atomic mass, indicating more neutron absorptions per initial ^{56}Fe nuclei. This change is due mainly to the smaller intershell mass for the higher T_b (as an AGB star evolves its intershell mass decreases; see chapter 3). This means that the concentration of the envelope material in the intershell will be higher even though the same total amount of mixing is assumed.

In order to investigate the importance of the conditions chosen to represent the average conditions in the intershell a series of calculations were carried out for different temperature density conditions. The initial abundances for each calculation were held at the same level for each case so that the only parameters changed for each calculation were the temperature and density. These calculations do not represent any 'real' mixing event, but are simply carried out in order to investigate the importance of correctly choosing the proper average conditions. The results of these calculations are given in table 4.4. Column 1 of table 4.4 corresponds to zone 43, columns 2 and 3 to zone 38, and columns 4 and 5 to zone 33 for the intershell where $T_b = 2.4 \times 10^8$ °K. From table 4.4 the importance of correctly choosing the average conditions for the intershell can be seen, since slight, but significant, differences in the relative element ratios can occur for build up under the different neutron fluxes. For example, the Zn/Cu ratio changes from roughly 1.0 for zone 43 to 0.8 for zone 38.

However, none of these heavy element enhancement calculations have so far accounted for the effect of intershell splitting as discussed in chapter 3. The effect of intershell splitting on the heavy element build up is likely to be significant since it was shown in chapter 3 how intershell splitting can have a very significant effect on the neutron density that is produced, within the intershell region, following the ingestion of envelope material. Heavy element build up due to significantly different neutron fluxes is likely to lead to differences in the relative enhancements of the elements (as can be seen from table 4.4). The effect of intershell splitting on the heavy elements is

investigated in the following section. In order to simulate the build up of the heavy elements in the situation where intershell splitting occurs, the calculations presented in chapter 3, in which the neutron densities arising after intershell splitting were calculated, are used in order to calculate the average neutron flux for a given ingestion rate. The heavy element build up under this average neutron flux is then followed for the required period of time.

Table 4.4

Enhancements for different average flux conditions

Neutron Flux ₂ (neutrons/cm ² /s)	8.4 (21)	1.5 (21)	1.5 (21)	1.3 (20)	1.3 (20)
Temperature (10 ⁶ K)	2.1	1.9	1.9	1.7	1.7
Mass Density (g/cm ³)	3020	2510	2510	2000	2000
Thermalised	Yes	Yes	No	Yes	No
Fe	0.008	0.008	0.007	0.01	0.009
Co	4.1	3.7	3.1	2.6	2.4
Ni	7.8	7.5	7.1	6.9	6.7
Cu	144	134	128	131	128
Zn	148	109	140	104	111
Ga	582	494	610	508	541
Ge	836	944	881	855	888
As	769	692	669	547	570
Se	964	1285	1214	1541	1563
Br	754	955	912	1041	1055
Kr	1329	2049	1575	2654	1857
Rb	1326	1992	3104	2440	3878
Sr	196	332	559	422	1041
Y	94	138	221	218	496
Zr	159	206	309	226	517
Nb	45	77	109	132	297
Mo	51	34	48	31	70

4.3) Fe to Mo Enhancement Including Intershell Splitting

a) Total Element Enhancement

Detailed calculations covering a wider range of initial conditions are now investigated for calculations which include the effect of intershell splitting on the average neutron flux encountered in the intershell (the description as to how the neutron flux following intershell splitting is calculated is given in chapter 3). These calculations are listed in table 4.5. The models listed correspond to the following:- (unless otherwise stated the initial abundances correspond to table 3.2 and the unthermalised nuclei are included)

Model A; The diffusion of the ^{13}C -rich matter into the hot region of the intershell following an initial mixing of $2.5 \times 10^{-5} M_{\odot}$ material at an ingestion rate of $10^{-3} M_{\odot}/\text{year}$. The intershell has $T_b = 2.4 \times 10^8 \text{ }^{\circ}\text{K}$. This model corresponds to column 2 of table 3.5.

Model B; This is as model A only for an intershell with $T_b = 2.75 \times 10^8 \text{ }^{\circ}\text{K}$. This corresponds to column 2 of table 3.6.

Model C; This is as model B only assuming that all the nuclei are thermalised.

Model D; As model B only for the light heavies and heavy elements (i.e. $A > 27$) put to an initial value of 0.1 solar value.

Model E; Repeat of model D only with the initial value of ^{22}Ne put to

0.1 of value listed in table 3.2 (i.e. ^{22}Ne initial mass fraction put to 0.001).

Model F; In this model a higher degree of initial mixing is assumed. A total of $2.5 \times 10^{-4} M_{\odot}$ material at a mixing rate of $10^{-3} M_{\odot}/\text{year}$ is first mixed in to the top of the intershell. Such a degree of mixing is predicted at the post-AGB phase (Iben et al. 1983). The intershell has $T_b = 2.75 \times 10^8 \text{ }^{\circ}\text{K}$. This model corresponds to the calculation of column 3 table 3.6.

Model G; A lower degree of initial mixing corresponding to $2.5 \times 10^{-6} M_{\odot}$ of envelope matter ingested at a rate of $10^{-3} M_{\odot}/\text{year}$ was assumed. The intershell has $T_b = 2.75 \times 10^8 \text{ }^{\circ}\text{K}$. This model then corresponds to column 1 of table 3.6.

Models H, I and J; These models correspond to the calculations of table 3.8 where the $^{13}\text{C}/^{14}\text{N}$ ratio was arbitrarily varied, and are listed here for comparison purposes. Model H corresponds to column 2 of table 3.8, and models I and J correspond to column 4 of table 3.8 for thermalised and unthermalised calculations respectively.

In order to obtain a clearer picture of the build up of heavy elements listed in table 4.5, the enhancements can be plotted as function of time. Figure 4.2 shows the enhancements of Br to Zr as a function of time passed since the start of the calculations. These calculations are for the conditions of model B of table 4.5. Figure 4.2 shows also the behaviour of the neutron number fraction, indicated by right hand scale (in figures 4.2 to 4.4 the right hand scale corresponds only to the neutron abundance). This figure displays the total

overabundance of each element i.e. the sum of all the isotopes of a given element divided by the solar abundance (Cameron 1981) of that element. At about 10^4 s significant enhancement of the heavy elements commences. This is due to the large number of neutrons now being produced over this time interval from the $^{13}\text{C}(\alpha, n)^{16}\text{O}$ source. The drop following peak abundance is due to further neutron absorption by the enhanced elements. After 10^6 s most of the ^{13}C is destroyed and consequently the neutron density falls to such a level that no more significant heavy element processing occurs. The changes in the enhancements following 10^6 s can be attributed to subsequent beta decays from relatively long lived isotopes.

For the other calculations similar diagrams can be obtained with the main difference being the time taken for the heavy element build up to commence increasing as the initial average neutron density decreases. A clear example of this can be seen by comparing the time for build up using the lower neutron flux of 1.5×10^{21} neutrons/cm²/s used for the 2nd model of table 4.4 (no intershell splitting assumed here). The enhancements as a function of time for this model are shown in figure 4.3a and figure 4.3b. As can be seen in this case the enhancement commences at roughly 10^5 s for this reduced neutron flux. The drop in peak abundances is not as significant in these calculations due to the lower neutron exposure.

From table 4.5 it can be seen that very different heavy element enhancements occur for the different models investigated. These results reveal the many factors which control and influence the heavy element enhancements arising from a single mixing on the low-mass AGB. Comparison with table 4.3 also reveals the importance of the phenomenon

Table 4.5

Enhancements after intershell splitting

Model	A	B	C	D	E
Average Neutron Flux (neutrons/cm ² /s)	1.3 (22)	2 (22)	2 (22)	2.3 (22)	2.5 (22)
Fe	5 (-4)	1 (-3)	1 (-3)	9 (-4)	1 (-2)
Co	6 (-2)	0.12	0.11	8 (-2)	1.3
Ni	0.28	5 (-2)	4 (-2)	2 (-2)	0.52
Cu	6.3	0.74	0.64	0.24	6.8
Zn	18	1.6	1	0.22	6.9
Ga	79	6.9	5.4	1	40
Ge	137	11	10	1	42
As	127	8.2	7.0	0.56	23
Se	444	36	31	1.9	88
Br	316	26	22	1.4	64
Kr	4667	873	787	6.4	329
Rb	11230	2450	2145	13	706
Sr	5056	1689	1511	6	345
Y	3047	1145	1031	4.2	298
Zr	12070	5340	4861	12	537
Nb	3295	1612	1386	5.2	394
Mo	9770	4986	4559	8.7	279

Table 4.5 (Cont.)

Model	F	G	H	I	J
Average Neutron Flux (neutrons/cm ² /s)	3.9 (21)	7.8 (21)	8.5 (21)	8.6 (21)	8.6 (21)
Fe	0.49	1 (-2)	5(-3)	9 (-4)	9 (-4)
Co	77	1 (-2)	2	0.18	0.19
Ni	5.6	9.4	6.1	1.6	1.7
Cu	34	160	120	35	37
Zn	7.7	159	183	67	89
Ga	15	516	664	327	375
Ge	7.9	476	769	636	583
As	4.6	477	795	537	543
Se	5.8	539	1203	1514	1508
Br	4.1	423	928	1109	1105
Kr	4.7	561	1930	6818	6141
Rb	5.8	727	2800	11221	11890
Sr	1.5	107	493	3340	3456
Y	0.8	42	218	1915	1897
Zr	2.1	63	382	5098	4904
Nb	0.9	17	102	1584	1526
Mo	1.2	19	129	2801	2639

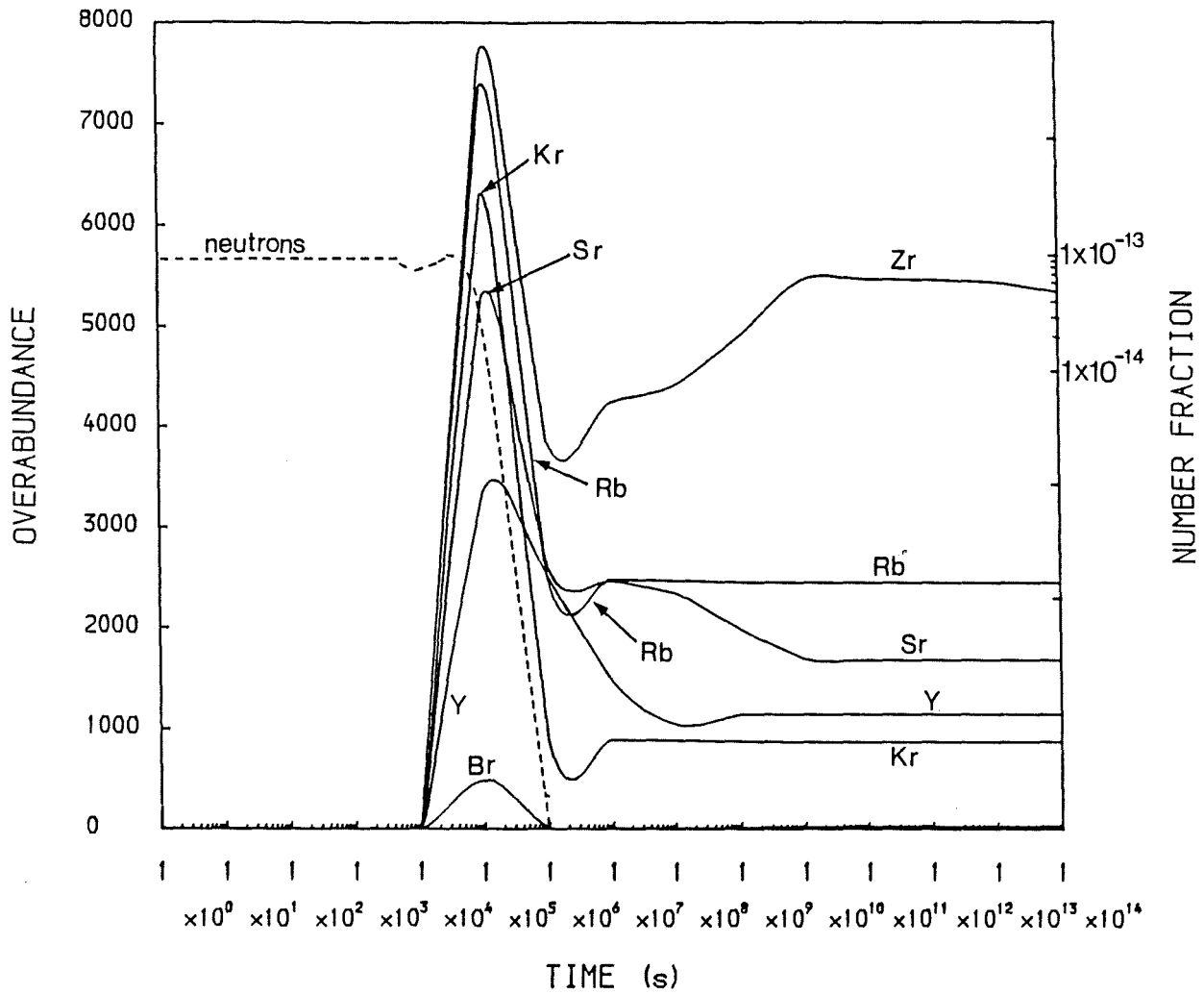


Figure 4.2 Heavy element enhancements Br to Zr as function of time (from model B table 4.5)

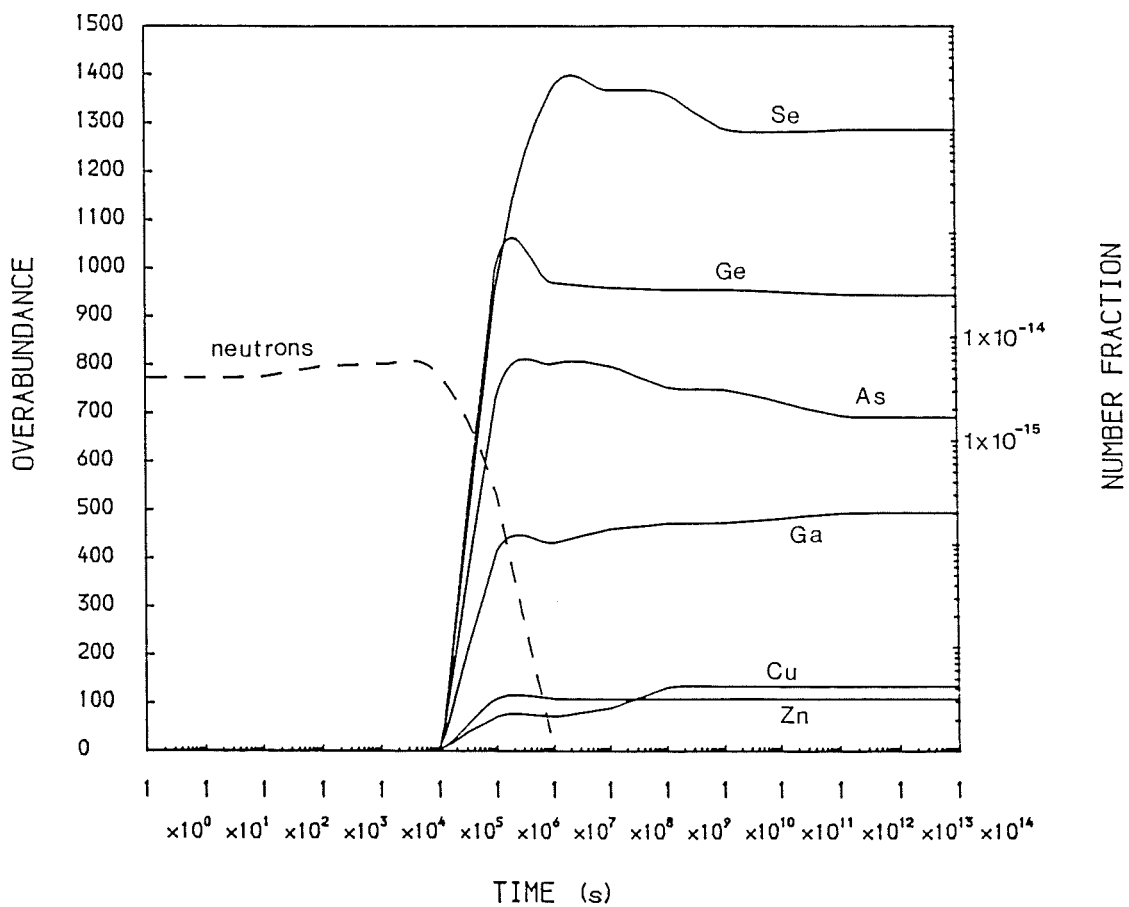


Figure 4.3a Heavy element enhancements Cu to Se as function of time

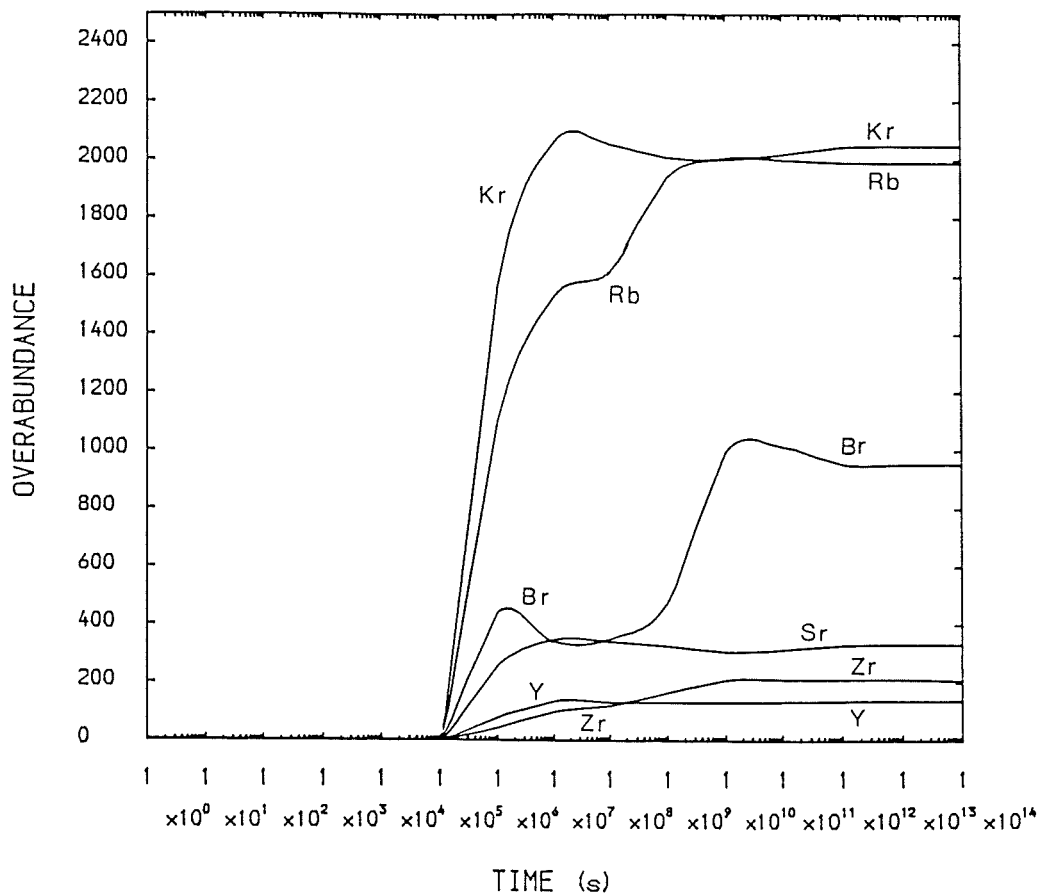


Figure 4.3b Heavy element enhancements Br to Zr as function of time (from 2nd model table 4.4)

of intershell splitting has on the heavy element enhancements. Models A and B from table 4.5 show the differences arising from using different intershell base temperatures. The changes in the enhancements can be attributed here to the different initial relative abundances of the isotopes due to the difference in the intershell mass (as discussed in section 4.2). The reason no large shift in the peak of the heavy element distribution occurs (as it did for the calculations of table 4.3) in this case is due to the lower $^{13}\text{C}/^{14}\text{N}$ ratio. The lower $^{13}\text{C}/^{14}\text{N}$ ratio is a direct consequence of the intershell splitting. Comparison of models B and C show that the effect of the unthermalised nuclei is not as significant as it was in earlier calculations. This is simply due to the fact that differences in the beta decay rates of the unthermalised nuclei are not as important under the high neutron flux calculations of models B and C. That is, for these calculations the neutron flux is such that whether an isotope beta decays or not before further neutron absorption does not depend on whether the isotope is in a thermalised state or not since the high neutron flux in this case ensures further neutron absorption. The models D and E show the very interesting effects of varying the initial abundances of ^{22}Ne , ^{56}Fe and the light heavy and heavy nuclei. For model D where the initial ^{56}Fe and the light heavy and heavy elements are put to 0.1 of the solar value, it can be seen that very little heavy element enhancement has occurred. In fact what has happened in this situation is that a large number of neutron captures per initial ^{56}Fe seed have occurred which pushes the heavy element peak well beyond the Fe to Mo range. As a result any enhancements which did occur in the Fe to Mo range have been destroyed by further neutron captures. The reason that a large number of captures per initial ^{56}Fe nuclei have occurred in this case is mainly

due to the lower initial abundance of ^{56}Fe . It is also due to the fact that the ^{13}C abundance (and therefore the neutron abundance) remained at a high level for a longer period of time for this calculation. This was due to the lower ^{56}Fe abundance allowing the $^{12}\text{C}(n, \gamma)^{13}\text{C}$ reaction to be more dominant (as discussed in section 3.3). For model E where the initial ^{22}Ne was also lowered (to 0.001 by relative number) another interesting event occurred. In this calculation the heavy element peak was again pushed beyond the Fe to Mo region. However, in this case a small amount of fresh Fe is produced as a result of neutron build up on ^{22}Ne . This fresh Fe then undergoes further neutron capture resulting some modest heavy element enhancements in the Fe to Mo range. The reason this effect did not also occur for model D is due to the high initial ^{22}Ne abundance in model D remaining at a high level and acting as a neutron poison. With the ^{22}Ne remaining high fewer neutrons are captured by the ^{22}Ne progeny. The low enhancements for model F, for which $2.5 \times 10^{-4} M_{\odot}$ mixing is assumed, are simply a result of the high ^{14}N initial abundance. This acts as a strong neutron poison and therefore leaves fewer neutrons available for absorption by ^{56}Fe . Model G shows the enhancements as a result of $2.5 \times 10^{-6} M_{\odot}$ mixing. As can be seen the somewhat surprising conclusion is reached that this model which has a mixing a factor of 100 lower than that of model F gives rise to the greater heavy element enhancements in the Fe to Mo range. This again highlights the importance of the $^{13}\text{C}/^{14}\text{N}$ ratio. The dependence of the enhancements on this ratio is further shown by the results listed for models H, I and J where their higher $^{13}\text{C}/^{14}\text{N}$ ratios result in more significant enhancements.

It was mentioned earlier that the temperature-density conditions of the intershell were changed after 10^9 s in order to simulate the cooling of the intershell region following peak flash. It is worthwhile here to point out the dangers of not properly accounting for this effect. This can be seen from figure 4.4 where the build up of the elements from Br to Zr is shown for idealised circumstances where the temperature remains high at 2.4×10^8 °K over the entire 10^{14} s. The unthermalised nuclei are included in this calculation. The build up due to the high neutron flux commences at 10^4 s and a second build up takes place at 10^9 s. This second build up is at a much reduced neutron density of about 10^7 neutrons/cm³ and thus at a slower rate. As can be seen this second build up can change significantly the relative abundance enhancements. The second build up can be explained by helium burning occurring profusely after about 10^9 s (see figure 4.5). After the ^{13}C is initially destroyed it reaches a steady number fraction of about 8×10^{-12} at about 5×10^7 s. This value is maintained from the $^{17}\text{O}(\alpha, n)^{20}\text{Ne}$ and the $^{12}\text{C}(n, \gamma)^{13}\text{C}$ reactions. At about 10^9 s the helium burning reactions are dominant and the α particles become significantly reduced as they burn with each other forming ^{12}C , on ^{12}C forming ^{16}O and on ^{13}C creating neutrons. After the helium is destroyed the ^{13}C begins to be enhanced since it no longer suffers destruction via helium burning and consequently during this period there is no rise in the number of neutrons produced. This second slow rise could be a significant effect in higher mass AGB stars where high temperatures exist well after the initial mixing. The importance will depend crucially on the evolution with time of the intershell temperature grid of such stars. For the low-mass AGB stars considered here this late slow addition is not important since the temperature grid is too low after 10^9 s.

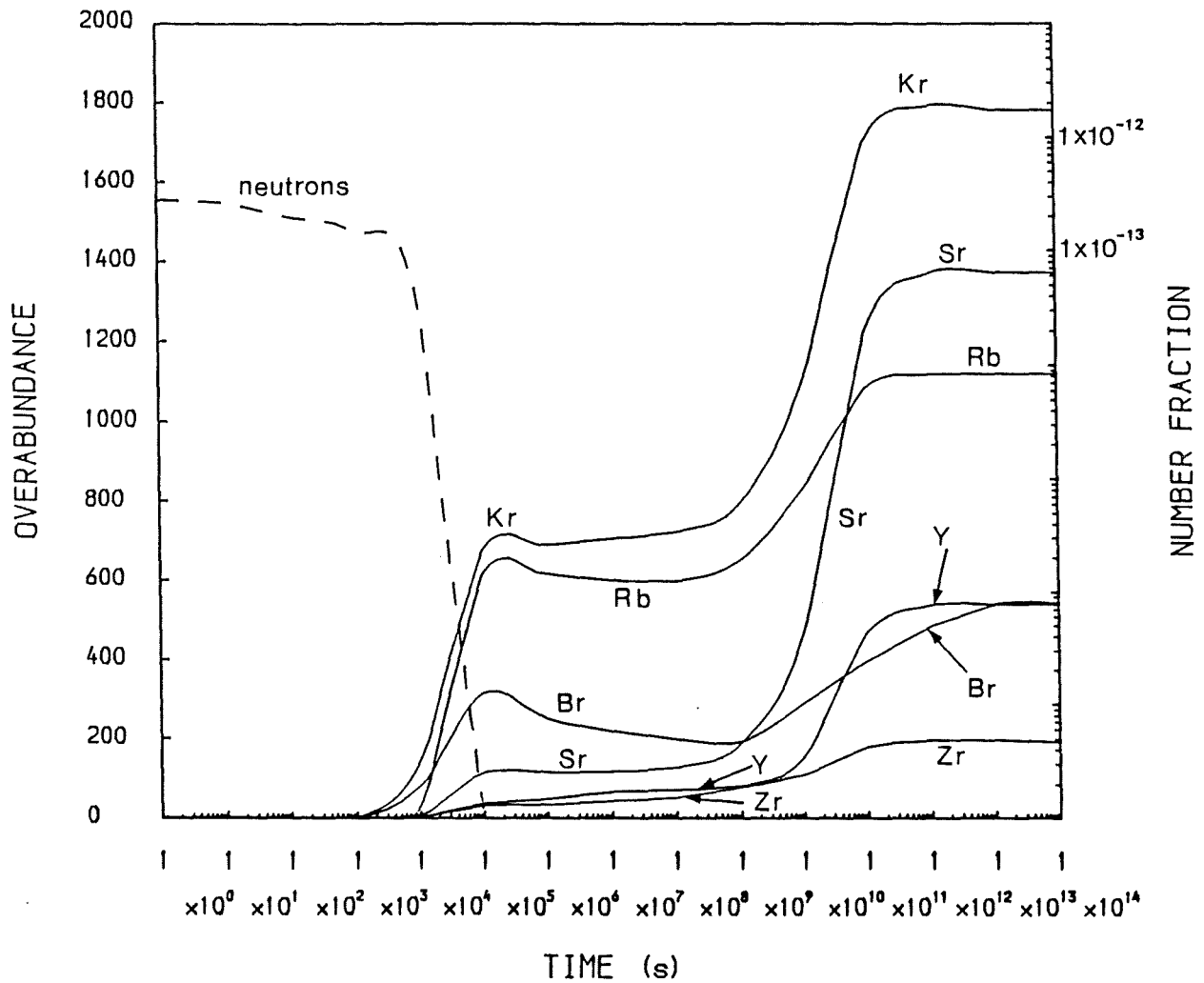


Figure 4.4 Late slow flux on total element enhancements

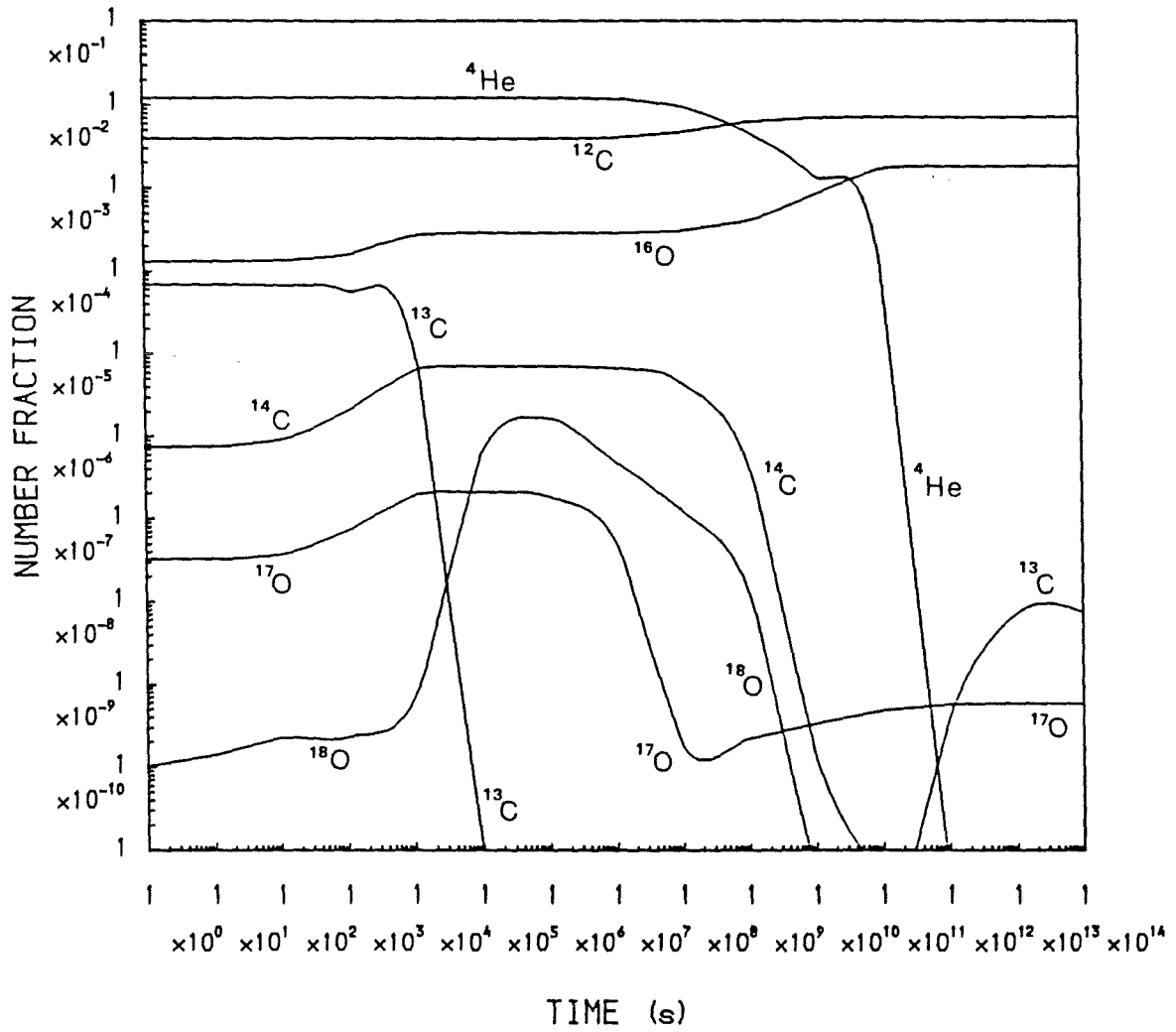


Figure 4.5 Light particle reactions

b) Individual Isotopic Enhancement

The previous tables and figures have listed the total element enhancements obtained for the different models. These total element enhancements are calculated by summing over all the isotopes of a given element. Enhancements tabulated in this fashion are more useful for direct comparison with observation since it is the total element enhancement which is usually determined from stellar spectra. However, by tabulating the enhancements in this fashion some of the subtle, but none the less important, differences arising from using different mixing models can be lost. In order to see such differences the enhancements of individual isotopes (relative to the solar value taken from Cameron 1981) for some of the mixing models of table 4.5 are listed in table 4.6. The differences in the results discussed for the total element enhancements can now be seen more from the individual isotopic enhancements. The results of table 4.6 will be further discussed when a comparison is made with calculations simulating repeated mixing events. The importance of the unthermalised nuclei in certain circumstances can be more clearly seen by investigation of the isotopic enhancements rather than the total enhancements. This can be seen from figure 4.6 where the full lines correspond to enhancements from calculations which include the unthermalised nuclei (the calculations here are from model H of table 4.5) and the dashed lines to the corresponding calculations where all the nuclei are assumed thermalised. In figure 4.6 the long halflife of the thermalised ^{85}Kr (several years) causes the main neutron path to bypass ^{85}Rb . This is the cause of the low value of the ^{86}Rb for the thermalised calculations. For the unthermalised calculations the

Table 4.6

Enhancements of the individual isotopes of table 4.5

Model	A	B	C	E	G	H
^{56}Fe	2 (-4)	6 (-4)	5 (-4)	7 (-3)	3 (-3)	1 (-3)
^{57}Fe	4 (-3)	1 (-2)	9 (-3)	0.1	8 (-2)	3 (-2)
^{58}Fe	5 (-2)	0.1	0.1	2	3	0.7
^{59}Co	6 (-2)	0.1	0.1	1	8	2
^{60}Ni	0.5	0.1	9 (-2)	1	20	12
^{61}Ni	0.7	0.1	0.1	2	30	18
^{62}Ni	1	0.2	0.2	2	43	27
^{64}Ni	9	1	0.9	8	209	165
^{63}Cu	3	0.5	0.4	5	120	80
^{65}Cu	12	1	1	10	249	209
^{66}Zn	9	0.8	0.7	5	146	137
^{67}Zn	26	2	2	9	381	384
^{68}Zn	30	2	2	15	306	345
^{70}Zn	1460	1	50	290	7215	10459
^{69}Ga	49	4	4	28	464	536
^{71}Ga	123	10	7	58	594	860
^{70}Ge	31	3	5	36	244	289
^{72}Ge	62	5	6	44	284	410
^{73}Ge	77	5	5	35	389	579
^{74}Ge	183	14	12	48	594	998
^{76}Ge	518	36	31	28	1290	2408
^{75}As	127	8	7	23	477	794
^{76}Se	210	23	20	110	433	788
^{77}Se	293	20	17	47	748	1409
^{78}Se	357	30	26	90	640	1297

Table 4.6 (Cont.)

Model	A	B	C	E	G	H
^{80}Se	630	51	43	106	581	1432
^{82}Se	40	3	2	1	19	59
^{79}Br	329	27	24	78	573	1178
^{81}Br	302	24	20	50	269	672
^{80}Kr	91	11	6	104	82	250
^{82}Kr	369	42	35	168	244	634
^{83}Kr	282	19	16	56	258	658
^{84}Kr	685	57	47	81	357	1029
^{86}Kr	24199	4800	4342	1466	1714	6849
^{85}Rb	369	30	30	39	188	547
^{87}Rb	36746	8140	7177	2270	1982	8063
^{86}Sr	571	68	24	186	205	628
^{87}Sr	106	21	5	146	23	75
^{88}Sr	6032	2030	1820	383	103	515
^{89}Y	3047	1144	1031	298	41	218
^{90}Zr	6692	2522	2276	309	57	331
^{91}Zr	19672	7586	6858	489	121	739
^{92}Zr	5528	3054	2790	659	25	157
^{94}Zr	18256	8604	7847	836	59	389
^{96}Zr	77192	39776	36387	1870	160	1066
^{93}Nb	3294	1612	1386	394	17	101
^{94}Mo	1	1 (-3)	3	3	3 (-5)	0.4
^{95}Mo	8033	2361	2123	134	32	204
^{96}Mo	11287	7120	6528	621	21	152
^{97}Mo	16208	7288	6645	439	34	227
^{98}Mo	13449	7596	6964	450	20	138
^{100}Mo	19859	9807	8960	74	28	181

short halflife of the unthermalised ^{85}Kr (several hours) causes more of the ^{85}Kr to beta decay to ^{85}Rb rather than undergoing further neutron capture and forming ^{86}Kr . The ^{85}Rb then undergoes neutron absorption, therefore explaining the large production of ^{86}Rb for the unthermalised calculations.

The neutron densities used in the above calculations are far greater than those expected to be responsible for the classical s-process which is thought to occur at roughly $N=10^7$ neutrons/cm³ (Blake and Schramm 1975). Cosner, Iben and Truran (1980) have pointed out the importance of properly accounting for the late addition of the last few neutrons during the period when the neutron density is falling rapidly. During this phase the neutron density more resembles that of a classical s-process and the enhancement of individual isotopes can be significantly changed during this period. This effect can be clearly seen again by investigating the individual isotopic enhancements. Figure 4.7 shows the behaviour of the ^{86}Sr , ^{87}Sr , ^{88}Sr , ^{86}Kr , ^{87}Rb and the neutron density (dashed line) as a function of time (again the calculations are from model H of table 4.5). During the earlier phases of the flash where the neutron flux is high, these classical s-process nuclei are by-passed by the neutron flow and they become depleted. However, they are built up again in the late stages of the flash when the neutron density falls and the flow passes through the low neutron nuclides.

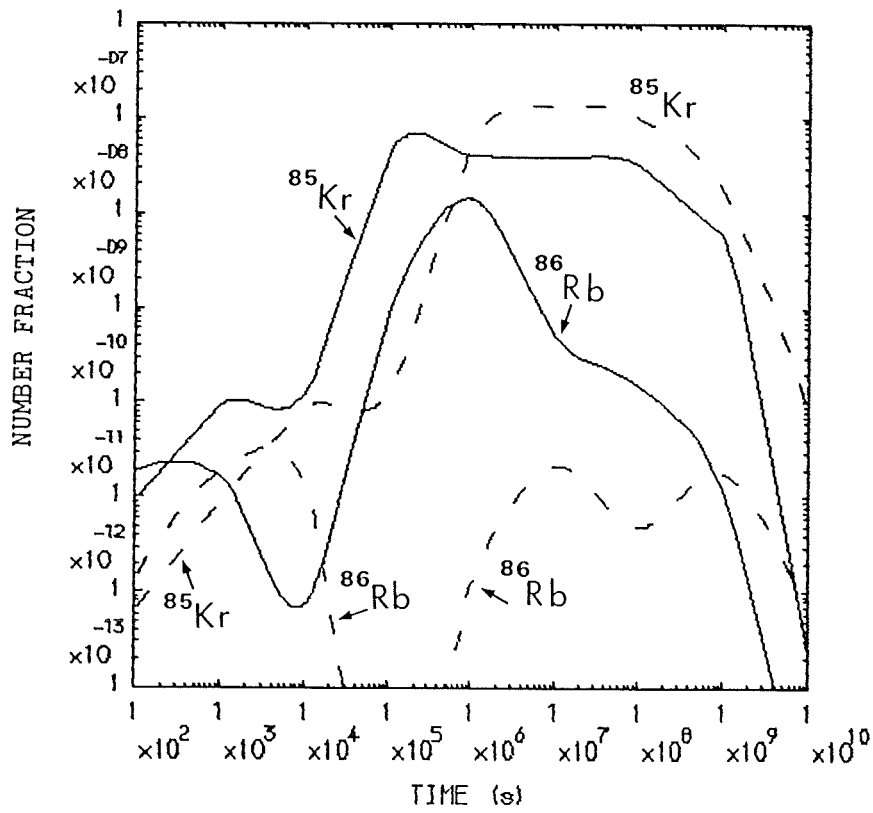


Figure 4.6 Importance of unthermalised nuclei

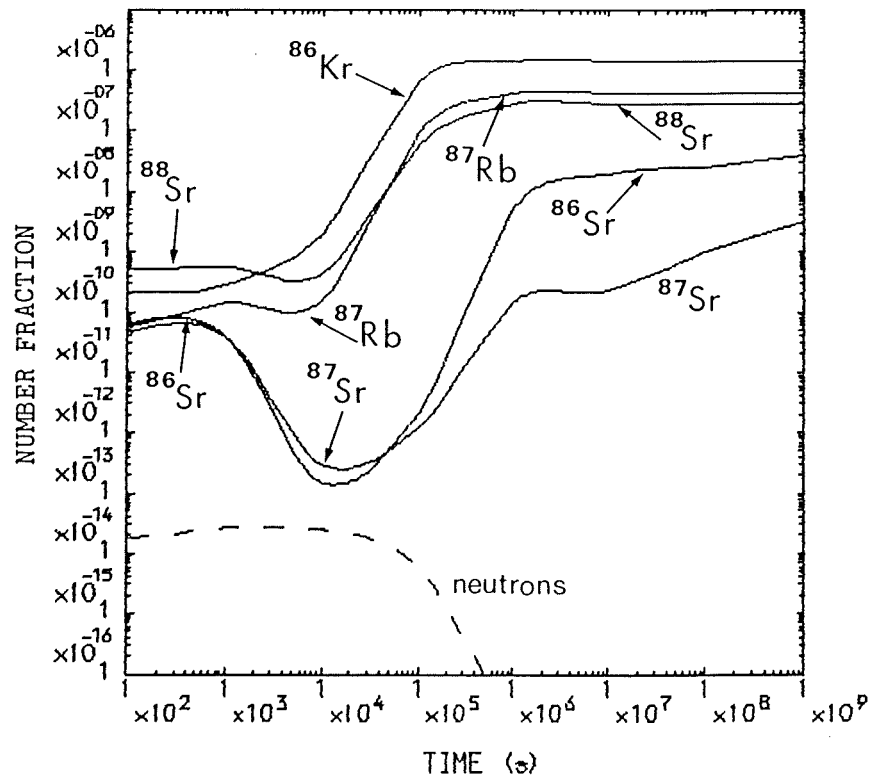


Figure 4.7 Late synthesis by slow flux on individual isotopes

4.4) Repeated Shell Flashes

In this section the heavy element build up in the Fe to Mo region will be investigated for repeated small scale mixing on the AGB. This will occur when a small amount of envelope matter is mixed into the intershell at each shell flash. In the first instance repeated mixing corresponding to the mixing mechanism of Iben and Renzini (1982a,b) is investigated. This at the present time is the most plausible mechanism for mixing on the AGB. At the start of each shell flash the initial abundances of the ^{13}C -rich matter are taken as those of model d of table 3.9 (as are the initial intershell abundances except ^{13}C and ^{14}N are initially set to zero in the intershell). This ^{13}C -rich matter is then ingested into the intershell at a rate of $10^{-3}M_{\odot}/\text{year}$. Such a rate of ingestion is consistent with the calculations of Iben and Renzini (1982b). The heavy element enhancements for this single mixing is then calculated assuming a temperature of $1.5 \times 10^8 \text{ }^{\circ}\text{K}$ and a mass density of $4 \times 10^4 \text{ g/cm}^3$. The isotopes produced are then allowed to beta decay for 3×10^5 years (since this is roughly the interflash period) and then the procedure is repeated for a second shell flash. The calculations are stopped following the 30th flash.

During the course of a thermal pulse the hydrogen burning shell is known to advance outwards in mass by an amount comparable with the mass of the intershell. This then means that an important parameter in the calculations will be the fractional overlap r , of the intershell for two successive shell flashes. That is, r represents the fraction of matter (by mass) within the intershell at shell flash n , which remains within the intershell at the onset of shell flash $n+1$. The parameter r is

known to decrease with increasing core mass, M_c (Truran and Iben 1977). For $M_c=0.59$ (M_c in solar mass units) Gingold (1974) found $r=0.864$, for $M_c=0.8$ Weigart (1966) found $r=0.6$, for $M_c=0.96$ Iben (1976) found $r=0.43$ and for $M_c=1.26$ Fujimoto, Nomoto, and Sugimoto (1976) found $r=0$. This last value is uncertain since the thermal pulses were not allowed to build up to full value. Using these results Truran and Iben (1977) give the following relation for the dependence of r on M_c ,

$$r = 0.43 - 1.17(M_c - 0.96)$$

For the stellar models of Schönberner (1979) this relationship then implies a value of $r=0.9$ for shell flash 1 down to a value of $r=0.76$ for shell flash 30. This can be seen from figure 4.8 where r is plotted as a function of shell flash number. It should be noted, however, that the actual range in r for those flashes where envelope mixing may occur is in fact smaller since a significant number of shell flashes are required before the flash has gained the strength enabling the intershell convection to extend up to the region of the hydrogen shell. This is typically 10 flashes for low-mass AGB stars (Schönberner 1979).

The initial abundances of any isotope in the intershell at the beginning of shell flash n will then be given by

$$Y_{\text{init}}(n) = rY_{\text{final}}(n-1) + (1-r)Y_{\text{env}}$$

where Y_{init} is the new initial abundance, Y_{final} is the abundance of the isotope in the intershell at the end of the previous shell flash and Y_{env} is the envelope abundance of the isotope. However, even though r is anticipated to change slightly from flash to flash, the approximation of assuming r to be a constant for successive shell flashes is usually made for repeated mixing calculations (e.g. Truran and Iben 1977).

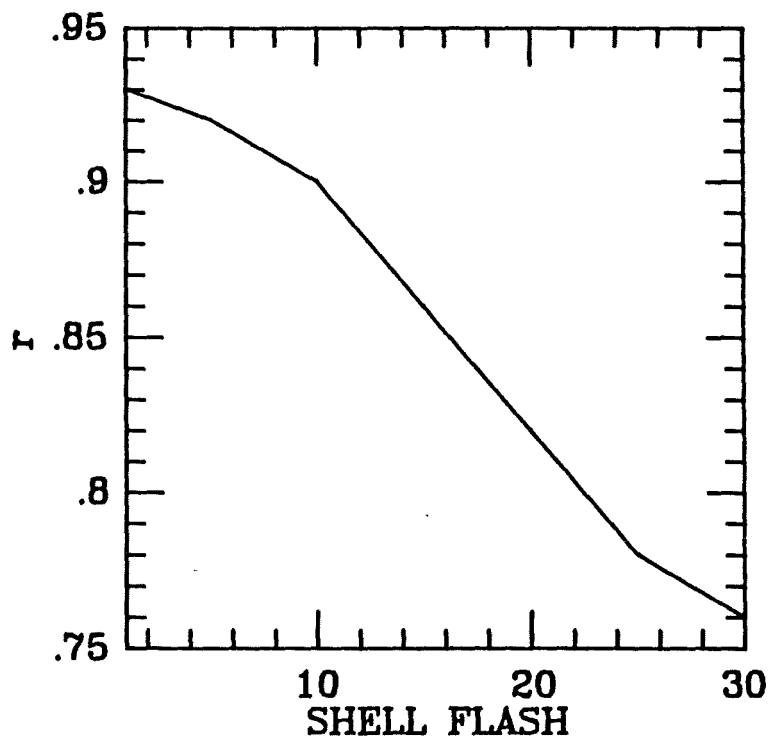


Figure 4.8 r as a function of shell flash

This approximation is made in the calculations presented here. The effect of varying the parameter r is later investigated by carrying out a series of successive shell flash calculations for constant values of r in the range 0.7 to 0.9 .

Figures 4.9 a and b show the heavy element enhancements within the intershell as a function of shell flash number for a constant value of $r=0.7$ and for all the nuclei assumed thermalised. The build up of the heavy elements can be seen to be quite rapid at first and then their rate of increase slowing down as they reach their asymptotic values. Figures 4.10 a and b show the enhancements for the same value of r but in this instance the unthermalised nuclei are included. Significant differences for certain elements can be seen between the thermalised and unthermalised calculations. Figures 4.11 a and b show the enhancements as a function of shell flash for a value of $r=0.8$. The unthermalised nuclei are included in this calculation. As can be seen the larger value of r leads to larger enhancements. Figures 4.12 a and b plot the enhancements for $r=0.85$ with all nuclei thermalised, and figures 4.13 a and b show the same calculation but including the unthermalised nuclei. Again an increase in the enhancements are found for the larger value of r and again the effect of the unthermalised nuclei can be seen. Figures 4.14 a and b plot the enhancements for $r=0.9$ with the nuclei thermalised, and figures 4.15 a and b shows the same calculation with the inclusion of the unthermalised nuclei. It can be from figures 4.9 to 4.15 seen that the main effect of increasing the overlap of the intershells is that an increase in the level of the heavy element enhancements is found. This is partly due to the smaller amount of fresh envelope ^{22}Ne introduced into the intershell for the high r

value. The lower ^{22}Ne in the intershell allows more of the neutrons to be absorbed by ^{56}Fe and its progeny. It is also partly due to the fact that a large proportion of the immediate progeny of Fe produced in the early flashes remain in the intershell for the later flashes.

The effect of varying the initial light heavy and heavy abundances in the intershell is now investigated. Figures 4.16 a and b plot the enhancements as a function of shell flash for $r=0.9$, with all the nuclei thermalised and for the initial light heavy and heavy abundances (including ^{56}Fe but not ^{22}Ne) set to 1/10 of their solar value. Figures 4.17 a and b show the calculation repeated for the inclusion of unthermalised nuclei. As can be seen, for the low initial Fe abundance the enhancement curves have a distinctly different shape. The enhancements of the individual elements quickly reach peak values before being rapidly depleted by further neutron capture and then slowly increasing again towards their asymptotic values at the later shell flashes. Figures 4.18 a and b plot the enhancements for $r=0.85$ again with the abundances set as for the calculation of figure 4.17. The unthermalised nuclei are included here. The main effect which can be seen from figures 4.16 to 4.18 is the reduction in the heavy element enhancements due to the lower initial ^{56}Fe abundance. It can also be seen that significant differences in the Zr/Y and Zr/Sr ratios can occur in the low initial ^{56}Fe calculations relative to those found for the higher initial ^{56}Fe calculations. This point will be discussed again later.

Calculations were also carried out with the initial ^{22}Ne mass fraction set to 0.01 and with the light heavies and heavies (including ^{56}Fe) set to their solar values. Figures 4.19 a and b plot the enhancements for this situation assuming $r=0.9$ and including unthermalised nuclei. The importance of the high ^{22}Ne in this case can be seen from a comparison with figures 4.15 a and b, where $r=0.9$ but a lower ^{22}Ne initial abundance is assumed. The enhancements of figure 4.19 are lowered with respect to figure 4.15 due to the high ^{22}Ne abundance absorbing more of the neutrons available for capture by ^{56}Fe . Finally, in order to investigate the importance of the initial ^{12}C and ^4He abundances, these initial abundances were both set to 0.483. The resulting enhancements are plotted in figures 4.20 a and b for $r=0.85$ and including unthermalised nuclei. From comparison with figure 4.13 it can be seen that the enhancements are lower due to the lower initial ^4He abundance reducing the $^{13}\text{C}(\alpha, n)^{16}\text{O}$ reaction rate.

The final enhancements following the 30th helium shell flash, and after allowing the isotopes to beta decay for 3.3×10^6 years, are listed in table 4.7 for each of the models corresponding to figures 4.9 to 4.20. The points discussed above can be easily seen from this table. The increase in the heavy element enhancements for increasing r (columns 4.9 to 4.15) can be clearly seen from table 4.7. Also significant differences in the relative enhancements of several elements due to the inclusion of unthermalised nuclei can also be seen (eg. Kr in 4.14 and 4.15). Important differences in the relative enhancements of the heavy elements are noticed for the low ^{56}Fe seed calculations (4.16 to 4.18) compared to the relative enhancements for the normal ^{56}Fe seed calculations (columns 4.9 to 4.15). The effect of the high initial

intershell ^{22}Ne abundance in lowering the enhancements can be seen by comparing columns 4.19 with 4.15, and the effect of the initial ^{12}C and ^4He intershell abundances can be seen from comparison of columns 4.20 and 4.13.

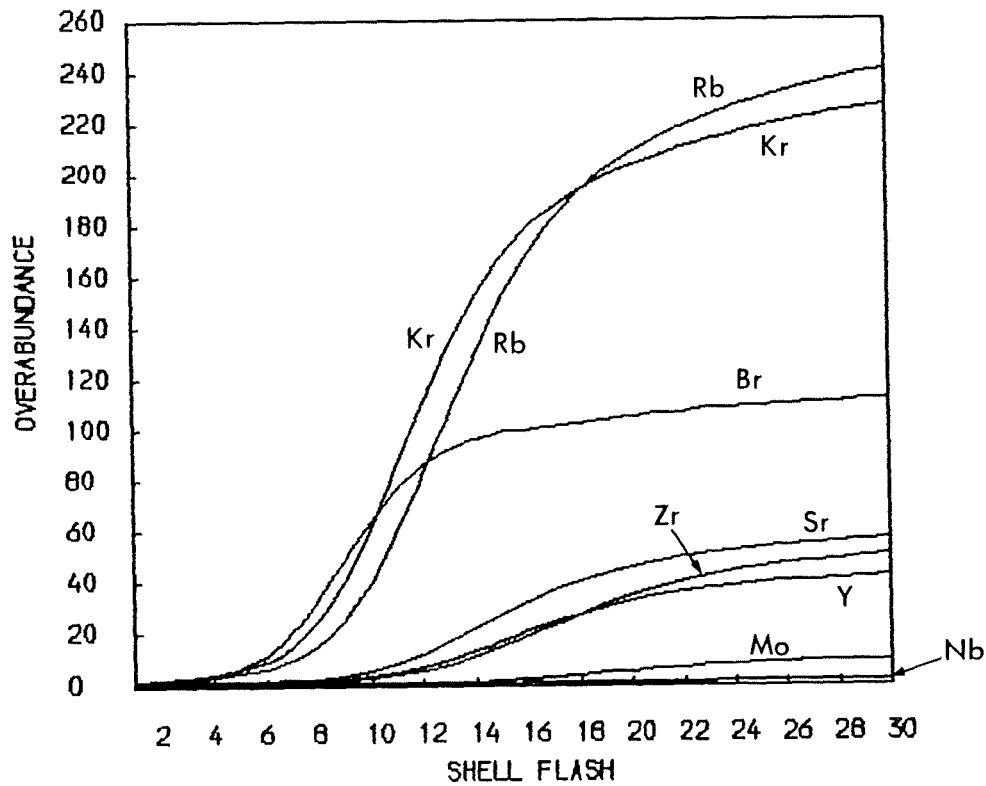
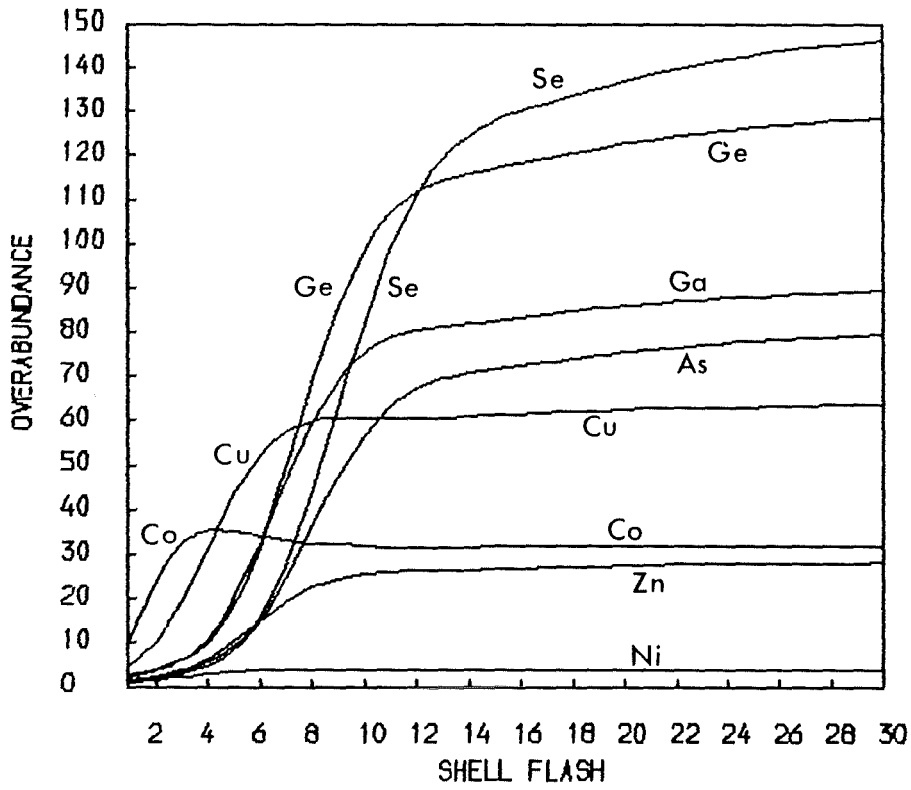


Figure 4.9a (top) and Figure 4.9b (bottom)
Repeated mixing for $r=0.7$, thermalised

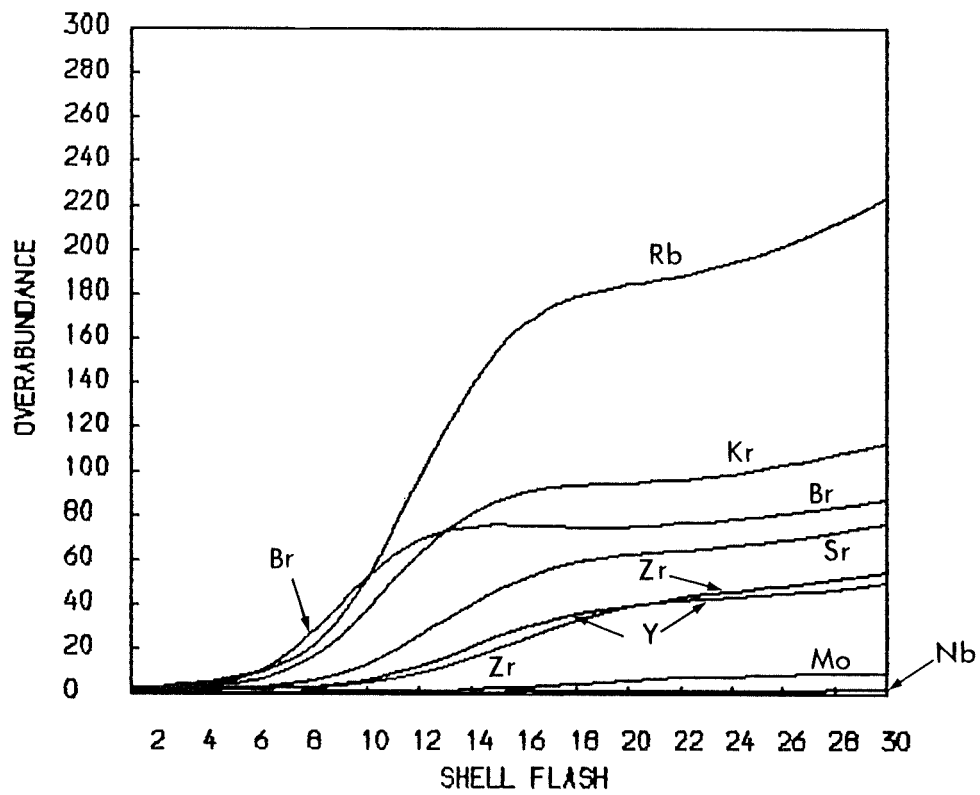
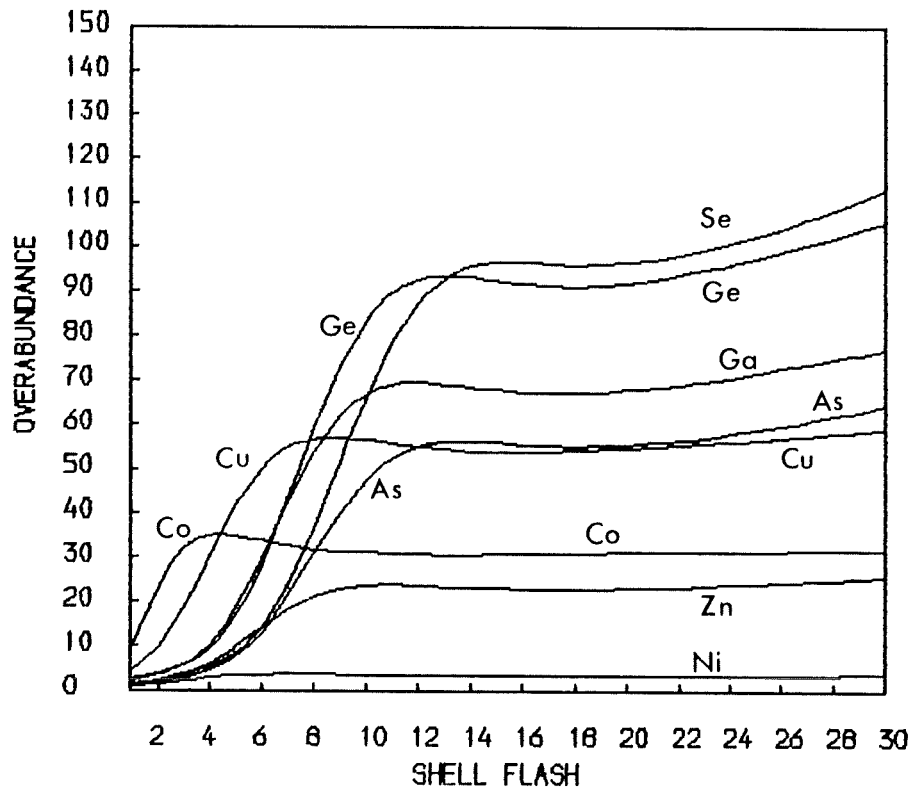


Figure 4.10a (top) and Figure 4.10b (bottom)
Repeated mixing for $r=0.7$, unthermalised

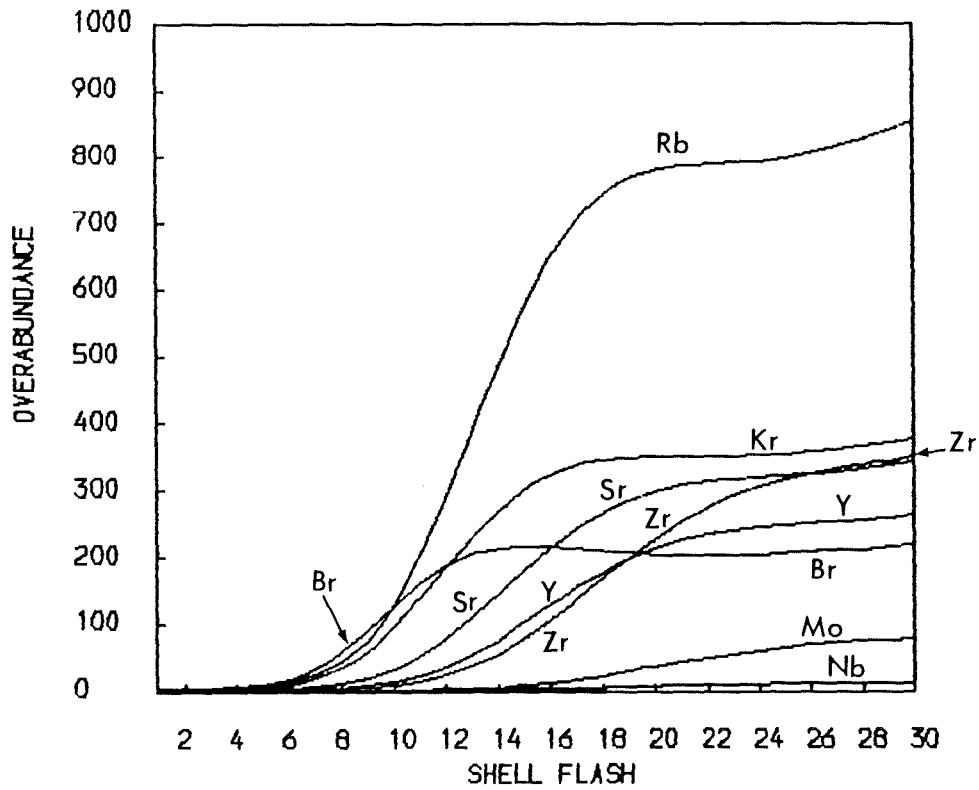
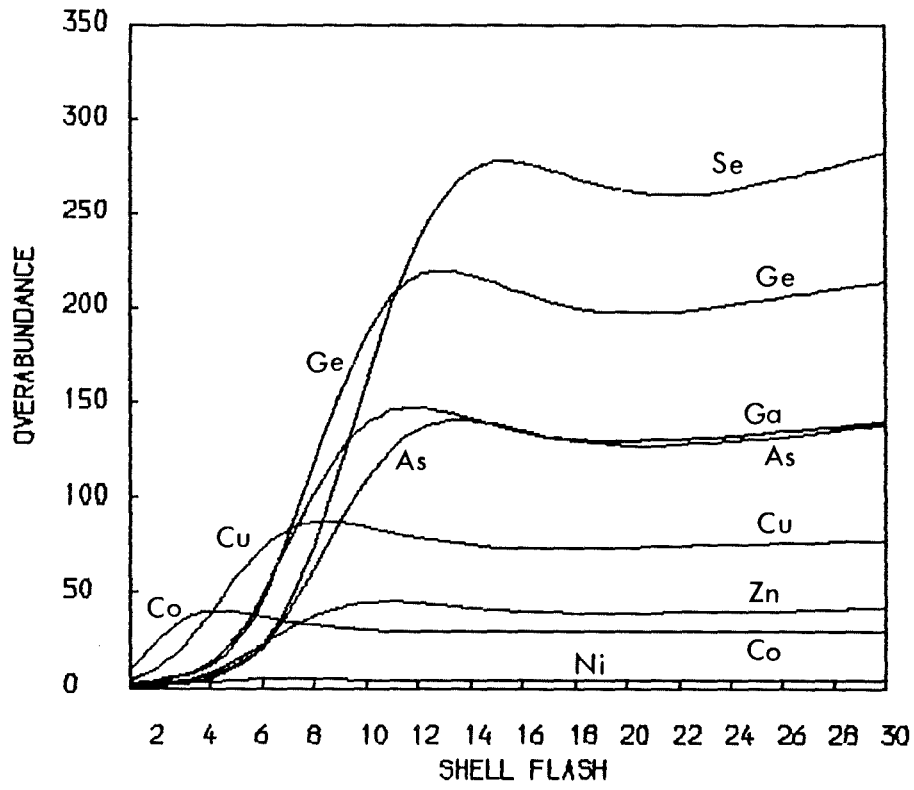


Figure 4.11a (top) and Figure 4.11b (bottom)
Repeated mixing for $r=0.8$, unthermalised

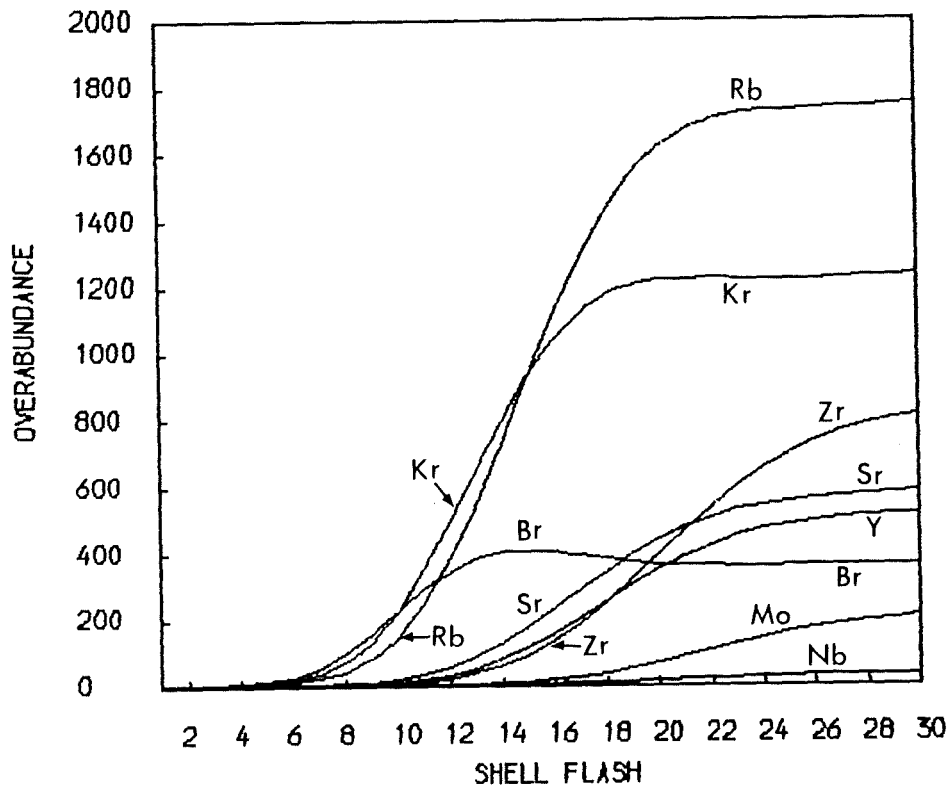
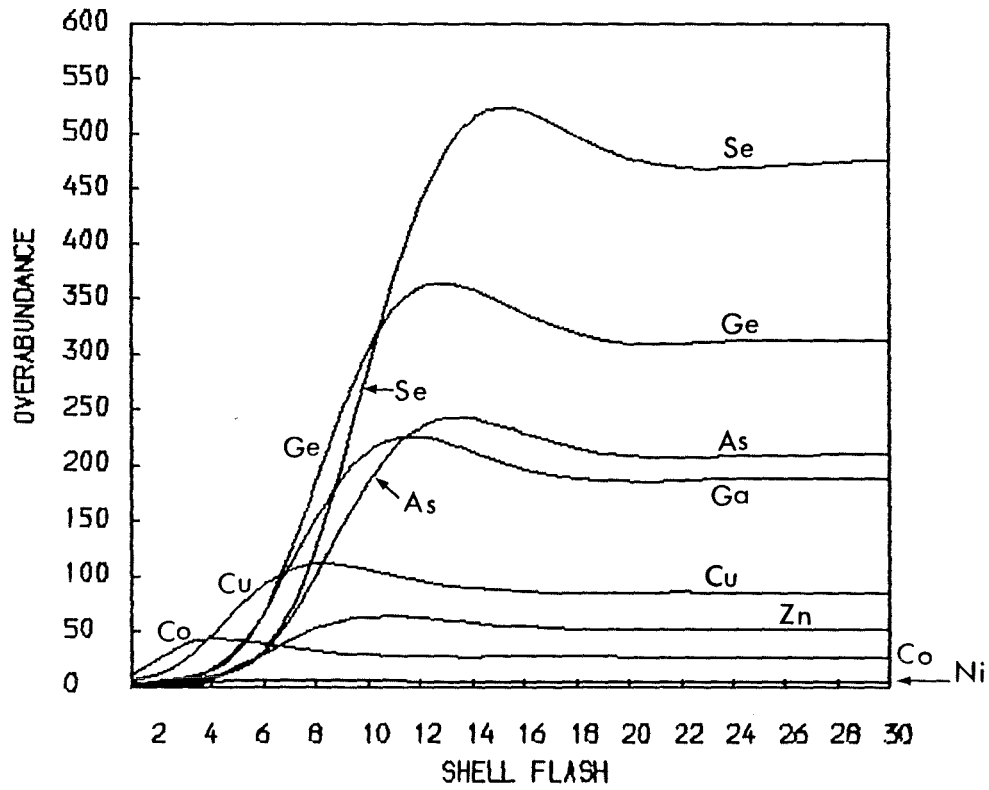


Figure 4.12a (top) and Figure 4.12b (bottom)
Repeated mixing for $r=0.85$, thermalised

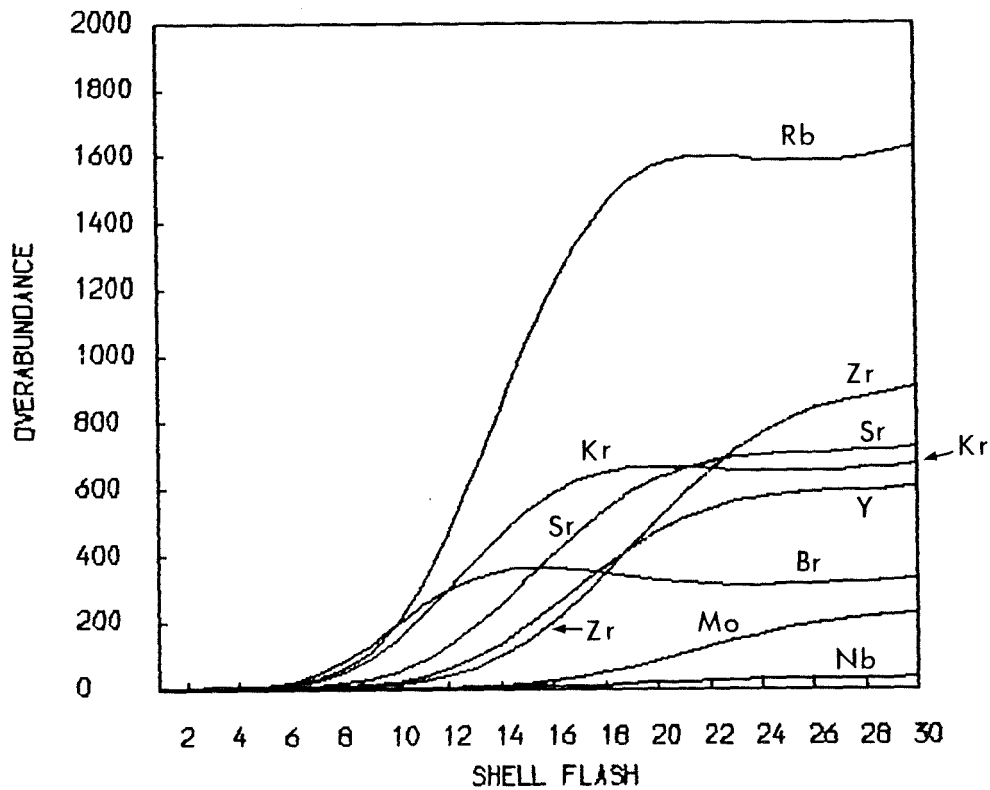
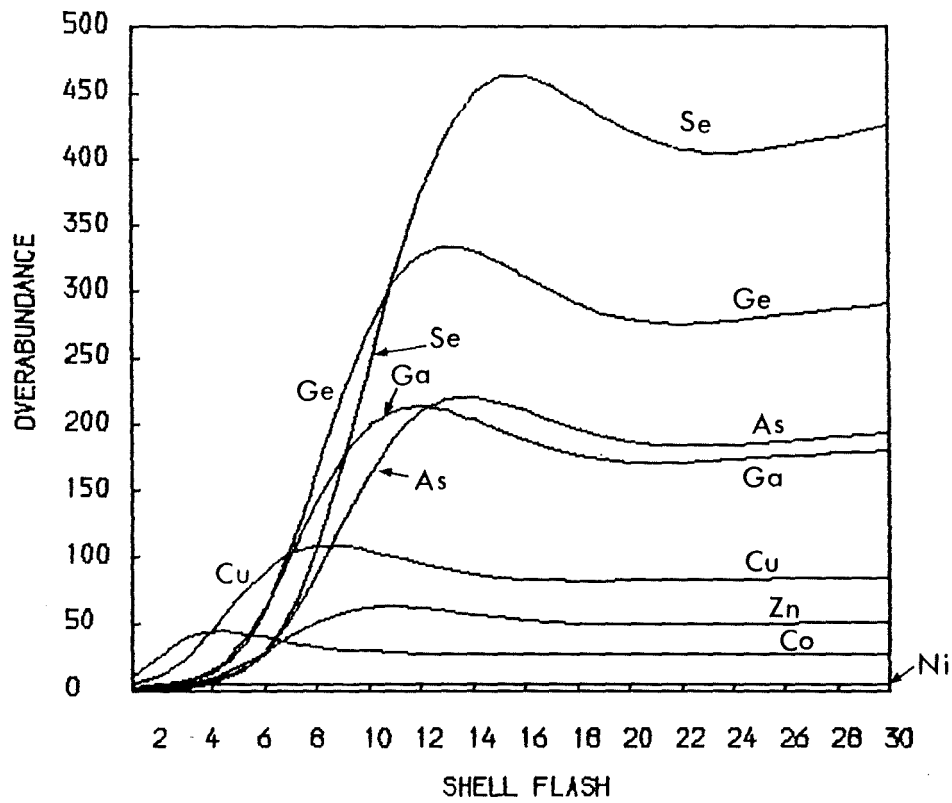


Figure 4.13a (top) and Figure 4.13b (bottom)
Repeated mixing for $r=0.85$, unthermalised

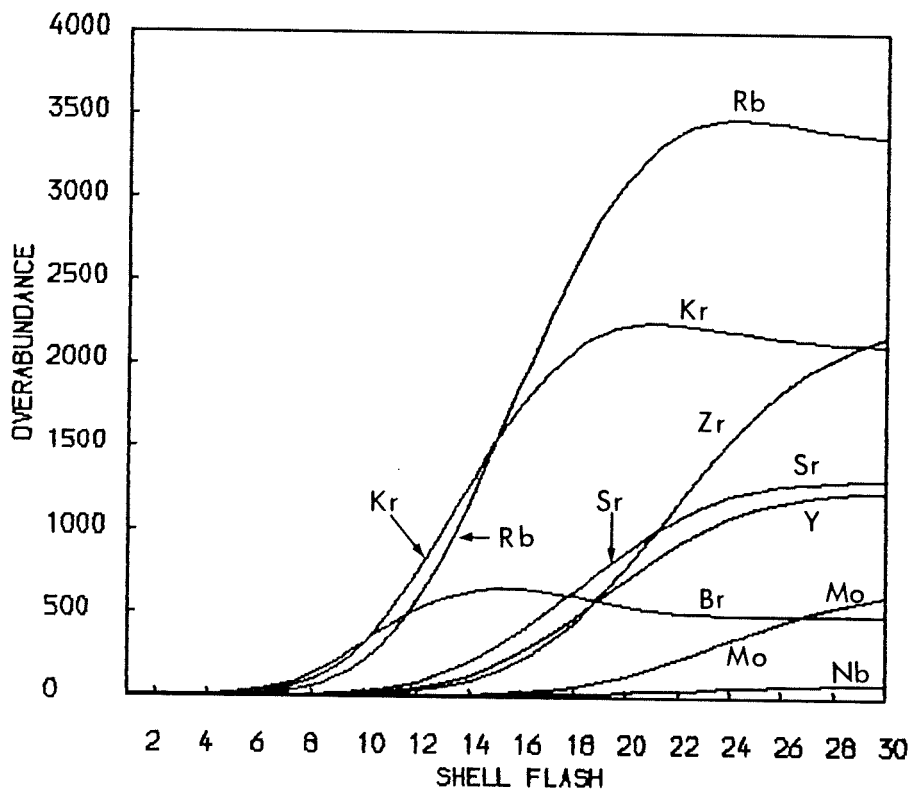
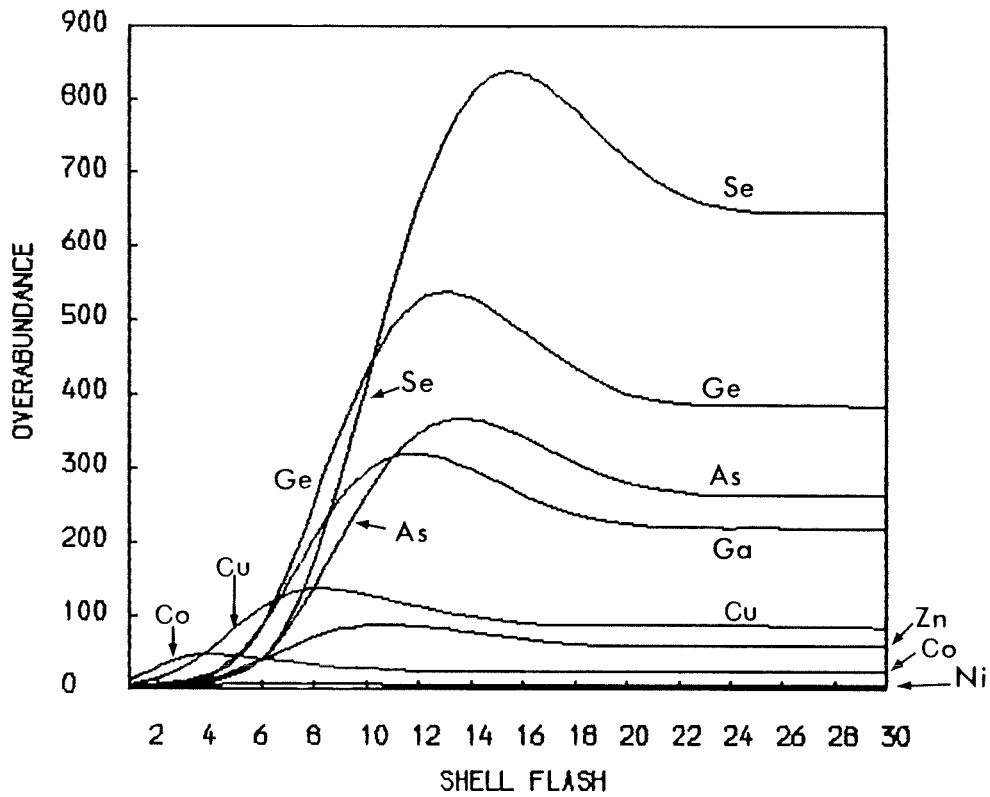


Figure 4.14a (top) and Figure 4.14b (bottom)
Repeated mixing for $r=0.9$, thermalised

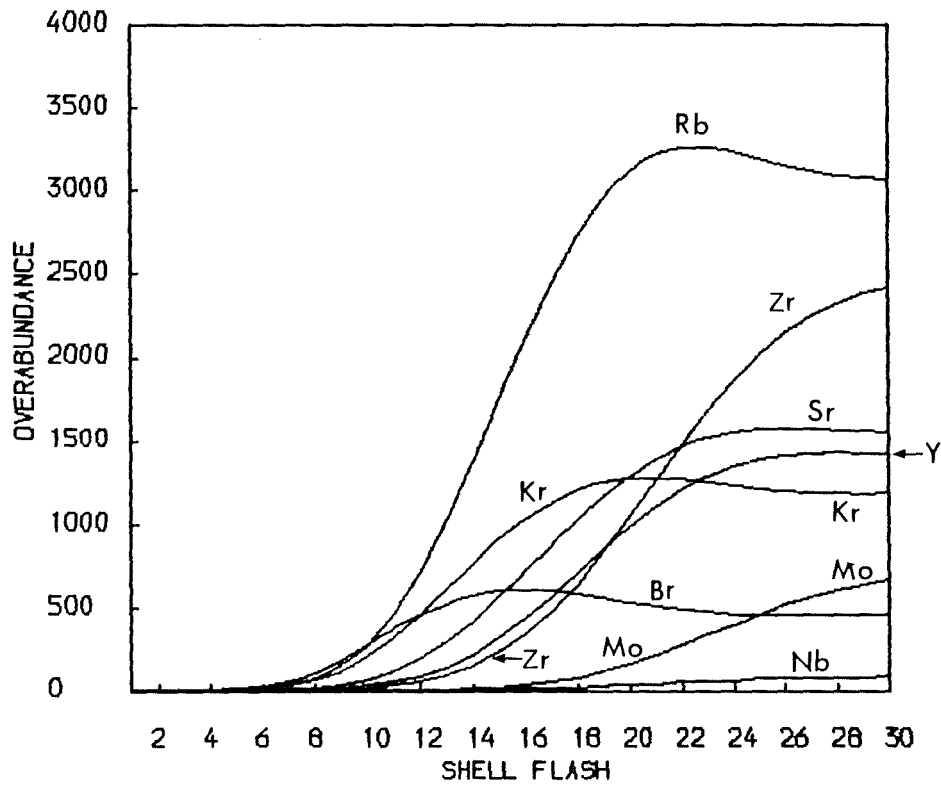
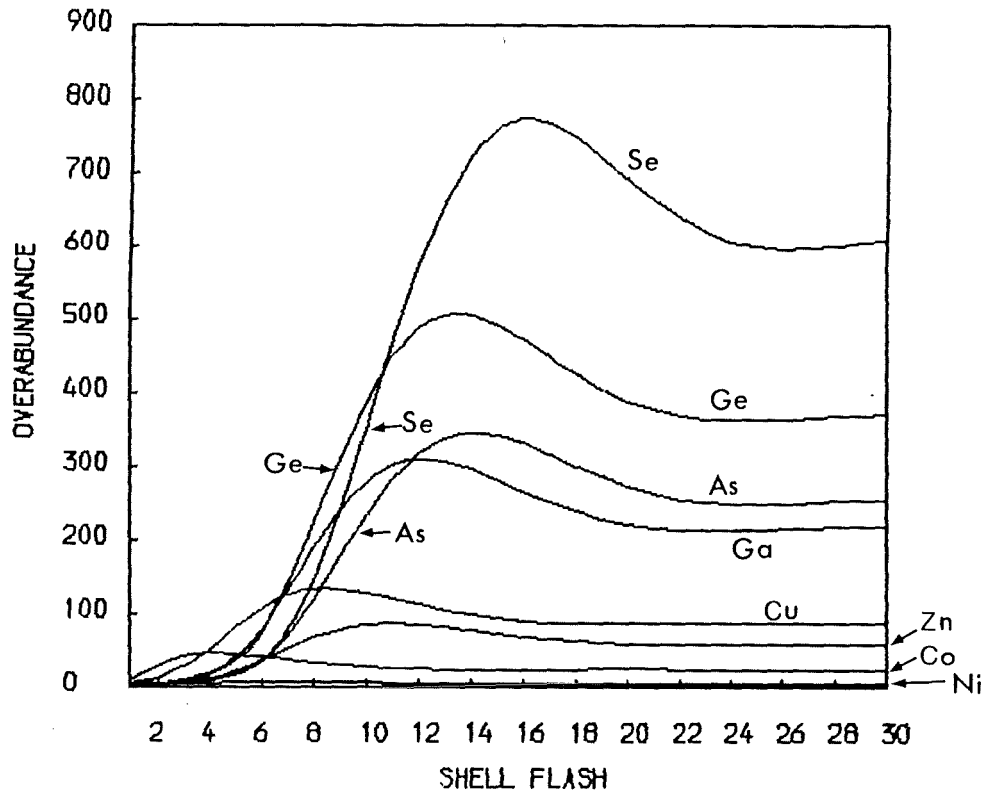


Figure 4.15a (top) and Figure 4.15b (bottom)
 Repeated mixing for $r=0.9$, unthermalised

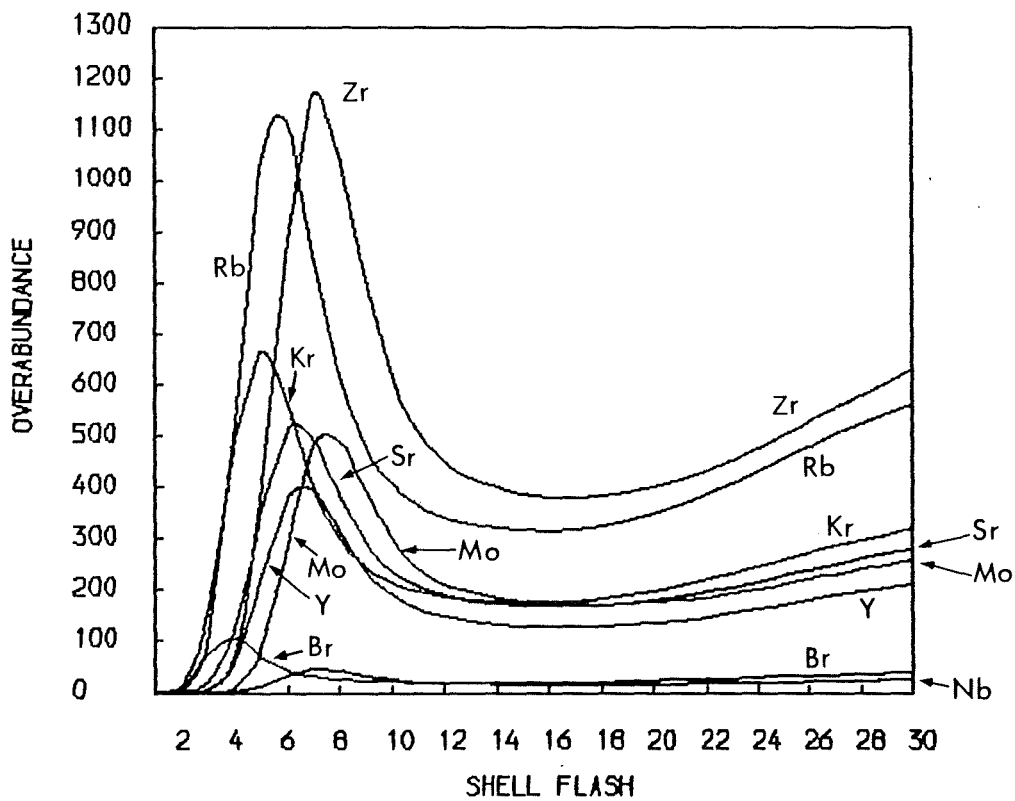
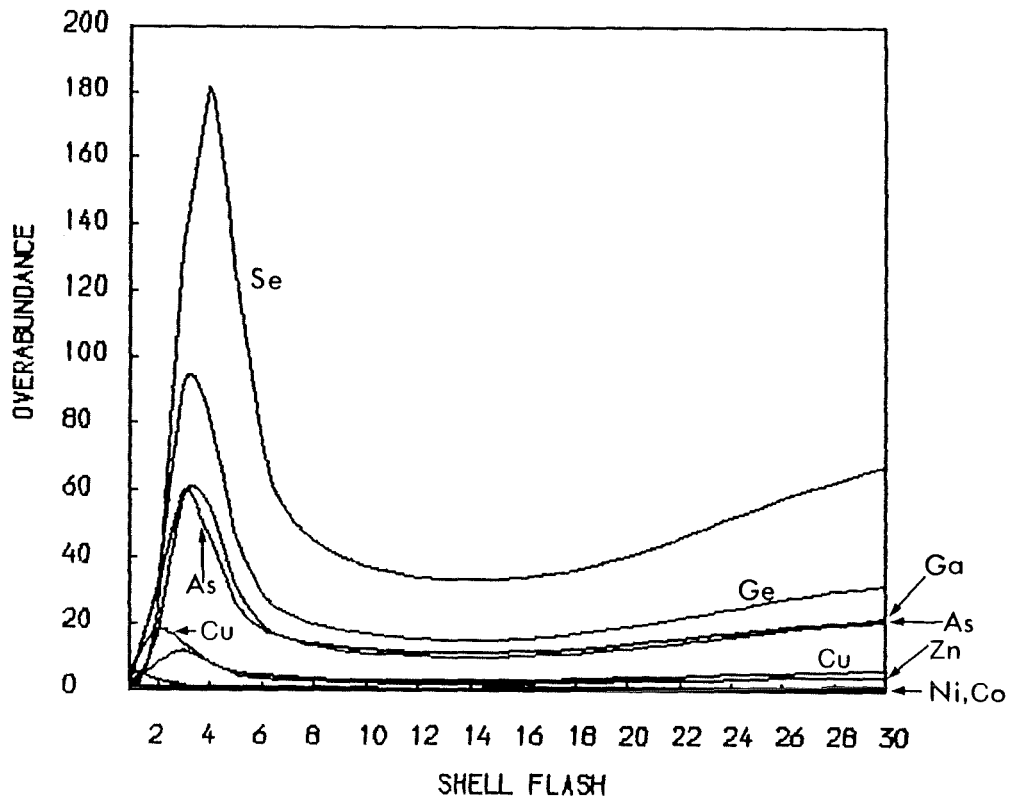


Figure 4.16a (top) and Figure 4.16b (bottom)
Repeated mixing for $r=0.9$, thermalised (0.1 solar seed)

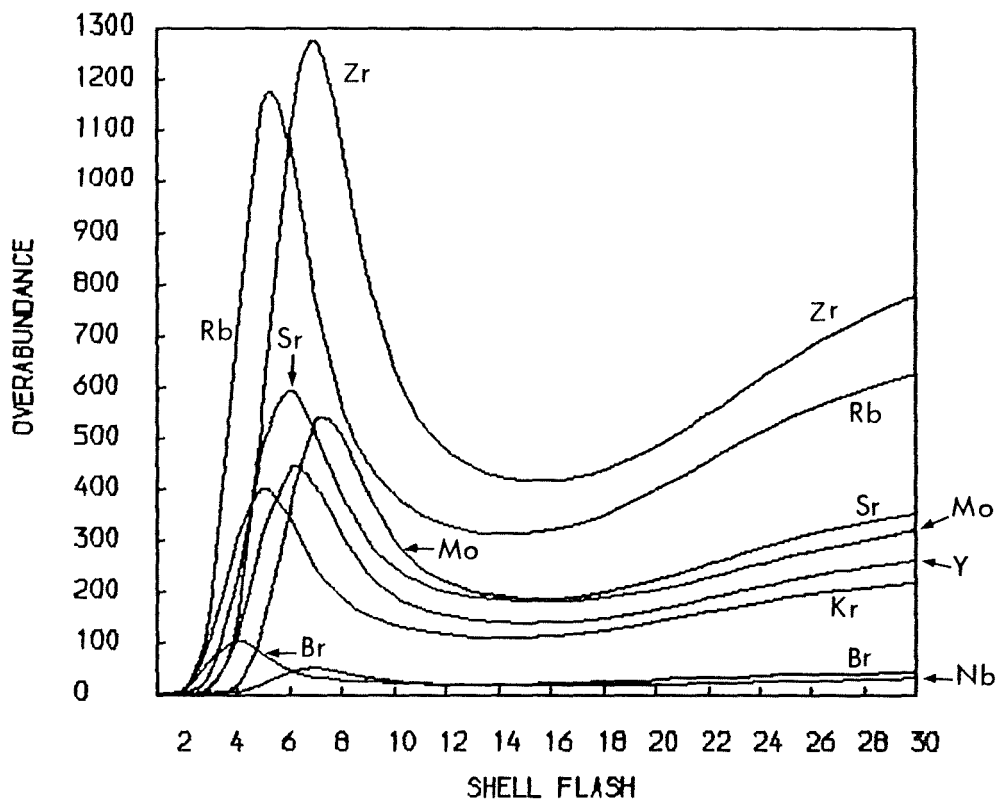
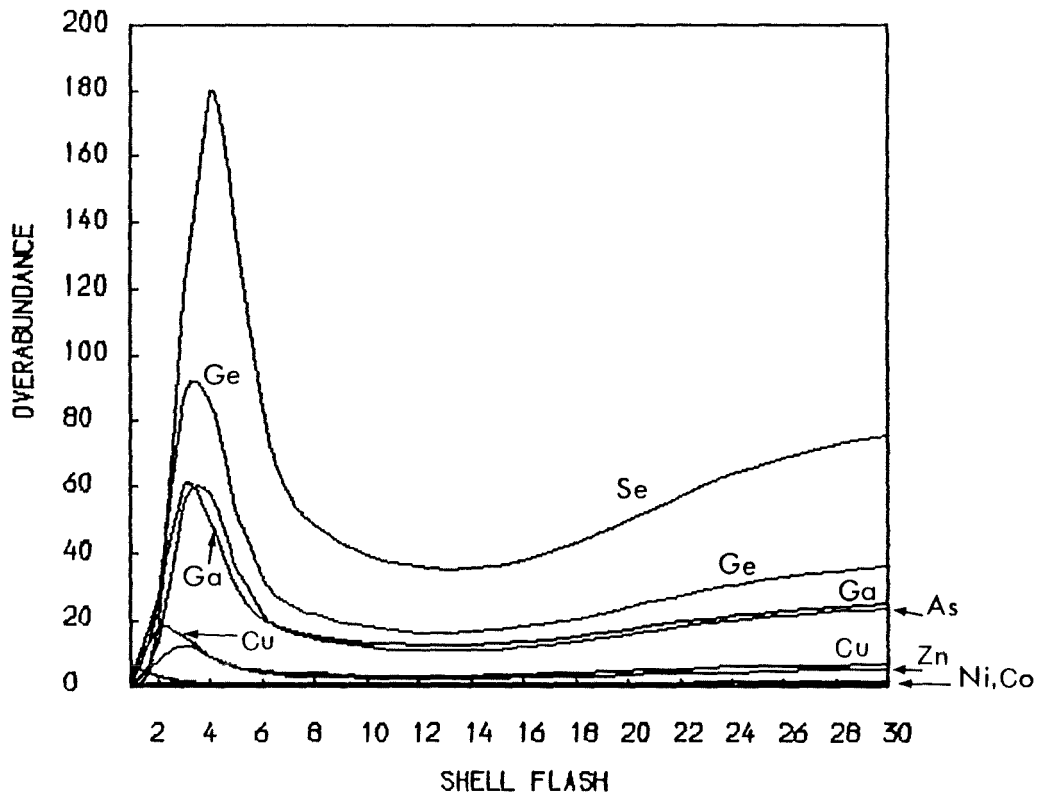


Figure 4.17a (top) and Figure 4.17b (bottom)
 Repeated mixing for $r=0.9$, unthermalised (0.1 solar seed)

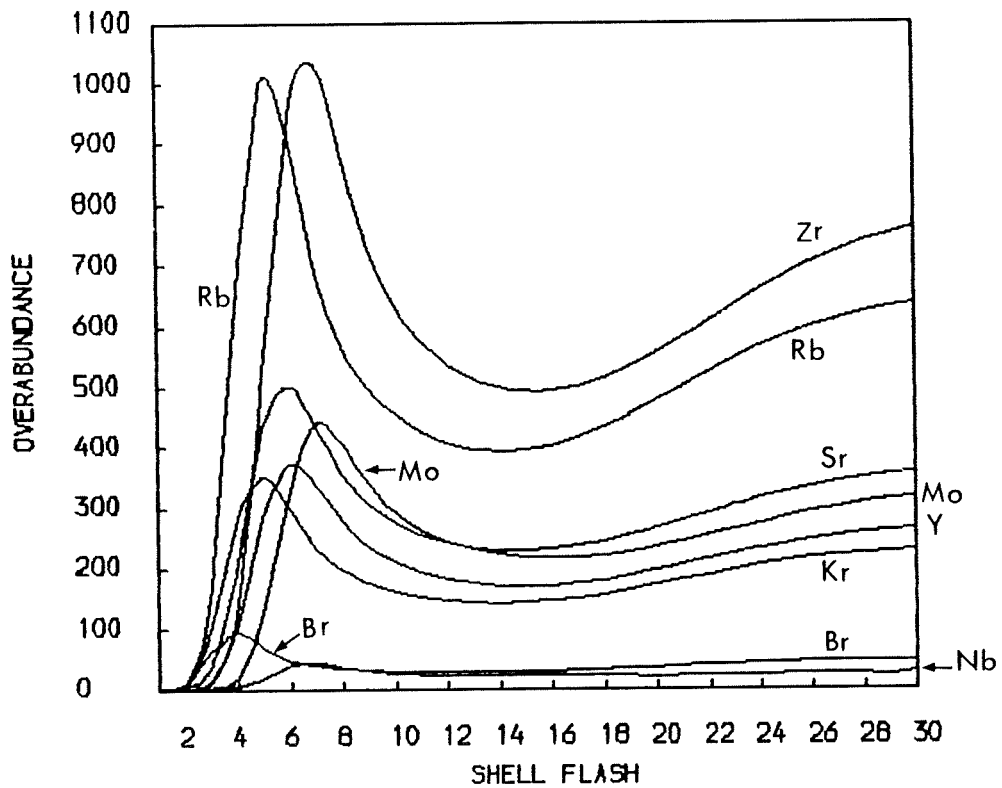
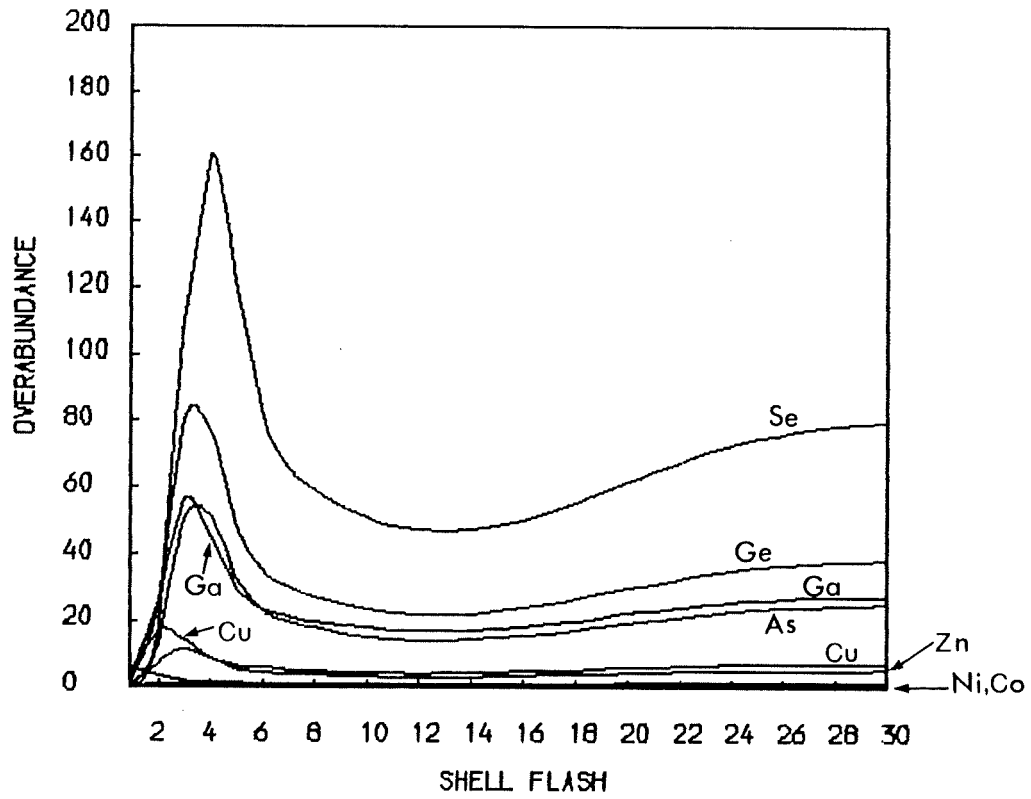


Figure 4.18a (top) and Figure 4.18b (bottom)
Repeated mixing for $r=0.85$, unthermalised (0.1 solar seed)

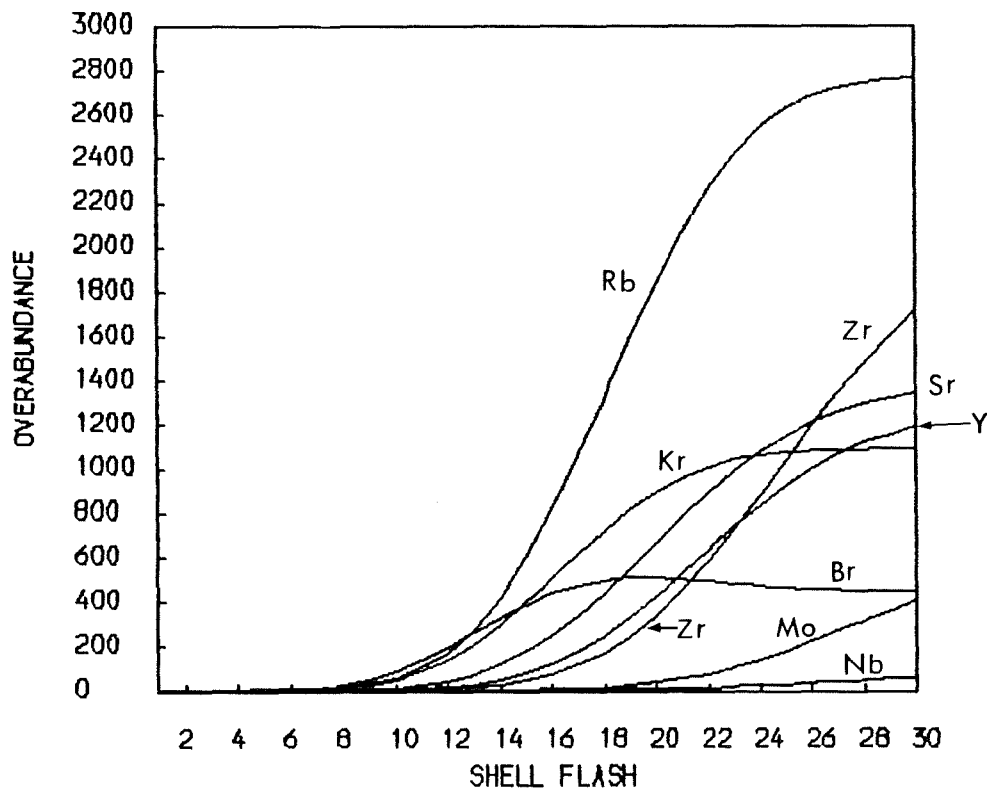
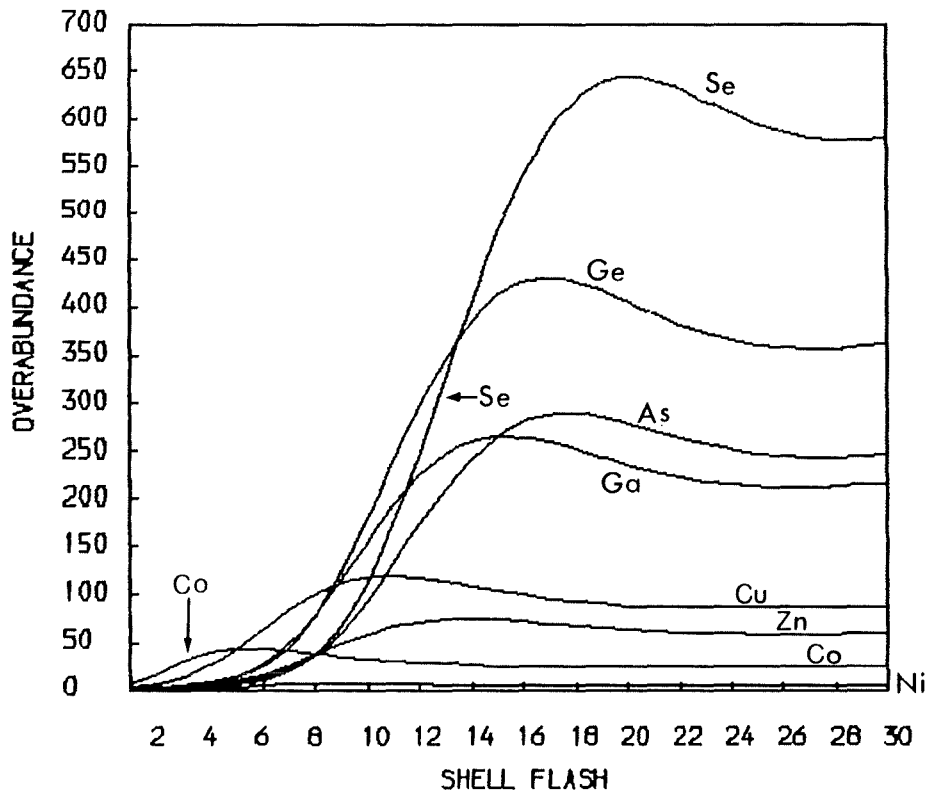


Figure 4.19a (top) and Figure 4.19b (bottom)
 Repeated mixing for $r=0.9$, unthermalised (initial $N_e=0.01$)

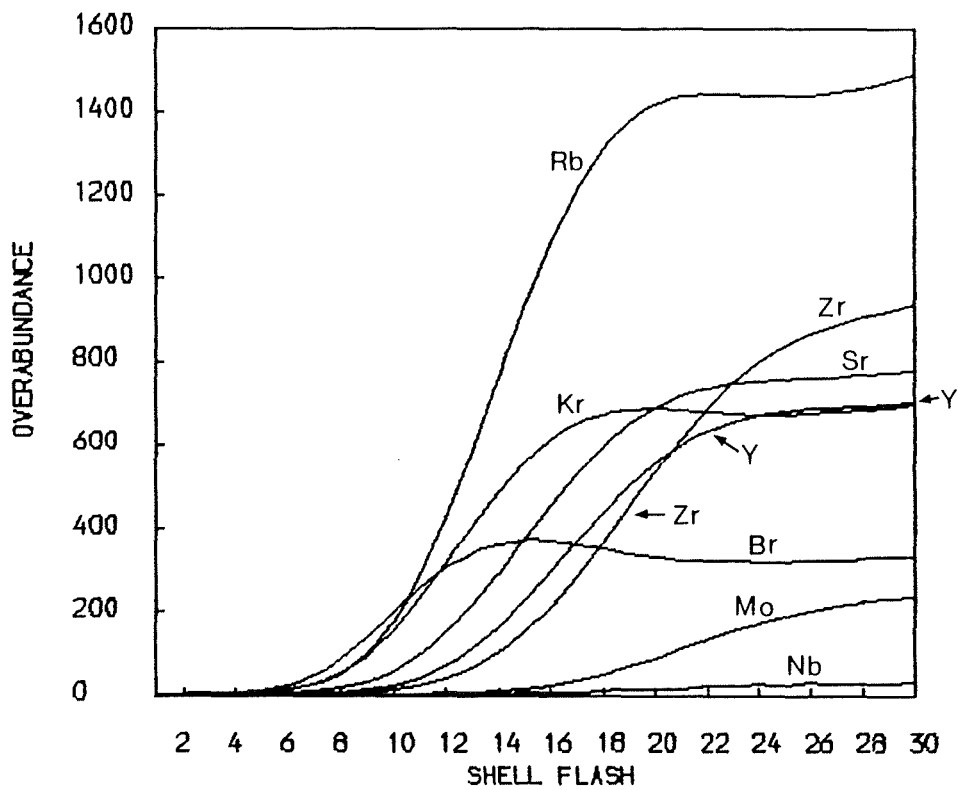
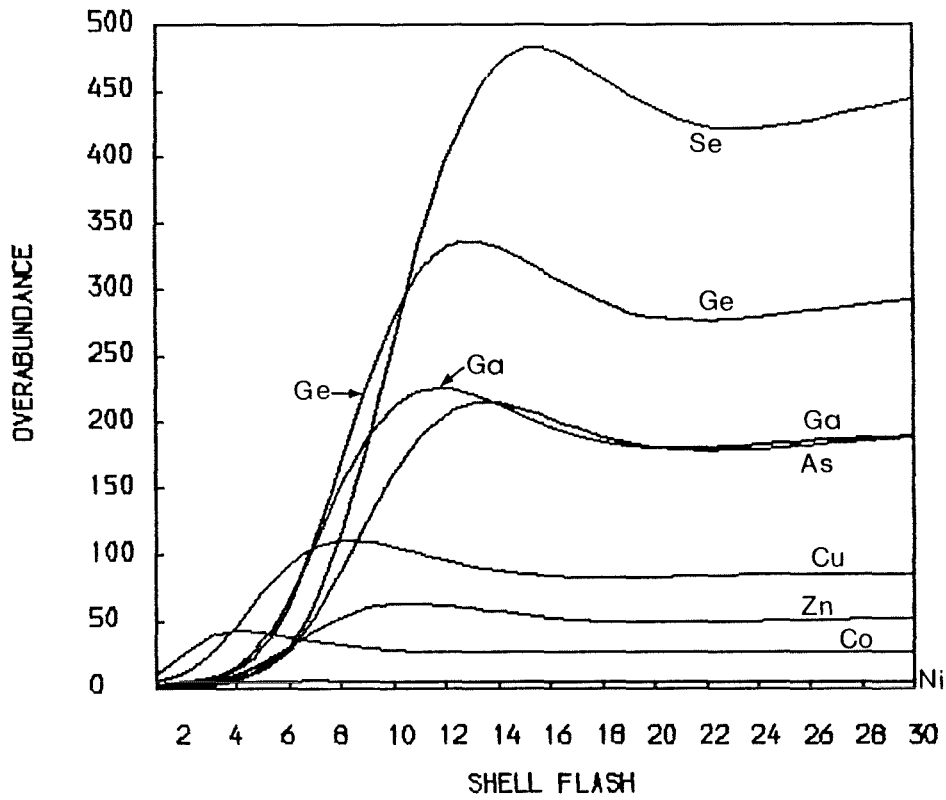


Figure 4.20a (top) and Figure 4.20b (bottom)
Repeated mixing for $r=0.85$, unthermalised (high initial ^{12}C)

Table 4.7

Final enhancements for figures 4.9 to 4.20

Model	4.9	4.10	4.11	4.12	4.13	4.14	4.15	4.16
Fe	0.591	0.62	0.502	0.396	0.423	0.294	0.319	0.01
Co	32.7	32.4	30.5	26.9	27.8	21.8	22.9	1.18
Ni	3.97	3.79	4.27	4.3	4.31	3.89	4.01	0.31
Cu	63.5	58.9	77.4	84.7	84.3	82.8	85.0	5.8
Zn	28.2	25.4	41.8	51.5	51.1	56.6	58.3	4.1
Ga	89.3	76.8	140	187	180	216	217	21.6
Ge	128	105	214	313	290	381	370	32.2
As	79.4	64.3	139	210	194	263	255	21
Se	146	113	282	475	426	644	607	67.2
Br	112	87.6	217	361	328	487	465	37.9
Kr	227	112	378	1237	674	2111	1183	320
Rb	240	223	855	1750	1628	3369	3073	564
Sr	56.6	75.7	343	581	724	1302	1554	282
Y	42.1	49.3	262	517	602	1235	1420	213
Zr	48.4	51.9	336	778	866	2067	2309	598
Nb	28.8	29.9	209	502	555	1362	1521	425
Mo	9.5	9.4	77.8	208	226	603	668	259

Table 4.7 (Cont.)

Model	4.17	4.18	4.19	4.20
Fe	0.01	0.01	0.346	0.42
Co	1.32	1.41	24.2	26.9
Ni	0.35	0.39	4.14	4.3
Cu	6.5	7.2	87.1	85.4
Zn	4.8	5.2	58.8	51.7
Ga	24.8	27.2	216	190
Ge	36.2	38.1	362	292
As	23.6	24.8	247	188
Se	75.5	79.5	579	445
Br	42.7	45.7	446	336
Kr	219	226	1090	697
Rb	627	636	2768	1487
Sr	353	355	1345	778
Y	263	262	1190	702
Zr	743	726	1652	896
Nb	527	520	980	552
Mo	321	316	406	235

Table 4.8

Isotopic enhancements for figures 4.9 to 4.20

Model	4.9	4.10	4.11	4.12	4.13	4.14
^{56}Fe	0.28	0.3	0.24	0.18	0.19	0.13
^{57}Fe	6.2	6.4	5.1	4.0	4.2	2.9
^{58}Fe	57	57	51	43	44	34
^{59}Co	33	32	30	26	27	21
^{60}Ni	5.4	5.2	5.3	5.1	5.1	4.3
^{61}Ni	37	36	38	36	37	30
^{62}Ni	35	33	39	39	40	36
^{64}Ni	67	60	83	96	93	96
^{63}Cu	61	57	70	71	73	68
^{65}Cu	69	62	92	109	107	113
^{66}Zn	37	33	52	63	62	68
^{67}Zn	61	55	87	107	104	115
^{68}Zn	68	59	104	137	131	155
^{70}Zn	5.1	49	97	11	129	13
^{69}Ga	115	98	177	238	227	274
^{71}Ga	49	43	83	108	108	127
^{70}Ge	125	103	193	270	250	315
^{72}Ge	130	108	212	301	284	361
^{73}Ge	109	91	181	258	242	311
^{74}Ge	144	117	251	378	350	473
^{76}Ge	75	56	126	205	179	263
^{75}As	79	64	138	209	193	263
^{76}Se	226	183	411	629	585	801
^{77}Se	106	85	192	299	275	382
^{78}Se	174	137	325	522	475	684
^{80}Se	154	115	308	546	481	764

Table 4.8 (Cont.)

Model	4.9	4.10	4.11	4.12	4.13	4.14
⁸² Se	0.1	0.1	0.1	0.18	0.16	0.22
⁷⁹ Br	152	122	291	468	432	618
⁸¹ Br	70	52	141	251	220	353
⁸⁰ Kr	137	86	228	394	315	522
⁸² Kr	179	135	386	692	621	991
⁸³ Kr	81	60	173	313	297	449
⁸⁴ Kr	116	85	262	506	440	757
⁸⁶ Kr	730	225	913	4742	1799	8650
⁸⁵ Rb	61	39	122	268	205	404
⁸⁷ Rb	658	654	2569	5214	4957	10314
⁸⁶ Sr	18	73	241	77	412	118
⁸⁷ Sr	5.2	46	158	31	280	52
⁸⁸ Sr	66	79	373	692	805	1559
⁸⁹ Y	42	49	261	516	602	1234
⁹⁰ Zr	48	54	323	708	801	1812
⁹¹ Zr	49	53	318	708	783	1807
⁹² Zr	42	45	302	710	790	1901
⁹⁴ Zr	45	45	354	913	999	2593
⁹⁶ Zr	67	63	536	1505	1566	4397
⁹³ Nb	28	30	208	501	555	1361
⁹⁴ Mo	0.2	0.2	1.9	3.9	5.3	11
⁹⁵ Mo	22	22	178	468	510	1341
⁹⁶ Mo	14	14	121	322	351	933
⁹⁷ Mo	10	10	87	236	255	689
⁹⁸ Mo	9	9	76	208	226	612
¹⁰⁰ Mo	3.8	3.6	31	89	93	266

Table 4.8 (Cont.)

Model	4.15	4.16	4.17	4.18	4.19	4.20
^{56}Fe	0.14	0.04	0.05	0.05	0.15	0.19
^{57}Fe	3.1	0.9	1.1	1.0	3.41	4.21
^{58}Fe	35	14	16	16	38	44
^{59}Co	22	11	13	14	24	26
^{60}Ni	4.4	5	5.5	6.5	4.6	4.8
^{61}Ni	32	15	16	18	34	37
^{62}Ni	37	20	22	25	39	40
^{64}Ni	96	84	93	101	96	94
^{63}Cu	71	40	45	50	73	74
^{65}Cu	115	97	108	118	116	109
^{66}Zn	69	47	53	57	70	63
^{67}Zn	116	81	90	98	117	106
^{68}Zn	155	120	134	144	154	133
^{70}Zn	164	34	472	517	148	74
^{69}Ga	272	215	239	257	270	232
^{71}Ga	133	217	260	294	132	124
^{70}Ge	304	251	272	292	302	258
^{72}Ge	355	252	289	305	350	290
^{73}Ge	305	233	265	277	300	247
^{74}Ge	458	419	471	496	446	358
^{76}Ge	239	376	427	439	217	115
^{75}As	254	210	236	247	246	188
^{76}Se	783	806	896	968	772	686
^{77}Se	369	377	421	450	358	282
^{78}Se	654	671	752	797	631	488

Table 4.8 (Cont.)

Model	4.15	4.16	4.17	4.18	4.19	4.20
⁸⁰ Se	709	827	932	974	669	494
⁸² Se	0.2	0.6	0.6	0.7	0.2	0.1
⁷⁹ Br	600	276	314	337	581	441
⁸¹ Br	326	484	541	579	308	227
⁸⁰ Kr	433	3307	3646	3965	411	339
⁸² Kr	941	1299	1432	1595	919	708
⁸³ Kr	425	405	452	485	411	290
⁸⁴ Kr	699	817	923	959	669	450
⁸⁶ Kr	3554	14183	7877	7981	3142	1827
⁸⁵ Rb	328	362	399	415	314	210
⁸⁷ Rb	9505	18033	20040	20317	8515	4473
⁸⁶ Sr	672	1222	1683	1868	661	527
⁸⁷ Sr	473	338	698	810	481	408
⁸⁸ Sr	1765	3242	4023	4015	1511	847
⁸⁹ Y	1420	2125	2629	2615	1190	701
⁹⁰ Zr	2045	3592	4478	4315	1559	851
⁹¹ Zr	1992	6718	8382	8158	1478	770
⁹² Zr	2130	6389	7868	7865	1519	823
⁹⁴ Zr	2887	8845	10957	10761	1838	1037
⁹⁶ Zr	4657	23117	28978	27664	2600	1247
⁹³ Nb	1521	4252	5268	5202	980	552
⁹⁴ Mo	16	13	16	0.04	15.5	0.7
⁹⁵ Mo	1486	1811	2314	2102	914	434
⁹⁶ Mo	1038	6517	8029	7988	648	458
⁹⁷ Mo	761	4227	5190	5221	452	278
⁹⁸ Mo	682	3005	3690	3719	402	247
¹⁰⁰ Mo	283	1180	1513	1348	154	60

The enhancements of individual isotopes for each of the models of table 4.7 are listed in table 4.8. Again these are listed following the 30th helium shell flash and after allowing the isotopes to beta decay for 3.3×10^6 years. The differences discussed for table 4.7 can be seen more clearly by considering the isotopic enhancements. Table 4.8 will also be useful for comparison with table 4.6, where the isotopic enhancements were listed for single mixing events. It can be seen from such a comparison of these two tables that two completely different abundance distributions have been produced.

The previous calculations of figures 4.9 to 4.20 all correspond to repeating hydrogen mixing events on the AGB by the mechanism proposed by Iben and Renzini (1982a,b). As pointed out earlier, this is the only theoretical calculation which predicts envelope ingestion on the low-mass AGB. Direct hydrogen mixing is prevented by an entropy barrier at the hydrogen shell as mentioned in chapter 3. However, since such direct mixing calculations have hitherto been carried out in an approximate manner and some important physical processes may have been excluded, it was considered a worthwhile exercise to carry out calculations assuming repeated direct hydrogen mixing on the AGB. Such calculations could then be compared with the enhancements calculated previously for the Iben and Renzini repeated mixing mechanism. Any differences arising from these two sets of calculations may then be used with future observations to carry out observational tests of the mixing mechanism on the low-mass AGB. Table 4.9 lists the final enhancements following the 30th helium shell flash and after allowing beta decay for 3.3×10^6 years, for mixing of hydrogen directly into the intershell at a

rate of $10^{-3} M_{\odot}/\text{year}$. A total of $2.5 \times 10^{-6} M_{\odot}$ of envelope material is assumed mixed into the intershell at each shell flash. The initial abundances of the envelope material and the intershell are set at those given in table 3.2 only with ^{22}Ne set at 0.001 and the light heavies and heavies given a solar seed distribution. The first column of table 4.9 represents calculations where all the nuclei are assumed thermalised, while the second column includes the unthermalised nuclei. The fractional overlap of the intershells was set to $r=0.85$. Table 4.10 lists the corresponding isotopic enhancements for these calculations. Figures 4.21 a and b (unthermalised nuclei included) shows how the higher neutron flux of the direct mixing calculations effects the build up of heavy elements at each shell flash. Figures 4.22 a and b show the same calculation this time with the unthermalised nuclei included. These calculations should be directly compared with those corresponding to figures 4.20, where the same initial abundances were used. The most noticeable difference of the direct mixing calculation to those of the more plausible mixing calculations is the higher enhancement of the Kr to Nb elements relative to the Co to Zn elements for the direct mixing calculations. This is simply a result of the direct mixing calculation giving rise to a large neutron exposure at each shell flash.

Table 4.9
Direct repeated mixing enhancements

	Thermalised	Unthermalised
Fe	8.6 (-3)	8.7 (-3)
Co	0.66	0.66
Ni	0.46	0.39
Cu	9.1	7.5
Zn	9.1	7.7
Ga	60	50
Ge	86	73
As	63	54
Se	257	224
Br	146	133
Kr	1576	930
Rb	2775	2602
Sr	1330	1560
Y	1150	1329
Zr	2453	2553
Nb	2076	2138
Mo	1275	1210

Table 4.10

Direct repeated mixing enhancements for isotopes

	Thermalised	Unthermalised
^{56}Fe	4.1 (-3)	4.1 (-3)
^{57}Fe	7.7 (-2)	7.8 (-2)
^{58}Fe	0.96	0.97
^{59}Co	0.66	0.66
^{60}Ni	0.75	0.64
^{61}Ni	1.9	1.6
^{62}Ni	2.6	2.3
^{64}Ni	14	11
^{63}Cu	5.2	4.5
^{65}Cu	18	14
^{66}Zn	9.5	7.6
^{67}Zn	16	13
^{68}Zn	29	23
^{70}Zn	8.5	84
^{69}Ga	53	42
^{71}Ga	70	62
^{70}Ge	61	48
^{72}Ge	68	59
^{73}Ge	61	53
^{74}Ge	125	107
^{76}Ge	48	40
^{75}As	62	53
^{76}Se	307	262
^{77}Se	121	103
^{78}Se	231	198
^{80}Se	332	291

Table 4.10 (Cont.)

	Thermalised	Unthermalised
^{82}Se	0.09	0.08
^{79}Br	82	73
^{81}Br	210	193
^{80}Kr	1382	1182
^{82}Kr	733	653
^{83}Kr	232	206
^{84}Kr	380	343
^{86}Kr	7010	3501
^{85}Rb	161	144
^{87}Rb	8911	8372
^{86}Sr	697	864
^{87}Sr	256	537
^{88}Sr	1508	1743
^{89}Y	1150	1328
^{90}Zr	1359	1512
^{91}Zr	2003	2164
^{92}Zr	2900	3072
^{94}Zr	4339	4281
^{96}Zr	8199	7291
^{93}Nb	2075	2138
^{94}Mo	36	37
^{95}Mo	698	683
^{96}Mo	3225	3105
^{97}Mo	2086	1956
^{98}Mo	1764	1639
^{100}Mo	132	113

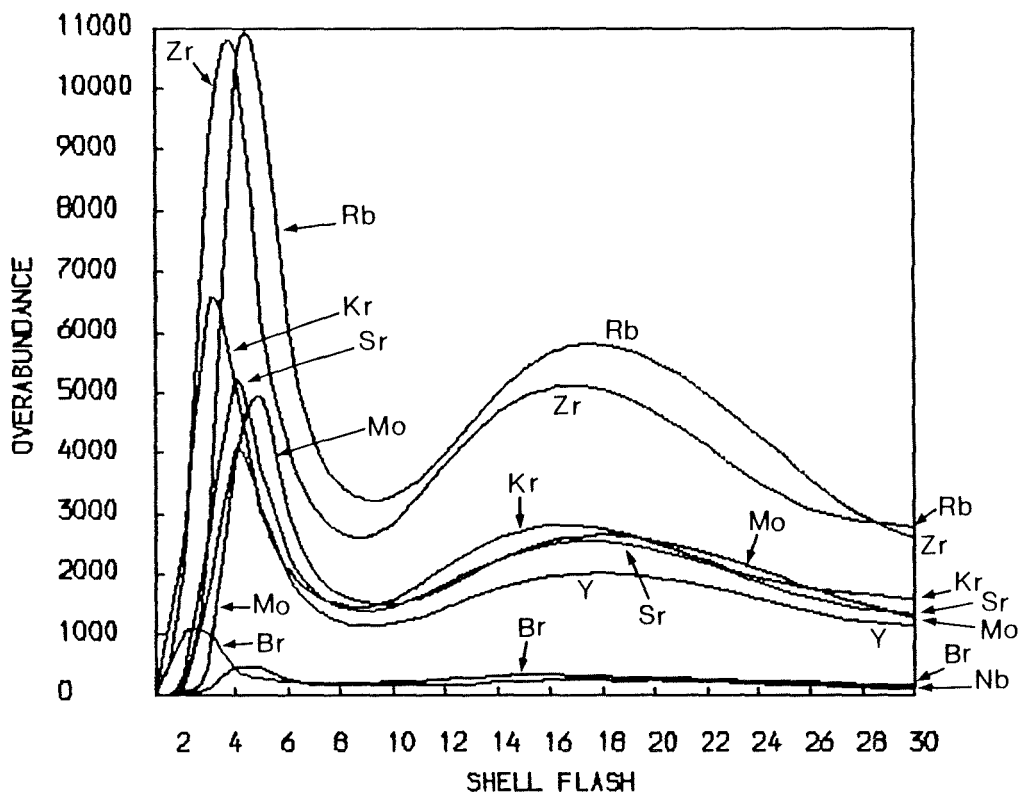
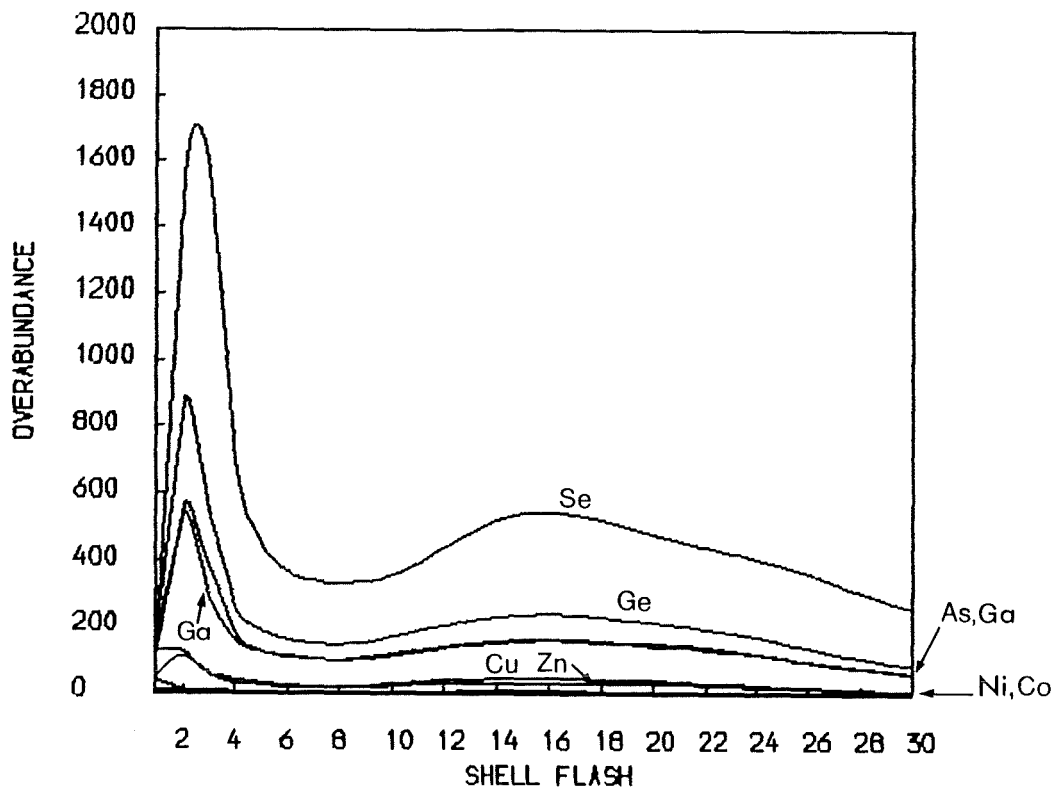


Figure 4.21a (top) and Figure 4.21b (bottom)
Repeated direct mixing for $r=0.85$, thermalised

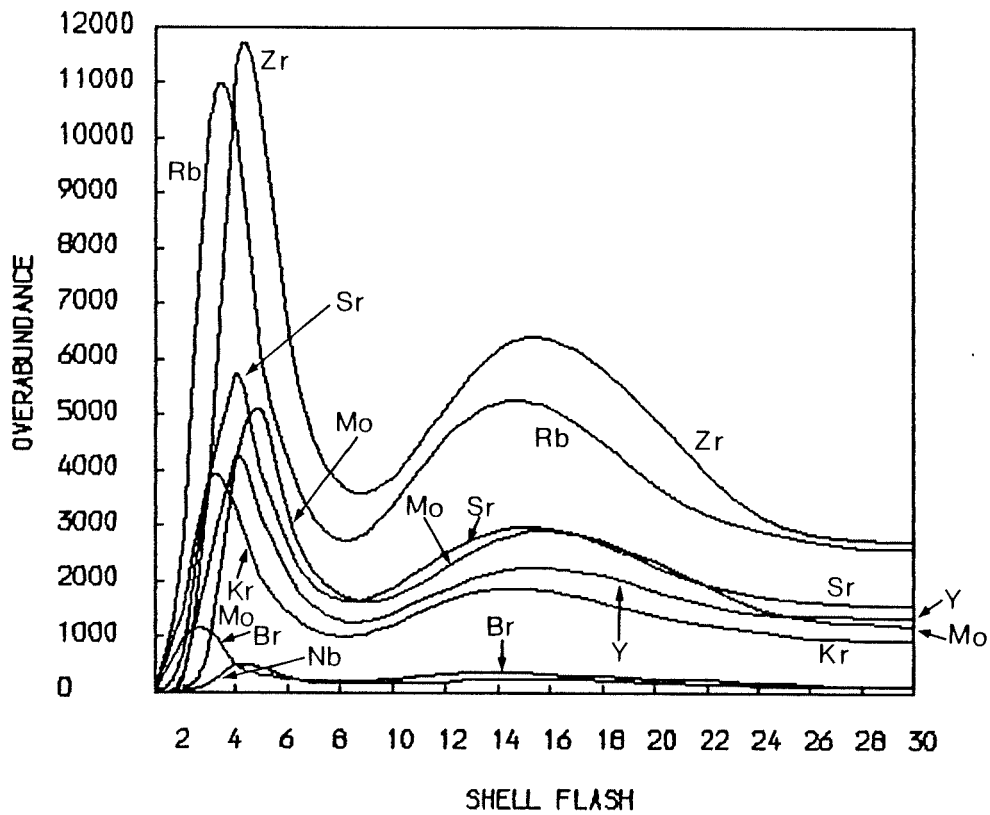
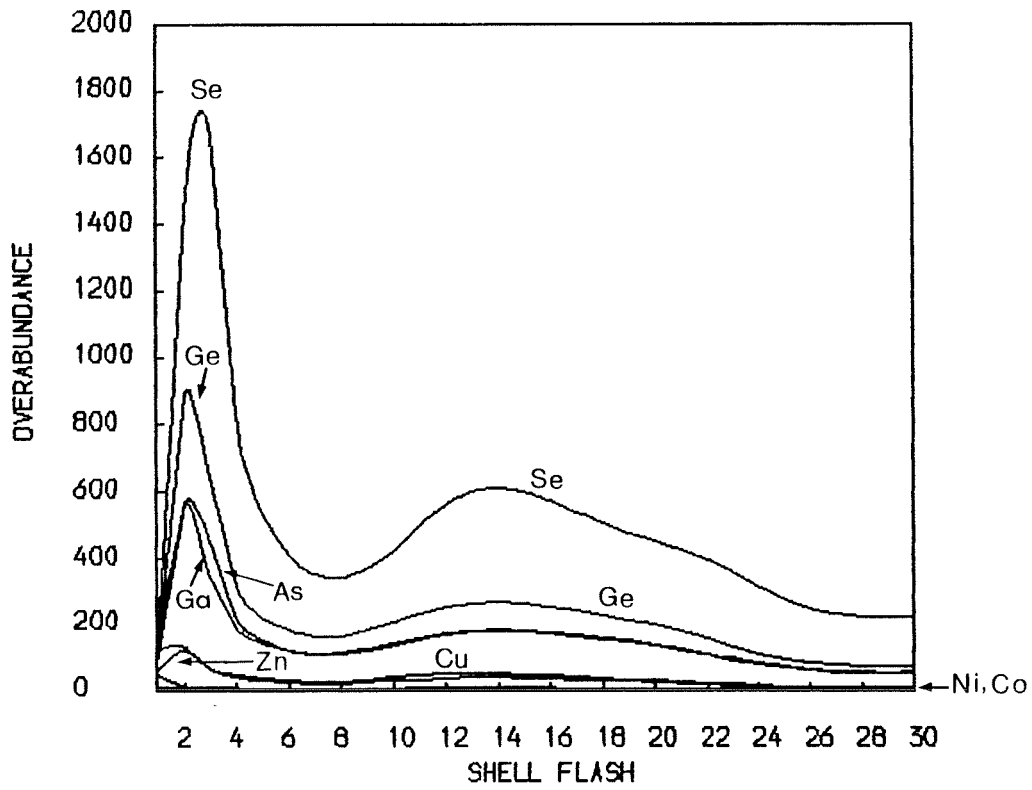


Figure 4.22a (top) and Figure 4.22b (bottom)
Repeated direct mixing for $r=0.85$, unthermalised

4.5) Conclusions

Calculations have been carried out in order to investigate the parameters influencing the enhancement of the heavy elements occurring at helium shell flashes. The inclusion of the phenomenon of intershell splitting on the enhancements was shown to be a significant effect which has to be taken into account in any detailed calculation. Calculations were carried out which investigated the enhancements resulting from a single mixing event. Such an event is predicted in the post-AGB stage of evolution. These calculations showed the importance of the degree of mixing and the resulting $^{13}\text{C}/^{14}\text{N}$ ratio on the s-process enhancements. The results of these calculations are listed in tables 4.5 and 4.6.

The enhancements resulting from repeated mixings arising from repeated helium shell flashes were also carried out. This is predicted to occur on the AGB phase of evolution. The importance of the fractional overlap of intershells, r , was stressed in these calculations. The results of these calculations are listed in tables 4.7 and 4.8. The most significant difference between the single mixing calculations and the repeated shell flash calculations is the distribution of the element abundances. This can be seen from a comparison of figures 4.23 and 4.24. Figure 4.23 shows the element abundances resulting from repeated mixing on the AGB with a fractional overlap $r=0.85$ (taken from column 4.13 of table 4.7). Figure 4.24 shows the element abundances resulting from a single mixing of $2.5 \times 10^{-5} M_{\odot}$ on the post-AGB (taken from model B of table 4.5). In both these figures the abundance was plotted on the $\text{Si}=10^6$ scale. As can be seen the two curves are quite distinct due to the different nature of the neutron

exposure occurring in each situation. High quality observations should be able to distinguish between the two abundance patterns and therefore determine the nature of any mixing event which actually occurred.

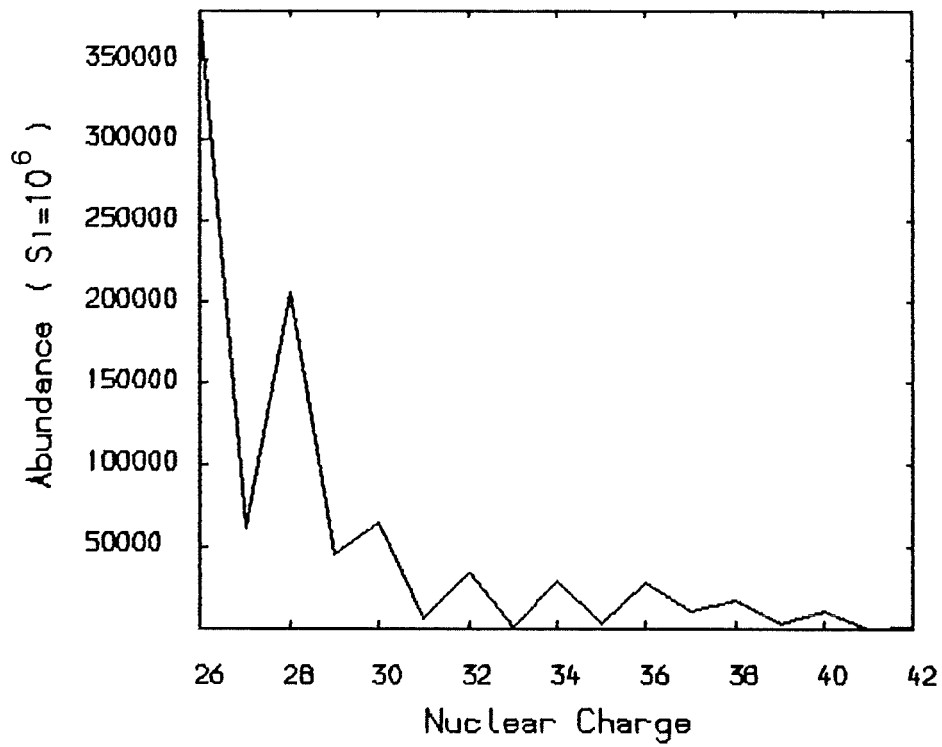


Figure 4.23 Repeated mixing distribution

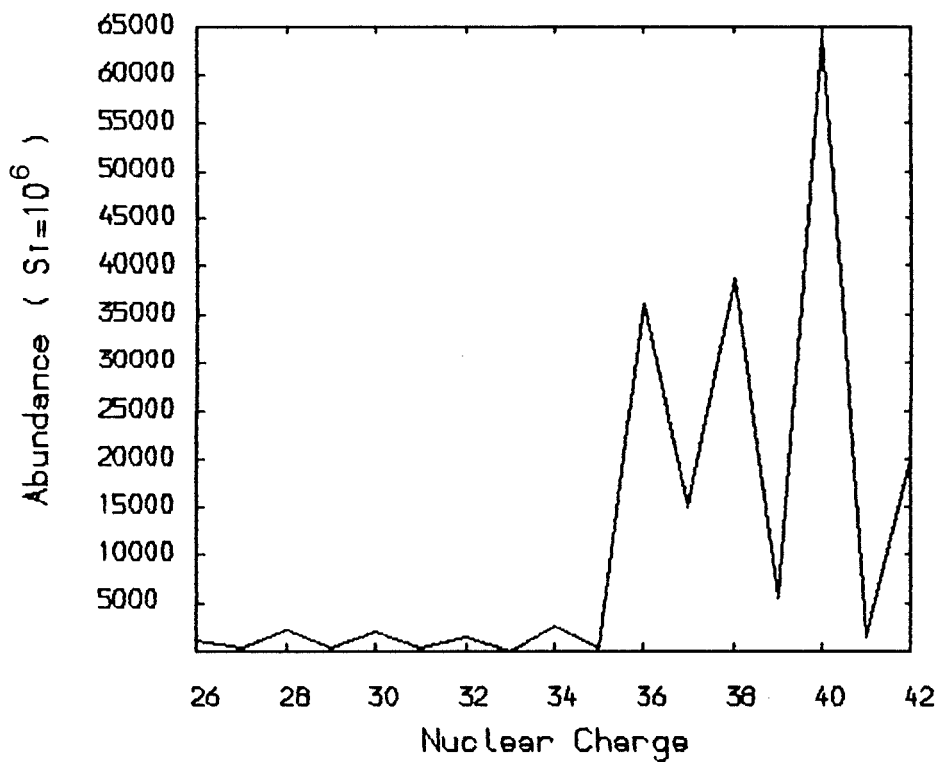


Figure 4.24 Single mixing distribution

CHAPTER 5. COARSE DIFFERENTIAL ABUNDANCE ANALYSIS OF U AQUARII

5.1) Discovery of Sr and Y Enhancements in U Aquarii

The spectral lines of any heavy element enhancements will not be observable in the visible spectrum of the EHe stars due to their hot effective temperatures. However, lines of some of these elements should be observable in the cooler atmospheres of the RCrB stars (T_{eff} of roughly 7000°K). Only two RCrB stars have been studied in detail. XX Cam and RCrB itself were found to have no significant heavy element synthesis by Cottrell and Lambert (1982) although Hunger et al. (1982) detected a Ba overabundance. However, Bond et al. (1979), while carrying out an objective prism survey in regions of high galactic latitude, discovered that the cool RCrB star U Aquarii (T_{eff} of roughly 6000°K) possessed large Sr and Y enhancements. They subsequently obtained higher dispersion ($47 \text{ \AA}/\text{mm}$) spectra of U Aquarii and found that this star possessed large Sr/Fe and Y/Fe but normal Ba/Fe ratios. From their data they concluded that Sr and Y were enhanced by about 100 times over their solar abundances with Ba having no significant enhancement, and that in order to explain such abundances the star must have undergone a single neutron exposure rather than the more usual exponentially weighted distribution of exposures thought to occur in other stars and believed to be responsible for the solar system abundances (Clayton et al. 1961). They concluded that the single neutron exposure had a value of $\tau = 0.6 \text{ mb}^{-1}$ and that this event most likely occurred due to hydrogen mixing at the helium core flash (Schwarzschild and Härm 1962).

This proposed scenario is in contradiction to the suggestion that the RCrB stars are remnant AGB stars (Schönberner 1979; Renzini 1979, 1981). Also the suggestion of a single exposure event in U Aquarii is perhaps slightly surprising since Ulrich (1973) showed that repeated mixing on the AGB would lead to an exponential distribution of neutron exposures. However, this is not to rule out a large single mixing on the AGB or at a post-AGB phase, which could give rise to a single neutron exposure. The importance of determining the nature of the single exposure is further discussed in chapter 6. Since the Sr and Y enhancements of U Aquarii had been estimated using somewhat low dispersion spectra, it was considered worthwhile to re-analyse this star using higher resolution data. The following sections are taken mainly from Malaney (1985).

5.2) Observations and Method of Analysis

Spectroscopic observations of U Aquarii were obtained by the author, when the star was at maximum, using the 3.9m Anglo-Australian Telescope (AAT) coupled with the Royal Greenwich Observatory (RGO) spectrograph and the Image Photon Counting System (IPCS) on 3 nights in April 1984. Spectra were obtained with a dispersion of 10 \AA/mm in the wavelength range 3900-4200 \AA . Further observations beyond 4200 \AA were not possible because of bad weather. However, the observed wavelength range contains the important SrII and YII lines of the star as well as some strong FeI and ZrII lines which are easily resolved at the 0.3 \AA resolution obtained. For comparison, observations over the same wavelength region were obtained for the non-variable hydrogen-deficient

carbon (HdC) star HD182040 (Warner 1967). Individual scans were combined into one spectrum for each star in order to maximise the signal-to-noise ratio. Wavelength calibration was achieved by comparison with the spectrum of the AAT copper-argon lamp recorded before, between and after pairs of stellar exposures. The data reduction was carried out using the Starlink package Spica. The reduced spectra of U Aquarii and HD182040 are shown in figures 5.1 and 5.2 respectively.

The wavelength region obtained is analysed in the same manner used by Bond et al. (1979). That is the Sr, Y and Zr abundances are determined differentially with respect to the HdC star HD182040. Justification for using this star in a differential analysis comes from the similarity in effective temperatures and surface gravities of these stars. Evidence for similarity in effective temperature is obtained from the UBV photometry of both stars shown in table 5.1. Before these measurements can be compared, interstellar reddening has to be accounted for. A rough estimate of the colour excess $E(B-V)$ is found from the constant gas to dust ratio formula of Burstein and Heiles (1978) which is based on neutral hydrogen column densities, N_H . The appropriate value of N_H for U Aquarii (galactic coordinates $l=39^\circ$, $b=-50^\circ$) and for HD182040 ($l=27^\circ$, $b=-13^\circ$) are found from the maps of Heiles (1976). Using this procedure $E(B-V)$ is determined as 0.25 for HD182040 and 0.02 for U Aquarii (extinction small in U Aquarii due to its high latitude). These values may be considered upper limits since although the stars are very distant (Warner 1967) they may not be completely beyond the matter causing the extinction. A value of the extinction at 2 kpc can be found from the interstellar reddening maps of FitzGerald (1968). These maps give $E(B-V)=0.2$ at 2 kpc in the direction of HD182040 which may be taken

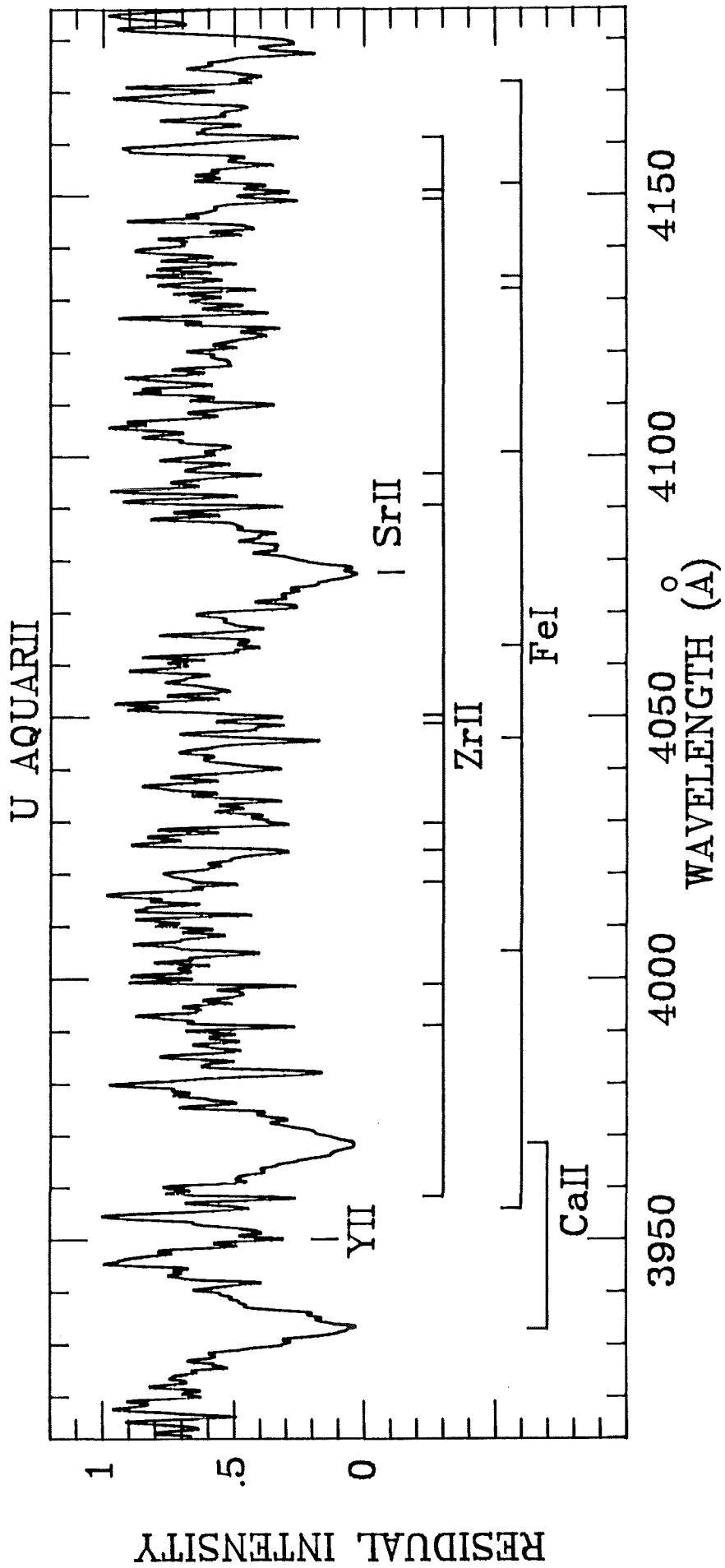


Figure 5.1 U Aquarii

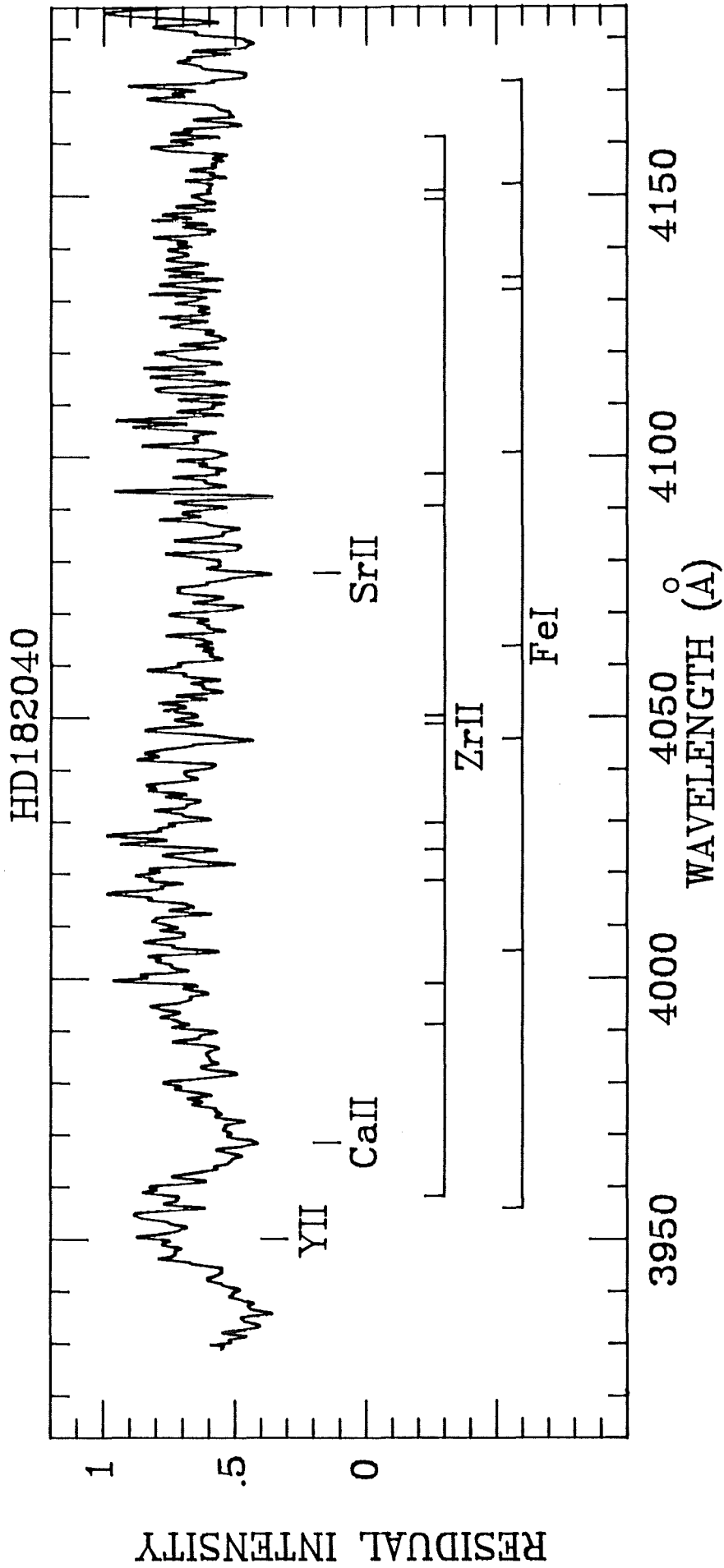


Figure 5.2 HD182040

as a lower limit to the extinction of HD182040. Assuming the ratio $E(U-B)/E(B-V)=0.7$ the estimated dereddened colours are then,

	(B-V)	(U-B)
U Aquarii	0.97 ^o	0.35 ^o
HD182040	0.84	0.45

Although the situation is further complicated by the possibility of intrinsic reddening in RCrB stars (Glass 1978) it is seen that both stars have similar colours and hence similar effective temperatures (the small difference in the colour values given above corresponds to a difference in T_{eff} between the stars of roughly 400^oK, Harris 1963). Evidence in support of equivalent surface gravities can be deduced from the small range of absolute magnitudes spanned by the HdC stars (Warner 1967, Feast 1975). In addition to the above arguments, Bond et al.(1979) found rough equality in the CaII/CaI ratio of both stars implying similar levels of ionisation and hence comparable gravities and effective temperatures of both stars. At the excitation temperature and electron pressure found for HD182040 by Warner (1967), it is found that the singly ionised state is the most important ionisation stage for Sr, Y and Zr in both stars. From this it is assumed that the difference in the SrII ion abundance between the two stars is equivalent to the difference in the total Sr element abundance between them, and likewise for Y and Zr. The error in the element ratios to be calculated on this assumption is for example about 0.4dex if the stars had a difference in excitation temperature of 400^oK. This error is due to the exclusion of differential ionisation effects in the following analysis.

The equivalent width W_ν of a stellar absorption line is given by the relation

$$W_\nu = \int_0^\infty A_\nu d\nu$$

where

$$A_\nu = 1 - F_\nu^l / F_\nu^c$$

and where F_ν^l and F_ν^c are the total surface flux in the line and continuum respectively. If it is assumed that line formation takes place in an isothermal layer in local thermodynamic equilibrium, then both the Milne-Eddington atmosphere (Milne 1921, 1930; Eddington 1917, 1926) and the Schuster-Schwarzschild atmosphere (Schuster 1905; Schwarzschild 1906) lead to the approximate relation

$$\frac{W_\nu}{2A_0 \Delta\nu_D} = \int_0^\infty \frac{b_0 H(a,b) db}{1 + b_0 H(a,b)} \quad (5.1)$$

In this relation A_0 is the central depth of the line, $\Delta\nu_D$ is the Doppler broadened full width to half maximum, and the function $H(a,b)$ is the Voigt (1913) function which expresses the behaviour of the absorption line coefficient as a function of the frequency ν . The damping parameter, a , is given by

$$a = \Gamma_d / (4\pi \Delta\nu_D)$$

where Γ_d is the damping constant for the line (this term is the sum of the damping constants for natural and collisional broadening), and

$$b_0 = \frac{\sqrt{\pi} e^2 f \lambda}{K m c V} N_{r,s} \quad (5.2)$$

where K is the continuum opacity, f is the oscillator strength, e is the

electronic charge, m the electronic mass and V the most probable velocity given by

$$V = (V_{\text{therm}}^2 + V_{\text{turb}}^2)^{1/2}$$

where V_{therm} is the most probable thermal velocity of an atom and V_{turb} the probable turbulent velocity of the stellar atmosphere. $N_{r,s}$ is the number of atoms in the s th state of the r th ionisation and is given by the Saha equation (Saha 1921)

$$N_{r,s} = \frac{N_r g \exp(-\chi/kT_{\text{exc}})}{U} \quad (5.3)$$

where N_r is the number of atoms in the r th stage of ionisation, g is the statistical weight of the s th level, U is the partition function and χ is the excitation potential of the s th level and k the Boltzmann constant. From equation 5.1 it is found that for $b_0 > 1000$ (i.e. strong lines on the damping part of the curve of growth) the equivalent width can be approximated by the relation

$$W_V = A_0 \Delta v_D (\pi a b_0)^{1/2}$$

Substituting from equations 5.2 and 5.3 we have

$$W_V = C (N_r/K)^{1/2}$$

where

$$C = A_0 \Delta v_D \left[\frac{16^{3/2} a e^2 f \lambda g \exp(-\chi/kT_{\text{exc}})}{m c V U} \right]^{1/2}$$

If the assumption is made that two stars, say star and comparison, with the same atmospheric parameters (i.e. T_{eff} , surface gravity and V_{turb}), are being analysed, then the ratio of equivalent widths for a given strong spectral line will be

$$\frac{W_{\text{star}}}{W_{\text{comp}}} = \left[\frac{N_r^{\text{star}} K_{\text{comp}}}{N_r^{\text{comp}} K_{\text{star}}} \right]^{1/2}$$

This follows due to the fact that the stellar and atomic parameters within the parameter C are assumed identical for the given spectral line seen in both stars.

Using the above assumptions, the simplification that the atmospheric parameters of U Aquarii and HD182040 are the same, the fact that the opacity is directly proportional to the number of contributing atoms, and since only lines lying on the square root part of the curve of growth will be used, the following expression for the ratio of equivalent widths of the same line in both stars is obtained,

$$\begin{aligned} \frac{W_{\text{el}}(\text{U Aqr})}{W_{\text{el}}(\text{HD182040})} &= \left[\frac{(N_{\text{el}}/N_{\text{op}})_{\text{U Aqr}}}{(N_{\text{el}}/N_{\text{op}})_{\text{HD182040}}} \right]^{1/2} \\ &= \left[\frac{(N_{\text{el}}/N_{\text{Fe}})_{\text{U Aqr}} (N_{\text{Fe}}/N_{\text{op}})_{\text{U Aqr}}}{(N_{\text{el}}/N_{\text{Fe}})_{\text{HD182040}} (N_{\text{Fe}}/N_{\text{op}})_{\text{HD182040}}} \right]^{1/2} \end{aligned}$$

where N_{op} is the number density of the species responsible for the continuous opacity. Given Warner's discussion for HD182040 this species is mainly carbon with a small amount of helium. The following expression is then obtained for the abundance of an element in U Aquarii relative to HD182040,

$$[N_{\text{el}}/N_{\text{Fe}}] = 2[W]_{\text{el}} - [N_{\text{Fe}}/N_{\text{op}}] \quad (5.4)$$

The square bracket notation of equation 5.4 represents the logarithmic

difference between U Aquarii and HD182040, i.e.

$$[X] = \log X_{U \text{ Aquarii}} - \log X_{HD182040}$$

It should be noted that such ratios will be close to the relative solar values since Warner (1967) concludes that all elements heavier than Na in HD182040 have essentially solar values relative to Fe.

5.3) Results

Lines identified in both stars and estimated to be least affected by error in the continuum placement and uncertainties due to blending are listed in table 5.2 along with their measured equivalent widths. For reference, measurements of those lines identified by Bond et al.(1979) are also listed.

In all late-type spectra, even at relatively high dispersion, line blending and the positioning of the continuum are the main sources of error in equivalent width measurements. This is even more so for U Aquarii and HD182040 due to their very crowded spectra. For table 5.2, lines were chosen for measurement on the basis that the major source of error was likely to be that due to continuum placement rather than blending. To estimate the error of the equivalent widths the following procedure was adopted. The continuum was placed by joining the highest points in the spectra at roughly 30 Å intervals. These points were then joined by a smooth curve. The continuum was then redrawn at a level approximately 5% higher than the first continuum. This new position of the continuum was the most extreme position which seemed reasonable. The equivalent width of each line was then measured for both continuum placements. The mean of these two measurements for

Table 5.1

UBV photometry of U Aquarii and HD182040

Star	V	B-V	U-B	Source
U Aquarii	11.25	0.99	0.38	Bond et al. 1975
U Aquarii	11.17	0.99	0.36	Kilkenny 1984
HD182040	7.01	1.09	0.63	Mendoza and Johnson 1965

Table 5.2

Equivalent Widths

Ion(multiplet)	Wavelength (Å)	Malaney ^o Eq. Widths (Å)		Bond et al. Eq. Widths (Å)	
		U Aqr	HD182040	U Aqr	HD182040
YII(1)	3950.36	1.0	0.2	1.6	<0.15
FeI(488)	3955.96	0.9	0.65		
ZrII(16)	3958.22	0.8	0.45		
CaII(1)	3968.47	10.0	8.0	9.8	16.1
ZrII(30)	3991.13	0.9	0.5		
ZrII(16)	3998.97	0.85	0.5		
FeI(43)	4005.24	0.9	0.65		
FeI(279)	4017.10	0.35	0.25		
ZrII(54)	4018.38	0.55	0.25		
ZrII(54)	4024.44	1.4	0.75		
ZrII(41)	4029.68	1.0	0.45		
FeI(43)	4045.82	1.75	1.45	1.4	1.6
ZrII(43)	4048.67	0.85	0.55		
ZrII(43)	4050.33	1.1	0.6		
FeI(43)	4063.60	0.7	0.6	0.7	1.2
SrII(1)	4077.71	12.5	2.1	11.4	2.4
ZrII(29)	4090.51	1.2	0.7		
ZrII(15)	4096.63	0.95	0.5		
FeI(18)	4100.74	0.55	0.55		
FeI(43)	4132.06	0.75	0.6		
FeI(697)	4134.43	0.7	0.7		
ZrII(41)	4149.20	1.15	0.7		
ZrII(42)	4150.97	1.35	0.7		
FeI(18)	4152.17	1.0	0.7		
FeI(695)	4153.91	0.8	0.7		
FeI(695)	4157.79	0.9	0.75		
ZrII(42)	4161.20	1.3	0.65		
FeI(650)	4171.90	0.7	0.55		

each line are the values listed in table 5.2. It was found that for most lines, the measurement of the low continuum line width was within 15% of the high continuum width. For some of the more weak lines ($W < 0.5 \text{ \AA}$) this discrepancy reached up to 20%. Such errors can be taken with some confidence as upper limits to the mean values listed in table 5.2.

The smallest equivalent width measured was that of YII 3950 in the comparison star. This is unfortunate since this is the only line available in the obtained spectra useful for the determination of the important Y abundance of U Aquarii. The measurement of this line in HD182040 is made even more difficult due to the presence nearby of relatively strong FeI lines. The procedure outlined above was used to determine the width of this line. However, due to the weakness of the line along with the nearby presence of FeI, the estimated error on this equivalent width was estimated somewhat higher at 25%. From their low resolution data, Bond et al. could only estimate an upper limit of 0.15 \AA on this line. Both their upper limit and the measurement presented here are compatible within their uncertainties. The measurement presented here allows an upper limit to be placed on the crucial Y abundance of U Aquarii. However, this upper limit should be treated with caution since the possibility remains of higher resolution data resolving the YII 3950 line into different components. It is clear that an abundance determination based on one poorly measured line is hardly ideal, and further observations will be required.

The values of $[N_{\text{Fe}}/N_{\text{op}}]=2[W]_{\text{el}}$ which are calculated for each FeI line using equation 5.4 are listed in table 5.3. The mean value of $[N_{\text{Fe}}/N_{\text{op}}]=0.18 \pm 0.1$ is larger than the value found for the same quantity by Bond et al. of $[N_{\text{Fe}}/N_{\text{op}}]=-0.3 \pm 0.2$. The difference could be attributed to the high dispersion data resolving the FeI 4063 line in the low dispersion data into two separate lines. Using the new value of $[N_{\text{Fe}}/N_{\text{op}}]$, $[N_{\text{el}}/N_{\text{Fe}}]$ is calculated using equation 5.4 for each of the other lines in table 5.2. The mean value for each element is given in table 5.4. The errors are calculated from the estimated error on the equivalent widths, or in the case of Zr from the standard error on the mean value of the 13 ZrII lines. No error due to differential ionisation is included in table 5.4.

An important line with regard to obtaining information on the nature of the neutron exposure in U Aquarii is the BaII 4554 line. Unfortunately the observations presented here did not extend to this wavelength region. However, Drs. D.Kilkenny and H.J.Walker have supplied the author with an equivalent width measurement for this line of 2.1 \AA taken from their 30 \AA/mm dispersion spectra of U Aquarii obtained recently at the South African Astronomical Observatory. Bond et al. (1979) measured an equivalent width of 1.4 \AA for this line from their spectra. If a mean value of $1.8 \pm 0.4 \text{ \AA}$ is taken for this line along with the 1.7 \AA measurement for the same line in HD182040 by Bond et al., and using the value of $[N_{\text{Fe}}/N_{\text{op}}]$ calculated here, we find $[\text{Ba}/\text{Fe}]=-0.1 \pm 0.5$. Of course this method of using equivalent widths obtained by different observers on different instruments is hardly ideal. This is reflected by the large error on the $[\text{Ba}/\text{Fe}]$ ratio. In summary, the following ratios shown in table 5.5 are found

Table 5.3

[$N_{\text{Fe}}/N_{\text{op}}$] For FeI Lines

FeI Line	[$N_{\text{Fe}}/N_{\text{op}}$]
3955.96	0.28
4005.24	0.28
4017.10	0.26
4045.82	0.16
4063.60	0.13
4100.74	0.0
4132.06	0.2
4134.43	0.0
4152.17	0.3
4153.91	0.12
4157.79	0.16
4171.90	0.21

Table 5.4

Logarithmic Abundances

Element	[$N_{\text{el}}/N_{\text{Fe}}$]
Ca	0.0 +/- 0.2
Sr	1.4 +/- 0.2
Y	1.2 +/- 0.4
Zr	0.4 +/- 0.15

Table 5.5

[El/Fe] Ratios Of U Aquarii Relative To HD182040

Element	[El/Fe] Malaney	[El/Fe] Bond et al.
Ca	0.0 (+/-0.5)	-0.1
Sr	1.4 (+/-0.5)	1.7
Y	1.2 (+/-0.6)	>2.4
Zr	0.4 (+/-0.4)	
Ba	-0.1 (+/-0.6)	-0.1

Table 5.6

Element Ratios In U Aquarii Compared To Ratios From An Exponential Exposure With $L_0=0.1\text{mb}^{-1}$

Element Ratio	U Aquarii	$L_0=0.1\text{mb}^{-1}$
log (Sr/Fe)	-3.1 (+/-0.5)	-2.9
log (Y/Fe)	-4.1 (+/-0.6)	-3.7
log (Zr/Fe)	-4.4 (+/-0.4)	-4.1
log (Sr/Ba)	2.2 (+/-0.6)	2.0
log (Y/Ba)	1.3 (+/-0.6)	1.2
log (Zr/Ba)	0.8 (+/-0.6)	1.0

in U Aquarii relative to HD182040. The errors are shown in the parenthesis (including an estimated error due to differential ionisation effects). Shown for comparison are the values from Bond et al. (1979)

It is concluded that Sr and Y are enhanced in U Aquarii, but by smaller factors than previously believed. Zr is found to be only slightly enhanced.

5.4) Conclusions

In light of the significant changes in the estimated values of the Sr/Fe and Y/Fe ratios as well as the Zr/Fe ratio having also now been determined, the question regarding the nature of the neutron exposure in U Aquarii is re-investigated. With the new measurements presented here it is now possible to represent the heavy element distribution of this star to a weak exponential distribution of exposures with a weighted function of the form

$$G \exp(-\tau/\tau_0)$$

where G is a constant, τ is the neutron exposure in mb^{-1} , and τ_0 is a constant of the weighting function in mb^{-1} which describes the resulting distribution of the elements. The fact that such a distribution of exposures can now fit the observations can be seen from figure 5.3, where the exact solution of Ulrich (1973) and Clayton and Ward (1974) using the above weighting function is shown for different values of parameter τ_0 . The absolute element ratios within U Aquarii (assuming Cameron 1981 solar abundances in HD182040) are shown in table 5.6 alongside the ratios taken from the $\tau_0=0.1\text{mb}^{-1}$ curve of figure 5.3. It

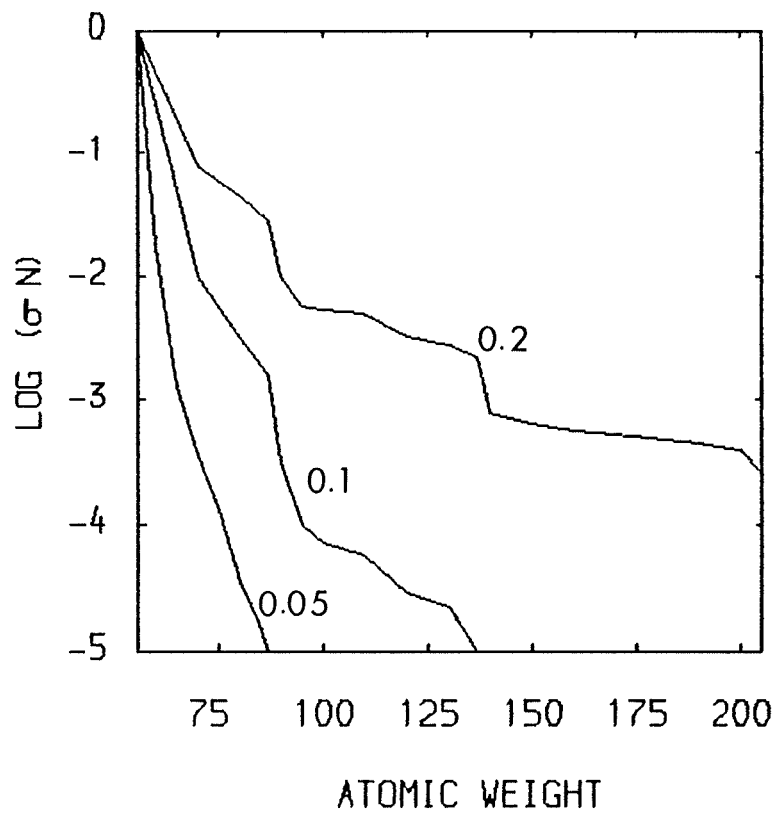


Figure 5.3 Abundances from exponential distribution of neutron exposures

can be seen that within the observational errors the abundance distribution of U Aquarii can be represented by an exponentially weighted distribution of exposures characterised by $\tau_0 = 0.1 \text{ mb}^{-1}$ (of course these are lower limits to the errors due to assumption of solar abundances in HD182040).

The discussion given by Ulrich (1973) a value of $\tau_0 = 0.1 \text{ mb}^{-1}$ is equivalent to a weak exposure, where the ratio of neutrons available for capture on ^{56}Fe to the number of ^{56}Fe seed is a constant throughout the exposure period and is given by N_n/N_{Fe} roughly equal to 1.5. The build up to heavier elements is then caused by decreasing fractions of the exposed material remaining in the neutron flux for longer periods of time. Such discussions as these are usually given in the context of the asymptotic production of heavy elements due to repeating helium shell flashes on the AGB, which lead naturally to an exponentially weighted distribution of neutron exposures (Ulrich 1973). In this context the value of $\tau_0 = 0.1 \text{ mb}^{-1}$ corresponds to the matter remaining in the intershell convective region of an AGB star undergoing 1.5 neutron captures per ^{56}Fe seed per shell flash. The calculations of chapter 3 show that $2.5 \times 10^{-6} M_\odot$ of envelope mixing into the intershell convective region of a low-mass AGB star can give rise to roughly 2 neutron captures per ^{56}Fe at each shell flash. Thus this amount of mixing at successive shell flashes (up to 34 shell flashes were found to occur as the star rises the AGB in the models of Schönberner 1979) would give rise to the heavy element distribution seen in U Aquarii. Such a small amount of mixing at each shell flash could arise from the mixing mechanism of Iben and Renzini (1982a,b), and a detailed comparison of the observations with the repeated shell flash calculations of chapter

4, which employ this mixing mechanism, will be given in the following chapter.

These new measurements have thus produced an alternative scenario with regard to the neutron exposure event in U Aquarii. Previous to these measurements presented here, it seemed that only a single neutron exposure could explain the observed enhancements of this star, and that an exponential distribution could not reproduce the enhancements. However, it has now been shown that, within the observational uncertainties, both scenarios are possible. Knowledge of the type of exposure which has occurred in U Aquarii would enable constraints to be placed on any proposed model of its evolution. This point is further discussed in chapter 6. In order to determine the nature of the exposure event in this star, a more accurate determination of its heavy element abundance enhancements is required. Accurate abundance determinations could be achieved by high resolution observations covering a wider range of the spectral region and by utilising model atmosphere and spectral synthesis techniques. However, due to the peculiar properties of a helium dominated atmosphere, substantial difficulties have to be overcome in order to use such techniques properly. The difficulties of analysing the spectra from a helium atmosphere are further discussed in chapter 8 where preliminary model atmosphere and synthesis calculations are carried out.

CHAPTER 6. THE ORIGIN OF U AQUARII

6.1) Hydrogen Deficiency

As stated in chapter 1, the origin of the extreme hydrogen deficiency of the RCrB stars remains unsolved. Mass loss via stellar winds on the AGB or post-AGB fails to account for such a deficiency since the effect of such mass loss is to accelerate the blueward movement of the star (Härm and Schwarzschild 1975; Schönberner 1979). Also, large scale mass ejection on the AGB raises another problem. If such an ejection took place, a compact remnant object would remain. It is known, however, that the energy released by a helium shell flash is insufficient to expand the intershell region to the large radii typical of RCrB stars (Schönberner 1979). It appears more likely that the disappearance of the original hydrogen envelope is connected in some manner to a mixing mechanism whereby the hydrogen envelope has been mixed into the stellar interior and destroyed. The heavy element enhancements observed in U Aquarii are good evidence of such an event having indeed occurred.

As already discussed the mixing of hydrogen into the intershell zone of a low-mass AGB star raises substantial theoretical difficulties. The problem of hydrogen deficiency is amplified even more when the envelope mass, M_e , of such an AGB star is considered (typically $M_e = 0.04M_\odot$). No calculations at the present time can accommodate the mixing of such a large amount of envelope material on the AGB. The main problem in attempting to simulate such an event in any calculation is well known, and has been discussed in many papers (e.g. Iben 1976, 1977;

Schönberner 1979). The lack of any mixing in the calculations arises from an entropy barrier at the hydrogen-helium interface, with the main cause of the jump at the interface being due to radiation pressure from the hydrogen burning region. During the long interpulse period, when the energy generation by the helium burning reactions drops to a negligible value, there is a rapid rise in the ratio of the radiation pressure to gas pressure through the hydrogen-helium interface. During the pulse all the energy liberated by the helium burning reactions is converted locally into thermal energy and into the work of expansion, thereby raising the entropy of the matter in the intershell region. However, this increase in entropy is never quite high enough to overcome the barrier set up during the interpulse phase. The only study to show penetration of the convective intershell zone with the hydrogen envelope was that of Schwarzschild and Härm (1967). This can be explained by the neglect of radiation pressure in their calculations.

If large scale mixing does indeed occur on the low-mass AGB, then some fundamental processes must be found which has hitherto not been included in any calculations. Iben and Renzini (1982a,b) have in fact discovered such a process which allows small scale mixing on the AGB. In this scenario, carbon generated by a previous flash sets up a semi-convective region at the top of the intershell region. This new region of convection mixes into the high lying levels of the intershell matter which has been processed through a hydrogen burning shell. During the next helium flash this matter (i.e. CNO isotopes) is swept down by the normal convection region to the hot regions of the intershell. Although this effect may be important with regard to heavy element enhancement, the amount of mixing found to occur is too small to offer an explanation for the disappearance of the large hydrogen

envelope of an AGB star.

A possible mixing mechanism when the star is in a post-AGB phase has been discussed by Renzini (1979,1981) and Schönberner (1979). This arises as a consequence of a final helium shell flash as the star approaches the white-dwarf regime. In this phase of stellar evolution the star has a very small envelope mass ($M_e < 2.7 \times 10^{-4} M_\odot$) due to mass loss via stellar winds. At this stage the hydrogen burning has diminished relative to its strength on the AGB and as a consequence the entropy barrier, discussed earlier, also diminishes. This allows penetration of the convective intershell zone, arising from the final helium flash, to reach the small remaining envelope. Renzini (1979,1981) has suggested that the entire remaining hydrogen envelope is engulfed into the intershell region as a result of the final helium flash, with the energy generated by the hydrogen burning causing the star to loop back to the low temperature high luminosity region of the H.R. diagram. This scenario is shown in figure 6.1. Renzini further suggests this scenario offers an explanation of the hydrogen deficiency of the RCrB stars. However, a problem arises due to the rapid evolutionary timescales of such a loop. The time spent on one of these loops is 1000 years, 170 years and only 20 years for stars with masses of $0.6 M_\odot$, $0.8 M_\odot$ and $1.2 M_\odot$ respectively. This then implies that the RCrB stars have masses $< 0.6 M_\odot$. Or alternatively, as suggested by Iben et al. (1983), the ingestion of the small remaining envelope is delayed by some unknown mechanism. Such a delay causes the loop to be of much longer duration (> 2000 years) after the mixing finally occurs. This is illustrated in figure 6.1 (lower loop). A final shell flash scenario for the production of RCrB stars also suffers from the lack of any proper calculations. This being due to the problems in

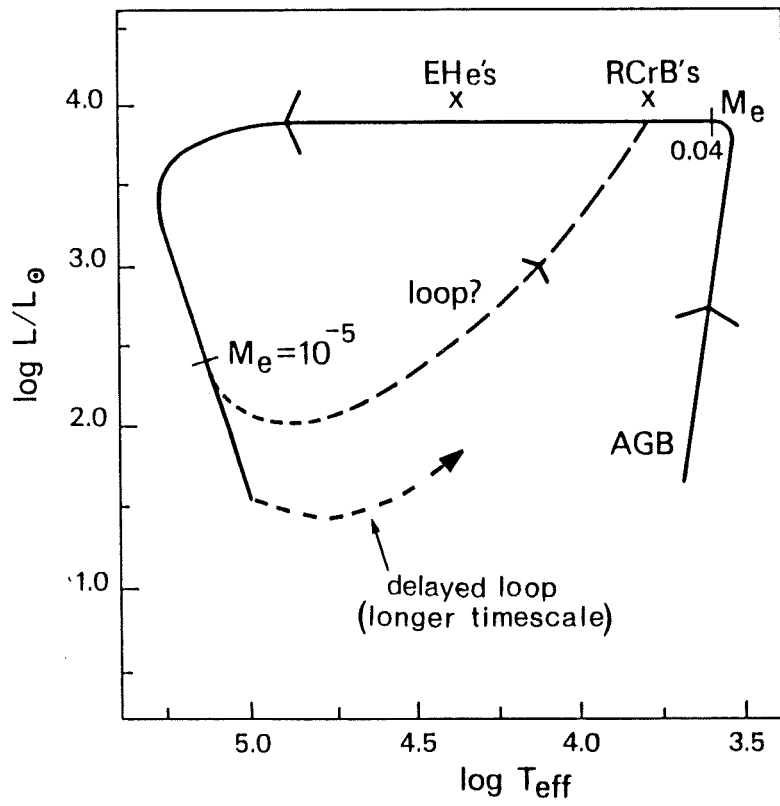


Figure 6.1 Loop mechanism for RCrB stars

properly treating the large amount of energy generation in an expanding convective region. Renzini (1982) identifies the peculiar giant FG Sagittae (Langer et al. 1974) as currently passing through the loop mechanism phase. This star is observed to be expanding and under going cooling. It was also observed to have been undergoing significant heavy element enhancements, the size of the enhancements increasing with time. These increases were observed during 1965-1978, but since 1978 the enhancements have been found to be constant (Acker 1983). Renzini identifies this star as a precursor of an RCrB star.

Most of the explanations regarding the origin of the RCrB stars have been mostly associated with the AGB or post-AGB phases. However, another phase of stellar evolution where hydrogen mixing may occur is at the helium core flash (Schwarzschild and Selberg 1962; Schwarzschild and Härm 1962; Härm and Schwarzschild 1964,1965; Thomas 1967,1970; Demarque and Mengel 1971). This occurs just prior to the horizontal branch when helium ignites for the first time in the degenerate core of a star at the tip of the first red giant branch. At the present time it is not clear whether significant envelope mixing into the stellar interior takes place at this point in the stars evolution (Cole and Deupree 1980,1981; Deupree and Cole 1983; Deupree 1984a). The recent work of Deupree (1984b) indicates that substantial mixing may in fact occur. The nucleosynthesis occurring at the helium core flash is likely to proceed at lower temperatures relative to the synthesis at the AGB or post-AGB phase (private comm. Deupree). Few evolutionary calculations have been carried out which investigate the future evolution of a star which has undergone significant envelope mixing at the helium core flash. The little work that has been carried out (eg. Rood 1972)

indicate that the star could become hydrogen depleted and climb to the large radii and high luminosities observed for the RCrB stars.

In this chapter, comparison with the calculated heavy element enhancements of chapter 4 are compared with the observed heavy element enhancements of U Aquarii presented in chapter 5. Calculations based on cooler temperature regions are also presented here and compared with the observations. Since the calculations cover conditions corresponding to the AGB phase, the post-AGB phase as well as conditions prevailing at the helium core flash, then it may be possible to gain information as to how, and at what phase in its evolution, the hydrogen deficiency of U Aquarii occurred by a comparison of the observed enhancements with calculated enhancements under differing temperature-density conditions.

6.2) AGB and Post-AGB Comparison

In this section an attempt is made to relate the above calculations to the observations of heavy element enhancements seen in the cool RCrB star U Aquarii. The observations presented in chapter 5 gave (in the usual bracket notation) $[\text{Sr}/\text{Fe}] = 1.4$, $[\text{Y}/\text{Fe}] = 1.2$ and $[\text{Zr}/\text{Fe}] = 0.4$. However, these values contain large errors of ± 0.5 , 0.6 and 0.4 respectively (these errors are lower limits due to the assumption of solar abundances in the comparison star). To compare the calculations with these observations a dilution of the irradiated material with envelope material of solar abundances (Cameron 1981) is carried out. In the equations to follow El_{star} is the observed number fraction of the element El, El_{I} is the calculated number fraction of the element found in the intershell, El_{\odot} is the solar abundance number fraction of the

element, El_c is the calculated enhancement of the element in the intershell i.e.

$$El_c = El_I / El_o$$

and d is the dilution factor given by

$$d = (M_1 + M_2) / M_1$$

where M_1 is the mass of the irradiated material and M_2 is the mass of the envelope. Now

$$\frac{El_{star}}{El_o} = \frac{(1/d) El_I + (1-1/d) El_o}{El_o} = \frac{1}{d} El_c + 1 - (1/d)$$

and since

$$\begin{aligned} [El/Fe] &= \log (El/Fe)_{star} - \log (El/Fe)_o \\ &= \log (El_{star}/El_o) - \log (Fe_{star}/Fe_o) \end{aligned}$$

we have

$$[El/Fe] = \log \{ (1/d) El_c + 1 - (1/d) \} - \log \{ (1/d) Fe_c + 1 - (1/d) \} \quad (6.1)$$

Using equation 6.1 the $[Sr/Fe]$, $[Y/Fe]$ and $[Zr/Fe]$ ratios for different dilution factors can then be calculated for any heavy element enhancement calculations presented in chapter 4. By doing this a comparison with the observed enhancements of U Aquarii may lead to information on the particular mixing model relevant to the actual mixing

event of U Aquarii. The two most plausible mixing mechanisms of chapter 4 will be further investigated here in order to carry out such a comparison. These mechanisms (both of which may have occurred in U Aquarii) are, a) the single mixing of a small remaining envelope ($M_e < 2.7 \times 10^{-4} M_\odot$) on the post-AGB (Renzini 1979, 1981), and b) repeated small scale mixing by the mixing mechanism proposed by Iben and Renzini (1982a, b).

For mixing mechanism a) the most realistic models of this event are those models of chapter 4 which investigated the mixing of up to $2.5 \times 10^{-4} M_\odot$ envelope material at an ingestion rate of $10^{-3} M_\odot/\text{year}$ into an intershell with $T_b = 2.75 \times 10^8 \text{ K}$ (since this intershell corresponds to a final helium shell flash on the post-AGB). The effect of intershell splitting (Sweigart 1974) would also be included in these models. Such models correspond to models B, C, D, E, F and G of table 4.5. The [Sr/Fe], [Y/Fe] and [Zr/Fe] ratios as a function of d are plotted in figures 6.2 to 6.5 for some of these models. Figure 6.2 corresponds to model B, figure 6.3 corresponds to model C, figure 6.4 corresponds to model E and figure 6.5 corresponds to model G. For a more direct comparison of the different models tables 6.1a and 6.1b list the calculated ratios for a dilution factors of $d=10$ and $d=30$ respectively for models B, C, E and G. Also listed is the observed abundances. An important point to note from tables 6.1a and 6.1b is that the [Zr/Fe] ratio is always at least the same value of [Y/Fe]. From the figures 6.2 to 6.5 it can be seen that this situation always prevails regardless of the dilution factor, and from equation 6.1 it can be seen that for a Zr enhancement greater than a Y enhancement, then $[\text{Zr/Fe}] > [\text{Y/Fe}]$ for all values of d (the opposite i.e. $[\text{Zr/Fe}] < [\text{Y/Fe}]$ was found only for very weak exposures, but this also results in very small enhancements).

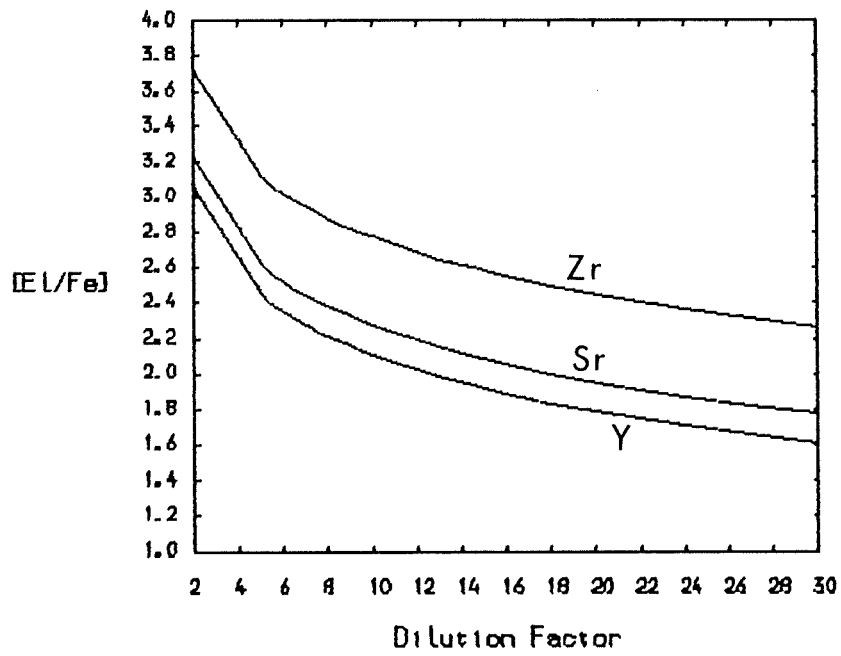


Figure 6.2 Model B ratios as a function of d

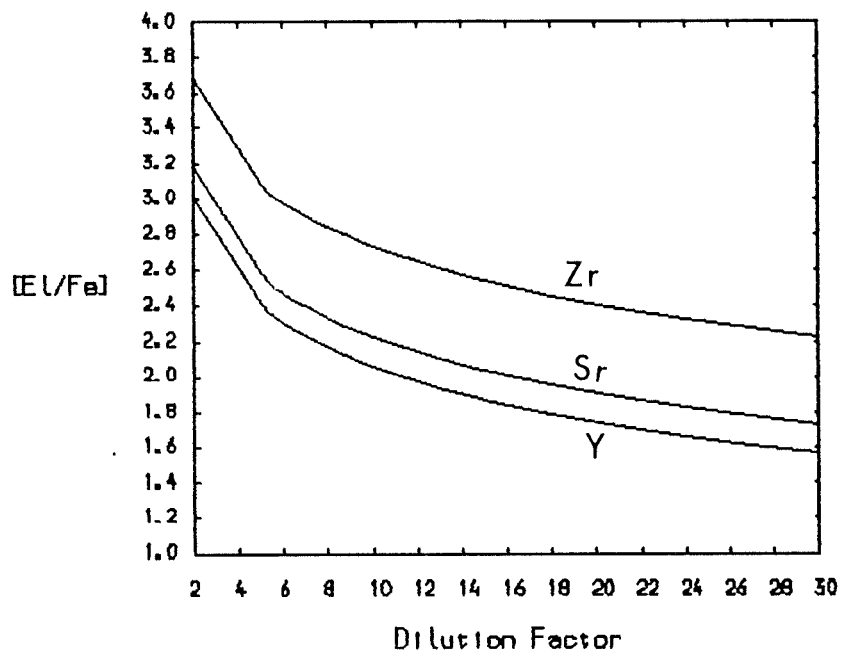


Figure 6.3 Model C ratios as a function of d

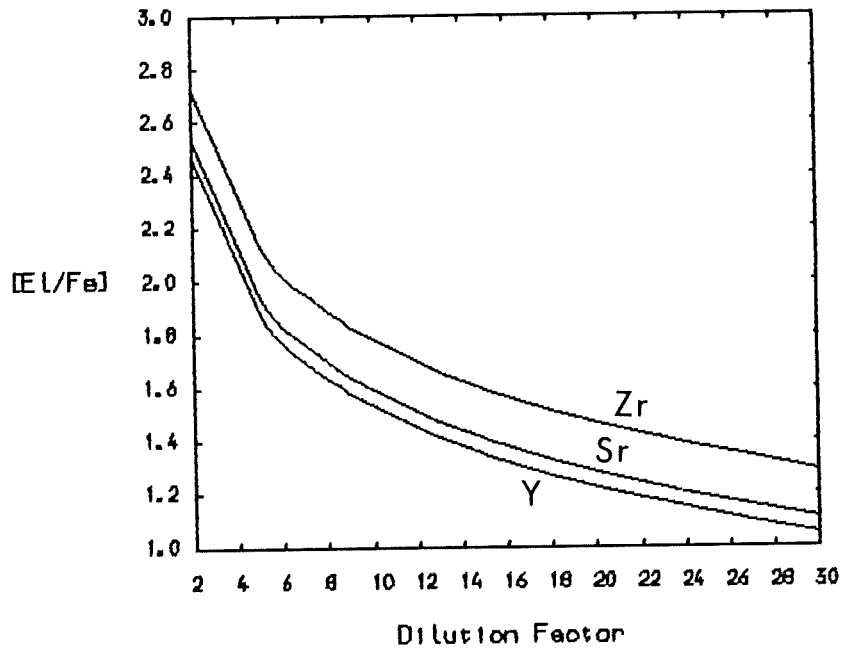


Figure 6.4 Model E ratios as a function of d

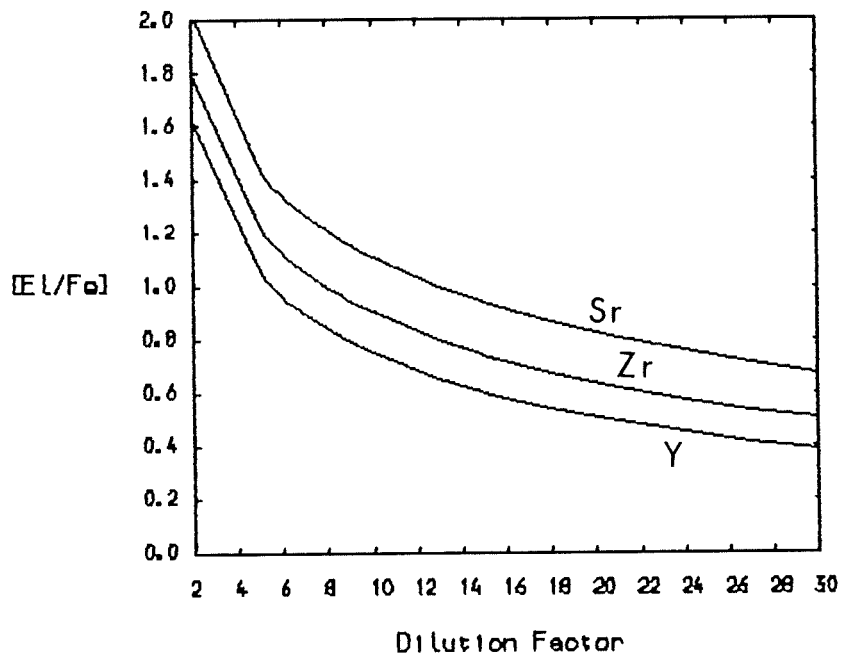


Figure 6.5 Model G ratios as a function of d

For the second most plausible mixing mechanism b), figure 6.6 plots the $[Sr/Fe]$, $[Y/Fe]$ and $[Zr/Fe]$ ratios for the calculation corresponding to the repeating shell flash calculation of table 4.8 where $r=0.85$ (column 4.13) and the initial Fe abundance is taken as solar. Figure 6.7 shows the same ratios as a function for d again for $r=0.85$ but in this case where the initial Fe abundance was taken as 0.1 of the solar value (column 4.18 of table 4.5). For a direct comparison table 6.2 lists the ratios for $d=10$ and $d=30$ for both initial Fe abundances. Again it can be seen that the $[Zr/Fe]$ always has a value of at least that of $[Y/Fe]$, with the low initial Fe calculations giving rise to the largest Zr enhancements relative to Sr and Y.

It is clear that for all the calculations presented in chapter 4 where the heavy element build up in low-mass AGB and post-AGB stars was simulated the resulting Sr, Y and Zr enhancements are always such that the $[Zr/Fe]$ ratio is never significantly below the $[Sr/Fe]$ and $[Y/Fe]$ values. Further, since different mixing models were used in these calculations it can be stated that this result is independent of the method of simulating the nucleosynthesis and that it is entirely due to the conditions of the intershell at the AGB, post-AGB phase of evolution. If the low observed Zr abundance relative to Sr and Y is a real effect (the large errors on these observations should be stressed here) then the calculated abundances raise a problem. This discrepancy in the Zr/Y and Zr/Sr ratios exists in all the calculations presented in chapter 4. For the discrepancy to be overcome a large Zr enhancement relative to the Y and Sr enhancements is required. This is not found in the calculations. Also, calculations with changes in the neutron cross

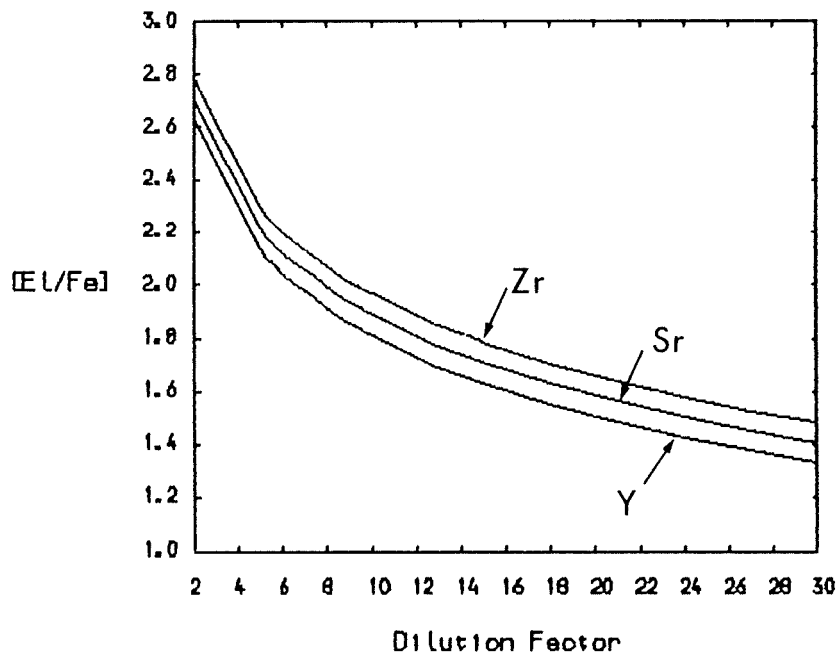


Figure 6.6 Repeated mixing for $r=0.85$, as a function of d (solar seed)

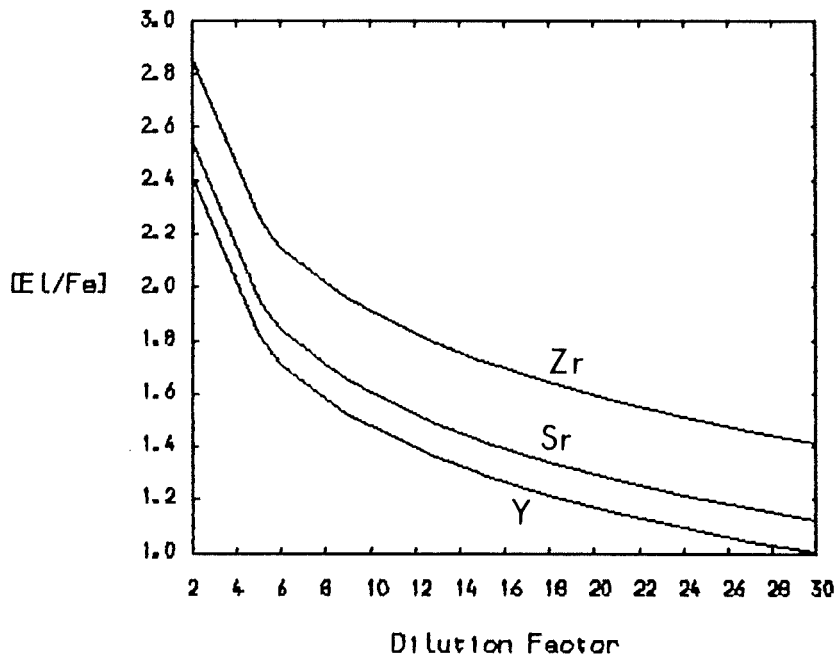


Figure 6.7 Repeated mixing for $r=0.85$, as a function of d (0.1 solar seed)

Table 6.1a

Comparison of models of table 4.5 for d=10

Model	B	C	E	G	Observed
[Sr/Fe]	2.28	2.23	1.59	1.1	1.4
[Y/Fe]	2.11	2.06	1.53	0.75	1.2
[Zr/Fe]	2.77	2.73	1.78	0.9	0.4

Table 6.1b

Comparison of models of table 4.5 for d=30

Model	B	C	E	G	Observed
[Sr/Fe]	1.78	1.75	1.11	0.68	1.4
[Y/Fe]	1.60	1.58	1.05	0.39	1.2
[Zr/Fe]	2.28	2.23	1.30	0.51	0.4

Table 6.2

Comparison of models for repeated shell flash calculations

Dilution	10	10	30	30
Initial Seed	Fe	Fe/10	Fe	Fe/10
[Sr/Fe]	1.89	1.61	1.41	1.12
[Y/Fe]	1.81	1.48	1.33	1.00
[Zr/Fe]	1.97	1.91	1.48	1.41

Table 6.3

Observed FG Sagittae enhancements

Date	May '65	July '69	Aug '70	Sep '71	Aug '72
[Sr/Fe]	0.87::				
[Y/Fe]	0.64	1.34:	1.38	1.69	1.59:
[Zr/Fe]	0.73	1.16	1.28	1.43	1.55

sections and the beta decay rates of all the isotopes in the network, by up to factors of ten (simulating the errors on these nuclear parameters), failed to remove the discrepancy. In view of this it is concluded that the only way the calculations and the observations can be compatible is if a more accurate determination of the abundances in U Aquarii show that $[Zr/Fe]$ has a value similar to $[Sr/Fe]$ and $[Y/Fe]$. Of course the large errors on the present observed values do not rule out this possibility.

6.3) Nature of the Neutron Exposure

The correct determination of the nature of the neutron exposure event that occurred in U Aquarii, as already discussed in chapter 5, would be an important step in determining the mixing mechanism which occurred in this star. In chapter 5 it was discussed how it was previously believed that only a single exposure event could have led to the observed heavy element enhancements of U Aquarii. However, it was shown that from the new observations presented there that an exponential distribution of neutron exposures could also have led to the observed distribution of heavy elements. This was a significant step since it meant that the repeated shell flash mixing scenario could still be the mixing mechanism responsible, whereas previous to this this mechanism would have to have been ruled out.

With regard to a single neutron exposure arising from a single mixing on the post-AGB, there has been little or no detailed work carried out which investigates the nucleosynthesis occurring in an expanding and cooling convective region. Such a situation could occur following a final helium shell flash on the post-AGB. The lack of calculations in this area reflects the large difficulties in coupling a nuclear reaction network directly with the convective motions of the surrounding matter. However, if a single mixing of the remaining small envelope has occurred at the post-AGB phase then it is likely that the resulting distribution of the heavy elements produced will resemble more closely that expected from a single neutron exposure. It is then interesting to compare the abundances calculated from the single mixing calculation with those of the repeated mixing calculations to see if any observational test can be found in order that the nature of the mixing mechanism can be determined. If the single mixing mechanism occurred then it is clear that some dilution of exposed material into unexposed material will have occurred due to there being no significant depletion of the Fe abundance observed in U Aquarii (any Fe present in the exposed material will be destroyed by neutron capture to form heavier elements). Knowledge of the dilution factor would enable some constraints to be placed on any single mixing model at the post-AGB phase, since the low mass of the hydrogen envelope at this phase ($M_e < 2.7 \times 10^{-4} M_\odot$) would require that a large part of the intershell would have to be the 'diluting medium'. That is, a significant fraction of the intershell would not be exposed to the neutron flux. It would be interesting to see if future work into neutron synthesis in an expanding convective region would predict such a scenario. The preliminary calculations of Sweigart (1974) indicate that this may be the case since

he found that the upper part of his split intershell region expanded at twice the rate of the lower part. If circumstances led to the expanded upper region not being swept down into the hotter regions of the intershell then this upper region could then act as a diluting medium.

Tables 6.1 and 6.2 compares single mixing calculations and repeated shell flash calculations both for dilution factors of $d=10$ and $d=30$. Although it is difficult to make any direct comparison of the different mixing mechanisms since there are many parameters which influence the exact pattern of the heavy element distribution (eg. dilution factor, number of neutron captures per ^{56}Fe seed, initial abundances), a general pattern is found in all comparisons with single and repeated mixings. This is more clearly illustrated by figure 6.8 where the enhancements are plotted for no dilution having occurred. The full line corresponds to a single mixing (model B table 4.5) and the dashed line to a repeated mixing (column 4.13 table 4.7). The abundances are plotted on the $\text{Si}=10^6$ scale. It can be seen that an accurate abundance determination of all the element abundances shown in these two figures would enable a determination to be made as to whether a single or a repeated mixing occurred (the differences in the two distributions will decrease, however, as the dilution factor becomes larger).

However, present observational material of U Aquarii, in which only the Sr/Fe, Y/Fe and Zr/Fe ratios are determined but not to any great accuracy, does not allow any decision to be made on whether a single or repeated mixing has occurred. Future observations should attempt to answer this crucial question.

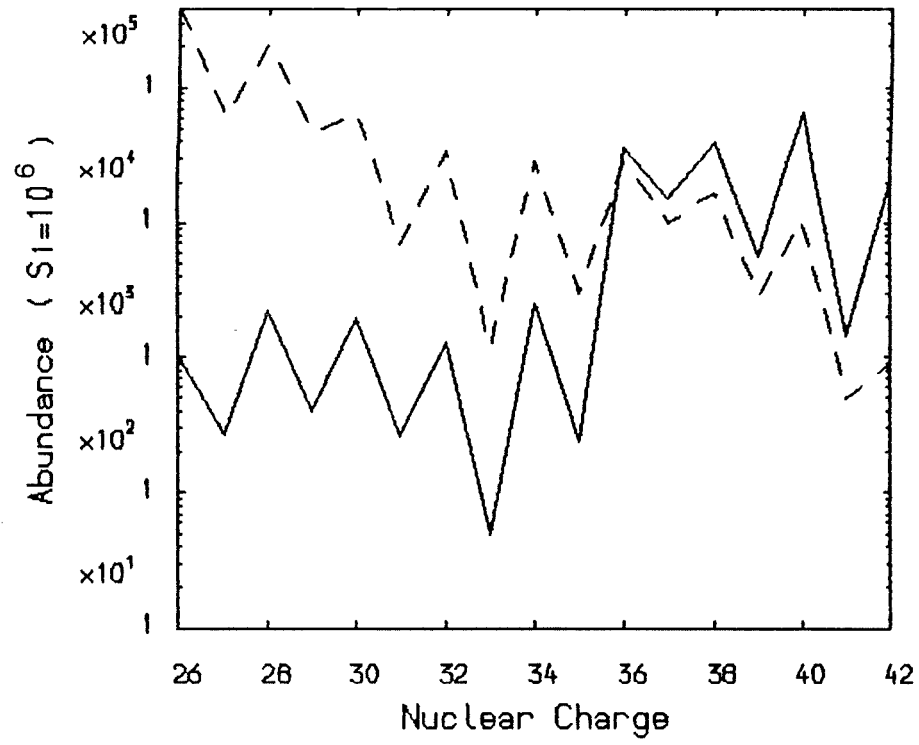


Figure 6.8 Comparison of single and repeated mixing distributions

6.4) Helium Core Flash

If more accurate determinations concluded that the observed Zr abundance is low relative to Sr and Y then this would imply that the synthesis of heavy elements in U Aquarii took place at cooler temperatures and thus lower neutron densities than previously considered in chapter 4. This can be seen in figure 6.9 where a temperature of 1.2×10^8 °K and density of 1100g/cm^3 is used and all the nuclei are assumed thermalised (similar result found for unthermalised case). Envelope mixing simulating roughly 30 neutron captures per ^{56}Fe seed was used with the envelope and the intershell abundances as given in table 3.2. The left hand scale of figure 6.9 gives the enhancements of the elements, and the right hand scale indicates the number fraction of neutrons. The neutron density is now very low at about 7×10^8 neutrons/cm³ and the build up now takes a much longer time commencing at about 10^9 s and as can be seen a low Zr enhancement relative to Y is now found. For a dilution of 200 this calculation would give $[\text{Sr}/\text{Fe}] = 1.2$, $[\text{Y}/\text{Fe}] = 1.0$ and $[\text{Zr}/\text{Fe}] = 0.6$ following beta decay for 3.3×10^6 years. This for the first time gives a $[\text{Zr}/\text{Fe}]$ value significantly lower than the $[\text{Y}/\text{Fe}]$ value. The important point to note here is the low neutron densities that were required in order to achieve this change.

The relative change in the Zr and Y abundances is due to the low neutron flux causing the nuclear flow to pass through the left of the nuclear flow chart of figure 2.4 rather than to the right as in the high flux cases. The different nuclear properties (i.e. cross sections, beta decays) of the isotopes on the different sides of this

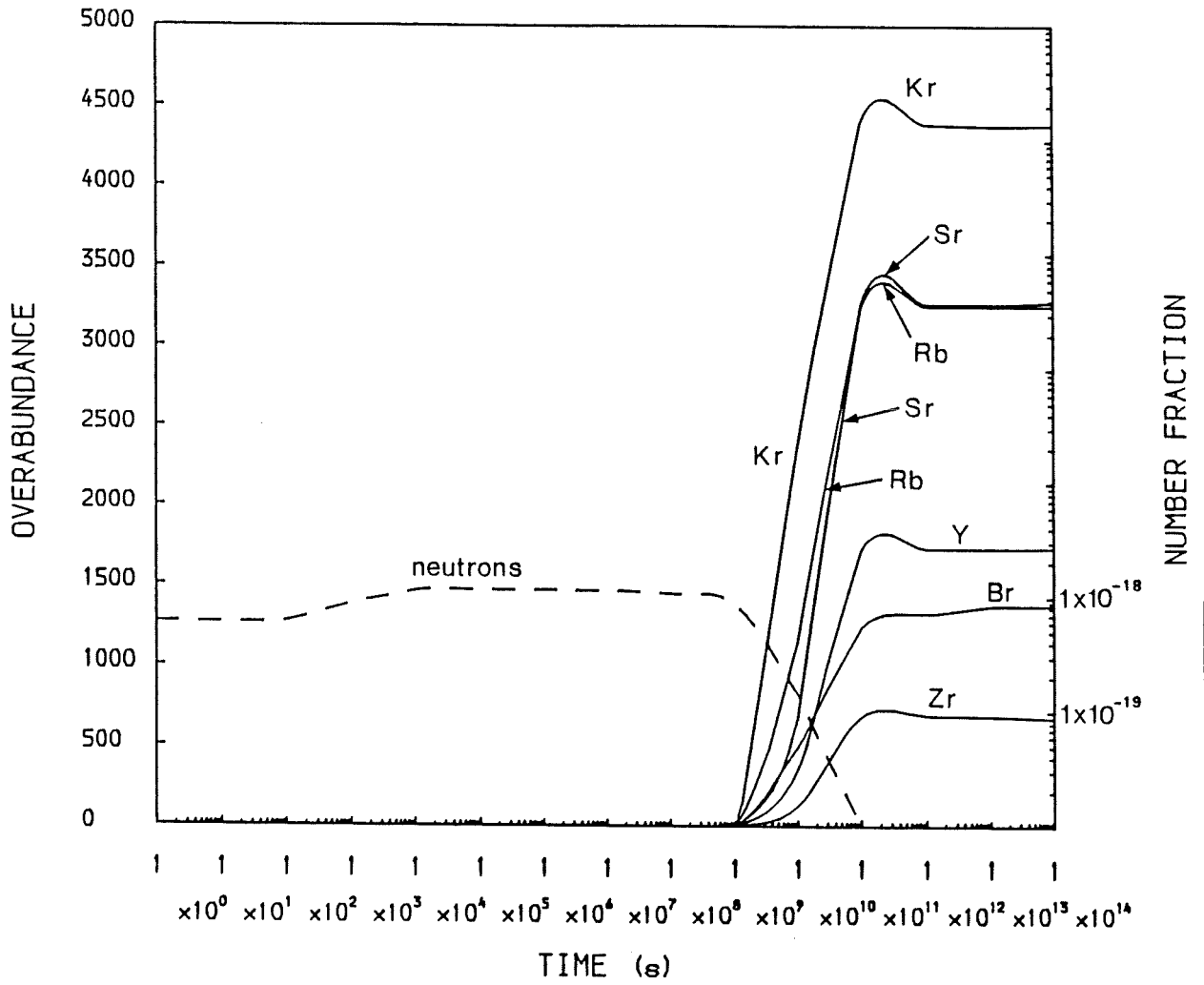


Figure 6.9 Core flash heavy element build up

chart explain the change in relative abundance of elements which have been enhanced under greatly different neutron fluxes. If the neutron synthesis did indeed take place at such cool temperatures, what circumstances on the AGB would allow this? Perhaps the expansion and cooling of the intershell following rapid high levels of mixing would enable the majority of the synthesis to take place at cooler temperatures. A more simple origin for a cool temperature synthesis would be a mixing event at an earlier phase of evolution prior to the AGB. The helium core flash (Schwarzschild and Härm 1962) would be the likeliest candidate. At the present time it is not clear whether significant envelope mixing into the star's interior takes place at this stage of evolution (Deupree 1984a,b). However, if such mixing did occur at this phase the neutron synthesis would occur at lower temperatures than expected for synthesis on the AGB. The conditions used for the calculation of figure 6.9 corresponds to the temperature and density at which neutron synthesis could occur in the interior of the star following a large scale mixing event arising from the helium core flash (Deupree priv.comm.).

6.5) FG Sagittae

Renzini (1982) suggested that the peculiar variable star FG Sagittae may be a precursor of an RCrB star. He suggests that its present position on the H.R. diagram is on one of the dashed tracks of figure 6.1. If this were the case then this implies that FG Sagittae has recently undergone a large scale mixing event due to a final helium shell flash on the post-AGB. Renzini further suggests that the fact FG

Sagittae still has hydrogen at its surface is an indication that it takes a certain amount of time before the envelope is completely ingested and burned. Due to the excess nuclear energy generated by the hydrogen mixing the star should now be expanding and cooling towards the RCrB regime.

Evidence in support of this scenario comes from the recent rapid increase in the observed s-process enhancements, indicating a recent mixing event, as well as the observed cooling rate of FG Sagittae. The spectroscopic and photometric behaviour of FG Sagittae prior to 1973 has been discussed by Herbig and Boyarchuk (1968) and by Langer, Kraft and Anderson (1974). Photometry of the star has been presented by Stone (1979). To summarize, it was established that FG Sagittae has grown progressively later in spectral type from B4 in 1955 (Henize 1961) to F4 in 1973 (Langer, Kraft and Anderson 1974) and that the continuum temperature was found to be cooling roughly at $300^{\circ}\text{K}/\text{year}$ (Stone 1979). Herbig and Boyarchuk (1968) concluded that the star was surrounded by an expanding gaseous envelope with an expansion velocity of 70km/s . The star is known to be at the centre of a planetary nebula with an outer radius of $18''$ which has been present since the earliest photographs taken at the beginning of the century. Another outstanding feature of this star is the rise in abundance of the s-process elements which began at about 1964, and rising to a peak abundance at about 1972 (Langer, Kraft and Anderson, 1974). Large enhancements were found, particularly for the elements La, Ce, Ba, Y and Zr which were found to be approximately 25 times the solar abundance in late 1972. Prior to 1964 these elements were known to have normal abundances in FG Sagittae (Herbig and Boyarchuk 1968). Cohens and Philips (1980) have shown that the s-process enhancements ceased increasing at about 1975,

and that between 1975 and 1978 the star cooled only by 500°K . Recent observations by Acker (1983) have shown that the enhancements remained the same over the period 1979-1982, and that the cooling ceased towards the end of 1980. It was concluded by Acker that the mixing event of FG Sagittae was now terminated.

It is clear that these past observations make FG Sagittae a very interesting object worth further detailed study. If this star has indeed engulfed its small remaining hydrogen envelope on the post-AGB then its observed enhancements would be expected to be similar to the calculations presented in tables 4.5 and 4.6 which were based on such an event. Table 6.3 lists the observed enhancements of the heavy elements in the Fe to Mo range (taken from Langer, Kraft and Anderson 1974). A colon indicates an abundance of low weight, and a double colon indicates an abundance determination of very low weight. It is clear that such observed abundances can be made compatible with a single mixing event on the post-AGB. For example, model G (table 4.5) with a dilution factor $d=14$ gives $[\text{Y}/\text{Fe}]=0.6$, $[\text{Zr}/\text{Fe}]=0.7$ and $[\text{Sr}/\text{Fe}]=1.0$ (e.g. agreement with May '85). However, agreement can also be found from the repeated mixing calculations e.g. figure 4.13 after 15 shell flashes and with $d=10$ gives $[\text{Y}/\text{Fe}]=1.3$ and $[\text{Zr}/\text{Fe}]=1.1$ (e.g. agreement with July '69). Further detailed abundance analysis of this very interesting object will be required in order to discriminate between the different mixing events.

6.6) Conclusions

A comparison of the theoretical calculations with the presently available observational material has been conducted in an attempt to gain information on the nature of the mixing event which led to the observed heavy element enhancements of U Aquarii. It was shown how the value of the neutron flux plays a crucial role in the abundance pattern of the Sr, Y and Zr enhancements, with low neutron fluxes leading to low Zr/Y ratios and vice-versa. Future observations should be able to measure this important abundance ratio more accurately and thus lead to an accurate determination of the neutron flux which occurred in U Aquarii. This would provide information on the temperature at which the synthesis occurred, which in turn would lead to a better understanding as to what phase in the star's evolution the synthesis occurred.

The importance of determining the nature of the neutron exposure has also been discussed. Future observations should enable a comparison to be made with the abundance patterns of figure 6.8 in order to determine the nature of the exposure. An observed abundance pattern similar to the full line of figure 6.8 would indicate a single mixing event while an observed pattern similar to that of the dashed line would indicate a repeating shell flash mixing event on the AGB.

CHAPTER 7. PHOTOMETRIC STUDY OF EXTREME HELIUM STARS

7.1) Purpose for Photometric Study of EHe Stars

Low-amplitude light variations have been reported for several members of the small group of hot, extreme helium (EHe) stars, (see, e.g. Hill 1969; Landolt 1968, 1973; Walker and Kilkenny 1980), but only BD+13^o3224 (V652 Her) has a clearly established period. Landolt (1975) observed BD+13^o3224 to vary with an amplitude < 0.1 mag and period of 0.108 day, and subsequently Hill et al. (1981) showed this variation to be due to radial pulsation. The ephemeris was improved by Kilkenny and Lynas-Gray (1982,1984), who found that the pulsation period is decreasing at a rate of 46×10^{-10} day cycle⁻¹. Lynas-Gray et al. (1984) employed ultraviolet measurements to obtain effective temperature and angular radius variations of the star over a pulsation cycle, and estimated its mass to be $0.7 M_{\odot}$. Jeffery (1984) constructed models identifying BD+13^o3224 with a post-giant branch star contracting towards the helium main-sequence, in which a hydrogen-burning shell at the base of a helium-rich envelope provides most of the luminosity. These results for BD+13^o3224 cannot, however, be used to infer masses for other EHe stars because it has a markedly-higher hydrogen abundance ($n_{\text{H}} \sim 10^{-2}$, Hill et al. 1981), and is less luminous ($\log L/L_{\odot} = 3.03$, Lynas-Gray et al. 1984) than other EHe stars with similar effective temperatures, for which $n_{\text{H}} < 10^{-3}$ and $3.55 < \log L/L_{\odot} < 4.60$ (Heber 1983).

The importance of such studies of EHe stars to the origin of RCrB stars comes from the possibility of an evolutionary link. Schönberner (1977) suggested that the EHe stars are remnants of post-AGB stars contracting to become white dwarfs, and postulated an evolutionary link between the EHe stars and the hydrogen-deficient RCrB type variables. However, Schönberner (1979) was unable to account for the EHe stars by the ejection of the hydrogen-rich envelopes of post-AGB stars via stellar winds. Alternative explanations for their origin, involving coalesced white dwarfs (Webbink 1984) and close binaries with components of intermediate initial masses (Iben and Tutukov 1985), could place the RCrB variables and EHe stars on a pre-white dwarf cooling track similar to that calculated by Schönberner (1977). The hypothesis of an evolutionary link between the EHe stars and the RCrB stars is supported by the discovery that the pulsation period of the RCrB star RY Sgr, 37.6 days (Alexander et al. 1972), may be decreasing at a rate of $5 \times 10^{-4} \text{ day cycle}^{-1}$ (Kilkenny 1982), consistent with Schönberner's evolutionary calculations for a contracting one solar mass helium star.

Since it is possible to derive a distance-independent mass estimate for stars which pulsate, searches for pulsation amongst other EHe stars are important in order to determine whether they are related to the RCrB stars. However, recent searches for periodic variations in the EHe star BD+10^o2179 failed to detect any photometric or spectroscopic variations (Hill, Lynas-Gray and Kilkenny 1984; Grauer, Drilling and Schönberner 1984). Observations were carried out at the South African Astronomical Observatory (SAAO), in order to determine whether or not variability in other EHe stars existed. Two EHe stars, BD-9^o4395 and BD+1^o4381 were investigated for variability. The author participated in these

observations, which formed part of a collaborative observational program involving P.W.Hill, C.S.Jeffery, K.Morrison and the author. The author's part in the observations consisted of a 5 week observing period at SAAO. Of the observations presented here, those taken between HJD 2445800 55-70 were taken by him. The frequency analysis of BD-9^o4395 was carried out by I. Skillen and the frequency analysis of BD+1^o4381 by C.S. Jeffery. Both frequency analyses were carried out using the frequency analysis package PULSAR written by I. Skillen at the University of St. Andrews. The following sections are mainly based on Jeffery and Malaney (1985), and Jeffery, Skillen, Hill, Kilkenny, Malaney and Morrison (1985).

7.2) Variability of BD-9⁰4395

a) Observations

The EHe star BD-9⁰4395 was discovered to be hydrogen-deficient by MacConnell, Frye and Bidelman (1972). A quantitative spectroscopic analysis by Kaufmann and Schönberner (1977) gave $T_{\text{eff}}=25000^{\circ}\text{K}$, $\log g=2.6$ and $n_{\text{H}}=1.5 \times 10^{-3}$. The values for $\log g$ and T_{eff} indicate that BD-9⁰4395 lies in a region of the $\log g$ vs. $\log T_{\text{eff}}$ diagram which is traversed by the evolutionary tracks of stars with condensed C/O cores and pure helium envelopes (Schönberner 1977). Comparison with these tracks yielded values for the mass, radius and luminosity of $M/M_{\odot}=0.8$, $R/R_{\odot}=7.4$ and $\log L/L_{\odot}=4.25$. Kaufmann and Schönberner noted that non-LTE effects may be present in the spectrum of BD-9⁰4395, and proposed the existence of a circumstellar envelope. High-resolution ultraviolet spectroscopic observations by Hamann, Schönberner and Heber (1982) confirmed the presence of a superionized stellar wind with a terminal velocity of $\sim 600\text{km/s}$ and an estimated mass loss rate of $10^{-8} M_{\odot}/\text{year}$. Photometric observations of this star by Landolt (1979 private communication) and Kilkeny (1980 private communication) indicated its variability, suggesting that systematic photometric and spectroscopic monitoring should be carried out. The latter observations appeared to rule out short-period variations, however, and implied that the variability occurs on a time-scale longer than ~ 1 day.

Photoelectric observations of BD-9^o4395 were made at the South African Astronomical Observatory (SAAO) on 28 nights during a period covering some 52 nights in 1984 May-July. The 0.5m telescope and pulse-counting People's photometer were used to obtain 'uvby' observations which were reduced to the standard Strömngren system (Crawford and Barnes 1970; Grønbech, Olsen and Strömngren 1976), usually with observations of 20 or more standard-stars per night. Each observational sequence normally consisted of a series of measurements of BD-9^o4395 (Vr) and two comparison stars, BD-9^o4385 (C) and BD-9^o4389 (Ck), in the order CVrCVrCkVrC. Integration times for each filter were chosen to obtain approximately 100 000 counts for the comparison stars and 30 000 counts for BD-9^o4395 in the sequence 'yvbubvy'. Sky measurements were made at least once during each sequence and more frequently when the moon was present. The total sequence occupied approximately forty-five minutes.

Following reduction to the standard system, each observation of BD-9^o4395 and BD-9^o4389 was further reduced to a differential magnitude in the sense $\langle Vr \rangle - \langle C \rangle$ and $\langle Ck \rangle - \langle C \rangle$, where $\langle Vr \rangle$ is a mean magnitude obtained from a series of measurements within an observation sequence. Mean magnitudes and colours of the three stars derived from all observations are

	<V>	<b-y>	<m1>	<c1>	n
BD-9 ^o 4395 (Vr)	10.506 (032)	0.133 (007)	-0.012 (011)	-0.071 (016)	93
BD-9 ^o 4385 (C)	8.121 (012)	0.071 (012)	0.092 (013)	0.587 (011)	93
BD-9 ^o 4389 (Ck)	9.004 (008)	0.297 (006)	0.158 (010)	0.717 (015)	81

where figures in parentheses are standard deviations about the means in millimagnitudes. The number of observed sequences, n , for each star is also listed. The Strömrgren indices $m1$ and $c1$ are defined as:

$$m1 = (v-b) - (b-y)$$

$$c1 = (u-v) - (v-b)$$

The journal of the photometric observations is presented in table 7.1. Times given therein are the mean heliocentric Julian date at which BD-9^o4395 was observed, whilst an entry of zero denotes that photometry of the check star has been omitted. The data of table 7.1 are partially illustrated in figure 7.1 which shows that BD-9^o4395 is variable over a range of 0.15 mag. The standard deviations of the differential magnitudes and differential colours of the comparison stars, in the sense (Ck-C), are each 0.008 mag. This value is not exceeded significantly by the dispersions of the differential colours of BD-9^o4395, and therefore represents an upper limit to any colour variations of the helium star.

Table 7.1

BD-9^o4395 photometryVariable (Vr) BD -9^o4395 Comparison (C) BD -9^o4385 Check (Ck) BD -9^o4389

HJD -2445800	C				Vr - C				Ck - C			
	V	b-y	v-b	u-b	V	b-y	v-b	u-b	V	b-y	v-b	u-b
39.498	8.130	0.089	0.150	0.899	2.398	0.066	-0.022	-0.743	0.886	0.225	0.292	0.710
39.535	8.129	0.086	0.153	0.895	2.393	0.068	-0.034	-0.731	0.879	0.232	0.285	0.693
41.361	8.139	0.080	0.159	0.902	2.384	0.060	-0.039	-0.733	0.000	0.000	0.000	0.000
41.443	8.146	0.078	0.152	0.901	2.392	0.058	-0.049	-0.752	0.875	0.227	0.292	0.715
41.577	8.122	0.085	0.148	0.904	2.404	0.052	-0.034	-0.745	0.875	0.223	0.291	0.711
42.309	8.112	0.066	0.167	0.913	2.425	0.058	-0.043	-0.735	0.885	0.230	0.286	0.707
44.451	8.101	0.065	0.159	0.903	2.413	0.059	-0.041	-0.747	0.872	0.219	0.288	0.710
44.507	8.120	0.070	0.168	0.914	2.427	0.054	-0.044	-0.735	0.000	0.000	0.000	0.000
44.536	8.119	0.065	0.166	0.915	2.425	0.059	-0.041	-0.735	0.876	0.228	0.288	0.710
44.562	8.127	0.071	0.165	0.915	2.422	0.066	-0.047	-0.741	0.867	0.224	0.290	0.713
46.329	8.124	0.066	0.170	0.921	2.358	0.072	-0.044	-0.748	0.880	0.235	0.286	0.711
46.406	8.107	0.061	0.160	0.901	2.374	0.061	-0.038	-0.741	0.000	0.000	0.000	0.000
46.462	8.100	0.062	0.153	0.885	2.392	0.051	-0.025	-0.736	0.000	0.000	0.000	0.000
48.305	8.111	0.066	0.160	0.905	2.366	0.063	-0.022	-0.731	0.877	0.224	0.298	0.724
48.370	8.119	0.067	0.159	0.918	2.358	0.055	-0.029	-0.692	0.874	0.223	0.291	0.712
48.450	8.126	0.065	0.163	0.910	2.352	0.064	-0.038	-0.742	0.883	0.224	0.292	0.708
48.517	8.124	0.067	0.158	0.904	2.356	0.060	-0.044	-0.745	0.885	0.217	0.295	0.718
49.298	8.105	0.073	0.165	0.915	2.355	0.069	-0.052	-0.749	0.890	0.231	0.280	0.701
49.328	8.114	0.069	0.164	0.913	2.369	0.059	-0.051	-0.745	0.888	0.223	0.291	0.717
49.437	8.120	0.070	0.162	0.909	2.383	0.059	-0.046	-0.747	0.886	0.226	0.281	0.706
49.476	8.116	0.074	0.158	0.909	2.389	0.055	-0.037	-0.740	0.881	0.226	0.290	0.709
49.519	8.114	0.072	0.163	0.908	2.384	0.072	-0.046	-0.748	0.000	0.000	0.000	0.000
49.554	8.111	0.077	0.161	0.904	2.387	0.070	-0.040	-0.741	0.000	0.000	0.000	0.000
57.378	8.122	0.068	0.160	0.910	2.370	0.062	-0.051	-0.763	0.887	0.225	0.297	0.726
57.426	8.121	0.067	0.164	0.916	2.365	0.060	-0.047	-0.760	0.889	0.220	0.288	0.710
57.522	8.123	0.068	0.162	0.911	2.361	0.061	-0.050	-0.753	0.883	0.224	0.292	0.718
58.292	8.112	0.068	0.162	0.921	2.359	0.059	-0.046	-0.755	0.891	0.225	0.293	0.721
58.373	8.116	0.070	0.162	0.915	2.345	0.069	-0.046	-0.750	0.884	0.225	0.299	0.710
58.525	8.118	0.067	0.160	0.916	2.337	0.070	-0.047	-0.757	0.880	0.233	0.284	0.703
59.304	8.106	0.065	0.164	0.911	2.303	0.066	-0.045	-0.753	0.888	0.228	0.286	0.716
59.384	8.112	0.069	0.162	0.909	2.302	0.061	-0.039	-0.749	0.887	0.227	0.288	0.712
59.482	8.117	0.070	0.161	0.907	2.292	0.059	-0.034	-0.747	0.888	0.224	0.301	0.717
59.515	8.119	0.072	0.164	0.914	2.302	0.059	-0.046	-0.757	0.886	0.226	0.279	0.710
60.301	8.119	0.070	0.166	0.925	2.395	0.057	-0.049	-0.748	0.891	0.222	0.293	0.725
60.381	8.120	0.069	0.163	0.912	2.398	0.054	-0.036	-0.728	0.881	0.227	0.299	0.707
60.472	8.123	0.073	0.163	0.907	2.415	0.048	-0.043	-0.731	0.884	0.229	0.294	0.721
60.499	8.126	0.069	0.162	0.910	2.403	0.059	-0.039	-0.735	0.884	0.223	0.297	0.706
61.268	8.130	0.073	0.172	0.932	2.437	0.055	-0.030	-0.723	0.897	0.231	0.301	0.734
61.360	8.135	0.075	0.162	0.915	2.433	0.060	-0.027	-0.720	0.878	0.226	0.297	0.729
61.486	8.131	0.068	0.168	0.916	2.438	0.057	-0.046	-0.729	0.879	0.233	0.289	0.718
62.280	8.117	0.077	0.159	0.927	2.426	0.041	-0.045	-0.751	0.888	0.223	0.305	0.734
62.305	8.113	0.078	0.161	0.925	2.394	0.062	-0.048	-0.756	0.873	0.221	0.300	0.714
62.351	8.111	0.072	0.167	0.918	2.410	0.052	-0.051	-0.761	0.894	0.219	0.287	0.735
62.425	8.106	0.071	0.168	0.912	2.370	0.066	-0.053	-0.746	0.873	0.221	0.292	0.713
62.485	8.119	0.068	0.163	0.912	2.363	0.066	-0.044	-0.739	0.862	0.226	0.286	0.723
63.265	8.104	0.078	0.162	0.918	2.405	0.076	-0.026	-0.726	0.893	0.216	0.319	0.729

Table 7.1 (Cont.)

HJD -2445800	C				V _r - C				C _k - C			
	V	b-y	v-b	u-b	V	b-y	v-b	u-b	V	b-y	v-b	u-b
65.268	8.113	0.065	0.162	0.910	2.366	0.067	-0.031	-0.709	0.879	0.234	0.285	0.709
65.303	8.121	0.063	0.161	0.910	2.393	0.060	-0.038	-0.736	0.877	0.227	0.302	0.714
65.332	8.123	0.065	0.166	0.908	2.386	0.063	-0.045	-0.720	0.895	0.237	0.274	0.714
65.361	8.132	0.064	0.165	0.910	2.384	0.074	-0.030	-0.721	0.900	0.217	0.316	0.721
66.259	8.124	0.069	0.169	0.923	2.382	0.054	-0.063	-0.750	0.901	0.221	0.286	0.681
66.298	8.121	0.070	0.165	0.918	2.367	0.068	-0.036	-0.754	0.888	0.222	0.295	0.704
66.354	8.125	0.065	0.169	0.911	2.373	0.061	-0.051	-0.754	0.884	0.228	0.287	0.710
66.390	8.124	0.064	0.170	0.913	2.376	0.055	-0.040	-0.756	0.879	0.230	0.294	0.704
66.414	8.122	0.071	0.161	0.906	2.379	0.051	-0.055	-0.749	0.893	0.214	0.295	0.714
66.441	8.122	0.073	0.162	0.906	2.369	0.057	-0.037	-0.747	0.881	0.223	0.290	0.716
66.490	8.124	0.066	0.162	0.911	2.356	0.052	-0.028	-0.733	0.873	0.220	0.298	0.725
66.510	8.122	0.065	0.169	0.913	2.367	0.075	-0.059	-0.748	0.883	0.223	0.279	0.707
73.251	8.122	0.074	0.164	0.922	2.405	0.063	-0.038	-0.740	0.879	0.217	0.295	0.716
73.366	8.123	0.070	0.164	0.906	2.387	0.066	-0.041	-0.737	0.875	0.225	0.292	0.726
73.500	8.128	0.067	0.163	0.911	2.381	0.051	-0.033	-0.737	0.872	0.234	0.282	0.702
74.233	8.120	0.081	0.168	0.923	2.354	0.056	-0.051	-0.750	0.882	0.217	0.299	0.723
74.351	8.120	0.071	0.166	0.907	2.361	0.058	-0.043	-0.745	0.883	0.227	0.290	0.720
74.491	8.121	0.069	0.163	0.905	2.371	0.068	-0.044	-0.746	0.882	0.229	0.298	0.722
75.226	8.112	0.068	0.171	0.928	2.475	0.059	-0.048	-0.742	0.885	0.229	0.285	0.706
75.334	8.114	0.066	0.166	0.918	2.475	0.059	-0.043	-0.733	0.882	0.229	0.291	0.707
76.234	8.104	0.070	0.178	0.931	2.417	0.069	-0.050	-0.755	0.883	0.228	0.280	0.706
76.285	8.107	0.069	0.165	0.915	2.414	0.057	-0.037	-0.740	0.878	0.235	0.293	0.698
76.334	8.103	0.068	0.166	0.913	2.418	0.054	-0.039	-0.741	0.883	0.224	0.292	0.718
76.386	8.106	0.070	0.167	0.906	2.407	0.066	-0.047	-0.754	0.880	0.227	0.287	0.712
76.477	8.122	0.067	0.164	0.911	2.399	0.071	-0.042	-0.746	0.870	0.224	0.292	0.718
77.224	8.106	0.069	0.163	0.926	2.373	0.061	-0.025	-0.739	0.877	0.225	0.299	0.713
77.271	8.110	0.071	0.170	0.917	2.382	0.056	-0.049	-0.744	0.889	0.216	0.293	0.714
77.483	8.129	0.071	0.166	0.914	2.386	0.065	-0.046	-0.742	0.884	0.225	0.282	0.718
78.230	8.129	0.068	0.173	0.935	2.442	0.068	-0.041	-0.750	0.874	0.237	0.283	0.707
78.485	8.130	0.069	0.170	0.918	2.407	0.062	-0.050	-0.742	0.882	0.228	0.287	0.711
79.224	8.131	0.069	0.168	0.930	2.381	0.074	-0.039	-0.743	0.890	0.224	0.294	0.709
79.274	8.119	0.069	0.161	0.913	2.376	0.071	-0.041	-0.737	0.885	0.228	0.294	0.721
79.293	8.116	0.063	0.159	0.912	2.387	0.062	-0.040	-0.748	0.889	0.232	0.298	0.704
79.323	8.127	0.064	0.161	0.914	2.376	0.064	-0.035	-0.747	0.885	0.236	0.296	0.716
79.341	8.141	0.069	0.166	0.917	2.376	0.070	-0.038	-0.740	0.894	0.229	0.290	0.716
79.387	8.123	0.061	0.162	0.898	2.365	0.072	-0.047	-0.745	0.888	0.229	0.283	0.710
79.406	8.147	0.065	0.173	0.915	2.367	0.080	-0.047	-0.738	0.892	0.239	0.281	0.722
79.430	8.158	0.075	0.169	0.922	2.368	0.058	-0.037	-0.741	0.884	0.219	0.297	0.721
79.448	8.156	0.075	0.171	0.917	2.365	0.048	-0.047	-0.749	0.864	0.224	0.291	0.723
79.472	8.157	0.078	0.153	0.916	2.380	0.048	-0.032	-0.749	0.000	0.000	0.000	0.000
84.293	8.120	0.070	0.165	0.913	2.382	0.058	-0.050	-0.754	0.878	0.227	0.291	0.715
84.401	8.116	0.072	0.162	0.905	2.378	0.051	-0.034	-0.739	0.889	0.208	0.309	0.717
85.421	8.125	0.071	0.161	0.918	2.433	0.065	-0.037	-0.728	0.000	0.000	0.000	0.000
86.421	8.132	0.070	0.162	0.916	2.427	0.065	-0.045	-0.742	0.000	0.000	0.000	0.000
87.431	8.124	0.173	0.163	0.914	2.372	0.058	-0.043	-0.741	0.000	0.000	0.000	0.000
89.424	8.123	0.069	0.163	0.915	2.424	0.060	-0.043	-0.739	0.000	0.000	0.000	0.000
91.359	8.113	0.074	0.161	0.913	2.366	0.067	-0.047	-0.758	0.000	0.000	0.000	0.000

It is evident from an inspection of figure 7.1 that the photometric variability of BD-9⁰4395 exhibits a complex behaviour and that, if the variability is periodic, it is multiply periodic. Although the number ($n = 93$) and timespan (52 days) of the observations are not large, the differential y -filter data were subjected to a power spectrum analysis in an attempt to identify their periodic content, that is to derive a representative model for the photometric variations of the form

$$\Delta V = A_0 + \sum_{i=1}^N A_i \sin \left[2\pi f_i (t - t_0) + \phi_i \right]$$

where A_0 is the mean differential magnitude, N is the number of periodic components, f_i are their frequencies in c day^{-1} , A_i are their amplitudes in magnitudes, ϕ_i are their initial phases in radians, t is the heliocentric Julian date (HJD) and t_0 is an arbitrary initial epoch, taken here to be $t_0 = 2445800.0$. These data are not suited to searching for frequencies higher than 1.7c day^{-1} , so the analysis was restricted to the frequency range 0 to 1.7c day^{-1} . The details of this analysis is presented in Jeffery et al. (1985).

The results of the frequency analysis are summarised in table 7.2, where the adopted frequency solution for the differential V light curve is listed. The uncertainties for the amplitudes and phases are standard errors. Phases are computed from the epoch $\text{HJD} = 2445800.0$. For each frequency, the corresponding period and value of the pulsation constant, Q , are given in days. However, it should be noted that due to the small timespan of the observations only two of the periods, namely the 11.2 day and 3.5 day periods, were determined unequivocally.

Table 7.2

Adopted frequency solution for BD-9^o4395

Frequency (c day ⁻¹)	Amplitude (mag)	Phase (rad)	Period (day)	Q (day)
0.08917	0.028 ± 0.002	-2.801 ± 0.079	11.215	0.496
0.13772	0.019 ± 0.002	-2.227 ± 0.107	7.261	0.321
0.28445	0.033 ± 0.019	-1.029 ± 0.059	3.516	0.156
0.31530	0.016 ± 0.002	+1.447 ± 0.132	3.172	0.140
0.42222	0.023 ± 0.002	+2.535 ± 0.084	2.368	0.105
0.50462	0.011 ± 0.003	-0.653 ± 0.227	1.982	0.088
0.54870	0.010 ± 0.002	+0.163 ± 0.201	1.822	0.081

Because of the inconclusive nature of the frequency analysis, the uncertainty that is associated with each of the frequencies in table 7.2 is the frequency resolution of the complete data set, defined by $1.5/T$, where T is the timespan of the data window (Loumos and Deeming 1978), and is equal to 0.029 c day^{-1} . This adopted frequency solution should be regarded as being in the nature of a 'working model' only, and not as the definitive frequency description of the photometric variability. More extensive observations are needed to verify the description of the frequency structure of the light curve.

b) Nature of The Variability

The photometric variations of $\text{BD}-9^{\circ}4395$ appear to be multiply periodic and the complexity of the light curve confirms that the star is not pulsating in a single radial mode as seems likely in the cases of $\text{BD}+13^{\circ}3224$ and RY Sgr. In the following discussion an attempt is made to elucidate the cause of the variability in $\text{BD}-9^{\circ}4395$.

Since $P \propto g^{-3/4}$ for pulsating stars which obey the period-mean density relation, $P \rho^{1/2} = Q$, the expected time-scale for radial pulsation in $\text{BD}-9^{\circ}4395$ can be estimated from the known periods in $\text{BD}+13^{\circ}3224$ and RY Sgr. Lynas-Gray et al. (1984) gave $\log g = 3.7$ for $\text{BD}+13^{\circ}3224$, and Schönberner (1975) derived $\log g = 0.65$ for RY Sgr. Bearing in mind the caveat imposed by the different hydrogen abundances and evolutionary states of these stars, the two estimates for the time-scale of radial pulsation in $\text{BD}-9^{\circ}4395$ are 0.7 and 1.3 days.

The periods suggested by the frequency analysis considerably exceed both of these estimates, and this, together with the absence of concomitant colour, and hence temperature, changes, implies that radial pulsation is not the cause of the observed variability in BD-9^o4395. The absence of colour variations is in contrast to BD+13^o3224, which displays considerable colour changes, particularly in (u-b). Furthermore, the radial-velocity variations in BD-9^o4395 (Jeffery et al. 1985), although present at a high level of significance, are small in amplitude, and this is also discordant with the observed variations in BD+13^o3224, which cover a range of 70km/s (Hill et al. 1981).

The pulsation constant Q , which can be expressed as $Q = P g^{3/4} M^{-1/4}$ day, is equal to 0.033 and 0.056 day respectively for BD+13^o3224 and RY Sgr, assuming a mass of $0.7M_{\odot}$ for BD+13^o3224 (Lynas-Gray et al. 1984), and $1.0M_{\odot}$ for RY Sgr (Schönberner 1975). In the case of BD-9^o4395, the Q -values corresponding to the proposed frequencies lie in the range 0.496 to 0.081 day. Theoretical Q -values have been computed for other classes of hot, luminous pulsating stars, for example the β Cephei variables (Lesh and Aizerman 1974), and supergiants (Lovy et al. 1984). Both these categories of variable stars are characterized by small-amplitude light and radial-velocity variations, and indeed, with $M_{bol} = -5.87$ mag and $T_{eff} = 25000^{\circ}K$ (Kaufmann and Schönberner 1977), BD-9^o4395 lies in the vicinity of both groups in the HR diagram. Although the mass and chemical composition of BD-9^o4395 differ appreciably from the β Cephei and supergiant variables, a comparison of their pulsation constants is, nonetheless, instructive, since theoretical Q -values are rather insensitive to changes in stellar parameters (cf., Cox 1980). Lesh and Aizerman (1974) give $Q=0.038$ for

the fundamental radial mode and $Q=0.026$ for the first overtone radial mode of pulsation in the β Cephei stars. The corresponding values for the supergiants, according to the computations of Lovy et al. (1984), are similar, the mean values for the B supergiants in their models being 0.039 and 0.029 respectively, although the range is somewhat greater than for the β Cephei variables. The non-radial f-mode for the β Cephei models has $Q=0.032$ while the non-radial p-mode has $Q=0.027$. The agreement of the observed Q-values for BD+13^o3224 and RY Sgr, both of which are radial pulsators, with these theoretical values for quite different stars is remarkably good. The considerably larger Q-values observed for BD-9^o4395 therefore provides further evidence that radial pulsation, and indeed, non-radial f- and p-modes, should not be invoked in the interpretation of its observed photometric behaviour.

Non-radial g-modes, on the other hand, have no upper limit to their spectrum of discrete eigenperiods. A comparison with the Q-values computed for non-radial g-modes based on linear, non-adiabatic analyses of non-radial oscillations in polytropes, and tabulated in Cox (1980), indicates that the observed variability in BD-9^o4395 can be consistently interpreted as being due to non-radial g-mode oscillations in a partially radiative star, that is, a star with polytropic index $n > 1.5$.

7.3) Variability of BD+1^o4381

The star BD+1^o4381 was discovered to be hydrogen deficient by Drilling (1979). Absolute flux measurements yielded an effective temperature of 9500K (Drilling et al. 1984), making BD+1^o4381 one of the coolest known EHe stars. Since the other EHe stars known to be variable extend in temperature from 12400K (HD168476) to 31900K (HD160641) (Drilling et al. 1984), it was considered important to observe BD+1^o4381 in order to ascertain whether variability extends to lower temperatures.

Observations were carried out over the same period and by the same methods as outlined in section 7.2. Mean magnitudes and colours of BD+1^o4381 and two comparison stars obtained from all observations, were:

	Key	<y>	<b-y>	<ml>	<cl>	n
BD+1 ^o 4381	(V)	9.525 (018)	0.184 (006)	0.030 (008)	0.159 (011)	47
BD+2 ^o 4257	(C)	9.251 (009)	0.131 (006)	0.151 (007)	1.013 (008)	47
BD+0 ^o 4598	(Ck)	10.069 (013)	0.166 (009)	0.111 (013)	0.487 (031)	21

Parenthesis indicate the standard deviations about the means in millimagnitudes. Table 7.3 contains the differentially corrected observations of BD+1^o4381 which are shown in figure 7.2. Zeros indicate where measurements of the check star were omitted. Table 7.3 also contains four observations obtained at SAAO in June 1983.

Although the time base of the observations is of the same order as the time-scale of the variation, and experience shows the EHe stars to have rather complex light curves, some important information is regarded to be present in the data. On the assumption that the light curve is singly periodic, the method of least squares was used to fit a sinusoidal light curve to the observations. The frequency was swept over a small range close to the estimated frequency in order to obtain the best solution, which takes the form:

$$y = c + a \sin 2\pi(ft + \phi), \text{ where}$$

$$c = 9.530 \pm 0.001 \text{ mag,}$$

$$a = 0.021 \pm 0.002 \text{ mag,}$$

$$f = 0.04711 \pm 0.0047 \text{ day,}$$

$$\phi = -0.097 \pm 0.011 \text{ and}$$

$$t = \text{HJD} - 2445800.$$

The frequency f corresponds to a period of 21.23 day; the 10 per cent error is only estimated but is consistent with the formal error expected had the data been equally spaced. A similar technique was applied to the b-y colour curve, but since the amplitude of the colour variation is small compared to the scatter in the data, the frequency obtained from the light curve was used. The resulting fit has the form:

$$b-y = c' + a' \sin 2\pi(ft + \phi'), \text{ where}$$

$$c' = 0.183 \pm 0.001 \text{ mag,}$$

$$a' = 0.004 \pm 0.001 \text{ mag and}$$

$$\phi' = -0.431 \pm 0.044$$

Figure 7.3 shows the light and colour curves folded with a period of 21.23 day. While the fit to the light curve is encouraging, further accurate photometry over an extended period will be required to determine whether BD+1⁰4381 is a singly periodic variable and to improve the period determination.

The observation that BD+1⁰4381 is a light variable is crucial because it completes a temperature sequence of variable hydrogen-deficient stars ranging from the hot EHe star HD 160641 to the cool RCrB stars such as RY Sgr. BD+1⁰4381 may be compared with linear models of radial pulsation in high-luminosity helium stars (Wood 1976) by assuming that it lies close to Schönberner's (1977) evolutionary track for EHe stars with a mass $1 M_{\odot}$ and a luminosity of $\log L/L_{\odot} = 4$. The suggested 21-day period and the observed effective temperature are consistent with Wood's models of pulsation in the fundamental radial mode, as is the case for the RCrB star RY Sgr which has a 38-day period (Alexander et al. 1972) and an effective temperature of 7100⁰K (Schönberner 1975). While the period remains poorly determined this possibility remains a conjecture. However, it emphasises the need for a more detailed study of the BD+1⁰4381 to determine how it and the other hot EHe stars are related to the RCrB stars.

Table 7.3

BD+1°4381 photometry

Variable (V) BD+1°4381	Comparison (C) BD+2°4257				Check (Ck) BD+0°4598							
HJD	C				V - C				Ck - C			
-2445000	y	b-y	v-b	u-b	y	b-y	v-b	u-b	y	b-y	v-b	u-b
504.646	9.254	0.000	0.000	0.000	0.262	0.000	0.000	0.000	0.814	0.000	0.000	0.000
517.442	9.250	0.130	0.277	1.595	0.283	0.065	-0.063	-0.952	0.000	0.000	0.000	0.000
517.570	9.240	0.127	0.282	1.582	0.279	0.060	-0.068	-0.949	0.000	0.000	0.000	0.000
518.599	9.241	0.127	0.276	1.578	0.270	0.058	-0.058	-0.943	0.000	0.000	0.000	0.000
844.651	9.254	0.128	0.288	1.598	0.266	0.028	-0.067	-0.996	0.000	0.000	0.000	0.000
849.612	9.239	0.132	0.280	1.577	0.303	0.054	-0.072	-0.987	0.813	0.045	0.120	0.098
849.649	9.239	0.136	0.277	1.579	0.300	0.044	-0.064	-0.982	0.793	0.056	0.119	0.089
857.617	9.246	0.131	0.279	1.580	0.261	0.057	-0.073	-0.987	0.000	0.000	0.000	0.000
858.605	9.257	0.121	0.280	1.582	0.255	0.060	-0.079	-0.999	0.829	0.023	0.120	0.119
858.656	9.258	0.122	0.275	1.578	0.252	0.052	-0.073	-0.993	0.802	0.034	0.140	0.099
859.594	9.249	0.133	0.283	1.586	0.256	0.052	-0.065	-0.990	0.813	0.034	0.118	0.111
859.639	9.255	0.133	0.266	1.592	0.256	0.053	-0.073	-1.003	0.820	0.027	0.130	0.094
860.577	9.247	0.127	0.283	1.582	0.257	0.058	-0.079	-1.002	0.810	0.045	0.121	0.083
860.613	9.253	0.127	0.263	1.575	0.254	0.054	-0.073	-0.993	0.820	0.034	0.120	0.087
860.659	9.245	0.131	0.275	1.573	0.260	0.049	-0.058	-0.986	0.820	0.032	0.136	0.095
861.441	9.262	0.142	0.267	1.580	0.253	0.056	-0.062	-0.988	0.851	0.046	0.125	0.217
861.530	9.255	0.136	0.286	1.588	0.252	0.046	-0.067	-1.001	0.826	0.030	0.124	0.122
861.563	9.247	0.131	0.282	1.577	0.253	0.046	-0.069	-0.995	0.798	0.045	0.116	0.101
861.649	9.248	0.126	0.277	1.572	0.250	0.057	-0.070	-0.998	0.814	0.036	0.126	0.111
862.533	9.253	0.134	0.282	1.581	0.272	0.054	-0.066	-0.996	0.835	0.041	0.122	0.132
862.567	9.251	0.128	0.284	1.588	0.275	0.055	-0.071	-1.004	0.823	0.038	0.134	0.116
862.630	9.252	0.131	0.284	1.579	0.279	0.053	-0.068	-1.002	0.811	0.035	0.126	0.095
866.564	9.241	0.136	0.282	1.581	0.289	0.043	-0.065	-0.995	0.827	0.019	0.125	0.111
866.604	9.254	0.129	0.279	1.581	0.281	0.054	-0.073	-1.006	0.825	0.028	0.120	0.100
866.645	9.260	0.122	0.280	1.573	0.281	0.047	-0.068	-0.991	0.816	0.017	0.154	0.132
873.571	9.248	0.121	0.282	1.577	0.298	0.056	-0.070	-0.998	0.000	0.000	0.000	0.000
873.610	9.244	0.128	0.276	1.559	0.288	0.053	-0.067	-0.981	0.000	0.000	0.000	0.000
873.637	9.245	0.131	0.271	1.564	0.292	0.052	-0.069	-0.990	0.000	0.000	0.000	0.000
873.662	9.244	0.130	0.279	1.572	0.293	0.050	-0.067	-0.993	0.000	0.000	0.000	0.000
873.678	9.238	0.133	0.285	1.575	0.301	0.051	-0.069	-1.002	0.000	0.000	0.000	0.000
874.556	9.249	0.118	0.286	1.578	0.286	0.062	-0.070	-0.988	0.817	0.028	0.126	0.107
874.598	9.241	0.124	0.287	1.577	0.288	0.061	-0.073	-0.991	0.000	0.000	0.000	0.000
874.625	9.237	0.136	0.267	1.571	0.293	0.052	-0.059	-0.988	0.808	0.032	0.125	0.084
874.651	9.242	0.126	0.280	1.578	0.290	0.051	-0.062	-0.989	0.000	0.000	0.000	0.000
874.672	9.240	0.127	0.286	1.572	0.293	0.057	-0.076	-0.993	0.000	0.000	0.000	0.000
875.576	9.264	0.123	0.287	1.587	0.291	0.057	-0.068	-0.988	0.000	0.000	0.000	0.000
875.600	9.249	0.136	0.275	1.565	0.282	0.047	-0.060	-0.975	0.000	0.000	0.000	0.000
875.632	9.252	0.127	0.284	1.578	0.285	0.053	-0.070	-0.990	0.000	0.000	0.000	0.000
875.655	9.254	0.136	0.284	1.577	0.283	0.053	-0.068	-0.983	0.000	0.000	0.000	0.000
875.670	9.259	0.138	0.289	1.581	0.278	0.049	-0.070	-0.979	0.000	0.000	0.000	0.000
876.560	9.268	0.137	0.283	1.580	0.275	0.052	-0.069	-0.990	0.000	0.000	0.000	0.000
876.654	9.266	0.133	0.277	1.568	0.273	0.054	-0.067	-0.984	0.000	0.000	0.000	0.000
877.552	9.254	0.131	0.280	1.576	0.273	0.054	-0.066	-0.981	0.000	0.000	0.000	0.000
877.582	9.258	0.130	0.283	1.581	0.259	0.065	-0.066	-0.981	0.000	0.000	0.000	0.000
877.600	9.261	0.132	0.284	1.574	0.269	0.054	-0.071	-0.986	0.000	0.000	0.000	0.000
877.629	9.258	0.131	0.280	1.571	0.273	0.058	-0.063	-0.978	0.000	0.000	0.000	0.000
877.650	9.270	0.128	0.286	1.581	0.266	0.056	-0.070	-0.981	0.000	0.000	0.000	0.000
877.666	9.275	0.132	0.284	1.581	0.277	0.045	-0.073	-0.982	0.000	0.000	0.000	0.000
878.546	9.249	0.132	0.283	1.580	0.271	0.055	-0.065	-0.983	0.000	0.000	0.000	0.000
878.629	9.244	0.131	0.282	1.574	0.276	0.058	-0.067	-0.980	0.000	0.000	0.000	0.000
878.651	9.249	0.133	0.279	1.579	0.279	0.053	-0.065	-0.982	0.000	0.000	0.000	0.000

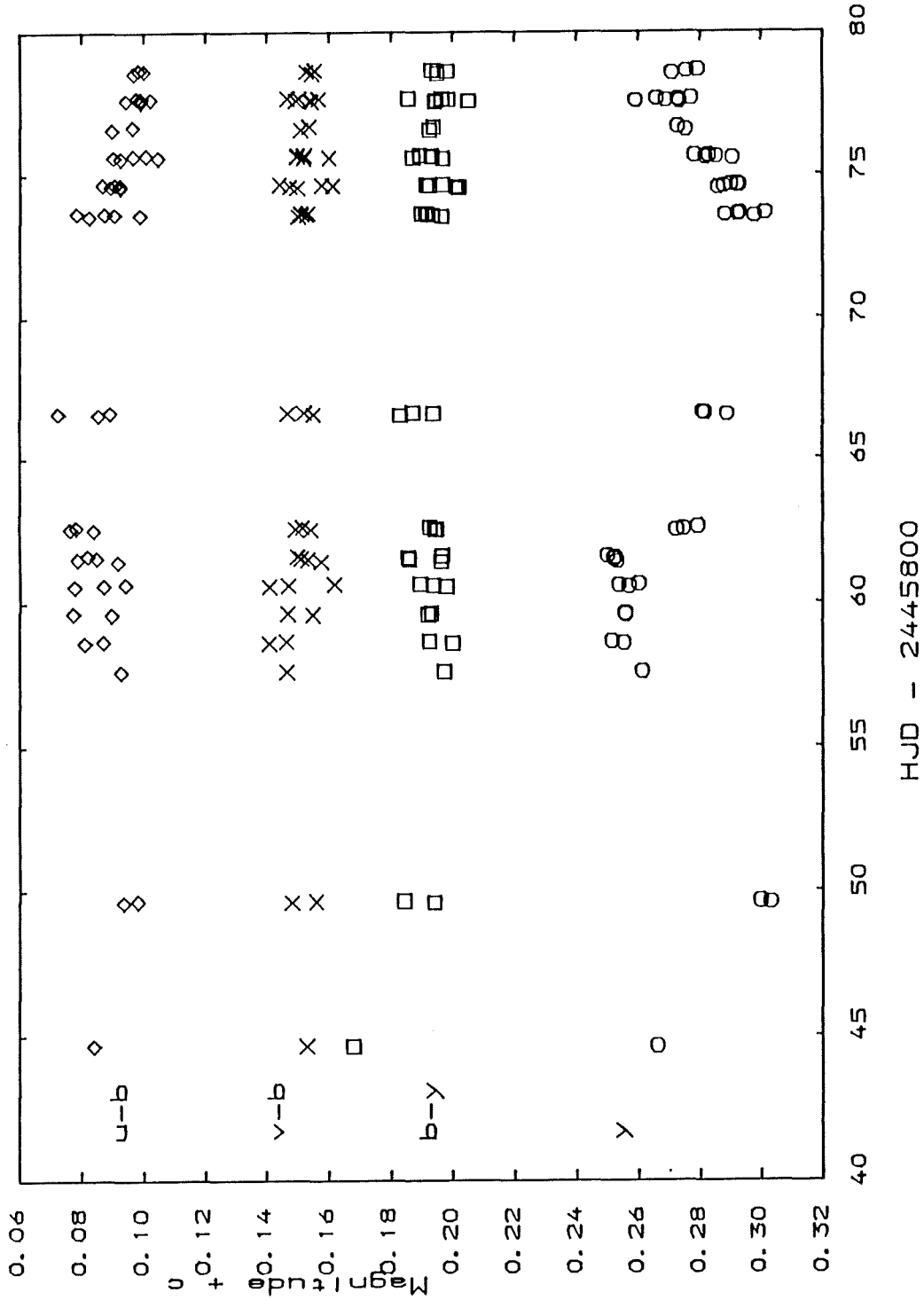


Figure 7.2 BD+1°4381 photometry

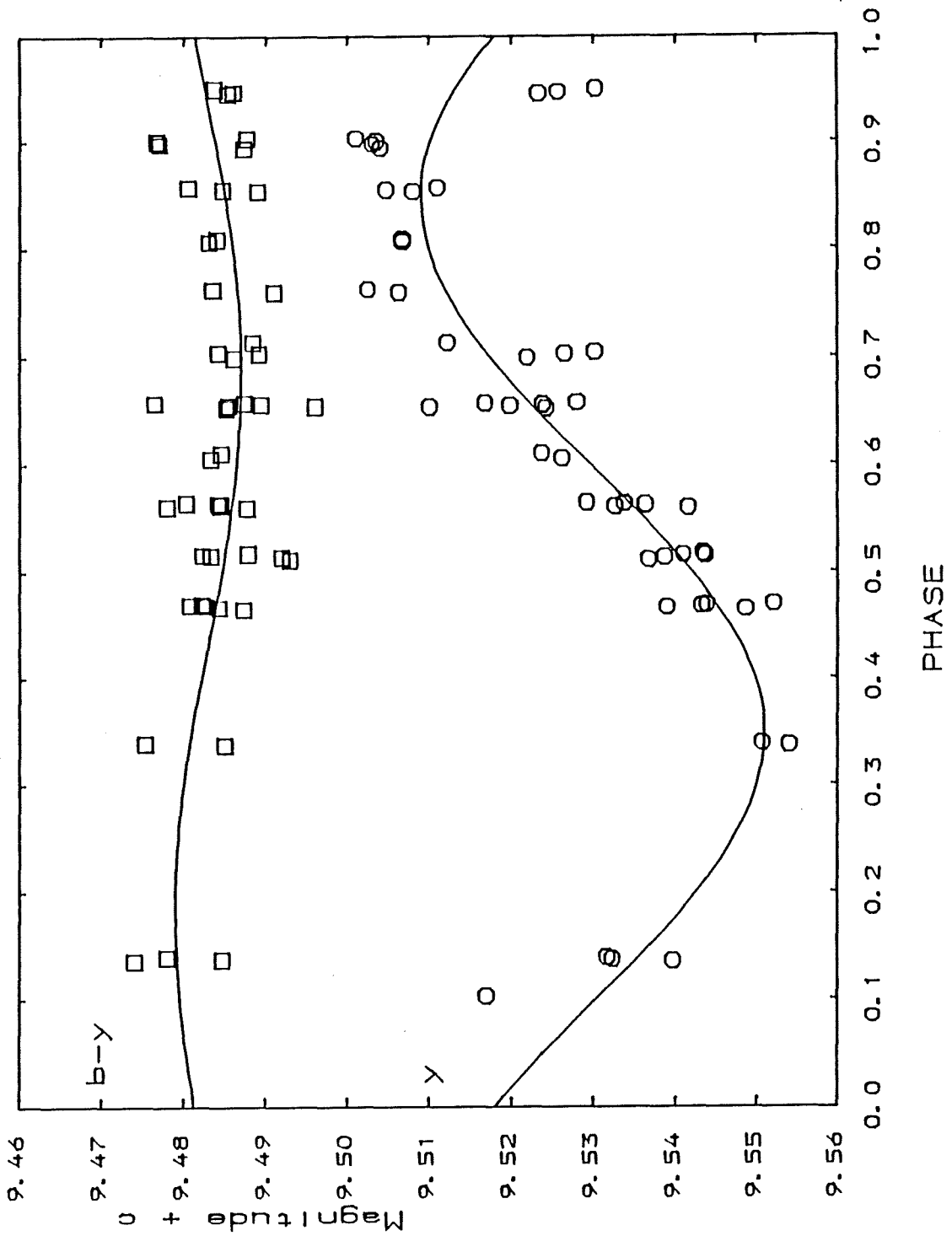


Figure 7.3 BD+1°4381 phased with period of 21.3 days

7.4) Conclusions

It has been established that the EHe star BD-9^o4395 is variable in its light output. Jeffery et al. (1985) also show that this star is variable in its radial velocity. A frequency analysis, although not conclusive, indicates that the photometric variations are multiply periodic, and the time-scales of the variations, together with an absence of detectable temperature changes accompanying the pulsation, suggest that the variability arises from non-radial g-mode oscillations in the star. Although the details of the frequency analysis are uncertain, this general conclusion is valid because the two principal periods, namely 3.5 and 11.2 days, have been determined unambiguously. The EHe star BD+1^o4381 has also been shown to be variable in its light output. A 21-day period is suggested which is consistent with pulsation in the fundamental radial mode. However, further observations are required of this star to properly test this hypothesis.

Variability has now been established in a number of EHe stars over a wide range of the effective temperature scale defined by Drilling et al. (1984). In addition to BD+13^o3224 (26500^oK), BD-9^o4395 (23000^oK), and BD+1^o4381 (9500^oK), photometric variability has been firmly established for HD160641 (31900^oK) and HD168476 (12400^oK) by Walker and Kilkenny (1980). Of these, HD160641 appears to have a period of 0.7 day, and HD168476, in addition to its photometric variability, shows small-amplitude radial-velocity variations (Walker and Hill 1985), but no periodicities have been detected in either its light or radial-velocity variations. On the other hand, BD+10^o2179 (17700^oK), as noted in section 7.1, and

HD124448 (15500°K) (Hill 1969) shows no evidence for variability, so that variability is clearly not a property of the class as a whole. In this context it is noted that Saio, Wheeler and Cox (1984) point out that the concept of an 'instability strip' for stars with high luminosity-to-mass ratios has little meaning because the blue edge of the instability region turns sharply bluewards at a luminosity which is a function both of stellar mass and composition, the critical luminosity increasing with increasing mass but decreasing with increasing metal abundance. The dichotomy between variability and non-variability amongst the EHe stars may, therefore, be a consequence of their different compositions, since Heber (1983) reports that the heavy metals in BD+10^o2179 are underabundant compared to HD168476 (Walker and Schönberner 1981) by one dex, the former star being the less luminous, also by one dex. A larger sample of abundance determinations and further variability studies, both observational and theoretical, are needed to test this hypothesis.

CHAPTER 8. CONCLUSIONS AND FUTURE WORK

8.1) Neutron Production in low-mass AGB and Post-AGB Stars

It was realised following the first discovery of helium shell flashes in AGB stars by Schwarzschild and Härm (1965,1967) that such flashes give rise to the possibility of ingestion of envelope material into the interior of these stars. Sanders (1967) showed how such mixing in low-mass AGB stars could lead to a potent source of neutrons via the sequence of reactions $^{12}\text{(p,\gamma)}^{13}\text{N}(\beta^+\gamma)^{13}\text{C}(\alpha,\text{n})^{16}\text{O}$. Until recently, most calculations on the possibility of hydrogen mixing on the AGB came to the conclusion that such mixing was prevented by an entropy barrier at the hydrogen burning shell (Iben 1976). Recent work by Iben and Renzini (1982a,b), however, show that envelope material can be ingested by a more indirect manner and that substantial neutron production takes place. It is also known that large scale ingestion of envelope matter can occur at the post-AGB phase of evolution since the hydrogen entropy barrier has decreased significantly at that stage (e.g. Fujimoto 1977). However, previous work concerned with the ^{13}C neutron source in low-mass stars (e.g. Sanders 1967; Despain 1977; Iben and Renzini 1982b) have been mainly concerned with the resulting build up of heavy elements and have not investigated in detail the parameters which could influence the level of neutron production in such stars. Since the level of the neutron flux has an important effect on the relative abundances of heavy element enhancements, it was decided to rectify this situation by carrying out a series of calculations which investigated the effects of different parameters and mixing mechanisms on the production of neutrons in low-mass AGB and post-AGB stars. In particular the effect of the

ingestion rate of envelope material, the initial abundances, the convective velocity, the degree of envelope mixing and the conditions of the intershell on the neutron production were all investigated.

The conclusions reached were that neutron densities covering a wide range (10^9 to 10^{14} neutrons/cm³) can be achieved under the range of parameter space and mixing model investigated. The main controlling factor in the neutron production was found to be the ingestion rate of the envelope matter into the intershell region of the star. The importance the initial intershell abundances was also found to be significant, particularly the initial ^{18}O and ^{22}Ne abundances. The ^{18}O , if at a high enough initial abundance, was found to compete favourably with ^{12}C for the available protons. This led to a reduction in the number of ^{13}C nuclei produced and consequently a reduction in the number of neutrons produced. If most of the ^{18}O forms ^{22}Ne via $^{18}\text{O}(\alpha, \gamma)^{22}\text{Ne}$ prior to any mixing, then an increase in the neutron density is found even though the ^{22}Ne acts to some extent as a neutron poison. The importance of including the effect of neutron absorptions by the heavy elements in any light particle network was stressed. The importance of the phenomenon of intershell splitting (Sweigart 1974) was also investigated. It was found that depending on the degree of envelope mixing, this phenomenon can have a very significant effect on neutron production. It was also established that since the mixing mechanism of Iben and Renzini (1982b) leads to the ^{13}C nuclei being burned at an early stage of a shell flash and consequently at cooler temperatures, the resulting neutron densities produced were significantly lower than any of the other mixing models investigated.

The two most plausible mixing mechanisms that can occur in low-mass AGB and post-AGB stars are mixing on the AGB by the mechanism by Iben and Reizini (1982a,b) (where the ^{13}C enriched region is ingested at roughly $10^{-3}M_{\odot}/\text{year}$), and mixing arising from a final helium shell flash while the star is in its post-AGB phase (ingestion again at roughly $10^{-3}M_{\odot}/\text{year}$ and the effect of intershell splitting included). It was found that neutron densities of typically 10^8 to 10^{11} neutrons/cm³ occur for the former mixing mechanism (i.e. on the AGB) while densities of typically 10^{14} neutrons/cm³ occur for the latter type of mixing mechanism. A determination of the neutron density which prevailed at the time of the synthesis of the heavy elements in low-mass stars (which are observed to have heavy element enhancements) would lead to an understanding as to what type of mixing event occurred in the star and at what phase of its evolution.

8.2) Heavy Element Production

Most previous detailed calculations regarding the synthesis of heavy elements have been concerned with more massive stars ($M > 3M_{\odot}$) since it is believed that the heavy elements produced in these stars are the main contributors to the solar system s-process distribution (e.g. Truran and Iben 1977). The neutron source believed to operate in these stars is the $^{22}\text{Ne}(\alpha, n)^{25}\text{Mg}$ source. The work which has been done on the ^{13}C source in low-mass stars (e.g. Despain 1977) again have mainly been concerned with attempts to model the solar system s-process distribution. Such calculations are of limited value for direct comparison of the observed enhancements of individual stars. In order

for such a comparison of theory and observation to be worthwhile new calculations were required which took into account several effects hitherto not included collectively in s-process synthesis calculations modelled on low-mass AGB and post-AGB stars. These effects included nuclear branching, the non-thermalisation of the excited states of several key nuclei and the time dependence of the neutron density. In addition to including these effects it was important to investigate the dependence of the heavy element enhancements on the type of mixing model and on the conditions of the intershell. Such a series of calculations were carried out and the results presented in chapter 4. Firstly the enhancements arising from a single mixing on the post-AGB were investigated. It was found that different values of the total enhancements and different relative enhancements occurred for the different conditions of the intershell, for the different mixing models and for the inclusion of the non-thermalised nuclei. These results are listed in tables 4.5 and 4.6.

The results of these single mixing calculations can be compared with those expected from repeated small scale mixing on the AGB arising from the mixing mechanism of Iben and Renzini (1982a,b). The parameter r which gives the fractional overlap of the intershells for successive helium shell flashes, was discovered to be a crucial parameter in the repeated mixing calculations. The final enhancements following 30 helium shell flashes for different values of r and different initial abundances are listed in tables 4.7 and 4.8. For the core mass, M_c , used in these calculations a value of $r=0.85$ is most appropriate. Again it was found that differences in the element enhancements occurred for the different conditions and models investigated. The most significant difference between the heavy element

abundances arising from a single mixing on the post-AGB and those arising from repeated mixing on the AGB is the shape of the distribution curve for the elements (see figure 6.8). The single mixing distributions give a more "peaked" shape structure than those distributions corresponding to repeated mixings. Such a difference in the distribution of the heavy elements provides an observational test for the type of mixing event which has occurred in a given star. A more exact observational test would be the determination of the individual isotopic abundances of the heavy elements. Such observations usually require very high resolution ($< 0.1\text{\AA}$) of the molecular band lines (e.g. Zr) in cool stars. These observations could be compared with the isotopic enhancements listed in tables 4.6 and 4.8 in order to estimate the level of the neutron density at which the synthesis of the heavy elements occurred and as to whether the envelope mixing was of the single or repeated nature.

8.3) Origin of the RCrB and EHe Stars

It has been discussed how previous to the new observations of the RCrB star U Aquarii presented here, it was believed that only a single mixing event could account for its observed heavy element enhancements. The new observations here show that this claim is no longer justified, since it is shown that within the observational uncertainties the observed enhancements can be modelled by both a single mixing event and a repeated mixing event. This can be seen from table 8.1 where calculations from single mixing and repeated mixing calculations are listed alongside the observed enhancements (relative to HD182040). The single mixing calculation is that of model G table 4.5 with a dilution

Table 8.1

Comparison of single with repeated mixing

	Single mixing	Repeated mixing	Observed
[Sr/Fe]	1.0	1.0	1.4 (+/-0.5)
[Y/Fe]	0.6	0.7	1.2 (+/-0.6)
[Zr/Fe]	0.7	0.5	0.4 (+/-0.4)

factor of $d=14$. The repeated mixing calculation is that of figure 4.13 taken after 11 flashes and assuming a dilution factor of $d=10$.

Unfortunately due to the fact that only the Sr/Fe, Y/Fe and Zr/Fe ratios can be measured with the present observations and also since these limited measurements have large errors associated with them, it is not possible at the present time to determine unambiguously the type of mixing event that occurred in U Aquarii. Future observations in comparison with the calculations presented here should be able to determine the mixing mechanism which occurred. However, some important points can still be made from a comparison of the presently determined heavy element ratios with the calculations. It was found that if a single mixing event occurred then it was more likely to be that due to a weak neutron exposure arising from a small amount of hydrogen ingestion ($< 2.5 \times 10^{-6} M_{\odot}$, e.g. model G table 4.5) since it can be seen from tables 4.5 and 6.1 that large single hydrogen mixing events (i.e. model B table 4.5) would not give the correct Zr/Y ratio for any dilution factor even after allowing for the large uncertainties in the observed enhancements). From the repeated mixing calculations, the calculation where the initial heavy element seed was taken as the solar values results in an Zr/Y ratio more in agreement with the observed ratio than the Zr/Y ratio calculated assuming an initial seed distribution at 1/10 the solar values. This can be seen from investigation of figures 4.9 to 4.20 and calculating the Y/Fe and Zr/Fe ratios for a given shell flash and given dilution factor. To suggest that the initial heavy element abundances in U Aquarii prior to any s-processing event were solar, would be compatible with the observed heavy element abundances of the other RCrB stars so far analysed, which are known not to have undergone

any significant s-process synthesis (see Schönberner 1975; Cottrell and Lambert 1982). That is, the initial distribution of the heavy elements in the RCrB stars would be the same. It was also found that the Zr/Sr, Zr/Y ratios arising from the calculations carried out at lower temperatures than those anticipated on the AGB or post-AGB, were lower than any of the previous calculations. Such low temperatures are more consistent with neutron synthesis at the helium core flash. It would be important then to determine from more accurate measurements whether or not U Aquarii has low Zr abundance relative to Sr and Y. However, due to the large uncertainties in the presently observed ratios, it would be tentative at best to suggest that this was indeed evidence of a hydrogen mixing event at the helium core flash having occurred in U Aquarii (this is the scenario suggested by Bond et al. 1979 as a possible explanation for the enhancements of U Aquarii). Any conclusion regarding this will have to await improved observational data. It has been shown however, how the Zr abundance relative to Sr and Y can be used as an important neutron density indicator and hence a good indicator of the temperature at which the nucleosynthesis occurred.

In summary, with regard to the origin of the extreme hydrogen deficiency in the RCrB star U Aquarii, the three proposed mixing scenarios viz., a single mixing at the helium core flash, a single mixing at the post AGB-phase and repeated mixing at the AGB phase are all still consistent with the present observations. Previously it was thought that only the single mixing scenarios were consistent. Of the two single mixing scenarios the helium core flash mixing results in the lower Zr/Y ratio. Both the single mixing scenarios can at least qualitatively account for the extreme hydrogen deficiency whereas the repeated mixing mechanism cannot. Although the repeated mixing on the

AGB would be consistent with the heavy element enhancements, such small scale mixing alone would not account for the loss of the large hydrogen envelope which an AGB star possess at this phase of its evolution. Some unknown mechanism would have to be invoked to account for the loss of the envelope.

With regard to the other RCrB stars and the EHe stars the question arises as to whether these stars too have excesses of s-process elements in their atmospheres. If the hydrogen deficiency of all these stars is formed by the same mixing mechanism then it could be expected that they too should have a distribution of heavy elements similar to those of U Aquarii. This makes the lack of any significant s-process enhancements in RCrB, XX Cam and RY Sgr (Schönberner 1975; Cottrell and Lambert 1982) somewhat confusing. If a hydrogen mixing event did occur in these stars then either the ^{13}C nuclei produced by the hydrogen burning were not mixed to a high enough temperature enabling them to react with alpha particles, or the s-process elements produced did not reach the stellar surface. Either way, why this should occur in RCrB, XX Cam and RY Sgr and not in U Aquarii is perplexing. Alternatively, perhaps a more plausible explanation is that the RCrB stars although having certain striking similarities have in fact evolved to their extreme hydrogen deficient state by different evolutionary paths. It is clear that a large amount of additional abundance analysis of the RCrB stars are required before any clarification of these problems will be forthcoming. The EHe stars are in general too hot for any s-process element spectral lines to be seen in the visible wavelengths. Such lines should however be present in the Ultra-Violet. Observations of the EHe stars should be carried out in this wavelength range in order to investigate this.

The importance of further photometric observations such as those presented in chapter 7 would help decide whether the RCrB stars themselves were all on a similar evolutionary path, in addition to identifying any link between them and the EHe stars. A detailed photometric study of U Aquarii would be very useful in this respect. A period determination and a rate of change of period determination of U Aquarii would give vital information with regard to its evolutionary status, since such observations could be compared with the same parameters already observed for RY Sgr (Alexander et al. 1972).

8.4) Future Analyses of RCrB Type Spectra

It is clear that in order to improve on the abundance analysis of U Aquarii presented in chapter 5, a wider region of the spectral region of U Aquarii should be observed. Ideally a fine analysis of this data should be carried out using model atmosphere spectral synthesis techniques. The present observational material did not warrant such a detailed analysis. However, it is worthwhile to carry out some preliminary model synthesis calculations in order to point out the difficulties which will be faced and which will have to be overcome in order to correctly synthesise the peculiar spectrum of this star (the same difficulties will be faced of course in analyses of the spectra of other RCrB stars).

For a normal stellar atmosphere the following parameters are usually required before a model atmosphere can be constructed, T_{eff} , $\log g$ and the microturbulent velocity v_t . T_{eff} is set by the requirement that the abundance of a species be independent of the lower excitation potential (χ) of the line. The surface gravity g is provided by the condition that neutral and ionised lines of an element give the same abundance. The third parameter, v_t is found from the requirement that individual abundances of a single species be independent of the reduced width ($\log W_\lambda/\lambda$). These three parameters could be found for U Aquarii from further spectroscopic observations. Of course in the coarse differential analysis presented in chapter 5 the determination of these parameters were not required as they were assumed to be the same for both stars.

A grid of model atmospheres for T_{eff} between 5000°K and 7000°K , and for $\log g$ between 0.0 and 1.0 was constructed in order to investigate what other parameters have a major effect on the atmospheric structure (and thus on the spectrum) of U Aquarii. The model atmospheres were generated under the U.K. Collaborative Computing Project No.7 (CCP7) by A.E. Lynas-Gray (University College London) and the author. The models were constructed using the model atmosphere program SAM1 (Wright and Argyos 1975), which was originally written and developed by R.L. Kurucz (1970). The latter two references discuss details of the model and the method of computation. This model atmosphere package makes the usual assumptions of plane parallel geometry, constant flux, radiative equilibrium and the validity of LTE. The computations were carried out using the University Of London Cray computer. The model atmospheres were then input into the spectral synthesis package SSG, written and

developed by R.A. Bell (University Of Maryland). This package was kindly supplied to the author by R.A. Bell. The basic techniques used for calculation of the synthetic spectra can be found in Bell (1970a,b). The package requires in addition to the model atmosphere the following parameters as input.

- i) Data on the wavelengths, oscillator strengths, excitation potentials and identification of thousands of spectral lines.
- ii) Element abundance ratios.
- iii) A Doppler broadening velocity and a damping constant.

The source of the data for the atomic lines is listed by Bell (1970a).

A stellar atmosphere corresponding to $T_{\text{eff}}=6500^{\circ}\text{K}$, $\log g=0.5$, a C/He ratio of 0.01 (by number) and a hydrogen abundance of $H=10^{-4}$ (by number) was generated. The input value for Sr was 25 times the solar value and the input Y was 25 times the solar value. Figures 8.1 and 8.2 show the synthesised spectra, using this model atmosphere, for the SrII 4077 and the YII 3950 lines respectively. The dashed line in these figures corresponds to the observed spectrum of U Aquarii. The synthesised spectra were binned and filtered in order to have the same resolution and instrumental profile of the observed spectrum. However the main problem of computing a synthesised spectrum for U Aquarii lies in determining accurately the abundances of the elements which are the main contributors to the continuous opacity. The C/He ratio is crucial in this respect. Since there is no a priori argument by which to determine the C/He ratio a spectroscopic determination is necessary.

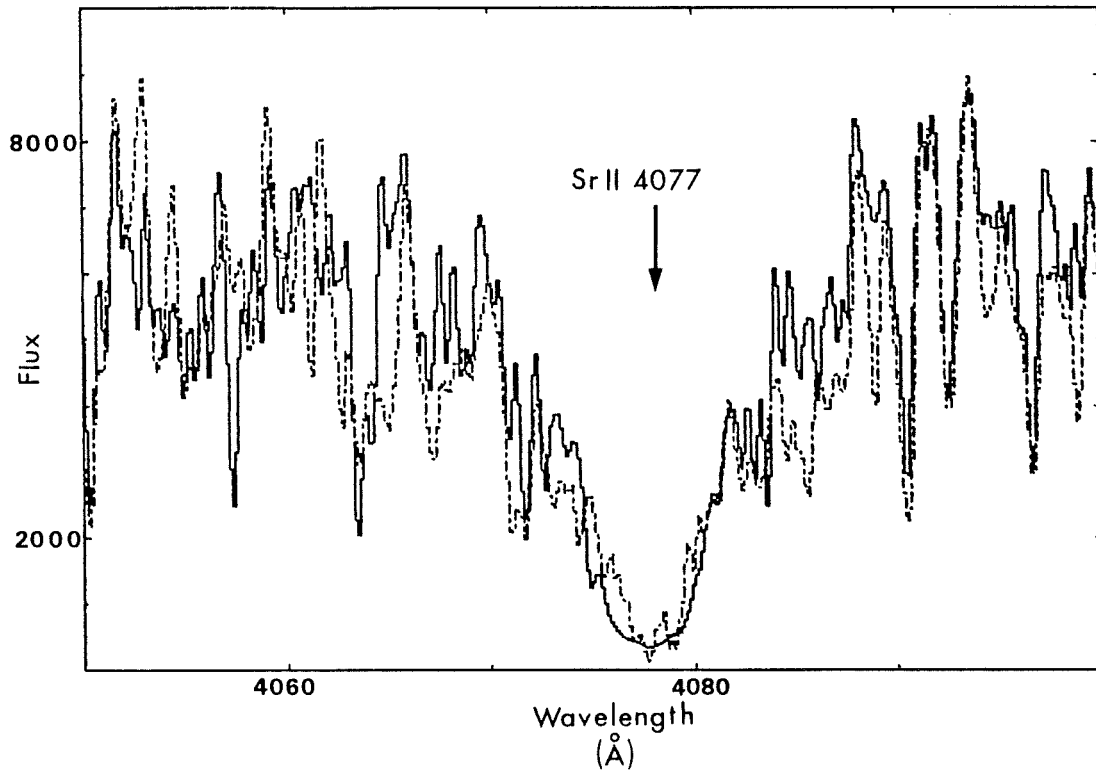


Figure 8.1 Synthesized SrII 4077 for C/He=0.01

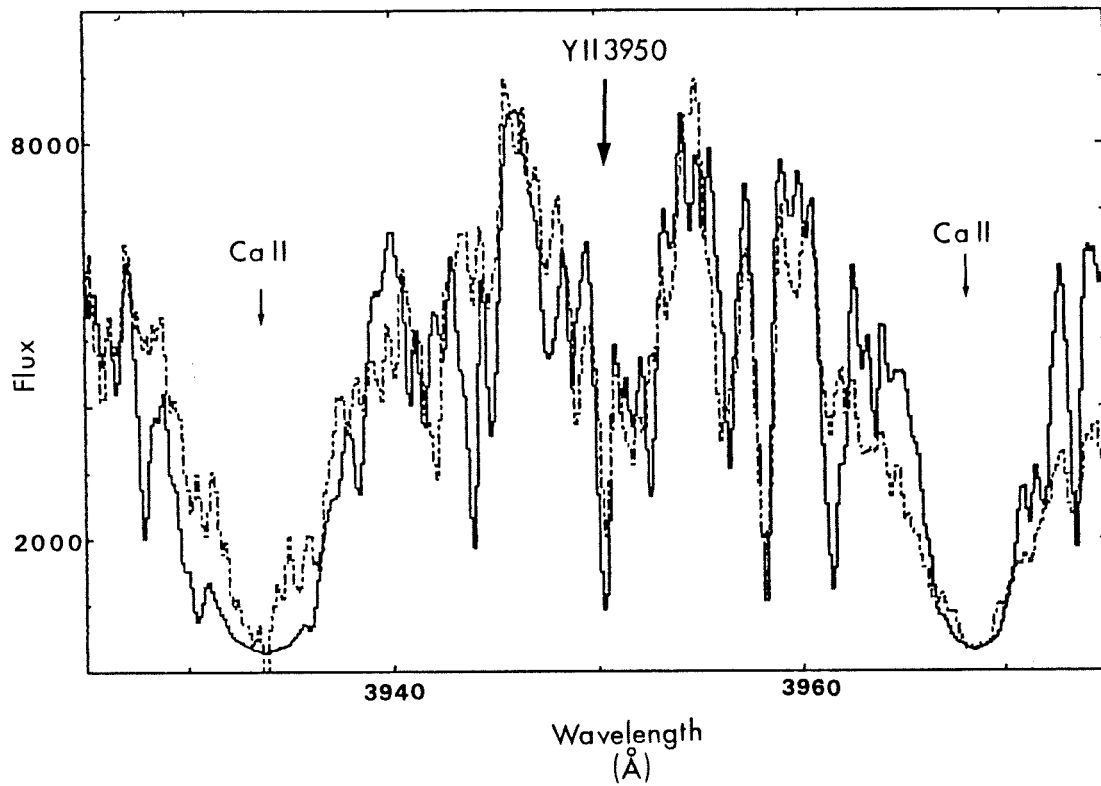


Figure 8.2 Synthesized YII 3950 for C/He=0.01

Also, since C is the leading contributor to the continuous opacity (Schönberner 1975), the C/He ratio will greatly effect the structure of the atmosphere and therefore must be determined before the spectrum can be synthesised. But since C is a minor species ($C \ll He$) it is crucial that an accurate determination of this ratio is found in order that an accurate abundance determination of the other elements can be made. This problem does not arise in normal stars since H is the most abundant species and the main contributor to the continuous opacity.

The SrII line of figure 8.1 was synthesised using for $C/He=0.01$. Figure 8.3 shows the synthesis for SrII using the same atmosphere except that $C/He=0.03$. Figure 8.4 repeats this only using $C/He =0.001$. The dashed line in these figures is the observed spectrum. The change in the SrII line profile can easily be seen for the different C/He ratios. This change is directly a result of the differing C/He ratios changing the value of the continuous opacity. The importance of determining the C/He ratio accurately is clearly apparent. Next to the photoionisation of carbon, C^- is the next most important opacity source in this type of atmosphere (Warner 1967, Cottrell and Lambert 1982). However, the model atmosphere package used here did not include this important opacity source. Before any accurate analysis of U Aquarii is attempted the C^- source should be included in the calculations.

Recently, Sackmann and Boothroyd (1985) have demonstrated the importance of carbon to the opacity of RCrB type atmospheres. They stress the importance of the carbon molecular opacities in cool atmospheres ($T_{\text{eff}} < 6000^{\circ}\text{K}$). They also make the interesting observation that computationally, the carbon opacity can be simulated by an equal

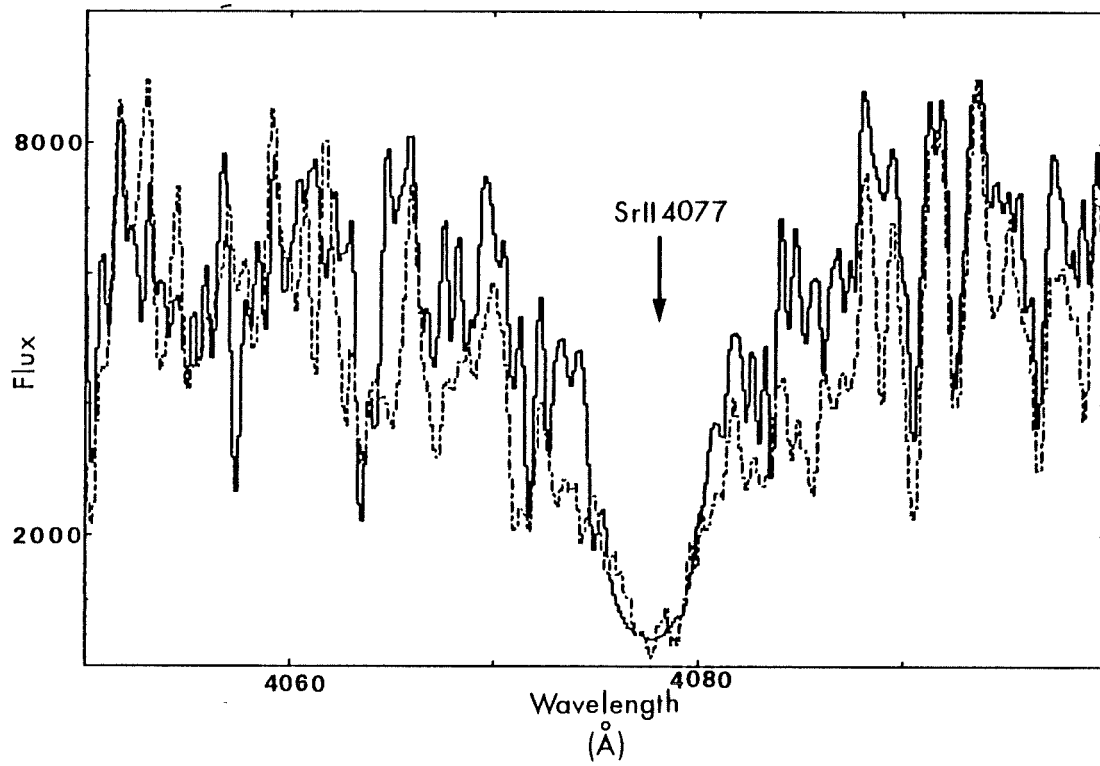


Figure 8.3 Synthesized SrII 4077 for C/He=0.03

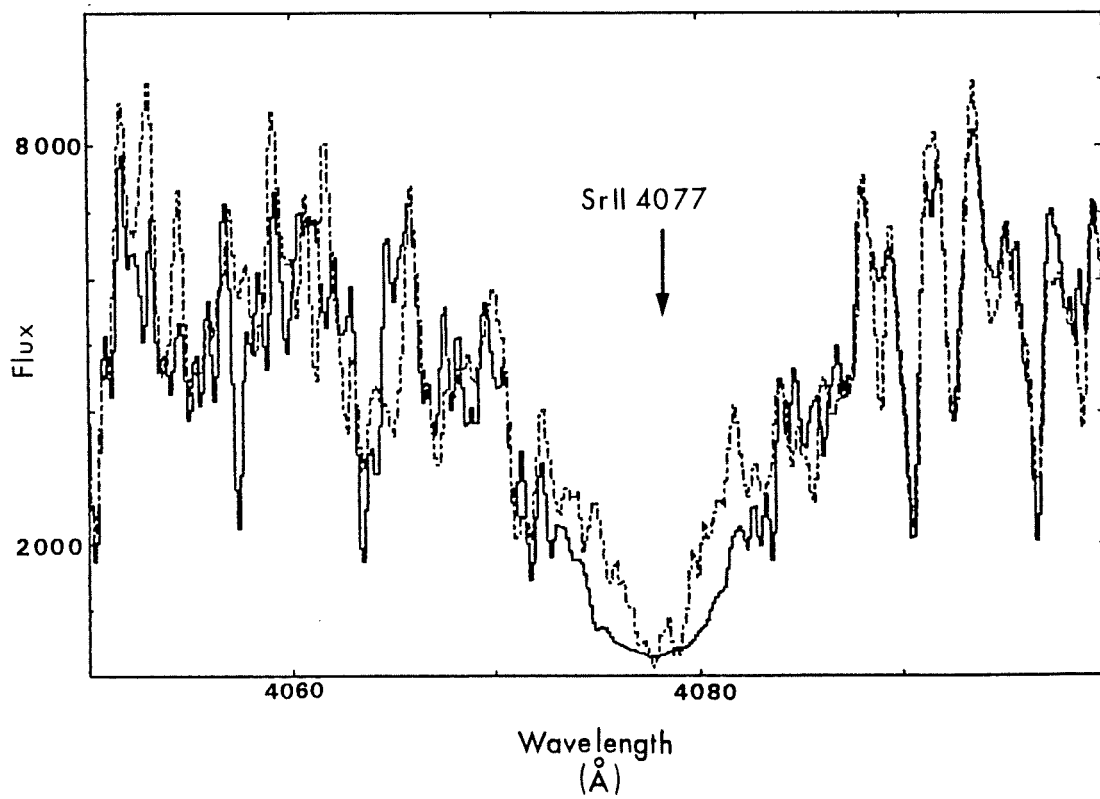


Figure 8.4 Synthesized SrII 4077 for C/He=0.001

mass of hydrogen. This is interesting since another unknown parameter which will have to be determined from the spectral synthesis is in fact the hydrogen abundance. The importance this can have on the synthesised spectrum is seen from comparison of figures 8.5 and 8.6. In figure 8.5 $T_{\text{eff}}=6500^{\circ}\text{K}$, $\log g=0.5$, $v_t=2\text{km/s}$ and the hydrogen abundance is set at $H=10^{-4}$. C/He is set at 0.01, and Sr and Y are both set as before at 25 times the solar value. In figure 8.6 the same parameters are used except the hydrogen abundance is set at 10^{-5} . As can be seen the hydrogen abundance even at these low abundance values can still have a significant effect on the spectrum. This is due to the H^- making a contribution to the continuous opacity. It is therefore clear that an accurate determination of the hydrogen depletion in U Aquarii is also desirable.

The spectral synthesis should also take into account the molecular opacities at low temperatures. Another important effect neglected is that of line blanketing. In the spectrum of U Aquarii, rich in spectral lines, the neglect of line blanketing could be a major source of error. In summary, in order to carry out an abundance analysis of U Aquarii utilising spectral synthesis techniques, the following parameters have to be determined. T_{eff} , $\log g$, v_t , C/He and the hydrogen abundance. Although clearly a difficult task, further high resolution observations of U Aquarii should be obtained in order that an accurate determination of the peculiar abundances of this important star be attempted.

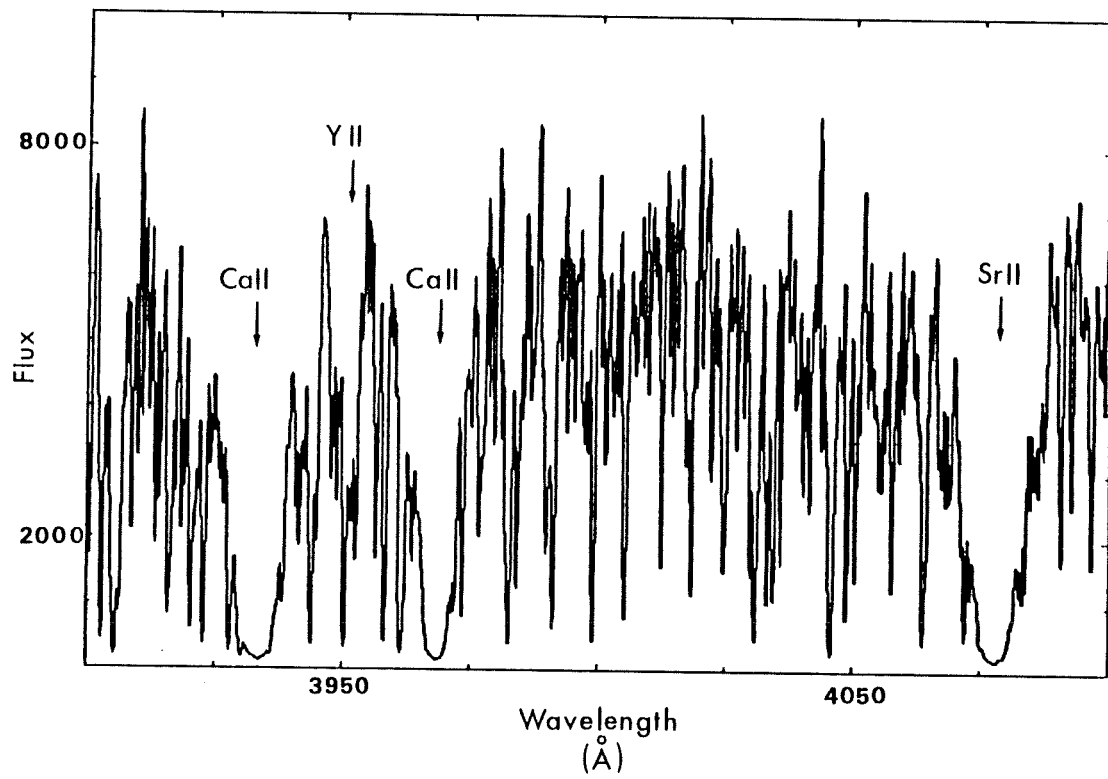


Figure 8.5 Synthesized spectra for $H=10^{-4}$

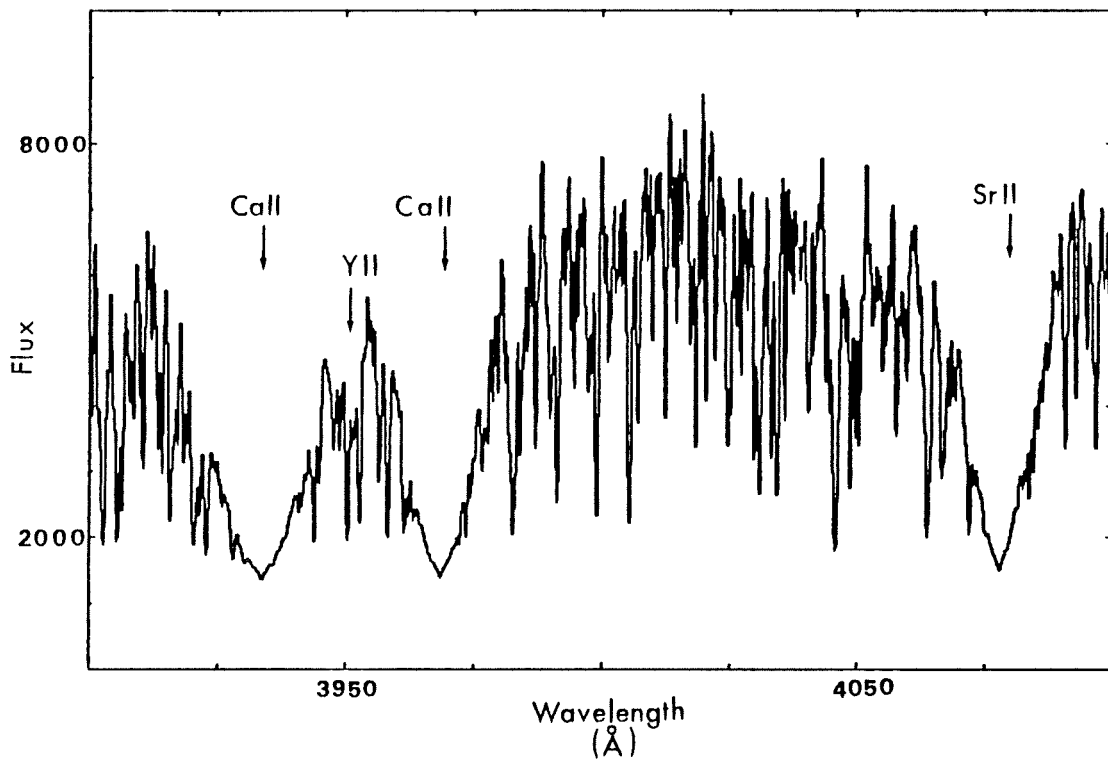


Figure 8.6 Synthesized spectra for $H=10^{-5}$

8.5) Future Calculations

The most significant source of error in the calculations presented in this thesis is in the treatment of the excess nuclear energy generated by the hydrogen mixing. For those ingestion rates which were believed to be high enough for the excess energy generation to have a significant effect on the structure of the stellar interior, an intershell splitting (Sweigart 1974) was simulated in a schematic manner. Apart from this, the effect of the the excess energy on the interior structure of the star was neglected. Such an approximation is usual in stellar nucleosynthesis calculations. Ideally the reaction networks used in these calculations should be directly coupled to an evolutionary stellar model. However, such calculations would be very difficult due to the problems of properly accounting for the energy generation from each reaction in a fully convective region of a star (the lifetime of a proton in the intershell roughly equals the convective turnover time), and they would also be very expensive with regard to computing time. The intrinsic uncertainties in such calculations would not warrant such a large amount of effort until such time as a more proper treatment of stellar convection theory was available.

Future calculations could however improve on the schematic treatment of turbulent diffusion that was used in the neutron production calculations presented here, and on the assumption of an average flux in the heavy element calculations. This could be achieved by the inclusion of the diffusion equation

$$\frac{dY_i}{dt} = \frac{1}{\rho r^2} \frac{d}{dr} \left[\rho r^2 D \frac{\partial Y_i}{\partial r} \right]$$

into the reaction network. In this equation Y_1 is the number fraction of an isotope at a distance r from the stellar centre at time t . ρ is the mass density and D is the diffusion coefficient. The inclusion of this equation, however, further compounds the problem by coupling the abundance at a point not only to all other abundances locally but also to the abundance everywhere else in the intershell region. This has the effect of changing the size of the matrix to be solved from an $n \times n$ matrix to an $(n \times z) \times (n \times z)$ matrix, where z is the number of zones used in the calculation (in these calculations $z=50$). It is therefore clear that a large increase in computational time required could be expected as the price for a more exact treatment of diffusion (c.p.u. time goes as m^3 , m being the order of the matrix). Such calculations should be worthwhile if a new and faster numerical technique was developed. Although the most significant s-process enhancements which would be observable in low-mass AGB stars would be expected to be roughly at the Sr-Y magic peak, it would be worthwhile extending the calculations presented here to higher mass regions. A reaction network similar to that of figure 2.4 extending up to the Ba magic peak would be of particular value.

To summarise, although the calculations presented here should be useful for comparison with observations of heavy element enhancements in the Fe to Mo region, future calculations which take into account the effect of the excess energy generation on the structure and evolution of the star, a more exact treatment of turbulent diffusion and an extension of the heavy element reaction network would be desirable as more observational material became available. Since such calculations would present a significant challenge, as would further observations and

analyses of RCrB and related stars, a great deal of interesting and demanding work is anticipated in the future.

APPENDIX

The nuclear properties of the isotopes in the Fe to Mo range used in the calculations given in chapter 4 are presented here. The thermally averaged neutron absorption cross sections for 30 KeV are given in millibarns (mb). The beta decay, electron capture and gamma decay half lives are given in seconds. The isomeric nuclei included in the calculations are listed separately. The isomeric branching ratio, f , listed for these nuclei, gives the fraction of the isotope which is in its ground state.

Isotope	Cross Section (mb)	Electron Emission	Electron Capture	Positron Emission
^{54}Fe	28			
^{55}Fe	46.6		5.2 (8)	
^{56}Fe	13.5			
^{57}Fe	30			
^{58}Fe	16			
^{59}Fe	12	3.8 (6)		
^{60}Fe	4	9.4 (12)		
^{59}Co	35			
^{60}Co	53	1.5 (7)		
^{61}Co	26	5943		
^{62}Co	30	834		
^{58}Ni	29			
^{59}Ni	73		1.2 (13)	9.6 (14)
^{60}Ni	30			
^{61}Ni	80			
^{62}Ni	20			
^{63}Ni	24	1.8 (8)		
^{64}Ni	15			

Isotope	Cross Section (mb)	Electron Emission	Electron Capture	Positron Emission
^{65}Ni	19	9097		
^{66}Ni	20	1.96 (5)		
^{63}Cu	49			
^{64}Cu	62	1.2 (5)	6.6 (5)	2.6 (5)
^{65}Cu	42			
^{66}Cu	75	297		
^{67}Cu	22	2.23 (5)		
^{64}Zn	50			
^{65}Zn	144		7.1 (7)	3 (8)
^{66}Zn	40			
^{67}Zn	160			
^{68}Zn	23			
^{69}Zn	160	3480		
^{70}Zn	16			
^{69}Ga	130			
^{70}Ga	287	1266		
^{71}Ga	120			
^{72}Ga	245	5.1 (4)		
^{73}Ga	100	1.76 (4)		
^{70}Ge	67			
^{71}Ge	436		5.9 (6)	
^{72}Ge	65			
^{73}Ge	270			
^{74}Ge	35			
^{75}Ge	130	2.98 (5)		
^{76}Ge	53			
^{77}Ge	68	4.07 (4)		

Isotope	Cross Section (mb)	Electron Emission	Electron Capture	Positron Emission
^{78}Ge	30	5292		
^{75}As	490			
^{76}As	723	9.51 (4)		
^{77}As	214	1.4 (5)		
^{78}As	250	5460		
^{79}As	400	540		
^{76}Se	100			
^{77}Se	340			
^{78}Se	60			
^{79}Se	200	3 (9)		
^{80}Se	20			
^{81}Se	20	1116		
^{82}Se	36			
^{83}Se	31	1380		
^{79}Br	600			
^{80}Br	579	1400	1.2 (5)	4.9 (4)
^{81}Br	317			
^{82}Br	584	1.28 (5)		
^{83}Br	200	8681		
^{84}Br	200	1908		
^{80}Kr	140			
^{81}Kr	1030		7.1 (11)	
^{82}Kr	80			
^{83}Kr	225			
^{84}Kr	28			
^{85}Kr	152	3.2 (8)		
^{86}Kr	4.6			
^{87}Kr	20	4552		

Isotope	Cross Section (mb)	Electron Emission	Electron Capture	Positron Emission
⁸⁸ Kr	10	1 (4)		
⁸⁵ Rb	360			
⁸⁶ Rb	476	1.6 (6)	2.6 (9)	
⁸⁷ Rb	14	4.2 (17)		
⁸⁸ Rb	71	1068		
⁸⁹ Rb	50	924		
⁸⁶ Sr	74			
⁸⁷ Sr	109		5.3 (17)	
⁸⁸ Sr	6.9			
⁸⁹ Sr	46	4.5 (6)		
⁹⁰ Sr	20	8.89 (8)		
⁹¹ Sr	40	3.48 (4)		
⁹² Sr	80	9792		
⁹³ Sr	20	480		
⁹⁴ Sr	20			
⁸⁸ Y	1364			
⁸⁹ Y	21			
⁹⁰ Y	162	2.3 (5)		
⁹¹ Y	21	5.1 (6)		
⁹² Y	467	1.27 (4)		
⁹³ Y	285	3.67 (4)		
⁹⁴ Y	40	1218		
⁹⁵ Y	50	654		
⁹⁰ Zr	12			
⁹¹ Zr	68			
⁹² Zr	34			
⁹³ Zr	81	4.6 (13)		
⁹⁴ Zr	20			

Isotope	Cross Section (mb)	Electron Emission	Electron Capture	Positron Emission
^{95}Zr	72	5.5 (6)		
^{96}Zr	30			
^{97}Zr	26	6.12 (4)		
^{93}Nb	285			
^{94}Nb	534	1.4 (4)	2.7 (13)	
^{95}Nb	285	3 (6)		
^{96}Nb	534	2.3 (4)		
^{97}Nb	290	4320		
^{94}Mo	80			
^{95}Mo	430			
^{96}Mo	90			
^{97}Mo	350			
^{98}Mo	150			
^{99}Mo	201	2 (5)		
^{100}Mo	100			
^{101}Mo	171	876		
^{102}Mo	100	660		
^{99}Tc	800	1.4 (9)		
^{100}Tc	999	16.6		
^{102}Tc	500	840		
^{102}Tc	800	5		

Isomers

Isotope	Cross Section (mb)	Electron Emission	Positron Emission	Gamma Decay	f
^{69}Zn	160			5 (4)	0.082
^{85}Kr	152	1.98 (4)		7.9 (4)	0.32
^{87}Sr	109		1 (6)	1.4 (6)	0.993
^{90}Y	162	6.3 (7)		1.1 (4)	0.455

REFERENCES

- Acker, A., 1983. *Astron. Astrophys. Suppl.*, 54, 293.
- Aleneida, J. & Käppelen, F., 1983. *Astrophys. J.*, 265, 417.
- Alexander, J.B., Andrews, P.J., Catchpole, R.M., Feast, M.W., Lloyd Evans, T., Menzies, J.W., Wisse, P.N.J. & Wisse, M., 1972. *Mon. Not. R. astr. Soc.*, 158, 305.
- Allen B.J., Gibbons J.H., & Macklin R.L., 1971. *Adv. Nuc. Phys.* 4, 205.
- Allen, B.J. & Macklin, R.L., 1980, private comm. from Woosley, S.E.
- Aller, L.H., 1954. *Liege Collection in 8^{VO} XV*, No. 357, 353.
- Arnett, W.D. & Truran, J.W., 1969. *Astrophys. J.*, 157, 339.
- Bachall, J.N., 1962. *Phys. Rev.*, 126, 1143.
- Bachall, J.N., 1966. *Phys. Rev. Letters*, 17, 398.
- Bateman, H., 1910. *Proc. Cambridge Phil. Soc.*, 15, 423.
- Bateson, F.M., 1972. *Info. Bull. Variable Stars* No. 661.
- Beer, H., Spencer, R.R. & Ernst, A., 1979. *Astr. Astrophys.*, 37, 197.
- Bell, R.A., 1970a. *Mon. Not. R. astr. Soc.*, 148, 25.
- Bell, R.A., 1970b. *Mon. Not. R. astr. Soc.*, 149, 179.
- Bethe, H.A., 1937. *Rev. Mod. Phys.*, 9, 69.
- Bidelman, W.P., 1952. *Astrophys. J.*, 116, 227.
- Blake, J.B. & Schramm, D.N., 1975. *Astrophys. J.*, 197, 615.
- Blatt, J.M. & Weisskopf, V.F., 1952. *Theoretical Nuclear Physics*, New York-Wiley.
- Bond, H.E., Luck, R.E. & Newman, M., 1979. *Astrophys. J.*, 233, 205.
- Breit, G. & Wigner, E., 1936. *Phy. Rev.*, 49, 519.
- Brillioun, L., 1926. *J. Phys. Radium*, 7, 353.
- Bues, I., 1970. *Astr. Astrophys.*, 7, 91.
- Burbidge, E.M., Burbidge, J.R., Fowler, W.A. & Hoyle, F., 1957. *Rev. Mod. Phys.* 29, 597.
- Burstein, D. & Heiles, G., 1978. *Astrophys. J.*, 225, 40.
- Cameron, A.G.W., 1981. *Essays In Nuclear Astrophysics*, p23. Eds. Barnes, C.A., Clayton, D.D. & Schramm, D.N. (Cambridge Univ. Press).
- Cameron, A.G.W. & Fowler, W.A., 1971. *Astrophys. J.*, 154, 111.
- Cameron, A.G.W., 1955. *Astrophys. J.*, 121, 144.

- Cameron, A.G.W., 1960. *Astron. J.*, 65,485.
- Chiu, H.-Y., 1968. *Stellar Physics*. (Blaisdell. Massachusetts, Toronto, London)
- Christy-Sackmann, I.J. & Paczynski, B., 1975. *Mem. Roy. Soc. Liege Ser. 6*, 8,335.
- Clayton, D.D. & Ward, R.A., 1974. *Astrophys. J.*, 193,197.
- Clayton, D.D., Fowler, W.A., Hull, T.C. & Zimmerman, B.A., 1961, *Ann. Phys.* 12,21 (CFHZ).
- Clayton, D.D., 1968. *Principles of Stellar Evolution and Nucleosynthesis* (New York, McGraw-Hill).
- Cohens, J.G. & Philips, A.C., 1980. *Astrophys. J.*, 237,99.
- Cole, P.W. & Deupree, R.G., 1980. *Astrophys. J.*, 239,284.
- Cole, P.W. & Deupree, R.G., 1981. *Astrophys. J.*, 247,607.
- Conte, S.D. & Boor, C.de, 1965. *Elementary Numerical Analysis* (McGraw-Hill Kogakusha).
- Coryell, C.D., 1956. *Laboratory for Nuclear Studies, MIT Ann. Rept.*
- Cosner, K., 1982. *Phd. Thesis, University of Illinois.*
- Cosner, K., Iben, I. Jr. & Truran, J.W., 1982. *Astrophys. J.*, 238,L91.
- Cottrell, P.L. & Lambert, D.L., 1982. *Astrophys. J.*, 261,595.
- Couch, R.G., Schmiedekamp, A.B. & Arnett, W.D., 1974. *Astrophys. J.*, 190,95.
- Cowan, J.J. & Rose, W.K., 1977. *Astrophys. J.*, 212,149.
- Cox, J.P., 1980. 'Theory of Stellar Pulsation', Princeton University Press, Princeton, New Jersey.
- Crawford, D.L. & Barnes, J.V., 1970. *Astr. J.*, 75,978.
- Danziger, I. J., 1965. *Mon. Not. R. astr. Soc.*, 130,199.
- Demarque, P. & Mengel, J.G., 1971. *Astrophys. J.*, 164,317.
- Dennis, T. R., 1971. *Astrophys. J.*, 167,311.
- Despain, K.H., 1977. *Astrophys. J.*, 212,774.
- Deupree, R.H., 1984a. *Astrophys. J.*, 282,274.
- Deupree, R.H., 1984b. *Astrophys. J.*, 287,268.
- Deupree, R.H. & Cole, P.W., 1983. *Astrophys. J.*, 269,676.
- Drilling, J.S., 1973. *Astrophys. J.*, 179,L31.
- Drilling, J.S., 1978. *Astrophys. J.*, 223,L29.
- Drilling, J.S., 1979. *Astrophys. J.*, 228,491.

- Drilling, J.S., Schönberner, D., Heber, U. & Lynas-Gray, A.E., 1984. *Astrophys. J.*, 278, 224.
- Duff, I.S., 1980. U.K. Atomic Energy Authority, A.E.R.E. R-8730.
- Eddington, A.S., 1917. *Mon. Not. R. astr. Soc.*, 77, 16.
- Eddington, A.S., 1926. *The Internal Constitution of the Stars*. Cambridge Univ. Press.
- Feast, M.W., 1975. in IAU Symposium 67, p129, Eds. Sherwood, V.E & Plaut, L.
- Feast, M.W., 1978. IAU Colloquium No. 46, 246.
- Fernie, J.D., 1972. *Q. J. Roy. Soc.*, 13, 81.
- Fernie, J.D., Sherwood, V. & Dupuy, D.L., 1972. *Astrophys. J.*, 172, 383.
- FitzGerald, M.P., 1968. *Astr. J.* 73, 983.
- Fowler, W.A. & Hoyle, F., 1964. *Astrophys. J. Suppl.*, 9, 201.
- Fowler, W.A. & Vogl, J.L., 1964. *Lectures in Theoretical Physics VI*, 379, University of Colorado Press.
- Fowler, W.A., Caughlan, G.R. & Zimmerman, B.A., 1967. *Ann. Rev. Astr. Astrophys.* 5, 525.
- Fowler, W.A., Caughlan, G.R. & Zimmerman, B.A., 1975. *Ann. Rev. Astr. Astrophys.* 13, 69.
- Froberg, C.E., 1955. *Rev. Mod. Phys.*, 27, 399.
- Fujimoto, M.Y., 1977. *Publ. Astron. Soc. Japan* 29, 331.
- Fujimoto, M.Y., Nomoto, K. & Sugimoto, D., 1976. *Pub. Astr. Soc. Japan*, 28, 89.
- Gamow, G., 1928. *Z. Physik* 51, 204.
- Giannone, P. & Weigart, A., 1967. *Zs. f. Ap.*, 67, 41.
- Gingold, R.A., 1974. *Astrophys. J.*, 193, 177.
- Glasby, J.S., 1968. *Variable Stars*. Anchor Press, Essex.
- Glass, I.S., 1978. *Mon. Not. R. astr. Soc.* 185, 23.
- Gould, N.L., Herbig, G.H. & Morgan, W.W., 1957. *Publ. astr. Soc. Pacific*, 69, 242.
- Grauer, A.D., Drilling, J.S. & Schönberner, D., 1984. *Astr. Astrophys.*, 133, 285.
- Greenstein, J.L. & Wallerstein, G., 1958. *Astrophys. J.*, 127, 239.
- Grønbech, B., Olsen, E.H. & Strömberg, B., 1976. *Astr. Astrophys. Suppl.*, 26, 155.
- Gurney, R.W. & Condon, E.U., 1928. *Phys. Rev.* 33, 127.
- Gurney, R.W. & Condon, E.U., 1928. *Nature*, 122, 493.
- Hack, M., 1967. *Modern Astrophysics*, Gauthier-Villars, Paris.

- Halperian, J., Johnson, C.H., Winters, R.R. & Macklin, R.L., 1980. Phys.Rev.C 21,545.
- Hamann, W.-R., Schönberner, D. & Heber, U., 1982. Astr.Astrophys., 116,273.
- Härm, R. & Schwarzschild, M., 1964. Astrophys.J., 139,594.
- Härm, R. & Schwarzschild, M., 1966. Astrophys.J., 145,496.
- Härm, R. & Schwarzschild, M., 1975. Astrophys.J., 200,324.
- Harris, D.L., 1963. Basic Astronomical Data, p263, Ed. Strand K.A. (University of Chicago Press).
- Harris, M.J., Fowler, W.A., Caughlan, G.R. & Zimmerman, B.A., 1984. Ann.Rev. Astr.Astrophys. 21,165.
- Heber, U., 1983. Astr.Astrophys., 118,39.
- Heiles, G., 1976. Astrophys.J., 204,379.
- Henize, K., 1961. Publ.astr.Soc.Pacific, 73,159.
- Henry, C.G. & Ulrich, R.K., 1972. Astrophys.J., 173,109.
- Herbig, G.H., 1967. Trans. IAU A13,530.
- Herbig, G. & Boyarchuk, A. 1968. Astrophys.J., 153,397.
- Hill, P.W., 1964. Mon.Not.R.astr.Soc. 127,113.
- Hill, P.W., 1965. Mon.Not.R.astr.Soc. 129,137.
- Hill, P.W., 1969. Inf. Bull. Variable Stars No. 357.
- Hill, P.W., 1970. Obs., 90,10.
- Hill, P.W., Lynas-Gray, A.E. & Kilkenny, D., 1984. Mon.Not.R.astr.Soc., 207,823.
- Hill, P.W., Kilkenny, D., Schönberner, D. & Walker, H.J., 1981. Mon.Not.R.astr. Soc., 197, 81.
- Holden, N.E., & Walker, F.W., 1972. Chart of the Nuclides. Gen.Elect. Energy Division.
- Holmes, J.A., Woosley, S.E., Fowler, W.A. & Zimmerman, B.A., 1976. Atomic Data and Nuclear Data Tables, Vol 18, 4,306.
- Horowitz, P., Papiolios, C. & Carleton, N.P., 1971. Astrophys.J. 163,L5.
- Hoshi, R., 1968. Progr.Theoret.Phys. (Kyoto) 39,957.
- Hull, M.H., & Breit, G., 1959. Handbuch der Physik Vol. XLI p408.
- Humphrey, R. & Ney, P., 1974. Astrophys.J., 190,339.
- Hunger, K., 1975. Problems In Stellar Atmospheres p57. Ed. Baschak, B., Kegel, W.H. & Traving, G. (Springer-Verlag).

- Hunger, K. & Klinglesmith, D.A., 1969. *Astrophys. J.*, 157, 721.
- Hunger, K., Schönberner, D. & Steenbock, W., 1982. *Astr. Astrophys.* 107, 93.
- Iben, I. Jr., 1967. *Rev. Astron. Astroph.* 5, 571.
- Iben, I. Jr., 1975a. *Astrophys. J.*, 196, 525.
- Iben, I. Jr., 1975b. *Astrophys. J.*, 196, 549.
- Iben, I. Jr., 1976. *Astrophys. J.*, 208, 165.
- Iben I. Jr., 1977. *Astrophys. J.*, 217, 788.
- Iben I. Jr., 1982. *Astrophys. J.*, 260, 821.
- Iben, I. Jr., 1983. *Astrophys. J.*, 275, L65.
- Iben, I. Jr. & Truran, J.W., 1978. *Astrophys. J.*, 220, 980.
- Iben, I. Jr. & Renzini, A., 1982a. *Astrophys. J.*, 259, L79.
- Iben, I. Jr. & Renzini, A., 1982b. *Astrophys. J.*, 263, L23.
- Iben, I. Jr. & Tutukov, A.V., 1985. Preprint.
- Iben, I. Jr., Kaler, J.B., Truran, J.W. & Renzini, A., 1983. *Astrophys. J.*, 264, 605.
- Jeffery, C.S., 1984. *Mon. Not. R. astr. Soc.*, 210, 731.
- Jeffery, C.S. & Malaney, R.A., 1985. *Mon. Not. R. astr. Soc.*, 213, L61.
- Jeffery, C.S., Skillen, I., Hill, P.W., Kilkenny, D., Malaney, R.A. & Morrison, K., 1985. *Mon. Not. R. astr. Soc.*, (in press).
- Kaufmann, J.P. & Schönberner, D., 1977. *Astr. Astrophys.*, 57, 169.
- Kilkenny, D., 1982. *Mon. Not. R. astr. Soc.*, 200, 1019.
- Kilkenny, D., 1984. private communication.
- Kilkenny, D. & Lynas-Gray, A.E., 1982. *Mon. Not. R. astr. Soc.*, 198, 873.
- Kilkenny, D. & Flanagan, C., 1983. *Mon. Not. R. astr. Soc.*, 203, 19.
- Kilkenny, D. & Whittet, D.C.B., 1984. *Mon. Not. R. astr. Soc.*, 208, 25.
- Kilkenny, D. & Lynas-Gray, A.E., 1984. *Mon. Not. R. astr. Soc.*, 208, 673.
- Kippenhanh, R., 1967. *Zs. f. Ap.*, 67, 271.
- Klemola, A.R., 1961. *Astrophys. J.*, 134, 130.
- Kramers, H.A., 1926. *Z. Physik*, 39, 828.
- Kurucz, R.L., 1970. SAO Special Report No. 309.
- Lamb, S.A., Howard, W.M., Truran, J.W. & Iben, I. Jr., 1977. *Astrophys. J.*,

217,213.

Landolt, A.U., 1968. Publ. astr. Soc. Pacific, 80, 318.

Landolt, A.U., 1973. Publ. astr. Soc. Pacific, 85, 661.

Landolt, A.U., 1975. Astrophys. J., 196, 789.

Langer, G.E., Kraft, R.P. & Anderson, K.S., 1974. Astrophys. J., 189, 509.

Lesh, J.R. & Aizenman, M.L., 1974. Astr. Astrophys., 34, 203.

Levy, E.H. & Rose, W.K., 1974. Astrophys. J., 193, 419.

Loumos, G.L. & Deeming, T.J., 1978. Astrophys. Space Sci., 56, 285.

Lovy, D., Maeder, A., Noels, A. & Gabriel, M., 1984. Astr. Astrophys., 133, 307.

Lynas-Gray, A.E., Schönberner, D., Hill, P.W. & Heber, U., 1984. Mon. Not. R. astr. Soc., 209, 387.

MacConnell, D.J., Frye, R.L. & Bidelman, W.P., 1972. Publ. astr. Soc. Pacific, 84, 388.

Maeder, A., 1983. Astr. Astrophys., 120, 113.

Malaney, R.A., 1985. Mon. Not. R. astr. Soc., 216, 743

Marraco, H.G. & Milesi, G., 1982. Astron. J., 87, 1775.

Mayall, M.W., 1972. J. Roy. Astron. Soc. Can., 66, 233.

Mendoza, V.E.E. & Johnson, H.L., 1965. Astrophys. J., 141, 161.

Merrill, P.W., 1952. Science 115, 485.

Michaud, G., Scherk, L. & Vogt, E. 1970. Phys. Rev. C, 1, 864.

Milne, A.E., 1921. Mon. Not. R. astr. Soc., 81, 361.

Milne, A.E., 1930. Handbuch der Astrophysik 3, 80.

Musgrove, A.R. de L., Allen, B.J., Bolderman J.W., Chan, D.M.H. & Macklin, R.L., 1976. Nucl. Phys. A, 259, 365.

Musgrove, A.R. de L., Allen, B.J., Bolderman J.W., Chan, D.M.H. & Macklin, R.L., 1977. Nucl. Phys. A, 279, 317.

Newman, M.J., 1973. Masters Thesis, Rice University.

Orlov, M.Ya. & Rodriguez, M.H., 1974. Astr. Astrophys., 31, 203.

Osmer, P.S. & Peterson, D.M., 1974. Astrophys. J., 187, 117.

Paczynski, B., 1971. Acta. Ast. 21, 1.

Pandey, M.S., Gang, J.B., Macklin, R.L. & Halperian, J., 1977. Phys. Rev. C, 15, 615.

Peters, J.G., 1960. Astrophys. J., 154, 225.

- Popper, D.M., 1942. *Publ. astr. Soc. Pacific*, 54, 160.
- Reimer, D., 1975. *Mem. Soc. R. Sci. Liege*, 6e Ser. B, 369.
- Renzini, A., 1979. in, *Stars And Star Systems*, p155, Ed. Westerlund, B.E. (Reidel).
- Renzini, A., 1981. in, *Effects Of Mass Loss On Stellar Evolution*, p319, Eds. Chiosi, C. & Stalio, R. (Reidel).
- Renzini, A., 1982. in, *Wolf-Rayet Stars: Observations, Physics, Evolution*, p413. Eds. Loore, C.W.H. de & Willis, A.J. (Reidel).
- Richer, H.B., 1981. *Astrophys. J.*, 243, 744.
- Richtmyer, R.D. & Morton, K.W., 1957. *Difference Methods For Initial Value Problems* (Wiley & Sons).
- Rood, R.T., 1972. *Astrophys. J.*, 177, 681.
- Rose, W.K., 1966. *Astrophys. J.*, 146, 838.
- Rose, W.K., 1967. *Astrophys. J.*, 150, 193.
- Rose, W.K., 1972. *Stellar Evolution*. Ed. Chiu, H-Y., Cambridge-MIT Press.
- Rose, W.K. & Smith, R., 1972. *Astrophys. J.*, 173, 385.
- Sackmann, I.J., 1977. *Astrophys. J.*, 212, 159.
- Sackmann, I.J. & Boothroyd, A.I., 1985. *Astrophys. J.*, 293, 154.
- Sackman I-J., Smith R.L. & Despain K.H., 1974. *Astrophys. J.*, 187, 555.
- Saha, M.N., 1921. *Proc. Roy. Soc. London* A99, 135.
- Saio, H., Wheeler, J.C. & Cox, J.P., 1984. *Astrophys. J.*, 281, 318.
- Salpeter, E.E., 1954. *Austr. J. Phys.*, 7, 373.
- Sanders, R.H., 1967. *Astrophys. J.*, 150, 971.
- Scalo, J.M., 1980. *Physical Processes In Red Giants*, p77. Ed. Renzini, A. & Iben, I. Jr. (Reidel).
- Scalo, J.M. & Ulrich, R.K., 1973. *Astrophys. J.*, 183, 151.
- Schönberner, D., 1975. *Astr. Astrophys.* 44, 383.
- Schönberner, D., 1977. *Astr. Astrophys.* 57, 437.
- Schönberner, D., 1979. *Astr. Astrophys.* 79, 108.
- Schönberner, D. & Wolf, R.E.A., 1974. *Astron. Astrophys.*, 37, 87.
- Schuster, A., 1905. *Astrophys. J.*, 21, 1.
- Schwarzschild, K. Von, 1906. *Nach. Ges. Gott.*, 195, 41.

- Schwarzschild, M. & Härm, R. 1962. *Astrophys. J.*, 136, 158.
- Schwarzschild, M. & Härm, R. 1965. *Astrophys. J.*, 142, 855.
- Schwarzschild, M. & Härm, R., 1967. *Astrophys. J.*, 150, 961.
- Schwarzschild, M. & Selberg, H., 1962. *Astrophys. J.*, 136, 150.
- Searle, L., 1961. *Astrophys. J.* 133, 531.
- Seeger, P.A., Fowler, W.A. & Clayton, D.D., 1965. *Astrophys. J.*, Suppl. No. 9, 11, 21.
- Spencer, R.R. & Macklin, R.L., 1976. *Nucl. Sci. & Eng.*, 61, 346.
- Steiglitz, R.G., Hockenluey, R.W. & Block, R.C., 1971. *Nucl. Phys. A*, 163, 592.
- Stone, R.P., 1979. *Publ. astr. Soc. Pacific*, 91, 389.
- Stothers, R. & Chin, C-W., 1972. *Astrophys. J.*, 177, 155.
- Suess, H.E., & Urey, H.E., 1956. *Rev. Mod. Phys.* 28, 53.
- Sweigart, A.V., 1974. *Astrophys. J.*, 189, 289.
- Taylor, A., 1921. *Proc. London Math. Soc. ser. 2*, 20, 196.
- Thomas, H.-C., 1967, *Zs. Ap.*, 67, 420.
- Thomas, H.-C., 1970. *Ap. Space Sci.*, 6, 400.
- Thackeray, A.D. & Wesselink, A.J., 1952. *Obs.*, 72, 248.
- Totochava, A.G., 1973. *Astron. Circ. U.R.S.S. No. 791*, 7.
- Trimble, V., 1972. *Mon. Not. R. astr. Soc.*, 156, 411.
- Truran, J.W. & Iben, I. Jr., 1977. *Astrophys. J.*, 216, 797.
- Truran, J.W., 1973. *Proc. of the Red Giant Conference*, p394. Eds. Johnson, H.R., Mutsschleener, J.P. & Peery, B.F., Bloomington: Indiana University.
- Ulrich, R.K., 1973. in *Explosive Nucleosynthesis*, p139, Eds. Schramm, W.D., Arnett, D.N. (Austin: University of Texas Press).
- Ulrich, R.K. & Scalo J.M., 1972. *Astrophys. J.*, 176, L37.
- Unno, W., 1970. *Publ. astr. Soc. Pacific*, 22, 299.
- Van Horn, H.M. & Salpeter, E.E., 1967. *Phys. Rev.*, 157, 751.
- Voigt, W., 1913. *Phys. Zeits.*, 14, 377.
- Walker, H.J. & Hill, P.W., 1985. (submitted to *Astron. Astrophys. Suppl.*).
- Walker, H.J. & Kilkenny, D., 1980. *Mon. Not. R. astr. Soc.*, 190, 299.
- Walker, H.J. & Schönberner, D., 1981, *Astr. Astrophys.*, 97, 291.
- Walker, H.J., 1979. Ph.D. Thesis, University of St. Andrews.

- Walter, G., Käppelen, F. & Bao, Z.Y., 1982. Ann.Rept.Kernforechungerzentrum, Karlsruhe, KfK3427.
- Ward, R.A. & Newman, M.J., 1978. Astrophys.J., 219, 195.
- Ward, R.A., & Newman, M.J. & Clayton, D.D., 1976. Astrophys.J. Suppl., 31, 33.
- Warner, B., 1967. Mon.Not.R.astr.Soc. 137, 119.
- Waters, B.H.J., 1966. R.astr.Soc.N.Zealand Circular 119.
- Webbink, R.F., 1984. Astrophys.J., 277, 355.
- Weigert, A., 1966. Zs.f.Ap., 64, 395.
- Weigmann, H., Macklin, R.L., & Harvey, J.A., 1976. Phys.Rev.C, 14, 1328.
- Wentzel, G., 1926, Z.Physik 38, 518.
- Wood, P.R., 1976. Mon.Not.R.astr.Soc., 174, 531.
- Wood, P.R., 1981. Physical Processes In Red Giants, p135. Ed.Renzini, A. & Iben, I.Jr. (Reidel).
- Wood, P.R., 1982. preprint.
- Woosley, S.E., Fowler, W.A., Holmes, J.A. & Zimmerman, B.A., 1978. Atomic Data and Nuclear Data Tables, Vol. 22, 5, 306.
- Wright, S.L., & Argyros, J.D., 1975. Comm.Univ. of London Obs. No. 76.